frontiers | Research Topics

High-throughput field phenotyping to advance precision agriculture and enhance genetic gain, volume II

Edited by
Andreas Hund, Urs Schmidhalter, Fred Van Eeuwijk,
Wei Guo, David Matthew Deery and Sindhuja Sankaran

Published in
Frontiers in Plant Science

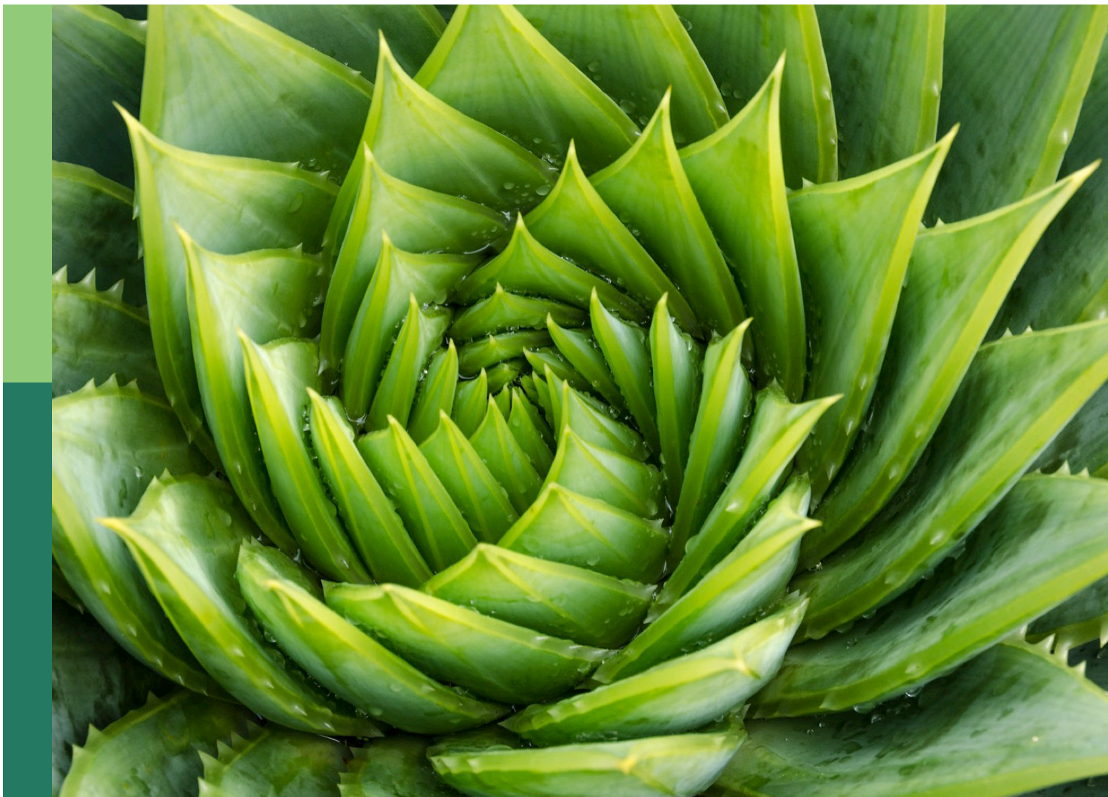

ISSN 1664-8714
ISBN 978-2-8325-4545-4
DOI 10.3389/978-2-8325-4545-4

About Frontiers

Frontiers is more than just an open access publisher of scholarly articles: it is a pioneering approach to the world of academia, radically improving the way scholarly research is managed. The grand vision of Frontiers is a world where all people have an equal opportunity to seek, share and generate knowledge. Frontiers provides immediate and permanent online open access to all its publications, but this alone is not enough to realize our grand goals.

Frontiers journal series

The Frontiers journal series is a multi-tier and interdisciplinary set of open-access, online journals, promising a paradigm shift from the current review, selection and dissemination processes in academic publishing. All Frontiers journals are driven by researchers for researchers; therefore, they constitute a service to the scholarly community. At the same time, the *Frontiers journal series* operates on a revolutionary invention, the tiered publishing system, initially addressing specific communities of scholars, and gradually climbing up to broader public understanding, thus serving the interests of the lay society, too.

Dedication to quality

Each Frontiers article is a landmark of the highest quality, thanks to genuinely collaborative interactions between authors and review editors, who include some of the world's best academicians. Research must be certified by peers before entering a stream of knowledge that may eventually reach the public - and shape society; therefore, Frontiers only applies the most rigorous and unbiased reviews. Frontiers revolutionizes research publishing by freely delivering the most outstanding research, evaluated with no bias from both the academic and social point of view. By applying the most advanced information technologies, Frontiers is catapulting scholarly publishing into a new generation.

What are Frontiers Research Topics?

Frontiers Research Topics are very popular trademarks of the *Frontiers journals series*: they are collections of at least ten articles, all centered on a particular subject. With their unique mix of varied contributions from Original Research to Review Articles, Frontiers Research Topics unify the most influential researchers, the latest key findings and historical advances in a hot research area.

Find out more on how to host your own Frontiers Research Topic or contribute to one as an author by contacting the Frontiers editorial office: frontiersin.org/about/contact

High-throughput field phenotyping to advance precision agriculture and enhance genetic gain, volume II

Topic editors
Andreas Hund – ETH Zürich, Switzerland
Urs Schmidhalter – Technical University of Munich, Germany
Fred Van Eeuwijk – Wageningen University and Research, Netherlands
Wei Guo – The University of Tokyo, Japan
David Matthew Deery – Commonwealth Scientific and Industrial Research Organisation (CSIRO), Australia
Sindhuja Sankaran – Washington State University, United States

Citation
Hund, A., Schmidhalter, U., Van Eeuwijk, F., Guo, W., Deery, D. M., Sankaran, S., eds. (2024). *High-throughput field phenotyping to advance precision agriculture and enhance genetic gain, volume II*. Lausanne: Frontiers Media SA.
doi: 10.3389/978-2-8325-4545-4

Table of contents

frontiers | Frontiers in Plant Science

ORIGINAL RESEARCH
published: 15 April 2022
doi: 10.3389/fpls.2022.866301

Biangular-Combined Vegetation Indices to Improve the Estimation of Canopy Chlorophyll Content in Wheat Using Multi-Angle Experimental and Simulated Spectral Data

Weiping Kong[1]*, Wenjiang Huang[2]*, Lingling Ma[1], Chuanrong Li[1], Lingli Tang[1], Jiawei Guo[2,3], Xianfeng Zhou[4] and Raffaele Casa[5]

[1] *Key Laboratory of Quantitative Remote Sensing Information Technology, Aerospace Information Research Institute, Chinese Academy of Sciences, Beijing, China,* [2] *State Key Laboratory of Remote Sensing Science, Aerospace Information Research Institute, Chinese Academy of Sciences, Beijing, China,* [3] *School of Marine Technology and Geomatics, Jiangsu Ocean University, Lianyungang, China,* [4] *College of Life Information Science and Instrument Engineering, Hangzhou Dianzi University, Hangzhou, China,* [5] *Department of Agricultural and Forestry Sciences (DAFNE), Università degli Studi della Tuscia, Viterbo, Italy*

Canopy chlorophyll content (CCC) indicates the photosynthetic functioning of a crop, which is essential for the growth and development and yield increasing. Accurate estimation of CCC from remote-sensing data benefits from including information on leaf chlorophyll and canopy structures. However, conventional nadir reflectance is usually subject to the lack of an adequate expression on the geometric structures and shaded parts of vegetation canopy, and the derived vegetation indices (VIs) are prone to be saturated at high CCC level. Using 3-year field experiments with different wheat cultivars, leaf colors, structural types, and growth stages, and integrated with PROSPECT+SAILh model simulation, we studied the potential of multi-angle reflectance data for the improved estimation of CCC. The characteristics of angular anisotropy in spectral reflectance were investigated. Analyses based on both simulated and experimental multi-angle hyperspectral data were carried out to compare performances of 20 existing VIs at different viewing angles, and to propose an algorithm to develop novel biangular-combined vegetation indices (BCVIs) for tracking CCC dynamics in wheat. The results indicated that spectral reflectance values, as well as the coefficient of determination (R^2) between mono-angular VIs and CCC, at back-scattering directions, were mostly higher than those at forward-scattering directions. Mono-angular VIs at +30° angle, were closest to the hot-spot position in our case, achieved the highest R^2 among 13 viewing angles including the nadir observation. The general formulation for the newly developed BCVIs was $BCVI_{VI} = f \times VI_{(\theta 1)} - (1 - f) \times VI_{(\theta 2)}$, in which the VI was used to characterize chlorophyll status, while the subtraction of VI at θ1 and θ2 viewing angles in a proportion was used to highlight the canopy structural information. From our result, the values of the θ1 and θ2 around hot-spot and dark-spot positions, and the *f*

Edited by:
Urs Schmidhalter,
Technical University of Munich,
Germany

Reviewed by:
Luca Vitale,
Institute for Agricultural and Forestry
Systems in the Mediterranean (CNR),
Italy
Lei Deng,
Capital Normal University, China

***Correspondence:**
Weiping Kong
kongwp@aircas.ac.cn
Wenjiang Huang
huangwj@aircas.ac.cn

Specialty section:
This article was submitted to
Technical Advances in Plant Science,
a section of the journal
Frontiers in Plant Science

Received: *31 January 2022*
Accepted: *09 March 2022*
Published: *15 April 2022*

Citation:
Kong W, Huang W, Ma L, Li C,
Tang L, Guo J, Zhou X and Casa R
(2022) Biangular-Combined
Vegetation Indices to Improve
the Estimation of Canopy Chlorophyll
Content in Wheat Using Multi-Angle
Experimental and Simulated Spectral
Data. Front. Plant Sci. 13:866301.
doi: 10.3389/fpls.2022.866301

of 0.6 or 0.7 were found as the optimized values. Through comparisons revealed that large improvements on CCC modeling could be obtained by the BCVIs, especially for the experimental data, indicated by the increase in R^2 by 25.1–51.4%, as compared to the corresponding mono-angular VIs at +30° angle. The $\text{BCVI}_{\text{MCARI}[705,750]}$ was proved to greatly undermine the saturation effect of mono-angular MCARI[705,750], expressing the best linearity and the most sensitive to CCC, with R^2 of 0.98 and 0.72 for simulated and experimental data, respectively. Our study will eventually have extensive prospects in monitoring crop phenotype dynamics in for example large breeding trials.

Keywords: winter wheat, multi-angle hyperspectral remote sensing, canopy chlorophyll content, biangular combination, crop phenotype

INTRODUCTION

Canopy chlorophyll content (CCC) is defined as the total amount of chlorophyll present in the canopy per unit ground area. The CCC, as the product of leaf chlorophyll content (LCC) and leaf area index (LAI), is capable of indicating the overall characteristics of plant assemblages, to avoid the deficiency of LCC, which mainly involves the information of individual plant conditions. It is an important phenotypic trait for crop breeding since it can represent the plant's capacity to intercept and use sunlight through photosynthesis. Also, it is a key factor influencing crop biological function with consequences on many aspects, including crop phenotypes and plant stress, as well as crop quality and yield (Merzlyak et al., 1999; Huang et al., 2011; Gutierrez et al., 2015). In addition, CCC is proven to be very sensitive to N availability in the soil (Hinzman et al., 1986), thus precise monitoring of CCC plays an important role in optimizing N fertilizer strategy, and consequently, obtaining a higher yield, and at the same time, avoiding the waste of resources and the pollution of farmland ecosystem in the context of precision agriculture. In the past decades, the significance of CCC for crop growth and development status and agricultural management has motivated the interest and substantial efforts of researchers on high-throughput determination of crop CCC using remote-sensing data (Broge and Leblanc, 2001; Broge and Mortensen, 2002; Li et al., 2016), and has provided the rationale for improving our capability to remotely measure it at the field or larger scales.

Conventionally, CCC estimation was mostly based on spectral reflectance acquired from a near nadir direction. Several optical indices have arisen in the literatures and have been proven to be well-correlated with vegetation chlorophyll content (Daughtry et al., 2000; Sims and Gamon, 2002; Gitelson et al., 2006; Wu et al., 2008). As the significant relationship between leaf nitrogen and chlorophyll (Li et al., 2013), a series of nitrogen indices [e.g., Nitrogen Reflectance Index (NRI), Normalized Difference of the Double-peak Areas (NDDA), Ratio Vegetation Index (RVI), Normalized Difference Vegetation Index green-blue (NDVI_{g-b})] were proposed for tracking nitrogen changes according to spectral features of chlorophyll (Bausch and Duke, 1996; Hansen and Schjoerring, 2003; Xue et al., 2004; Feng et al., 2014), and in turn, they have also been investigated to assess crop chlorophyll status (Li et al., 2016). However, most of these vegetation indices (VIs) were prone to suffering from saturation (Sims and Gamon, 2002; Haboudane et al., 2004), thus, reducing their sensitivity to high chlorophyll content. Researchers have been hard at work finding ways to cope with this issue, although quite difficult, if not impossible, to achieve. One of the approaches is to use the red-edge bands to take the place of red bands partly due to the unique characteristics and potential of the red edge region for chlorophyll estimation (Blackburn, 1998). For example, Gitelson and Merzlyak (1994) focused on improving the commonly and widely used Normalized Difference Vegetation Index (NDVI) and Simple Ratio (SR) and proposed the NDVI[705,750] and SR[705,750]. Wu et al. (2008) developed the Modified Chlorophyll Absorption Ratio Index (MCARI[705,750]) and MCARI/Optimized Soil-adjusted Vegetation Index (MCARI/OSAVI[705,750]) based on previously published MCARI and MCARI/OSAVI (Daughtry et al., 2000), by taking into account the effect of quick saturation at the red band. Ground truth validation showed an appropriate result for high chlorophyll content estimation in winter wheat and maize. However, these VIs were calculated from the nadir spectral reflectance, which is mainly contributed by the upper leaves of the canopy (Li et al., 2013), making it very difficult to depict the chlorophyll information over the whole canopy, especially for the complicated canopies that vary in vegetation types, canopy structures, background contributions, etc. (Leblanc et al., 1997). Moreover, the lack of expression of information on the geometric structures and the shaded parts of vegetation canopy would limit the use of nadir-based VIs for accurate determination of chlorophyll status when upscaling to canopy level, and then, hardly an adequate description of characteristics of plant communities.

A possible alternative and complementary method to minimize these limitations presented above is the exploitation of multi-angle remote-sensing technology. Multi-angle observations contain much more information than the simple nadir observation since they capture the information of an area of interest from several different angles. It is demonstrated that multi-angle canopy reflectance has the ability of assessing three-dimensional canopy structure that is poorly detected by the nadir alone (Chen et al., 2003; Brown de Colstoun and Walthall, 2006), so they are expected to provide the possibility to evaluate CCC more accurately for crops. There have been studies showing that off-nadir spectral sensing generated more effective VIs for monitoring leaf biological parameters when compared to the nadir direction (Stagakis et al., 2010; Zhang et al., 2021). Several recent studies that used multi-angle spectral data also focused on developing new multi-angular VIs aiming to obtain truly better vegetation variables inversions (e.g., LAI, leaf nitrogen content, and water use efficiency) than the conventional VIs (Hasegawa et al., 2010; Wu et al., 2010; He et al., 2016; Zhang et al., 2021). Indeed, these VIs have enriched the methodology for vegetation parameters estimation with remote-sensing technology. Nevertheless, few researchers have reported the construction of multi-angular VIs for crop CCC retrieval.

In recent years, some multi-angle observing data are already available from sensors mounted on different remote sensing platforms. Compared to airborne and spaceborne platforms, such as Multi-angle Imaging Spectroradiometer (MISR), the Compact High-Resolution Imaging Spectrometer (CHRIS), the ground-based goniometers, are used more extensively, since they can measure vegetation canopy at higher spatial resolution, as well as extremely various directions, by adjusting angular sampling and viewing height in a very flexible way. In addition, the PROSPECT+SAILh (PROSAIL) model describes how light propagation within vegetation canopy and has been successfully used before to develop and test various VIs for estimating leaf parameters for multiple types of vegetation including wheat (Haboudane et al., 2004; Wu et al., 2008; Zhou et al., 2019). It allows for the simulation of reflectance at arbitrary viewing and illumination geometries and a set of leaf and canopy parameters, providing another convenient avenue to create multi-angle spectral data and characterize different traits for a wheat phenotype.

The main purpose of this study is to propose the BCVI that includes abundant chlorophyll and structural information of plant communities, yet, resistant to saturation limits, using multi-angle spectral data, then, benefits the high-throughput and nondestructive determination of crop CCC compared to the conventional mono-angular VIs. The analyses are based on a simulated canopy multi-angle hyperspectral reflectance dataset produced by PROSAIL model in combination with real ground measured data collected from 3-year field campaigns. The study is composed of three phases: (1) to analyze the characteristics of angular anisotropy in spectral reflectance; (2) to examine the performances of previously published mono-angular VIs in CCC estimation and identify the VIs that is sensitive to CCC of winter wheat; (3) to develop the new BCVIs by coupling spectral and angular information and compare their performances with the corresponding mono-angular VIs, to evaluate the improvement of CCC estimation when the multi-angle observation was used.

MATERIALS AND METHODS

Experimental Design

The experiments were conducted over 3 years (2004, 2005, and 2007) at Xiaotangshan National Precision Agriculture Experimental Site (116°120′E, 40°13.20′N), in Changping district, Beijing, China (**Figure 1**). This experimental site has been operational since 2001 and used for precision agriculture research. The crop selected in this study was winter wheat, which was cultivated in silty clay soil with sufficient water supply and uniform nutrient management. The nutrients of soil in the topsoil layer (0–.20 m depth) were as follows: 1.42–2.2% of organic matter, 117.6–129.1 mg/kg of available potassium, and 20.1–55.4 mg/kg of available phosphorus. Information on different measurement times, wheat cultivars, leaf colors, leaf structural types, and sampling dates were summarized in **Table 1**. All cultivars were sown with a row space of 25 cm, each cultivar was planted in a plot and repeated three times. A total of 60 datasets, including canopy multi-angle spectral reflectance and corresponding CCC, were collected during the 3 years.

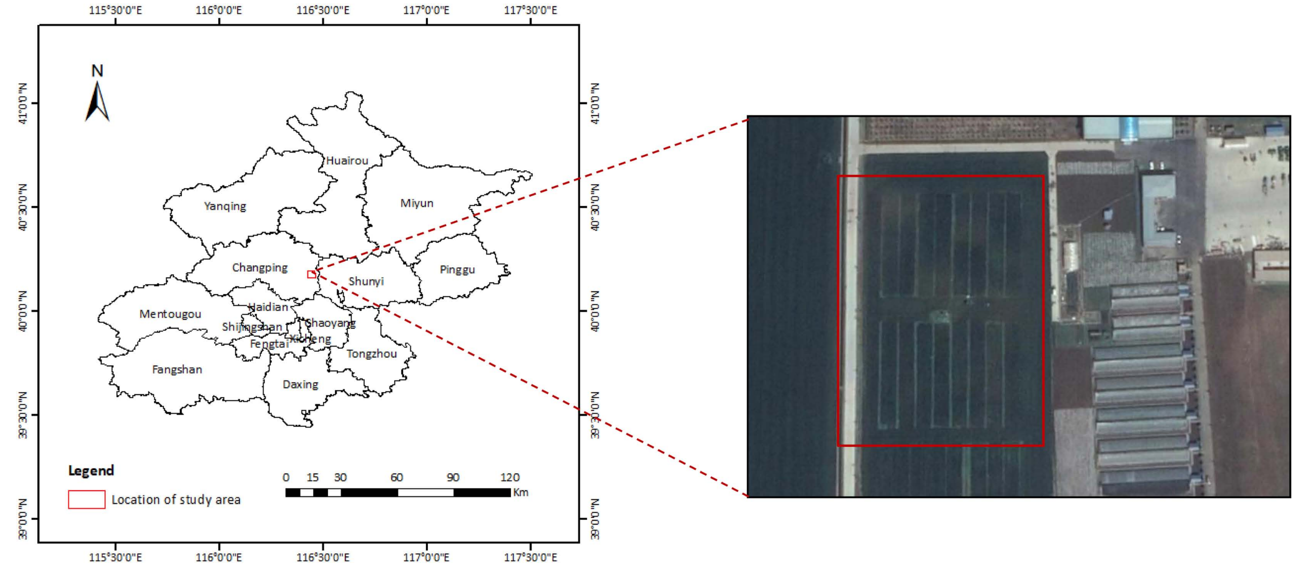

FIGURE 1 | The overview map of study area (cited from Kong et al., 2021).

TABLE 1 | Different measurement times, wheat cultivars, leaf colors, leaf structural types, and sampling dates for the experiments.

Year	Wheat cultivar	Leaf color	Leaf structural type	Sampling date
2004	Laizhou 3279	Dark green	Erective	Stem elongation (Z34), booting (Z47), heading (Z59)
	Linkang 2	Dark green	Loose	
	Jing 411	Light green	Erective	
	9507	Light green	Loose	
2005	Nongda 3291	Dark green	Erective	Stem elongation (Z34), booting (Z47), heading (Z59)
	Jingdong 8	Dark green	Middle	
	Linkang 2	Dark green	Loose	
	Lumai 21	Light green	Erective	
	Jingwang 10	Light green	Middle	
	9507	Light green	Loose	
2007	Laizhou 3279	Dark green	Erective	Stem elongation (Z31), stem elongation (Z34), booting (Z47), heading (Z59), milk-filling (Z73)
	I-93	Dark green	Erective	
	Linkang 2	Dark green	Loose	
	Jing 411	Light green	Erective	
	Jing 9428	Light green	Loose	
	9507	Light green	Loose	

In situ Measurements

Measurement of Canopy Multi-Angle Spectral Reflectance

Canopy multi-angle spectral reflectance was measured in each plot using an ASD FieldSpec 3 spectrometer (Analytical Spectral Devices, Boulder, CO, United States), with a 25° field-of-view fiber optics, under clear sky conditions between 11:00 and 13:00 (Beijing local time) when minimum variations in solar view angle occur. The instrument records spectral radiance with a sampling interval of 1.4 nm and a resolution of 3 nm between 350 and 1,050 nm, and a sampling interval of 2.0 nm and a resolution of 10 nm between 1,000 and 2,500 nm. It was held on a rotating bracket to enable spectral measurements of the same target from different angles in a short time. Canopy multi-angle spectral measurements were conducted in the solar principal plane (constructed by the direction of incident direct sunlight, and the direction of the normal to surface target) at different viewing zenith angles (θ). A total of 13 viewing angles varied from $-60°$ to $+60°$ with 10° incremental step (i.e., $\theta = 0°$, $\pm 10°$, $\pm 20°$, $\pm 30°$, $\pm 40°$, $\pm 50°$, and $\pm 60°$), where a positive angle refers to the back-scattering direction (the side facing away from the sun), a negative angle refers to the forward-scattering direction (the side facing into the sun). The nadir (i.e., $\theta = 0°$) spectral measurements were made at a height of approximately 1.3 m above the canopy top. A white Spectralon (Labsphere, Inc., NH, United States) reference panel was used under the same illumination conditions to convert the spectral radiance to reflectance before and after canopy spectral measurements. Twenty scans were performed and averaged to obtain canopy spectral reflectance per viewing angle. More detailed information about the multi-angle spectral measurements can be found in previous studies (Wu et al., 2010; Huang et al., 2011).

Determination of Canopy Chlorophyll Content

Four 1-m consecutive rows of wheat in the plot, within the footprint of canopy multi-angle reflectance acquisitions, were harvested by cutting off the aboveground portions, then, put in cooled black plastic bags and transported to the laboratory to measure the biological parameters. Leaves that fully expanded and showed homogenous color, as well as no visible sign of damage, were sampled from top to bottom of the canopy. Two leaf disks (about 0.25 cm^2) were cut-off from each leaf sample. One part of the disks were used for the chlorophyll extraction, which was carried out by immersing and grinding the disk in 10 mL aqueous acetone/distilled water buffer solution (80:20, volume proportion). After storing the solution in darkness for more than 24 h, the absorbance was measured with a UV-VIS spectrophotometer (Perkin-Elmer, Lambda 5, Waltham, MA, United States) at 645 and 663 nm wavelengths. Leaf chlorophyll *a* and chlorophyll *b* content (mg/L) were determined using Equations 1, 2 (Lichtenthaler, 1987). Another part of leaf disks was weighted after drying in an oven at 80°C for 48 h to determine leaf dry weight (DW, g), and then, used to compute leaf mass per area (LMA, g/cm^2), defined as the ratio between leaf dry weight and leaf area (Poorter et al., 2009). The LAI measurement was conducted by the laboratory analysis, 10% of all the sampled leaves were taken as a subsample for leaf area measurement using a Li-Cor 3100 area meter (Lincoln, NB, United States), and the weight of leaves was recorded to scale up to the LAI of the 1 m^2 area. The CCC (μg/cm^2) was calculated as the product of LCC (μg/cm^2) and LAI, as shown in Equation 6.

$$\mathrm{LCCa}\ (\mathrm{mg/L}) = 12.25\ \mathrm{A}_{663} - 2.79\ \mathrm{A}_{645} \tag{1}$$

$$\mathrm{LCCb}\ (\mathrm{mg/L}) = 21.50\ \mathrm{A}_{645} - 5.10\ \mathrm{A}_{663} \tag{2}$$

$$\mathrm{LCCa}\ (\mathrm{mg/g}) = [\mathrm{LCCa}\ (\mathrm{mg/L}) \times \mathrm{V_T}\ (\mathrm{ml})]/[\mathrm{DW}\ (\mathrm{g}) \times 1{,}000] \tag{3}$$

$$\mathrm{LCCb}\ (\mathrm{mg/g}) = [\mathrm{LCCb}\ (\mathrm{mg/L}) \times \mathrm{V_T}(\mathrm{ml})]/[\mathrm{DW}\ (\mathrm{g}) \times 1{,}000] \tag{4}$$

$$\mathrm{LCC}\ (\mu\mathrm{g/cm^2}) = [\mathrm{LCCa}\ (\mathrm{mg/g}) + \mathrm{LCCb}\ (\mathrm{mg/g})] \times \mathrm{LMA}\ (\mathrm{g/cm^2}) \times 1{,}000 \tag{5}$$

$$\mathrm{CCC}\ (\mu\mathrm{g/cm^2}) = \mathrm{LCC}\ (\mu\mathrm{g/cm^2}) \times \mathrm{LAI} \tag{6}$$

where A_{645} and A_{663} are the absorbances of extract solution at wavelength 645 and 663 nm, respectively; LCCa is leaf chlorophyll *a* content, LCCb is leaf chlorophyll *b* content, $\mathrm{V_T}$(ml) is the volume of extract solution.

PROSPECT+SAILh Model Simulation

In order to evaluate whether multi-angle observations can lead to the improved estimation of CCC, PROSAIL radiative transfer model, a coupled model of the leaf optical model PROSPECT and the canopy bidirectional reflectance model SAILh, was used for simulation of canopy multi-angle reflectance and sensitivity analysis of VIs. At the leaf level, PROSPECT model simulates leaf reflectance and transmittance between 400 and 2,500 nm at 1 nm increment, as a function of a series of biochemical parameters, including leaf mesophyll structure parameter (N), LCC, leaf carotenoid content (Car), leaf brown pigment content (C_{brown}), leaf equivalent water thickness (C_w), and leaf dry matter content (C_m). The SAILh model has the capacity to simulate canopy multi-angle spectral reflectance, which is described as a function of LAI, average leaf angle (ALA), hot-spot parameter (hspot), soil moisture parameter (psoil), a fraction of diffuse incident radiation (skyl), and the parameters controlled the view-sensor-illumination geometry, i.e., solar zenith angle, view zenith angle, and the relative azimuth angle between the sun and sensor. The combined PROSPECT+SAILh model has been extensively used in a large number of studies and applications (Jacquemoud et al., 2009).

To perform the PROSAIL simulation, we set the LCC ranged from 25 μg/cm^2 to 100 μg/cm^2 in steps of 5 μg/cm^2, whilst the LAI ranged from 1 to 8 in steps of 0.5, based on the field measured data regarding the wheat investigated in this study. The CCC was the product of the model input parameters LCC and LAI. The solar zenith angle was set to 30°, the values of view zenith angles were varied from 0° to 60° by changing the observation angle in 10° increments, as well as the relative azimuth angles between the sun and the sensor was set to 0° (corresponding to the back-scattering directions) and 180° (corresponding to the forward-scattering directions), which were all consistent with the field measurements. Input parameter C_{brown} was assigned a value of 0 since there were no brown leaves observed in the wheat canopy after visual inspection. Other input variables were either determined at the averaged values in accordance with the experimental plots or taken from the published literatures (Haboudane et al., 2004; Yu et al., 2014). A dataset of 3,120 canopy multi-angle reflectance simulations was generated by running PROSAIL model using a random combination of the input parameters (**Table 2**).

Mono-Angular and Biangular-Combined Vegetation Indices

Canopy spectral reflectance measured from different viewing angles was processed and analyzed as an individual dataset in this study. A total of 20 published VIs that were previously proposed for leaf chlorophyll and nitrogen estimates were selected. They were grouped into chlorophyll indices and nitrogen indices (**Table 3**). On one hand, these VIs were calculated from spectral reflectance obtained at a given viewing angle among 13 viewing angles, referred to as mono-angular VIs, then were tested for the potential of CCC estimation. On the other hand, we established a series of BCVIs based on the VIs shown in **Table 3**. The formula is given in Equation 7. The values of each VI at all the possible two-angle observations, selected from 13 viewing zenith angles between −60° and +60°, were combined in form of subtraction, with a parameter "*f*" changing from 0 to 1 at a step of 0.1 was used as an adjusting factor, resulting in 858 combinations of viewing angles and adjusting factor values. The BCVI built by a given VI was referred to as $BCVI_{VI}$. In the selection of the VI used in the BCVI, the VI should be highly sensitive to the dynamics of chlorophyll. So, the VIs that achieved better results in quantifying chlorophyll content at mono-angular observations (shown in **Figure 4** below) were chosen. Additionally, the value of *f* represented the proportion of VI at one angle (referred to as $VI_{(\theta1)}$), and the value of (1-*f*) represented the proportion of VI at the second angle (referred to as $VI_{(\theta2)}$). The difference of VI between the two angles was used to strengthen the canopy structural trait of the crop. As a consequence, this construction algorithm is expected to allow the CCC estimation with high accuracy when using the developed BCVI. All the calculations were implemented using MATLAB 8.3 (The MathWorks, Inc., Natick, MA, United States).

TABLE 2 | Input parameters of PROSAIL model.

Parameters	Units	Values	Steps
PROSPECT model			
Leaf mesophyll structure parameter (N)	–	1.55	–
Leaf chlorophyll content (LCC)	μg/cm^2	25–100	5
Leaf carotenoid content (Car)	μg/cm^2	10	–
Leaf brown pigment content (C_{brown})	μg/cm^2	0	–
Leaf equivalent water thickness (C_w)	cm	0.013	–
Leaf dry matter content (C_m)	g/cm^2	0.0045	–
SAILh model			
Leaf area index (LAI)	m^2/m^2	1–8	0.5
Average leaf angle (ALA)	Degree	Spherical	–
Hot-spot parameter (hspot)	–	0.15	–
Soil moisture parameter (psoil)	–	1	–
Fraction of diffuse incident radiation (skyl)	–	0.23	–
Solar zenith angle	Degree	30	–
View zenith angle	Degree	0–60	10
Relative azimuth angle between the sun and sensor	Degree	0–180	180

$$BCVI_{VI} = f \times VI_{(\theta1)} - (1 - f) \times VI_{(\theta2)}, \quad f = 0.1, 0.2, \cdots, 1 \tag{7}$$

Data Analysis

To investigate the angular anisotropy in spectral reflectance, the green, red, red edge, and near-infrared (NIR) bands (represent by 550, 680, 705, and 750 nm, respectively) were chosen because of their widespread use in deriving chlorophyll-related indices (Daughtry et al., 2000; Wu et al., 2008). We computed the normalized reflectance at all viewing zenith angles by normalizing the nadir reflectance as a reference for the above

TABLE 3 | Published vegetation indices used in the analyses.

Vegetation index	Formula	References
Chlorophyll indices		
PSNDa (pigment specific simple ratio for chlorophyll *a*)	$\frac{R_{800}-R_{680}}{R_{800}+R_{680}}$	Blackburn, 1998
PSNDb (pigment specific simple ratio for chlorophyll *b*)	$\frac{R_{800}-R_{635}}{R_{800}+R_{635}}$	Blackburn, 1998
NDVI[705,750] (normalized difference vegetation index using 705 and 750 nm bands)	$\frac{R_{750}-R_{705}}{R_{750}+R_{705}}$	Gitelson and Merzlyak, 1994
SR[705,750] (simple ratio using 705 and 750 nm bands)	$\frac{R_{750}}{R_{705}}$	Gitelson and Merzlyak, 1994
CI_{green} (chlorophyll index using green band)	$\frac{R_{790}}{R_{550}}-1$	Gitelson et al., 2006; Clevers and Kooistra, 2012
$CI_{rededge}$ (chlorophyll index using red edge band)	$\frac{R_{790}}{R_{710}}-1$	Gitelson et al., 2006; Clevers and Kooistra, 2012
MCARI (modified chlorophyll absorption ratio index)	$[(R_{700}-R_{670})-0.2(R_{700}-R_{550})]\left(\frac{R_{700}}{R_{670}}\right)$	Daughtry et al., 2000
MCARI[705,750] (modified chlorophyll absorption ratio index using 705 and 750 nm bands)	$[(R_{750}-R_{705})-0.2(R_{750}-R_{550})]\left(\frac{R_{750}}{R_{705}}\right)$	Wu et al., 2008
MCARI/OSAVI (MCARI/optimized soil-adjusted vegetation index)	$\frac{[(R_{700}-R_{670})-0.2(R_{700}-R_{550})]\left(\frac{R_{700}}{R_{670}}\right)}{(1+0.16)(R_{800}-R_{670})/(R_{800}+R_{670}+0.16)}$	Rondeaux et al., 1996; Daughtry et al., 2000
MCARI/OSAVI[705,750] (MCARI/OSAVI using 705 and 750 nm bands)	$\frac{[(R_{750}-R_{705})-0.2(R_{750}-R_{550})]\left(\frac{R_{750}}{R_{705}}\right)}{(1+0.16)(R_{750}-R_{705})/(R_{750}+R_{705}+0.16)}$	Wu et al., 2008
TCARI (transformed chlorophyll absorption ratio index)	$3\left[(R_{700}-R_{670})-0.2(R_{700}-R_{550})\left(\frac{R_{700}}{R_{670}}\right)\right]$	Haboudane et al., 2002
TCARI/OSAVI (TCARI/optimized soil-adjusted vegetation index)	$\frac{3\left[(R_{700}-R_{670})-0.2(R_{700}-R_{550})\left(\frac{R_{700}}{R_{670}}\right)\right]}{(1+0.16)(R_{800}-R_{670})/(R_{800}+R_{670}+0.16)}$	Haboudane et al., 2002
TCARI/OSAVI[705,750] (TCARI/OSAVI using 705 and 750 nm bands)	$\frac{3\left[(R_{750}-R_{705})-0.2(R_{750}-R_{550})\left(\frac{R_{750}}{R_{705}}\right)\right]}{(1+0.16)(R_{750}-R_{705})/(R_{750}+R_{705}+0.16)}$	Wu et al., 2008
TVI (triangular vegetation index)	$0.5[120(R_{750}-R_{550})-200(R_{670}-R_{550})]$	Broge and Leblanc, 2001
MTVI1 (modified TVI)	$1.2[1.2(R_{800}-R_{550})-2.5(R_{670}-R_{550})]$	Haboudane et al., 2004
REP (red edge position)	$700+40\times\frac{(R_{670}+R_{780})/2-R_{700}}{R_{740}-R_{700}}$	Clevers and Kooistra, 2012
Nitrogen indices		
$NDVI_{g-b}$ (normalized difference vegetation index using green and blue bands)	$\frac{R_{573}-R_{440}}{R_{573}+R_{440}}$	Hansen and Schjoerring, 2003
NRI (nitrogen reflectance index)	$\frac{R_{570}-R_{670}}{R_{570}+R_{670}}$	Bausch and Duke, 1996
NDDA (normalized difference of the double-peak areas)	$\frac{R_{755}+R_{680}-2\times R_{705}}{R_{755}-R_{680}}$	Feng et al., 2014
RVI (ratio vegetation index for nitrogen)	$\frac{R_{810}}{R_{560}}$	Xue et al., 2004

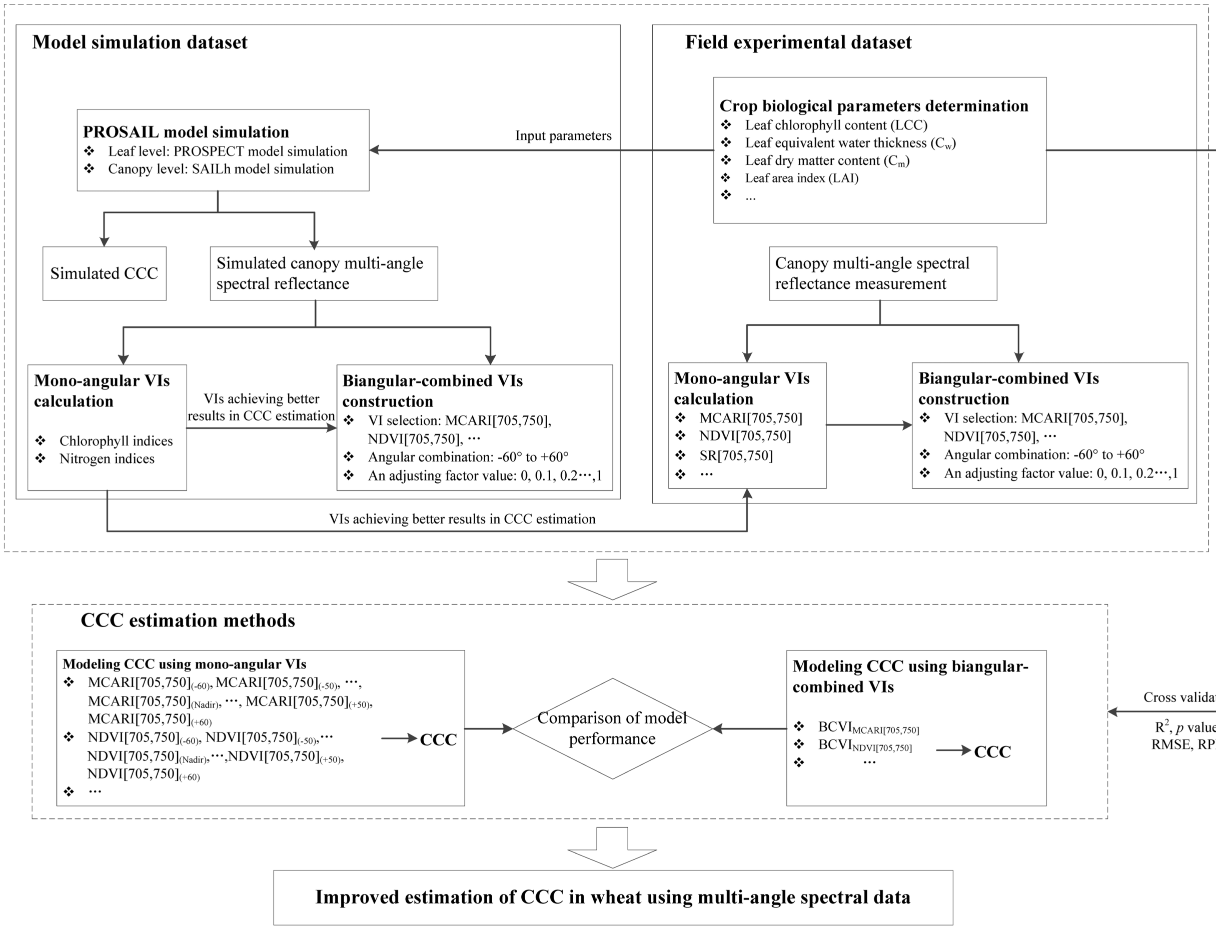

FIGURE 2 | A workflow diagram of canopy chlorophyll content estimation used in this study.

representative bands. Its formula was as follows:

$$\text{Normalized reflectance} = R_{(\theta)} / R_{(\text{Nadir})} \tag{8}$$

where $R_{(\theta)}$ and $R_{(\text{Nadir})}$ indicate the spectral reflectance obtained from a given viewing zenith angle among the 13 viewing angles between −60° and +60° and the nadir observation, respectively.

The abilities of mono-angular VIs and BCVIs in assessing CCC were evaluated using two datasets, one was a simulated dataset produced by the PROSAIL model, another was measured from the field campaigns. Linear regression was used to model the relationship between CCC and the two types of indices, while the leave-one-out cross-validation approach was used to validate the models. The coefficient of determination (R^2), p-value, and root mean square error (RMSE) were employed as indicators to evaluate the accuracy of estimation models. In addition, the ratio of performance to deviation (RPD), defined as the ratio between the standard deviations of the CCC to predict over RMSE (Richter et al., 2012), was also computed. The prediction ability of the model was interpreted according to the three classes of RPD: RPD > 2 is considered as excellent model performance, 1.4 < RPD < 2 is considered as good model performance, and RPD < 1.4 is considered as unacceptable model performance (Shepherd and Walsh, 2002; Razakamanarivo et al., 2011). The R^2, RMSE, and RPD were calculated as Equations 9–11. For each dataset, VIs that showed the highest R^2 and RPD, and the lowest RMSE with CCC was considered the optimal candidates for predicting CCC. Improvement of CCC estimation was assessed by comparing the estimations of CCC based on mono-angular data and based on multi-angular data. **Figure 2** shows the methodology of CCC estimation used in this study.

$$R^2 = \frac{\sum_{i=1}^{n}((y_{mea}^{i} - \bar{y}_{mea})(y_{est}^{i} - \bar{y}_{est}))^2}{\sum_{i=1}^{n}(y_{mea}^{i} - \bar{y}_{mea})^2 \sum_{i=1}^{n}(y_{est}^{i} - \bar{y}_{est})^2} \tag{9}$$

$$\text{RMSE} = \sqrt{\sum_{i=1}^{n}(y_{est}^{i} - y_{mea}^{i})^2 \Big/ n} \tag{10}$$

$$\text{RPD} = \frac{\text{SD}(mea)}{\text{RMSE}} \tag{11}$$

where y_{mea} is the measured CCC, $\bar{y}_{mea}$ is the average value of measured CCC, $\bar{y}_{est}$ is the estimated CCC, $\bar{y}_{est}$ is the average value of estimated CCC, n is the number of samples, and SD (mea) is the standard deviation of measured CCC.

RESULTS

Results Based on Model Simulation Data

Angular Anisotropy in Spectral Reflectance

The curves of normalized reflectance at different viewing angles for green, red, red edge, and NIR bands are shown in **Figure 3**. It was observed that angular anisotropies in spectral reflectance were pronounced. The reflectance obtained at back-scattering directions was higher than that at the nadir and forward-scattering directions over green to NIR bands, expressing larger normalized reflectance values ($R_{(\theta)}/R_{(Nadir)} > 1$). A dominant hot spot with the maximum reflectance appeared at +30° viewing angle at each band, which exactly matched the solar zenith angle in the principal plane. Compared to the back-scattering observations, changes of reflectance obtained from forward-scattering directions tended to be relatively stable. The dark-spot with the minimum reflectance occurred between −20° and −30° viewing angles. Judged by the fluctuations of normalized reflectance values, strong angular anisotropy was observed at chlorophyll absorbance band represented by the 680 nm, whereas weak angular anisotropy appeared in the 550 nm, the 705 nm, and particularly in the 750 nm.

Relationship of Mono-Angular Vegetation Indices With Canopy Chlorophyll Content

The linear regression models between the mono-angular VIs and CCC were established, the values of coefficient of determination (R^2) at different viewing observations are shown in **Table 4**. We found substantial variation in the ability of mono-angular VIs to accurately track the CCC of wheat. In general, the VIs that use bands in red edge and NIR performed better than those with similar formulas, but use bands in red and NIR across all observing angles, such as MCARI[705,750] vs. MCARI, MCARI/OSAVI[705,750] vs. MCARI/OSAVI, TCARI/OSAVI[705,750] vs. TCARI/OSAVI, NDVI[705,750] vs. PSNDa, which further confirmed the promising contribution of red edge bands in improving CCC estimate. Some VIs, however, showed a somewhat weaker

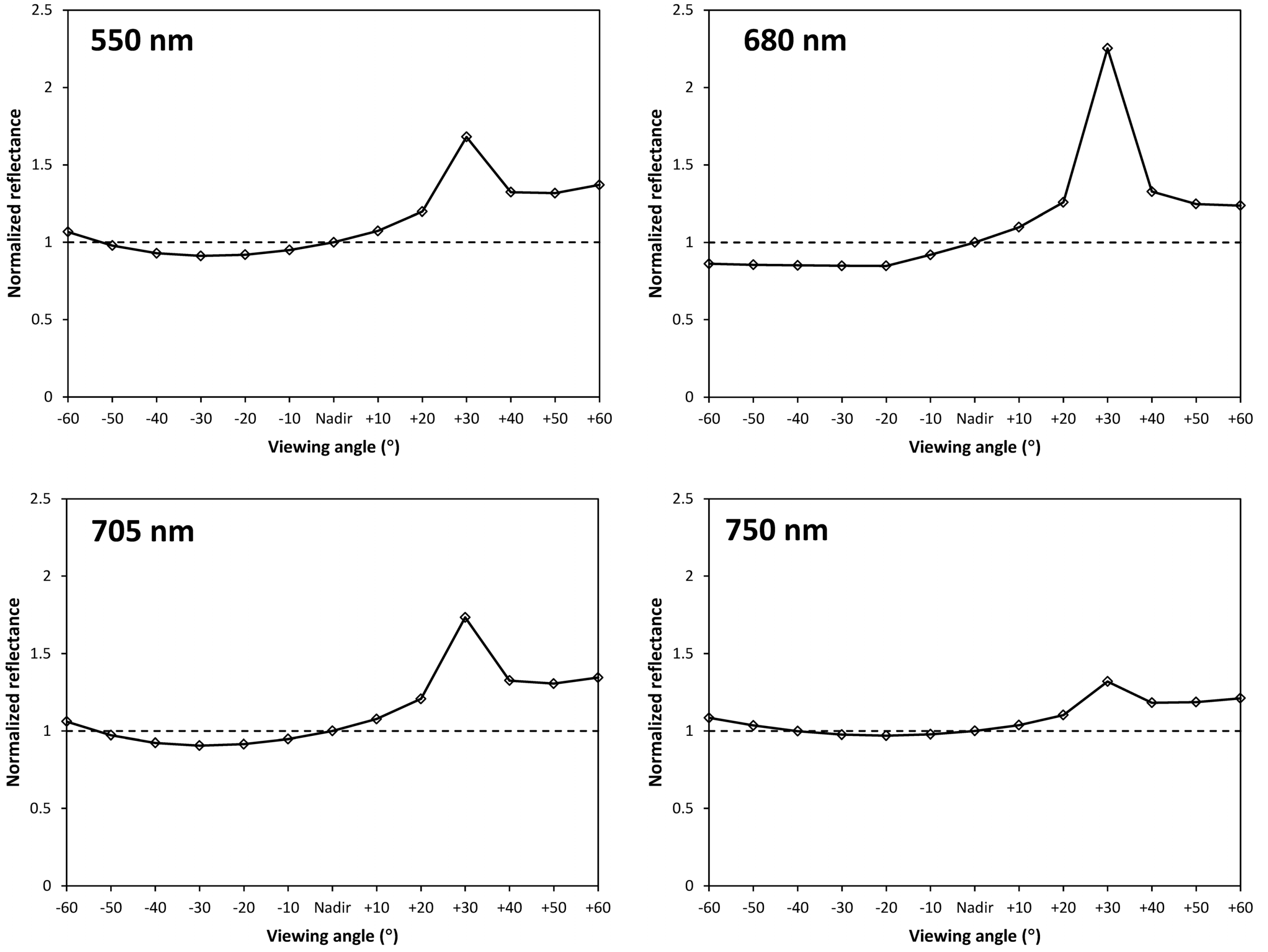

FIGURE 3 | The curves of normalized reflectance at different viewing angles for green (550 nm), red (680 nm), red edge (705 nm), and NIR (750 nm) bands. The viewing angles varied from –60° to +60° with 10° incremental steps, where a positive angle refers to the back-scattering direction, a negative angle refers to the forward-scattering direction. The dash lines indicate normalized reflectance = 1, where the reflectance was measured from the nadir direction.

TABLE 4 | The R^2 values of estimation models between canopy chlorophyll content and VIs at different viewing angles.

Vegetation index	−60	−50	−40	−30	−20	−10	Nadir	+10	+20	+30	+40	+50	+60
PSNDa	0.34**	0.34**	0.35**	0.36**	0.37**	0.37**	0.37**	0.38**	0.38**	0.46**	0.37**	0.35**	0.35**
PSNDb	0.51**	0.49**	0.48**	0.48**	0.48**	0.49**	0.49**	0.50**	0.51**	0.60**	0.52**	0.51**	0.52**
NDVI[705,750]	0.62**	0.65**	0.67**	0.68**	0.69**	0.69**	0.69**	0.70**	0.70**	0.77**	0.67**	0.64**	0.60**
SR[705,750]	0.71**	0.78**	0.82**	0.84**	0.85**	0.86**	0.85**	0.84**	0.83**	0.91**	0.78**	0.74**	0.68**
CI_{green}	0.74**	0.80**	0.84**	0.86**	0.88**	0.88**	0.88**	0.87**	0.86**	0.90**	0.81**	0.77**	0.71**
CI_{re}	0.75**	0.81**	0.84**	0.86**	0.87**	0.88**	0.87**	0.86**	0.85**	0.90**	0.80**	0.77**	0.72**
MCARI	0.16**	0.15**	0.14**	0.14**	0.14**	0.14**	0.14**	0.14**	0.13**	0.11**	0.15**	0.17**	0.20**
MCARI[705,750]	0.82**	0.87**	0.89**	0.90**	0.91**	0.91**	0.91**	0.91**	0.91**	0.93**	0.88**	0.85**	0.81**
MCARI/OSAVI	0.20**	0.19**	0.19**	0.19**	0.19**	0.19**	0.19**	0.19**	0.18**	0.16**	0.19**	0.21**	0.23**
MCARI/OSAVI[705,750]	0.82**	0.86**	0.88**	0.89**	0.90**	0.90**	0.90**	0.90**	0.89**	0.92**	0.87**	0.85**	0.81**
TCARI	0.24**	0.23**	0.23**	0.23**	0.22**	0.22**	0.21**	0.21**	0.19**	0.16**	0.20**	0.22**	0.24**
TCARI/OSAVI	0.36**	0.38**	0.40**	0.41**	0.42**	0.41**	0.41**	0.39**	0.37**	0.37**	0.35**	0.35**	0.34**
TCARI/OSAVI[705,750]	0.74**	0.81**	0.85**	0.87**	0.88**	0.88**	0.88**	0.87**	0.85**	0.90**	0.80**	0.76**	0.70**
TVI	0.07**	0.10**	0.12**	0.13**	0.14**	0.14**	0.15**	0.15**	0.16**	0.17**	0.14**	0.11**	0.08**
MTVI1	0.32**	0.35**	0.38**	0.39**	0.39**	0.40**	0.39**	0.39**	0.38**	0.36**	0.36**	0.34**	0.30**
REP	0.77**	0.80**	0.83**	0.84**	0.85**	0.85**	0.84**	0.83**	0.81**	0.76**	0.77**	0.76**	0.73**
$NDVI_{g-b}$	0.36**	0.38**	0.41**	0.43**	0.44**	0.45**	0.45**	0.44**	0.44**	0.47**	0.42**	0.40**	0.38**
NRI	NS	NS	NS	NS	NS	NS	NS	NS	NS	NS	NS	0.02*	0.06**
NDDA	0.49**	0.52**	0.53**	0.54**	0.54**	0.54**	0.54**	0.53**	0.51**	0.49**	0.49**	0.48**	0.47**
RVI	0.74**	0.80**	0.84**	0.87**	0.88**	0.88**	0.88**	0.87**	0.86**	0.91**	0.81**	0.77**	0.71**

Colors correspond to the level of performance, the dark green for large R^2 and the light green for small R^2.
*The symbols "**" and "*" indicate canopy chlorophyll content (CCC), and mono-angular VI were significantly correlated with $p < 0.01$ and $p < 0.05$, respectively. The NS indicates no significant correlation was found.*

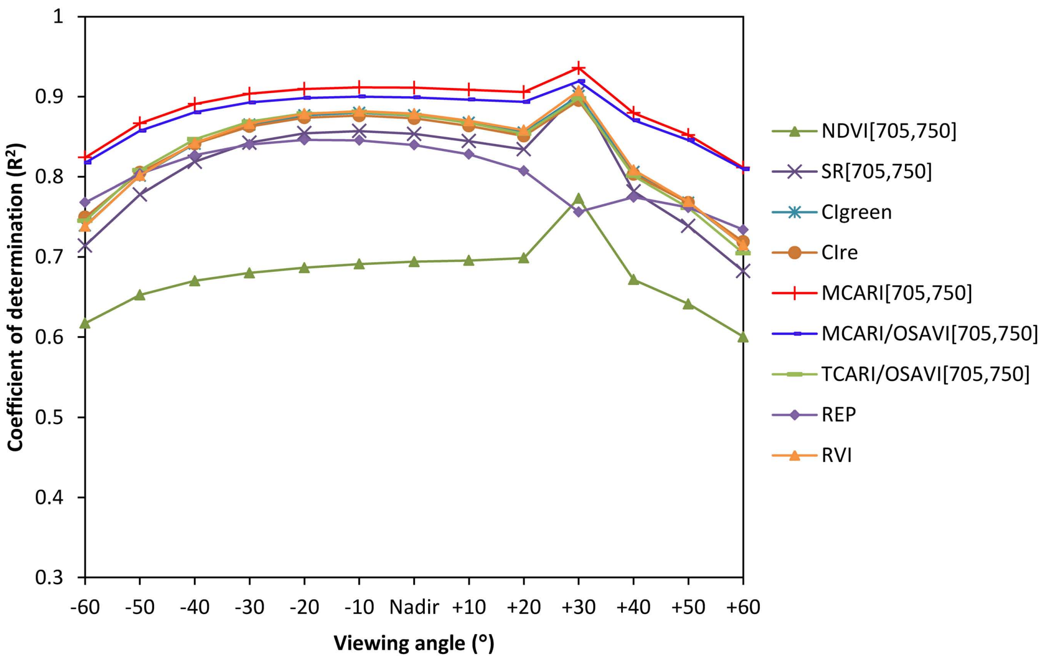

FIGURE 4 | The changing curves of R^2 values for VIs that performed well in canopy chlorophyll content (CCC) estimation at different viewing angles using model simulated data.

relationship with the CCC in particular for the TVI and NRI, with R^2 ranging from 0 to 0.17.

Figure 4 shows the performances of VIs that could explain more than 50% variations in CCC ($p < 0.01$) at different viewing angles, i.e., NDVI[705,750], SR[705,750], CI_{green}, CI_{re}, MCARI[705,750], MCARI/OSAVI[705,750], TCARI/OSAVI[705,750], and REP and RVI, which enabled efficient extraction of the most sensitive mono-angular VIs for CCC determination. We can observe that the coefficient of determination of all VIs exhibited similar trends along with the variety of viewing angles, except for the REP. The higher correlation between the mono-angular VIs and CCC occurred at −30° to +30° observations with the nadir direction included (R^2 ranged from 0.60 to 0.94), while the maximum R^2 appeared at the measurement closest to the hot-spot, which is 30° back-scattering angle in our study. Among all VIs tested, the MCARI[705,750] showed the greatest potential for CCC modeling with R^2 higher than 0.82 for all viewing angles. It gave rise to the most significant correlations with CCC at +30° angle with an R^2 of 0.93 ($p < 0.01$).

The Potential of Biangular-Combined Vegetation Indices for Canopy Chlorophyll Content Estimation

The R^2 of the linear estimation model based on the newly developed BCVIs was calculated with respect to the CCC. **Table 5** summarized the optimal two-angle combination (i.e., θ1 and θ2), the adjusting factor "*f*" constructed in each best performing BCVI and corresponding maximum R^2 values of CCC modeling. Results indicated that for almost all BCVIs, R^2 reached the peak when indices calculated from reflectance obtained from +30° and −20° or +30° and −30° angle combinations, and at the same time, f ranged from 0.6 to 0.7. As expected, the BCVI$_{MCARI[705,750]}$ was found to be advantageous over all the other BCVIs in CCC determination. The combination of θ1 = +30°, θ2 = −20°, f = 0.6 was selected from hundreds of angles and adjusting factor combinations, due to its outstanding performance in capturing variations in CCC with R^2 up to 0.98 (**Figure 5**). Furthermore, it should be noteworthy that the value of f appeared to be very significant in affecting the accuracy of CCC modeling at a given most sensitive two-angle combination. As shown in **Figure 5B**, R^2 of models derived from the BCVI$_{MCARI[705,750]}$ tended to be a bell-shape with increasing f values, with minimal R^2 appearing around f = 0.5. However, they achieved higher R^2 when f varied from 0.6 to 1 compared to f changed from 0 to 0.4, implying that the spectral reflectance obtained from back-scattering directions may contribute more than that collected from forward-scattering directions for enhancing CCC estimation in wheat.

TABLE 5 | The optimal two-angle combination (θ1 and θ2), the adjusting factor *f* constructed in each best performing BCVI, and the corresponding maximum R^2 for canopy chlorophyll content estimation using model-simulated data.

Biangular-combined vegetation index	θ 1	θ 2	*f*	R^2
BCVI$_{NDVI[705,750]}$	+30	−20	0.6	0.9
BCVI$_{SR[705,750]}$	+30	−20	0.7	0.97
BCVI$_{CIgreen}$	+30	−20	0.7	0.95
BCVI$_{CIre}$	+30	−30	0.7	0.95
BCVI$_{MCARI[705,750]}$	+30	−20	0.6	0.98
BCVI$_{MCARI/OSAVI[705,750]}$	+30	−20	0.7	0.93
BCVI$_{TCARI/OSAVI[705,750]}$	+40	−20	0.6	0.91
BCVI$_{REP}$	+30	−20	0.6	0.93
BCVI$_{RVI}$	+30	−30	0.7	0.96

An important piece of information revealed in **Table 5** was that all BCVIs showed better correlations with CCC than the corresponding VIs at any mono-angular observation, even including the most sensitive 30° back-scattering angle, as well as the nadir direction (**Table 4**). For instance, the BCVI$_{NDVI[705,750]}$ generated the biggest increase in R^2 by 16.9% in comparison of the mono-angular NDVI[705,750]$_{(+30)}$. To further explore how the biangular-combined and mono-angular VIs worked in CCC estimation, the scatterplots of relationships between CCC and the best performing BCVI$_{MCARI[705,705]}$ and mono-angular MCARI[705,750] at the nadir, +30°, −20° viewing angles were

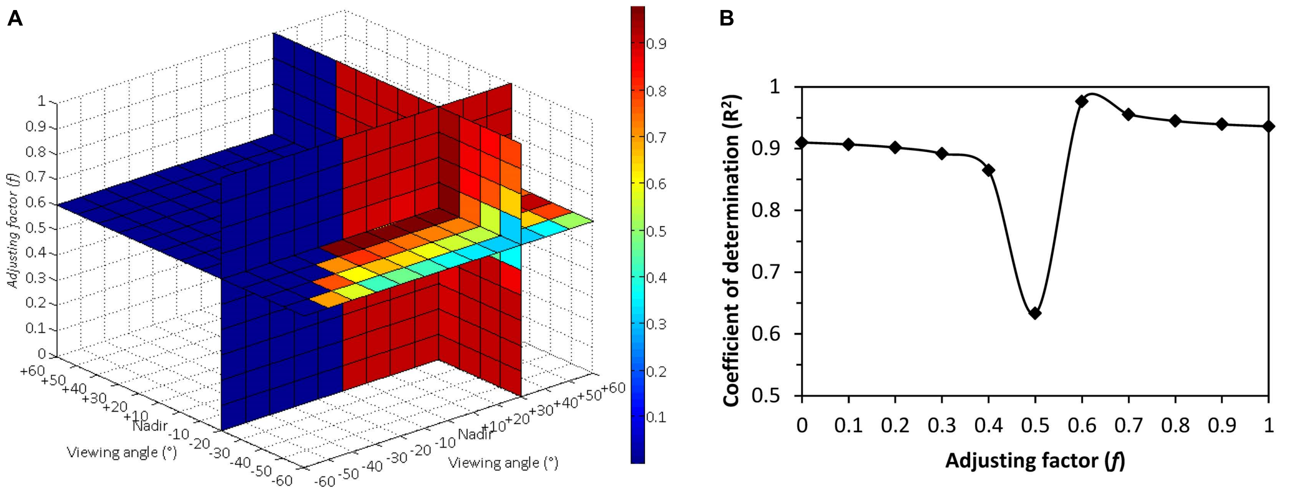

FIGURE 5 | (A) The optimum three-dimensional slice map of the coefficients of determination (R^2) for relationship between the canopy chlorophyll content and biangular-combined vegetation indices (BCVI)$_{MCARI[705,750]}$ calculated by the modified chlorophyll absorption ratio index (MCARI)[705,750] at all the possible two-angle observations selected from 13 viewing angles between –60° and +60°, in which an adjusting factor *f* varied from 0 to 1 at a step of 0.1. **(B)** Changing curve of R^2 for relationship between canopy chlorophyll content and BCVI$_{MCARI[705,750]}$ at +30° and –20° angle combination along with variety of *f* values.

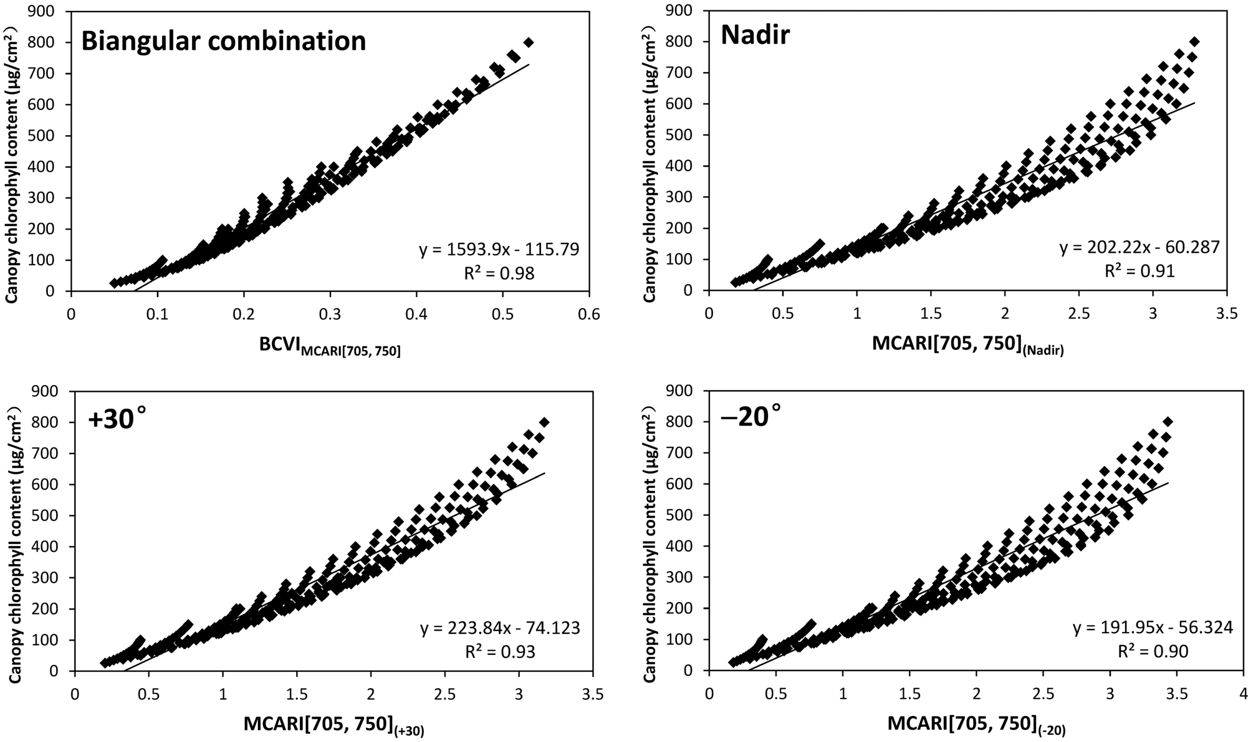

FIGURE 6 | Scatterplots of relationships between canopy chlorophyll content and the MCARI[705,750]$_{(Nadir)}$, MCARI[705,750]$_{(+30)}$, MCARI[705,750]$_{(-20)}$, and BCVI$_{MCARI[705,750]}$ for model simulated dataset.

taken as an example, as shown in **Figure 6**. Results demonstrated that on the one hand, the mono-angular MCARI[705,750] at the three different viewing angles all behaved rather more widely scattering against CCC compared to the BCVI$_{MCARI[705,750]}$. On the other hand, the mono-angular MCARI[705,750] reached a saturation level asymptotically when CCC at high values, whereas the BCVI$_{MCARI[705,750]}$ constructed based on +30° and −20° angular combination showed a better trend without a clear saturation; it was strongly and linearly related to the CCC.

Results Based on Field Experimental Data

Model Canopy Chlorophyll Content Using Mono-Angular Vegetation Indices

Nine VI showed in **Figure 4** that described the CCC better were tested with the ground truth measurements. **Figure 7** shows the results of the relationship between VIs derived from mono-angular spectral reflectance and ground measured CCC. Similar to the results of simulated data, in CCC determination, the +30° angle yielded greater significance than the other angles for all mono-angular VIs, except the REP which only had little sensitivity to the variations in CCC ($R^2 \leq 0.1$), making it barely suitable for CCC estimation. The model performances based on the mono-angular MCARI[705,750] and the mono-angular MCARI/OSAVI[705,750] were superior to the others, with comparative and highest R^2 of 0.51 and 0.50, respectively at +30° viewing angle. Apart from the REP, the analogous pattern of R^2 changes for all VIs at different viewing angles was observed: besides the +30° angle, the CCC also showed a better relationship with VIs at both the nadir and +40° directions; interestingly, for the forward-scattering observations, there were two weak peaks with relative high R^2, at −20° and −40° angles, predominating in CCC estimation for most of VIs (SR[705,750], CI$_{green}$, CI$_{re}$, MCARI[705,750], MCARI/OSAVI[705,750], and RVI).

Model Canopy Chlorophyll Content Using Biangular-Combined Vegetation Indices

A series of BCVIs was established with field measured datasets using the same method used in the section "The Potential of Biangular-Combined Vegetation Indices for Canopy Chlorophyll Content Estimation," and were examined the linearity to CCC. The BCVI$_{MCARI[705,750]}$ was chosen as an example to illustrate the process of the selection of three parameters (θ1, θ2, and f) composing in the BCVI. From the slice maps shown in **Figure 8**, R^2 varied intensely with changing of different combinations of MCARI[705,750] values at two viewing angles. The BCVI$_{MCARI[705,750]}$ that was calculated by the subtraction of MCARI[705,750] at +30° and −20° angular combination with $f = 0.6$ as an adjusting factor stood out among all combinations, with the soundest R^2 for CCC estimation ($R^2 = 0.72$), which was consistent with the previous results of dataset simulated by PROSAIL model. Meanwhile, the changing curve of R^2 values exhibited a slightly different shape but a similar trend, with the simulated BCVI$_{MCARI[705,750]}$ (**Figure 5B**), expressing

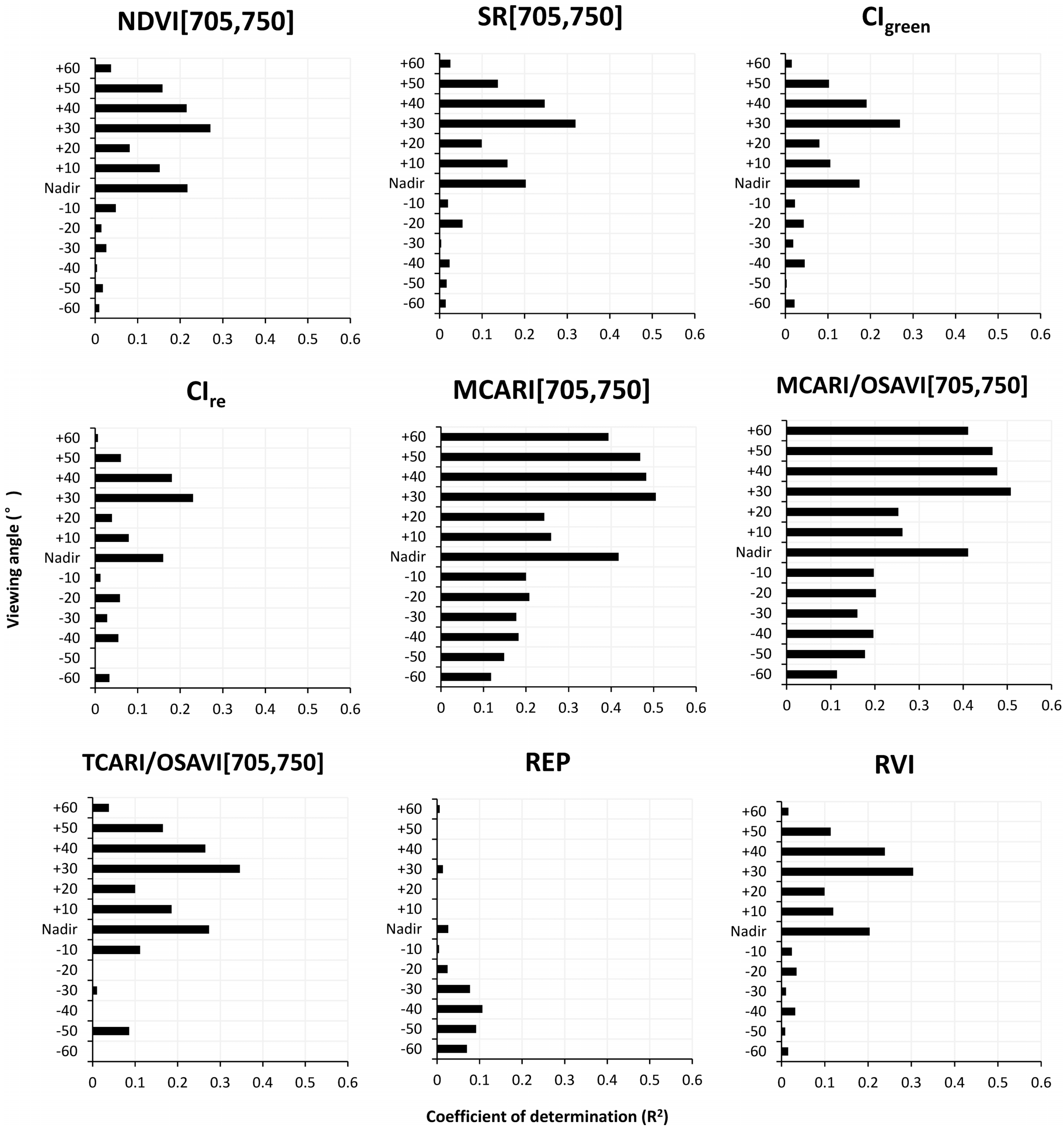

FIGURE 7 | The R^2 of relationship between better performing VIs (shown in **Figure 4**) and field measured canopy chlorophyll content at different viewing angles.

a more striking contrast between f of 0 to 0.3 and f of 0.6 to 1 (**Figure 8D**). This result put emphasis on the greater role of spectral information extracted at back-scattering directions than that at forward-scattering directions, in CCC determination when using the field measured data, in comparison to the simulated data. As for the other seven BCVIs, similar patterns of slice maps and R^2 changing curves occurred (not shown for brevity). We found that the best BCVIs for investigating changes in CCC was also generated at +30° and −20° or +30° and −30° angle combination, in which f was around 0.6 to 0.7, with R^2 of 0.34 to 0.71 (**Table 6**).

Comparison of Performances of Biangular-Combined Vegetation Indices and Mono-Angular Vegetation Indices

To explore what degree the multi-angular viewing capability of spectra can contribute to the improved CCC assessment of wheat compared to the mono-angular observations, we

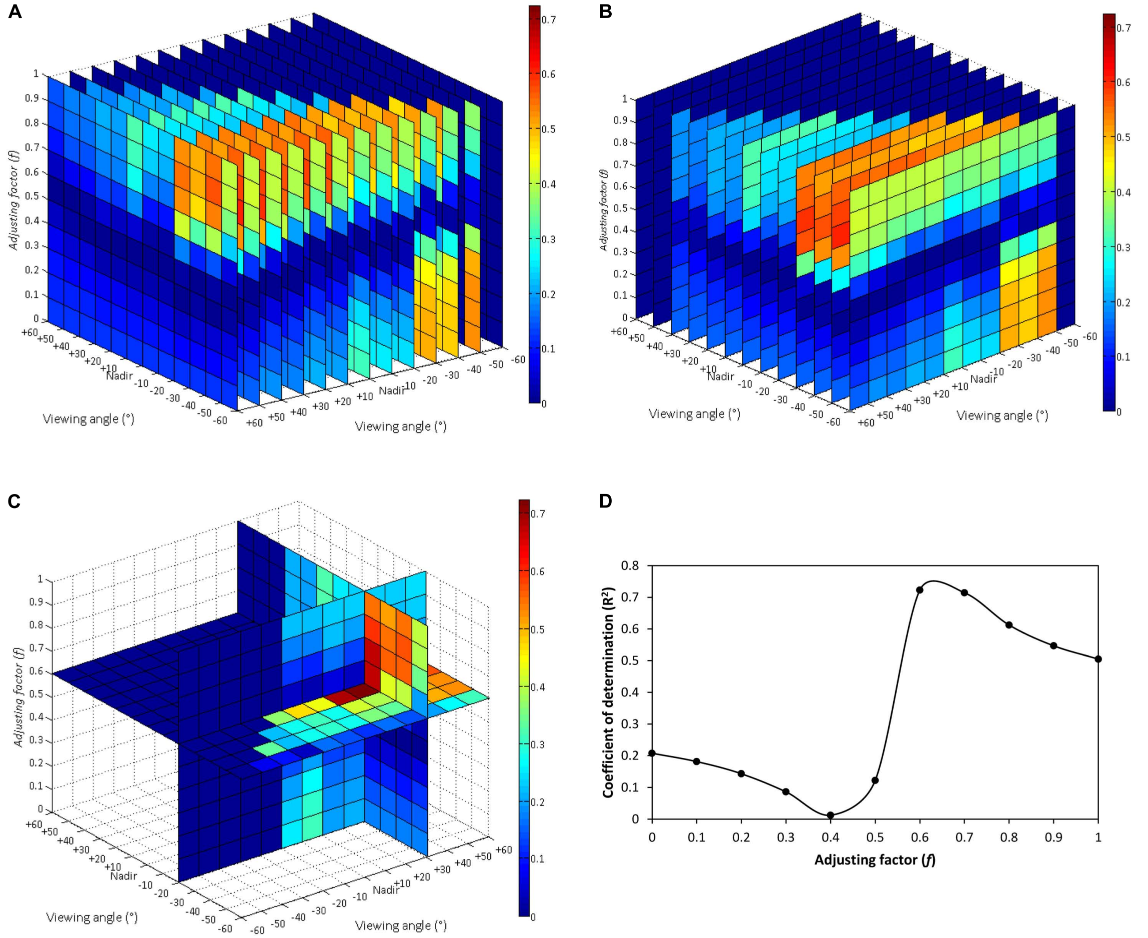

FIGURE 8 | The three-dimensional slice maps of the R^2 for relationship between field measured canopy chlorophyll content and $BCVI_{MCARI[705,750]}$ calculated by the subtraction of MCARI[705,750] at all the possible two-angle observations selected from 13 viewing angles between –60° and +60°, in which an adjusting factor *f* varied from 0 to 1 at a step of 0.1: **(A)** slice map for the first viewing angle (θ1) selection, **(B)** slice map for the second viewing angle (θ2) selection, **(C)** slice map for optimum two-angle and *f* value combination; **(D)** changing curve of R^2 for relationship between field measured canopy chlorophyll content and $BCVI_{MCARI[705,750]}$ at +30° and –20° angle combination along with variety of *f* values.

TABLE 6 | The optimal two-angle combination (θ1 and θ2), the adjusting factor *f* constructed in each best performing biangular-combined vegetation indices (BCVI), and the corresponding maximum R^2 for CCC estimation using field measured data.

Biangular-combined vegetation index	θ 1	θ 2	*f*	R^2
$BCVI_{NDVI[705,750]}$	+30	−30	0.6	0.41
$BCVI_{SR[705,750]}$	+30	−30	0.7	0.42
$BCVI_{CIgreen}$	+30	−20	0.7	0.38
$BCVI_{CIre}$	+30	−30	0.7	0.34
$BCVI_{MCARI[705,750]}$	+30	−20	0.6	0.72
$BCVI_{MCARI/OSAVI[705,750]}$	+30	−20	0.6	0.71
$BCVI_{TCARI/OSAVI[705,750]}$	+30	−20	0.6	0.45
$BCVI_{RVI}$	+30	−20	0.7	0.38

analyzed the performances of the newly developed BCVIs and the corresponding mono-angular VIs at the most sensitive +30° angle (**Figure 9**). The result revealed that the BCVIs showed a clear increase in R^2 by 25.1–51.4%, as compared to the mono-angular VIs, and were proven to be more effective and suitable in modeling CCC. The most significant improvement was observed in the comparison between indices of $BCVI_{NDVI[705,750]}$ and $NDVI[705,750]_{(+30)}$. As previously explained, the $BCVI_{MCARI[705,750]}$ and $MCARI[705,750]_{(+30)}$ showed the strongest correlation with CCC among all BCVIs and mono-angular VIs, respectively, but the $BCVI_{MCARI[705,750]}$ further improved the CCC estimation accuracy by 41.2%.

We further plotted the scatterplots of BCVIs and mono-angular VIs at the nadir, +30° and −20° or −30° viewing angles based on the MCARI[705,750] and NDVI[705,750] against CCC (**Figure 10**). For the two VIs, the BCVIs were characterized by less scattered relationships with CCC compared to their mono-angular counterparts derived from the nadir, +30° and −20°/−30° directions, in particular, for the $BCVI_{MCARI[705,750]}$. In consistent with the simulated result, as illustrated in **Figure 6**, $BCVI_{MCARI[705,750]}$ behaved linearly with CCC, with the scatter points evenly distributed around the fitting line, clearly depicting the dynamic changes of CCC (**Figures 10A–D**). As can be seen

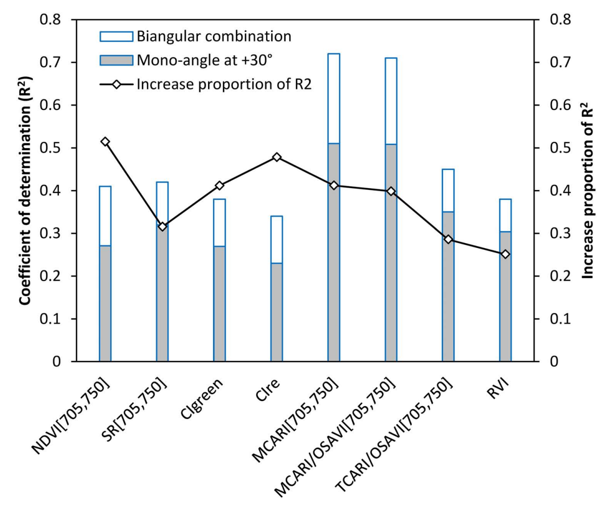

FIGURE 9 | Comparisons of R^2 values of relationships between biangular-combined vegetation indices (VIs) vs. canopy chlorophyll content and mono-angular VIs at +30° viewing angle vs. canopy chlorophyll content.

in **Figures 10E–H**, the sensitivities of NDVI[705,750]$_{\text{(Nadir)}}$ and NDVI[705,750]$_{(+30)}$ were most affected by high values of CCC, showing a saturation effect when CCC exceeded 400 μg/cm^2. However, the BCVI$_{\text{NDVI[705,750]}}$ improved the linearity and reduced the saturation limit of mono-angular NDVI[705,750] at the three viewing angles to a great extent.

Testing Canopy Chlorophyll Content Estimation Models

The mono-angular MCARI[705,750] at the nadir and +30° viewing angles, as well as the BCVI$_{\text{MCARI[705,750]}}$ were chosen to test the potential of these VIs in predicting the CCC by the means of cross-validation since they were proven to be reliable in CCC estimation both for simulated data and experimental data. The predictions of the three indices against the ground measured CCC were plotted in **Figure 11**. The CCC was well-predicted by MCARI[705,750]$_{(+30)}$ and MCARI[705,750]$_{\text{(Nadir)}}$, with RPDs larger than 2.12 and scattered in both plots fell into the 95% confidence intervals. The MCARI[705,750]$_{(+30)}$ generated relative higher accuracy than the MCARI[705,750]$_{\text{(Nadir)}}$ and R^2 of 0.50 ($p < 0.01$) were observed for the measured dataset with RMSE of 63.51. In comparison with the two mono-angular MCARI[705,750], we found a more consistent agreement between CCC values measured in the field and those estimated by the new derived BCVI$_{\text{MCARI[705,750]}}$, with coefficient of determination of 0.70 ($p < 0.01$), RMSE of 42.36, and RPD of 3.57. The results suggested that the BCVI$_{\text{MCARI[705,750]}}$ at +30° and −20° angle combination performed better and could be more preferable than the conventional nadir direction approach to remote sensing CCC in wheat.

DISCUSSION

In this study, we estimated crop CCC using simulated multi-angle remote-sensing data produced with the PROSAIL model and canopy multi-angle hyperspectral reflectance measured from the field of winter wheat. We developed the BCVIs by coupling, not only spectral but also angular information, and compared the performances of these BCVIs with the corresponding mono-angular VIs to evaluate whether the CCC estimate could be improved from multi-angle observations. From the characteristics of multi-angle spectral reflectance, angular anisotropy was greatly different at the chlorophyll absorbance and canopy reflective bands. This was mainly due to the discrepancy of the contrast between shadowed and illuminated canopy components at both two types of bands, which resulted from viewing and illumination geometry and the sensor's field of view (Kollenkark et al., 1982; Galvao et al., 2009). In the case of crop canopy, the reflectance at the green, red edge, and particular NIR bands had low absorbance but highly reflective values. The contrast at these bands was effectively reduced because of multiple scattering processes (Sandmeier et al., 1998), compared to the red absorbance band, weakening the expression of angular anisotropy as demonstrated in **Figure 3**. However, for all spectral bands tested, reflectance exhibited higher values at back-scattering directions than forward-scattering directions in the solar principal plane, primarily because more and more fractions of illuminated leaf surfaces were viewed by the sensor, along with its rotation from the side facing away from the sun to the side facing into the sun. As confirmed by the study of Sandmeier et al. (1998), the well-illuminated vegetation canopy would be less vulnerable to the shadow effect, which led to more signals from leaves that can be detected by the spectral reflectance measured from the back-scattering directions. Indeed, our results also indicated that almost all mono-angular VIs were more closely related to the CCC at the back-scattering directions than the forward-scattering directions for datasets of both model simulation and ground measurements (**Table 4** and **Figure 7**).

Angular effect presented in VIs can either be regarded as a superfluous uncertainty for vegetation parameters estimation or as a source of additional information that enhances the accuracy of the parameter assessment at canopy scale (Verrelst et al., 2008). In this study, the CCC estimation based on 30° back-scattering spectral data led to an improvement, as compared to the conventional nadir data. This can be attributed to the reduction of soil background impact which is mostly contained at the nadir observation. A similar result was also observed in the studies of He et al. (2016), Kong et al. (2017), and Inoue et al. (2008), who studied the improvements of physiological parameters estimation for crops (e.g., canopy nitrogen content, canopy carotenoid content, and photosynthetic efficiency) based on multi-angle hyperspectral remote-sensing. However, it is important to notice that the estimation of CCC improved even further than mono-angular VIs at any viewing angle when the multi-angular information was added, especially in the case of the ground truth measurement. There are several explanations for having excellent behavior. In this study, we developed the BCVIs based on existing VIs proposed for vegetation chlorophyll and nitrogen estimates, by applying an iterative optimization approach, since it can search for the optimal biangular combination from all the available viewing angles and the most suitable adjusting factor value used. The result

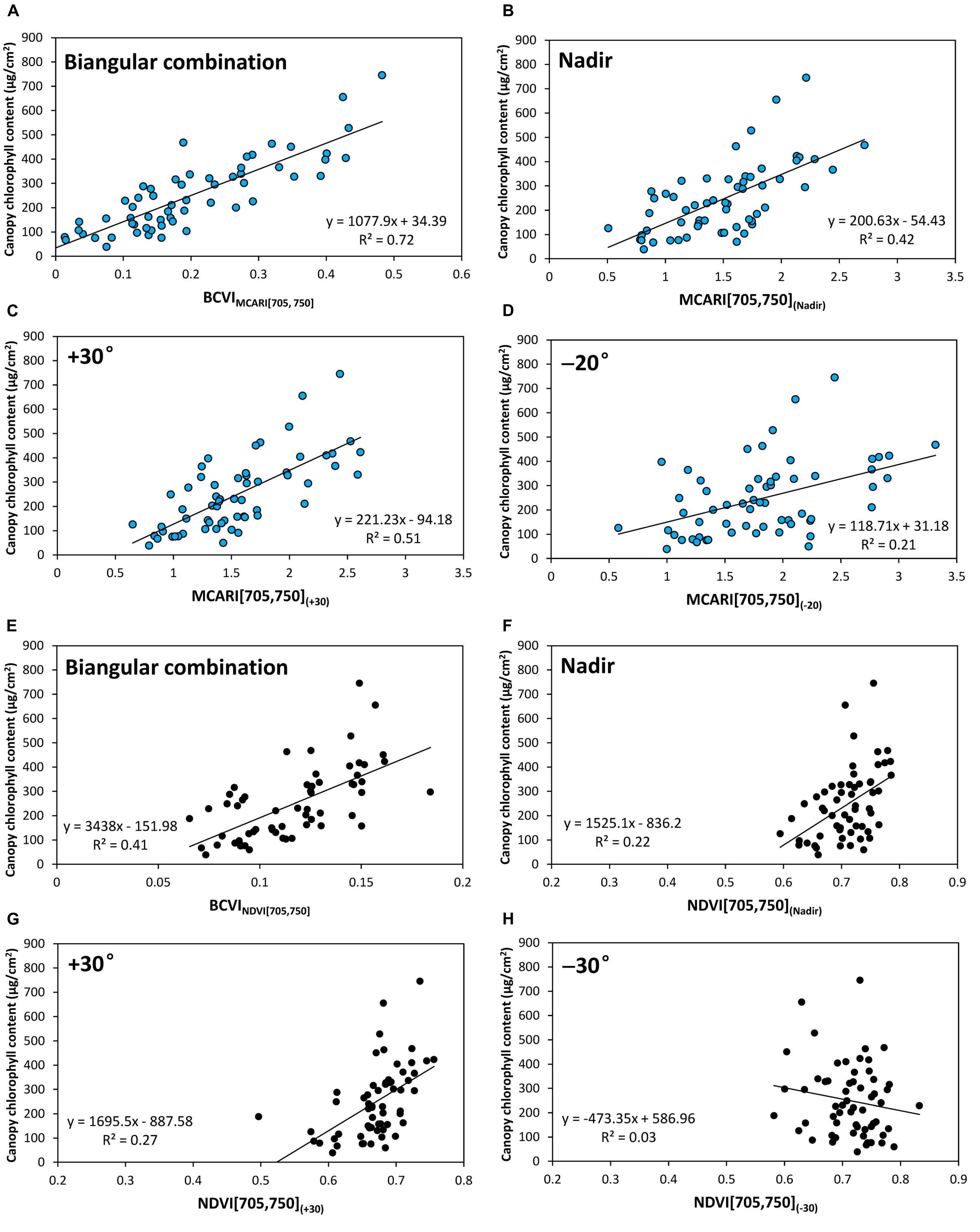

FIGURE 10 | Scatterplots of relationships between canopy chlorophyll content and BCVIs and the corresponding mono-angular VIs based on MCARI[705,750] and normalized difference vegetation index (NDVI)[705,750] for filed experimental datasets. The blue points **(A–D)** represent the $\text{BCVI}_{\text{NDVI}[705,750]}$, $\text{MCARI}[705,750]_{(\text{Nadir})}$, $\text{MCARI}[705,750]_{(+30)}$, and $\text{MCARI}[705,750]_{(-20)}$, respectively; the black points **(E–H)** represent the $\text{BCVI}_{\text{NDVI}[705,750]}$, $\text{NDVI}[705,750]_{(\text{Nadir})}$, $\text{NDVI}[705,750]_{(+30)}$, and $\text{NDVI}[705,750]_{(-30)}$, respectively.

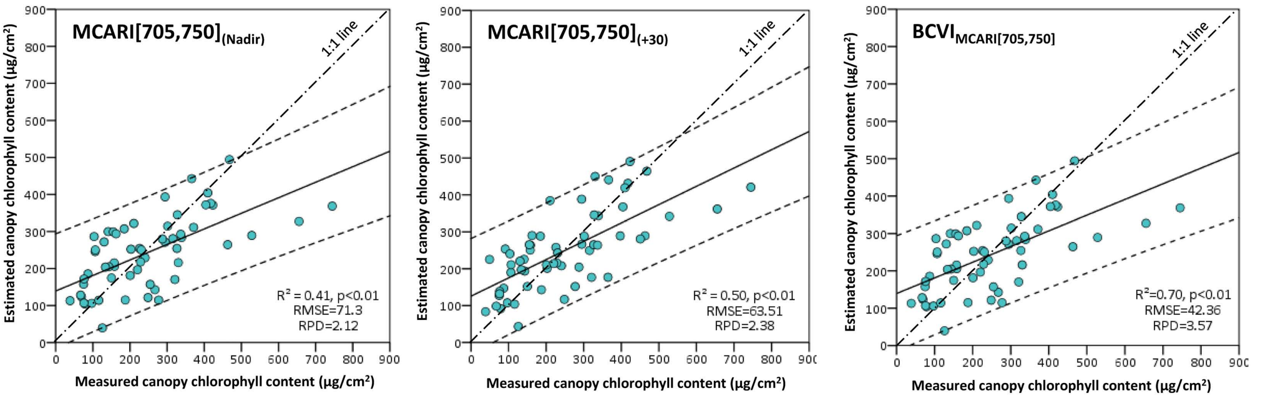

FIGURE 11 | Scatterplots between measured canopy chlorophyll content and estimated canopy chlorophyll content based on the MCARI[705,750]$_{(Nadir)}$, MCARI[705,750]$_{(+30)}$, and BCVI$_{MCARI[705,750]}$. The solid lines indicate the regression fitting lines, the dash lines indicate the 95% confidence intervals of prediction, the long and short dash lines indicate 1:1 lines.

showed that the angular combination composing of the best BCVI came close to the positions of hot-spot and dark-spot in the solar principal plane. For one thing, vegetation canopy is a non-Lambert in nature, multi-angle spectral reflectance can capture the uneven scattering of sunlight by vegetation, reaching the maximum at the hot-spot direction, and the lower value at the dark-spot position as suffering from the shadow effect. Because the composition of shadowed and illuminated canopy components is highly dependent on LAI, leaf orientation distributions, and other structural properties (Stagakis et al., 2010), the striking difference of VI values between hot spot and dark spot, that adjusted by the value of "*f*," not only facilitated to provide more information on chlorophyll than the VI at the solely mono-angle, but more importantly, made the information on three-dimensional vegetation structures prominent when the BCVI was used for tracking the changes of chlorophyll content at canopy scale. Additionally, our work also put heavy emphasis on the importance of the value of the adjusting factor "*f*" in the formula of BCVI for promoting the CCC estimation, but it has not yet received widespread attention from researchers working on quantifying CCC using multi-angle spectral data. We selected the value of "*f*" systematically, from 0 to 1 with a step of 0.1, and concluded that the BCVIs performed best when *f* was 0.6 or 0.7, which implied that the contribution of VIs around the hot-spot angle was greater than that of VIs around the dark-spot angle. This allowed more signals from sunlit leaves to be included, consequently, increasing the quality of vegetation biochemical parameters (e.g., chlorophyll) reflectance contained. For another, compared the reflectance spectra measured at a single viewing angle, the BCVIs derived from multi-angle spectral data may improve the CCC inversion by including additional information on leaf chlorophyll at different vertical layers within canopies (Huang et al., 2011).

A high amount of studies have demonstrated that many VIs are prone to saturation with increasing vegetation biological variables (Broge and Leblanc, 2001; Haboudane et al., 2004; Wu et al., 2008). This limitation of saturation was also found in the analysis of the relationship between mono-angular VIs and CCC for overall datasets in our study (**Figures 6**, **10**), including the best performing MCARI[705,750], which may restrict the reliability of their use in monitoring dense canopies with higher CCC. Nevertheless, the saturation phenomenon was overcame in large part by introducing the corresponding VI obtained from another viewing angle to construct the BCVI; results of the newly developed BCVI showed better linearity and higher accuracy (e.g., R^2 = 0.98 and 0.72 for BCVI$_{MCARI[705,750]}$ for PROSAIL-simulated and filed experimental datasets, respectively), and features the scattered display more intensively, along with the changing of CCC than those for any mono-angular VI. This is another reason why the BCVIs held more promising potential in CCC assessment.

For the simulated and experimental datasets, the accuracy of CCC estimation was all improved when using the BCVIs we proposed. However, there were evident discrepancies in the magnitude of improvement observed between both datasets. The main possibility was that the PROSAIL model was not capable of adequately reproducing the real physiological and morphological conditions of the wheat canopy that we used in this study. For instance, more and more studies have demonstrated that the vertical distribution of leaf biochemical variables (e.g., chlorophyll and nitrogen) was non-uniform within plant canopy (Ciganda et al., 2012; He et al., 2020), leading to different contributions of the vertical layers to canopy spectra (Li et al., 2015). Moreover, apart from leaves, the presence of other canopy components, such as wheat spikes and plant stems, would also have an impact on canopy reflectance (Haboudane et al., 2004; He et al., 2019) and as a result the quality of extracted crop CCC. But these factors are not taken into account in the PROSAIL model. In addition, to focus on exploring the sensitivities of different mono-angular VIs and the developed BCVIs to CCC variation, LCC and LAI were set as free variables, while the other vegetation parameters were set to fixed constants at their respective mean values when conducting the canopy multi-angled spectral reflectance simulation. Nevertheless, this vegetation parameter setting may become a primary source causing the differences with results of field measurements, since many parameters (e.g., leaf carotenoid, water, and fresh and dry matter), besides LCC and LAI, were continually changing with the growth of crops and the implementation of different agricultural managements in reality. Due to large improvements for field measurement dataset were obtained, our results establish the confidence in the use of the BCVIs we developed for crop CCC modeling in the future practical application. Nowadays, some space-borne sensors have been specifically designed to collect data from multi-angle observations (Barnsley et al., 2004; Roosjen et al., 2018), solid coupling of radiative transfer model, and multi-angle spectral information will be key to the successful assessment of chlorophyll content at canopy scale. Because the hot-spot reflectance is difficult to be adequately acquired and, thus, they might be interpolated from the adjacent measurements, future studies will be needed to further validate whether the BCVIs derived from satellite data could provide more accurate crop CCC estimation.

CONCLUSION

The CCC is a measure of photosynthetic potential at the canopy level and was retrieved as the product of leaf chlorophyll and LAI. Unlike previous analyses that mainly focused on establishing VI from mono-angular remote sensing data, we proposed a new method of developing the BCVIs for high-throughput estimation of crop CCC using canopy multi-angle observations. The BCVI was calculated by the subtraction of chlorophyll-sensitive VI values, computing from reflectance measured around hot-spot and dark-spot positions, with 0.6 or 0.7 as an adjusting factor. This algorithm involved both leaf chlorophyll and canopy structural information making the BCVIs derived from multi-angle spectral reflectance more effective when compared to solely using corresponding mono-angular VIs at arbitrary viewing angle for assessing CCC across PROSAIL model-simulated dataset and field experimental dataset. The MCARI[705,750] was proven to be the best mono-angular VI among previously published VIs tested, +30° back-scattering angle produced better performing VI than the nadir direction. However, as they were equally subject to the saturation limit with increasing of CCC based on the results, we developed the $\mathrm{BCVI}_{\mathrm{MCARI}[705,50]}$ at +30° and −20° angle combination, formulated as $0.6 \times \mathrm{MCARI}[705, 750]_{(+30)} - 0.4 \times \mathrm{MCARI}[705, 750]_{(-20)}$ where +30° and −20° angles were the closest measurements to the hot-spot and dark-spot positions in this study. We found that the $\mathrm{BCVI}_{\mathrm{MCARI}[705,750]}$ was not only resistant to the saturation effect, but also exhibited the highest sensitivity to CCC variation over all datasets. Our results demonstrate that the BCVI that taking spectral and angular information into account could substantially improve the estimation of crop CCC, and consequently offer more accurate information to understand crop's phenotypic trait across growth stages and their response to environmental changes in agro-ecosystem.

DATA AVAILABILITY STATEMENT

The raw data supporting the conclusions of this article will be made available by the authors, without undue reservation.

AUTHOR CONTRIBUTIONS

WK processed and analyzed the simulated and experimental datasets, and wrote sections of the manuscript. WH, CL, and LT guided the data analysis and provided suggestions for the study. LM, JG, and XZ designed the experiment and were involved in the ground data collection. RC provided the suggestions, and revised and edited the manuscript. All authors contributed to manuscript revision, read, and approved the submitted version.

FUNDING

This work was funded by the National Key Research and Development Program of China (Grant No. 2021YFB3900501), National Natural Science Foundation of China (Grant No. 41901369), the Key Research Program of the Chinese Academy of Sciences (Grant No. KFZD-SW-428-2), and Strategic Priority Research Program of the Chinese Academy of Sciences (Grant No. XDA28100500).

ACKNOWLEDGMENTS

We are grateful to Dr. Bin Wu and Dr. Huiqin Ma for their assistance in data collection. We are grateful to the reviewers for their helpful comments. We would also like to acknowledge the contributions from the field campaign at the National Experimental Station for Precision Agriculture, Beijing, China.

REFERENCES

Barnsley, M. J., Settle, J. J., Cutter, M. A., Lobb, D. R., and Teston, F. (2004). The PROBA/CHRIS mission: a low-cost smallsat for hyperspectral multiangle observations of the earth surface and atmosphere. *IEEE Trans. Geosci. Remote Sens.* 42, 1512–1520. doi: 10.1109/tgrs.2004.827260

Bausch, W. C., and Duke, H. R. (1996). Remote sensing of plant nitrogen status in corn. *Trans. ASAE* 39, 1869–1875.

Blackburn, G. A. (1998). Spectral indices for estimating photosynthetic pigment concentrations: a test using senescent tree leaves. *Int. J. Remote Sens.* 19, 657–675. doi: 10.1080/014311698215919

Broge, N. H., and Leblanc, E. (2001). Comparing prediction power and stability of broadband and hyperspectral vegetation indices for estimation of green leaf area index and canopy chlorophyll density. *Remote Sens. Environ.* 76, 156–172. doi: 10.1016/s0034-4257(00)00197-8

Broge, N. H., and Mortensen, J. V. (2002). Deriving green crop area index and canopy chlorophyll density of winter wheat from spectral reflectance data. *Remote Sens. Environ.* 81, 45–57. doi: 10.1016/s0034-4257(01)00332-7

Brown de Colstoun, E. C., and Walthall, C. L. (2006). Improving global scale land cover classifications with multi-directional POLDER data and a decision tree classifier. *Remote Sens. Environ.* 100, 474–485. doi: 10.1016/j.rse.2005.11.003

Chen, J. M., Liu, J., Leblanc, S. G., Lacaze, R., and Roujean, J. L. (2003). Multi-angular optical remote sensing for assessing vegetation structure and carbon absorption. *Remote Sens. Environ.* 84, 516–525. doi: 10.1016/s0034-4257(02)00150-5

Ciganda, V. S., Gitelson, A. A., and Schepers, J. (2012). How deep does a remote sensor sense? Expression of chlorophyll content in a maize canopy. *Remote Sens. Environ.* 126, 240–247. doi: 10.1016/j.rse.2012.08.019

Clevers, J., and Kooistra, L. (2012). Using hyperspectral remote sensing data for retrieving canopy chlorophyll and nitrogen content. *IEEE J. Sel. Top. Appl. Earth Obs. Remote Sens.* 5, 574–583. doi: 10.1109/jstars.2011.2176468

Daughtry, C. S. T., Walthall, C. L., Kim, M. S., de Colstoun, E. B., and McMurtrey, J. E. (2000). Estimating corn leaf chlorophyll concentration from leaf and canopy reflectance. *Remote Sens. Environ.* 74, 229–239. doi: 10.1016/s0034-4257(00)00113-9

Feng, W., Guo, B.-B., Wang, Z.-J., He, L., Song, X., Wang, Y.-H., et al. (2014). Measuring leaf nitrogen concentration in-winter wheat using double-peak spectral reflection remote sensing data. *Field Crops Res.* 159, 43–52. doi: 10.1016/j.fcr.2014.01.010

Galvao, L. S., Roberts, D. A., Formaggio, A. R., Numata, I., and Breunig, F. M. (2009). View angle effects on the discrimination of soybean varieties and on the relationships between vegetation indices and yield using off-nadir Hyperion data. *Remote Sens. Environ.* 113, 846–856. doi: 10.1016/j.rse.2008.12.010

Gitelson, A., and Merzlyak, M. N. (1994). Spectral reflectance changes associated with autumn senescence of *Aesculus hippocastanum* L and *Acer platanoides* L leaves-spectral features and relation to chlorophyll estimation. *J. Plant Physiol.* 143, 286–292. doi: 10.1016/s0176-1617(11)81633-0

Gitelson, A. A., Keydan, G. P., and Merzlyak, M. N. (2006). Three-band model for noninvasive estimation of chlorophyll, carotenoids, and anthocyanin contents in higher plant leaves. *Geophys. Res. Lett.* 33:L11402. doi: 10.1029/2006gl026457

Gutierrez, M., Paul Reynolds, M., and Klatt, A. R. (2015). Effect of leaf and spike morphological traits on the relationship between spectral reflectance indices and yield in wheat. *Int. J. Remote Sens.* 36, 701–718. doi: 10.1080/01431161.2014.999878

Haboudane, D., Miller, J. R., Pattey, E., Zarco-Tejada, P. J., and Strachan, I. B. (2004). Hyperspectral vegetation indices and novel algorithms for predicting green LAI of crop canopies: modeling and validation in the context of precision agriculture. *Remote Sens. Environ.* 90, 337–352. doi: 10.1016/j.rse.2003.12.013

Haboudane, D., Miller, J. R., Tremblay, N., Zarco-Tejada, P. J., and Dextraze, L. (2002). Integrated narrow-band vegetation indices for prediction of crop chlorophyll content for application to precision agriculture. *Remote Sens. Environ.* 81, 416–426. doi: 10.1016/s0034-4257(02)00018-4

Hansen, P. M., and Schjoerring, J. K. (2003). Reflectance measurement of canopy biomass and nitrogen status in wheat crops using normalized difference vegetation indices and partial least squares regression. *Remote Sens. Environ.* 86, 542–553. doi: 10.1016/s0034-4257(03)00131-7

Hasegawa, K., Matsuyama, H., Tsuzuki, H., and Sweda, T. (2010). Improving the estimation of leaf area index by using remotely sensed NDVI with BRDF signatures. *Remote Sens. Environ.* 114, 514–519. doi: 10.1016/j.rse.2009.10.005

He, J., Zhang, N., Su, X., Lu, J., Yao, X., Cheng, T., et al. (2019). Estimating leaf area index with a new vegetation index considering the influence of rice panicles. *Remote Sens.* 11:1809. doi: 10.3390/rs11151809

He, J. Y., Zhang, X. B., Guo, W. T., Pan, Y. Y., Yao, X., Cheng, T., et al. (2020). Estimation of vertical leaf nitrogen distribution within a rice canopy based on hyperspectral data. *Front. Plant Sci.* 10:1802. doi: 10.3389/fpls.2019.01802

He, L., Zhang, H. Y., Zhang, Y. S., Song, X., Feng, W., Kang, G. Z., et al. (2016). Estimating canopy leaf nitrogen concentration in winter wheat based on multi-angular hyperspectral remote sensing. *Eur. J. Agron.* 73, 170–185. doi: 10.1016/j.eja.2015.11.017

Hinzman, L. D., Bauer, M. E., and Daughtry, C. S. T. (1986). Effects of nitrogen fertilization on growth and reflectance characteristics of winter wheat. *Remote Sens. Environ.* 19, 47–61. doi: 10.1016/0034-4257(86)90040-4

Huang, W., Wang, Z., Huang, L., Lamb, D. W., Ma, Z., Zhang, J., et al. (2011). Estimation of vertical distribution of chlorophyll concentration by bi-directional canopy reflectance spectra in winter wheat. *Precis. Agric.* 12, 165–178. doi: 10.1007/s11119-010-9166-5

Inoue, Y., Penuelas, J., Miyata, A., and Mano, M. (2008). Normalized difference spectral indices for estimating photosynthetic efficiency and capacity at a canopy scale derived from hyperspectral and CO_2 flux measurements in rice. *Remote Sens. Environ.* 112, 156–172. doi: 10.1016/j.rse.2007.04.011

Jacquemoud, S., Verhoef, W., Baret, F., Bacour, C., Zarco-Tejada, P. J., Asner, G. P., et al. (2009). PROSPECT + SAIL models: a review of use for vegetation characterization. *Remote Sens. Environ.* 113, S56–S66. doi: 10.1016/j.rse.2008.01.026

Kollenkark, J. C., Vanderbilt, V. C., Daughtry, C. S. T., and Bauer, M. E. (1982). Influence of solar illumination angle on soybean canopy reflectance. *Appl. Opt.* 21, 1179–1184. doi: 10.1364/ao.21.001179

Kong, W. P., Huang, W. J., Liu, J. G., Chen, P. F., Qin, Q. M., Ye, H. C., et al. (2017). Estimation of canopy carotenoid content of winter wheat using multi-angle hyperspectral data. *Adv. Space Res.* 60, 1988–2000. doi: 10.1016/j.asr.2017.07.015

Kong, W. P., Huang, W. J., Ma, L. L., Tang, L. L., Li, C. R., Zhou, X. F., et al. (2021). Estimating vertical distribution of leaf water content within wheat canopies after head emergence. *Remote Sens.* 13:4125. doi: 10.3390/rs13204125

Leblanc, S. G., Chen, J. M., and Cihlar, J. (1997). NDVI Directionality in boreal forests: a model interpretation of measurements. *Can. J. Remote Sens.* 23, 369–380.

Li, H., Zhao, C., Huang, W., and Yang, G. (2013). Non-uniform vertical nitrogen distribution within plant canopy and its estimation by remote sensing: a review. *Field Crops Res.* 142, 75–84. doi: 10.1016/j.fcr.2012.11.017

Li, H., Zhao, C., Yang, G., and Feng, H. (2015). Variations in crop variables within wheat canopies and responses of canopy spectral characteristics and derived vegetation indices to different vertical leaf layers and spikes. *Remote Sens. Environ.* 169, 358–374. doi: 10.1016/j.rse.2015.08.021

Li, L., Ren, T., Ma, Y., Wei, Q., Wang, S., Li, X., et al. (2016). Evaluating chlorophyll density in winter oilseed rape (*Brassica napus* L.) using canopy hyperspectral red-edge parameters. *Comput. Electron. Agric.* 126, 21–31. doi: 10.1016/j.compag.2016.05.008

Lichtenthaler, H. K. (1987). Chlorophylls and carotenoids: pigments of photosynthetic biomembranes. *Methods Enzymol.* 148, 350–382. doi: 10.1515/znc-2001-11-1225

Merzlyak, M. N., Gitelson, A. A., Chivkunova, O. B., and Rakitin, V. Y. (1999). Non-destructive optical detection of pigment changes during leaf senescence and fruit ripening. *Physiol. Plant.* 106, 135–141. doi: 10.1034/j.1399-3054.1999.106119.x

Poorter, H., Niinemets, U., Poorter, L., Wright, I. J., and Villar, R. (2009). Causes and consequences of variation in leaf mass per area (LMA): a meta-analysis. *New Phytol.* 182, 565–588. doi: 10.1111/j.1469-8137.2009.02830.x

Razakamanarivo, R. H., Grinand, C., Razafindrakoto, M. A., Bernoux, M., and Albrecht, A. (2011). Mapping organic carbon stocks in eucalyptus plantations of the central highlands of Madagascar: a multiple regression approach. *Geoderma* 162, 335–346. doi: 10.1016/j.geoderma.2011.03.006

Richter, K., Atzberger, C., Hank, T. B., and Mauser, W. (2012). Derivation of biophysical variables from Earth observation data: validation and statistical measures. *J. Appl. Remote Sens.* 6:063557. doi: 10.1117/1.jrs.6.063557

Rondeaux, G., Steven, M., and Baret, F. (1996). Optimization of soil-adjusted vegetation indices. *Remote Sens. Environ.* 55, 95–107. doi: 10.1016/0034-4257(95)00186-7

Roosjen, P. P. J., Brede, B., Suomalainen, J. M., Bartholomeus, H. M., Kooistra, L., and Clevers, J. G. P. W. (2018). Improved estimation of leaf area index and leaf chlorophyll content of a potato crop using multi-angle spectral data – potential of unmanned aerial vehicle imagery. *Int. J. Appl. Earth Obs. Geoinf.* 66, 14–26. doi: 10.1016/j.jag.2017.10.012

Sandmeier, S., Muller, C., Hosgood, B., and Andreoli, G. (1998). Physical mechanisms in hyperspectral BRDF data of grass and watercress. *Remote Sens. Environ.* 66, 222–233. doi: 10.1016/s0034-4257(98)00060-1

Shepherd, K. D., and Walsh, M. G. (2002). Development of reflectance spectral libraries for characterization of soil properties. *Soil Sci. Soc. Am. J.* 66, 988–998. doi: 10.1371/journal.pone.0151536

Sims, D. A., and Gamon, J. A. (2002). Relationships between leaf pigment content and spectral reflectance across a wide range of species, leaf structures and developmental stages. *Remote Sens. Environ.* 81, 337–354. doi: 10.1016/s0034-4257(02)00010-x

Stagakis, S., Markos, N., Sykioti, O., and Kyparissis, A. (2010). Monitoring canopy biophysical and biochemical parameters in ecosystem scale using satellite hyperspectral imagery: an application on a *Phlomis fruticosa* Mediterranean ecosystem using multiangular CHRIS/PROBA observations. *Remote Sens. Environ.* 114, 977–994. doi: 10.1016/j.rse.2009.12.006

Verrelst, J., Schaepman, M. E., Koetz, B., and Kneubuehler, M. (2008). Angular sensitivity analysis of vegetation indices derived from CHRIS/PROBA data. *Remote Sens. Environ.* 112, 2341–2353. doi: 10.1016/j.rse.2007.11.001

Wu, C., Niu, Z., Tang, Q., and Huang, W. (2008). Estimating chlorophyll content from hyperspectral vegetation indices: modeling and validation. *Agric. For. Meteorol.* 148, 1230–1241. doi: 10.1016/j.agrformet.2008.03.005

Wu, C. Y., Niu, Z., Wang, J. D., Gao, S. A., and Huang, W. J. (2010). Predicting leaf area index in wheat using angular vegetation indices derived from in situ canopy measurements. *Can. J. Remote Sens.* 36, 301–312.

Xue, L. H., Cao, W. X., Luo, W. H., Dai, T. B., and Zhu, Y. (2004). Monitoring leaf nitrogen status in rice with canopy spectral reflectance. *Agron. J.* 96, 135–142. doi: 10.2134/agronj2004.0135

Yu, K., Lenz-Wiedemann, V., Chen, X., and Bareth, G. (2014). Estimating leaf chlorophyll of barley at different growth stages using spectral indices to reduce soil background and canopy structure effects. *ISPRS J. Photogramm. Remote Sens.* 97, 58–77. doi: 10.1016/j.isprsjprs.2014.08.005

Zhang, H. Y., Liu, M. R., Feng, Z. H., Song, L., Li, X., Liu, W. D., et al. (2021). Estimations of water use efficiency in winter wheat based on multi-angle remote sensing. *Front. Plant Sci.* 12:614417. doi: 10.3389/fpls.2021.614417

Zhou, X. F., Huang, W. J., Zhang, J. C., Kong, W. P., Casa, R., and Huang, Y. B. (2019). A novel combined spectral index for estimating the ratio of carotenoid to chlorophyll content to monitor crop physiological and phenological status. *Int. J. Appl. Earth Obs. Geoinf.* 76, 128–142. doi: 10.1016/j.jag.2018.10.012

Conflict of Interest: The authors declare that the research was conducted in the absence of any commercial or financial relationships that could be construed as a potential conflict of interest.

frontiers | Frontiers in Plant Science

TYPE Review
PUBLISHED 24 August 2022
DOI 10.3389/fpls.2022.935748

EDITED BY
Wei Guo,
The University of Tokyo, Japan

REVIEWED BY
Ravi Valluru,
University of Lincoln, United Kingdom
Honglong Zhao,
Center for Excellence in Molecular Plant Sciences (CAS), China

*CORRESPONDENCE
Weiguo Liu
lwgsy@126.com

SPECIALTY SECTION
This article was submitted to Technical Advances in Plant Science, a section of the journal Frontiers in Plant Science

RECEIVED 04 May 2022
ACCEPTED 21 July 2022
PUBLISHED 24 August 2022

CITATION
Li X, Xu X, Chen M, Xu M, Wang W, Liu C, Yu L, Liu W and Yang W (2022) The field phenotyping platform's next darling: Dicotyledons. *Front. Plant Sci.* 13:935748. doi: 10.3389/fpls.2022.935748

The field phenotyping platform's next darling: Dicotyledons

Xiuni Li[1,2,3], Xiangyao Xu[1,2,3], Menggen Chen[1,2,3], Mei Xu[1,2,3], Wenyan Wang[1,2,3], Chunyan Liu[1,2,3], Liang Yu[1,2,3], Weiguo Liu[1,2,3]* and Wenyu Yang[1,2,3]

[1]College of Agronomy, Sichuan Agricultural University, Chengdu, China, [2]Sichuan Engineering Research Center for Crop Strip Intercropping System, Chengdu, China, [3]Key Laboratory of Crop Ecophysiology and Farming System in Southwest, Ministry of Agriculture, Chengdu, China

The genetic information and functional properties of plants have been further identified with the completion of the whole-genome sequencing of numerous crop species and the rapid development of high-throughput phenotyping technologies, laying a suitable foundation for advanced precision agriculture and enhanced genetic gains. Collecting phenotypic data from dicotyledonous crops in the field has been identified as a key factor in the collection of large-scale phenotypic data of crops. On the one hand, dicotyledonous plants account for 4/5 of all angiosperm species and play a critical role in agriculture. However, their morphology is complex, and an abundance of dicot phenotypic information is available, which is critical for the analysis of high-throughput phenotypic data in the field. As a result, the focus of this paper is on the major advancements in ground-based, air-based, and space-based field phenotyping platforms over the last few decades and the research progress in the high-throughput phenotyping of dicotyledonous field crop plants in terms of morphological indicators, physiological and biochemical indicators, biotic/abiotic stress indicators, and yield indicators. Finally, the future development of dicots in the field is explored from the perspectives of identifying new unified phenotypic criteria, developing a high-performance infrastructure platform, creating a phenotypic big data knowledge map, and merging the data with those of multiomic techniques.

KEYWORDS
high-throughput phenotyping platform, dicotyledonous crops, field, research progress, development direction

Introduction

With the increasing popularity of sequencing technology and the scale of materials to be tested, a new issue has arisen: a lack of suitable high-throughput phenotype acquisition technology to obtain corresponding phenotypic information. In addition, based on a large amount of crop genome information, determining how to analyze the interaction mechanisms of gene function, plant phenotype, and environmental response efficiently and with a high resolution has become a new challenge (Furbank and Tester, 2011). In this context, genomics, corresponding to the phenomics concept, has arisen at a historic moment (Zhao et al., 2019). The essence of the phenotype is a plant genome sequence three-dimensional expression, and its regional differentiation characteristics and evolution are intergenerational (Tardieu et al., 2017; Zhao, 2019), so the plant phenotypic group contains information with a complexity far beyond the estimates. Therefore, the genotype–phenotype–environment relationship can be systematically and deeply explored from an omic perspective to reveal the response mechanism of structural and functional characteristics of plants to genetic information and environmental changes at multiple scales (Pan, 2015; Tardieu et al., 2017; Zhou et al., 2018).

Currently, crop phenotype research is primarily conducted in the United States, Germany, France, Australia, the United Kingdom, Italy, Japan, Canada, Mexico, India, and China (Xiao et al., 2021). Research objects have included maize (Souza and Yang, 2021; Xie et al., 2021; Shao et al., 2022), rice (Mishra et al., 2021; Muharam et al., 2021; Xiao et al., 2021), wheat (Prey and Schmidhalter, 2020; Furbank et al., 2021; Zelazny et al., 2021), and other monocotyledons. This focus on monocotyledons probably occurred because their morphological structure is relatively simple, and the difficulty of image acquisition and data analysis is relatively low. Leaf counting has been realized in maize, sorghum, and other monocotyledons over the entire growth period (Miao et al., 2021). However, studies on the leaves of dicotyledonous species such as soybean and cotton have focused only on comprehensive indicators such as canopy coverage and compactness due to the severe occlusion between leaves and complex plant types (Moreira et al., 2019; Li et al., 2020), which has led to the loss of many details. Leaves are closely related to plant photosynthesis, thus affecting biomass accumulation, which in turn is related to yield formation, so the loss of information is not conducive to the in-depth study of the phenotypes of dicotyledons. A significant positive correlation exists between the panicle number and the yield at maturity, and this number can be identified and counted directly at a certain regional scale in most monocotyledons. There was a significant positive correlation between panicle number and yield at the maturity stage, and it could be recognized and counted directly on a certain regional scale in most monocotyledons (Jun et al., 2021; Wanli et al., 2021). However, in many dicotyledons, researchers can predict yields using only a large number of other indicators or measure the yield by picking and laying out fruits at maturity (Casagrande et al., 2022) or by picking and spreading out fruits at maturity (Li et al., 2021; Xiaobin et al., 2022), which greatly increases labor costs and is not beneficial to the development of high-throughput phenotypes.

Branching is an important common feature of dicotyledons. The quantity of branches and their position influence yields and are connected to the lodging resistance. Studies have shown that by reducing the position of branches and increasing the number of effective branches in oilseed rape, the lodging resistance can be improved, and the yield per plant can be increased (Fan et al., 2021; Amoo et al., 2022). The branching ability guarantees the yield formation in soybean (Xiaobo et al., 2012; Yu-Shan et al., 2015). The major goal of breeders is to increase upland cotton yields by controlling the branch type and using appropriate mechanical picking methods. Therefore, Wu et al. (Wu et al., 2021; Zhan et al., 2021; Sun et al., 2022) carried out a series of studies on branching development. These studies have contributed to improved breeding by providing great genes for improving plant accessions. However, few studies involving the use of high-throughput phenotyping platforms have been conducted, which has severely slowed the breeding of dicotyledonous plants.

Dicotyledons account for 4/5 of the total number of angiosperms and play an important role in agricultural production (Chuanji, 1982). Soybean, broad bean, rape, cotton, and other dicotyledonous species are commonly cultivated and are all directly tied to human existence. According to imprecise statistics, the global demand for soybeans is ≈388 million tons per year. With an annual consumption of almost 600 million tons (searched in the U.S. Department of Agriculture data), rapeseed is the world's second-largest oil crop species. Therefore, high-throughput phenotypic studies on dicotyledons are highly important.

The current high-throughput phenotyping research environment mainly includes indoor potted plants (Bodner et al., 2021; Zea et al., 2022) because indoor imagining, which can swiftly and accurately obtain a large number of phenotype images for later analysis and verification, faces fewer restrictive factors. Thousands of phenotypic experiments carried out in environmentally controlled growth facilities or fields each year can provide a vast amount of phenotypic data. Due to the impact of environmental variations, the replication of results by the same researcher and the repeatability of results in separate tests by other laboratories are frequently unsatisfactory (Poorter et al., 2012). Environmental aspects are critical and should be given at least as much attention as the characteristics being assessed, which leads to the next question: how does one quantify all environmental impacts? The phenotyping platform is systematically presented in this paper, and the determination of the phenotype of dicotyledons against the backdrop of the rapid development of the field phenotyping platform is

---

Abbreviations: 3D, Three Dimensions; CNN, Convolutional Neural Network; CSIRO, Commonwealth Scientific and Industrial Research Organisation; CT, Computed Tomography; DCNN, Deep Convolutional Neural Network; EB, Integrated Baggies; ETH, Ethiopia; εc, Biomass; εe, Photochemical Energy; GWAS, Genome-Wide Association Studies; IPPN, International Plant Phenotype Network; MRI, Magnetic Resonance Imaging; NASA, National Aeronautics and Space Administration; OSP, Optical Sensing-based Phenotyping; PGP, Pretty Good Privacy; PHIS, Phenotypic mixed Information System; QTL, Quantitative Trait Loci; RGB, An abbreviation for three primary colors; SAM, Shoot Apical Meristem; SMAP, Soil Moisture Active Passive; SFM, Multiview Structure From Motion; SNP, Scottish National Party; UAVs, Unmanned Aerial Vehicles; UK, Britain.

discussed. This paper guides investigating high-throughput phenotypic application technology for dicotyledons in the field, enhancing precision agriculture and increasing genetic gains.

Overview of high-throughput phenotyping of dicotyledonous crops in the field

We collected statistics on field phenotyping facilities and the number of publications since 2010 to better understand how the high-throughput phenotyping of field dicot crops should be developed. In 2016,according to statistics from the International Plant Phenotype Network (IPPN), the phenotyping platform is used in the United States, Australia, China, Germany, and other countries. Nearly 200 large-scale phenotyping facilities are in operation around the world (the most notable being the Australian National Plant Phenotyping Facility "Plant Accelerator," the British National Plant Phenotyping Center, the German Julich Phenotyping Research Center, the Netherlands Plant Eco-phenotyping Centre, and the German IPK Greenhouse Automation). There are ≈82 indoor mechanized phenotyping platforms and 81 European field mechanized phenotyping platforms (including 26 intensive and 55 barren types). Asian field mechanized phenotyping platforms are yet to be counted. However, over the last 5 years, many countries, led by the United States and China, have increased their investments in field mechanization platforms.

The development of phenotyping platforms has provided a solid foundation for crop phenotyping research. Only 25% of all global high-throughput phenotyping platforms are used for field research, and only 49% of the platforms are actually used to obtain high-throughput phenotyping information in the field (Figure 1A). The number of papers published on crop phenotypes has increased annually; in 2019, the number of papers published each year had surpassed 300. Additionally, among many countries and regions that are involved in high-throughput phenotyping studies of plants, the United States is ahead in terms of research results. We list only the top 10 countries or regions in Figure 1B. Dicotyledonous crops account for only 23% of the research results, which is substantially lower than monocotyledons. Arabidopsis is the most studied dicot crop, most likely because it is a commonly used model crop and using it to analyze new phenotypes can greatly decrease the difficulty of research. Furthermore, soybeans, cotton, tobacco, peanuts, rape, and other crops have gradually entered the academic research field. Finally, we compiled statistics on dicotyledonous crop research topics. According to the statistical findings, dicotyledonous plant research topics mainly focus on six aspects: yields, physiology and biochemistry, genes, biotic stress, abiotic stress, and growth dynamics. Genes were the most studied topic, followed by yield (Figure 1C). These research topics are covered in the following chapter.

Research progress of field high-throughput phenotypic information platforms

Platforms are generally classified into three types based on the different spatial areas in which they operate: ground-based platforms, air-based platforms, and space-based platforms (Huichun et al., 2020). Ground-based platforms encompass all plant phenotyping platforms that are in contact with the ground while being built or used. Based on their loading modes, sensors are classified into conveyor belt types, gantry types, suspension cable types, vehicle types, and self-propelled plant phenotyping platforms (Figure 2A). Air-based platforms include all platforms that collect phenotypic data in the air, which are classified as unmanned aerial vehicles (UAVs) or manned aircraft depending on whether or not a human pilot is present (Figure 2B). Space-based platforms collect phenotypic data using satellite remote sensing (Figure 2C).

Ground-based platforms

Research has been conducted on ground-based platforms, with Crop Design in Belgium being the first company in the world to develop a commercialized large-scale phenotyping measurement platform (Reuzeau et al., 2006). Foundation platforms have advantages and disadvantages in their use (Table 1). The conveyor belt-type foundation platform can detect plant phenotypic indicators in real time, and the detection objects can be flexibly replaced based on individual needs. However, this device is better suited for indoor use. The gantry-type platform has a walking device, an automatic control module for mechanical motion, and a high-precision sensor array. It is not affected by the environment, has a low impact, and can take measurements repeatedly every day. However, the cost is high, and only a fixed area can be observed. Suspension-type platforms have the advantages of not requiring guards, continuous operation (such as at night), good repeatability, and high measurement accuracy, but they are typically expensive and can detect only a limited number of areas. Vehicle-mounted platforms are typically agricultural machinery platforms, such as tractors, that are outfitted with various sensors to form phenotype platforms. They can meet the application requirements of most researchers and small businesses to the greatest extent possible due to their low cost, constant perspective, easy installation, and simple operation. However, due to the wide wheel, low body height, and high vibration, agricultural machinery is primarily suitable for short plants and is limited by row spacing and plant space. Currently, the vehicle-borne phenotypic platform is being used to collect biomass (Busemeyer et al., 2013), plant height (Comar et al., 2012), leaf area, stem diameter, canopy temperature, and other

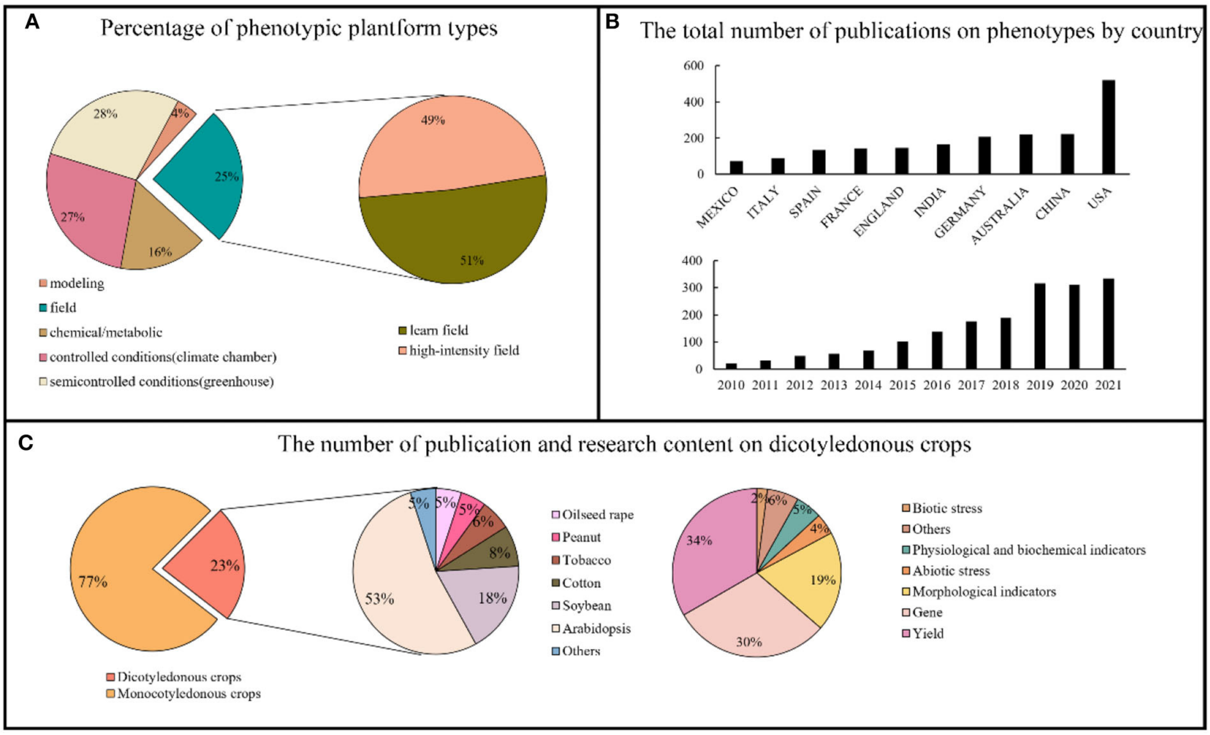

FIGURE 1
Overview of high-throughput phenotyping research. **(A)** The proportion of different phenotypic platforms and the composition of phenotypic platforms in the field (searched in IPPN, https://www.plant-phenotyping.org/ippn-survey_2016). **(B)** Ranking and annual number of phenotypic papers published by countries in the world (2010–2021) (searched in Web of Science). **(C)** Proportion of high-throughput phenotypes studied in monocotyledons and dicotyledons and the main subjects studied in dicotyledons (searched in Web of Science).

phenotypic data for wheat (Andrade-Sanchez et al., 2013), cotton (Sun et al., 2018), and other crops. Researchers should examine the impact of the weight of agricultural machinery on the soil structure and the root system of plants. An increasing number of researchers are experimenting with compact self-propelled ground mobile platforms to carry phenotyping sensors to minimize costs, increase the measurement accuracy, and reduce environmental side effects (Bai et al., 2016; Young et al., 2018). Nonetheless, business solutions are lacking, making promotion extremely difficult. Furthermore, by using the chassis of commercial self-propelled ground rovers, several researchers have created phenotypic platforms for various applications (Shafiekhani et al., 2017), offering a novel approach to the creation of self-propelled phenotyping platforms.

Li et al. (2020) identified new I-trait indicators (plant density, relative frequencies, and entropy, among others) that accurately reflect the response of cotton to drought stress at the seedling stage. By merging high-throughput phenome, genome, and transcriptome data, researchers found that two unannotated genes, GhA040377 and GhA040378, were considerably upregulated in response to drought. Finally, this study advocated the use of phenomics to improve the genetics of cotton and was the first phenomics research publication on drought resilience in cotton.

Air-based platforms

Air-based platform research is still in its early stages, but it is progressing quickly. This type of platform has the advantage of scanning a large area of land in a short period of time, but there are also some drawbacks such as a low information accuracy, an insufficient payload, limited endurance, and weather vulnerability. Currently, air-based phenotyping platforms primarily include UAVs and manned helicopters. When compared to manned helicopters, UAVs have lower costs, lower flying altitudes, and superior information acquisition precision. As a result, numerous studies have been conducted on the acquisition of field phenotypic information *via* UAVs. The number of sensors that a UAV can carry is limited due to its low payload capacity compared to ground-based platforms. Remote sensing analysis of crop phenotypes (Liu et al., 2016) and maturity evaluation (Malambo et al., 2018) is performed using RGB cameras, infrared imaging,

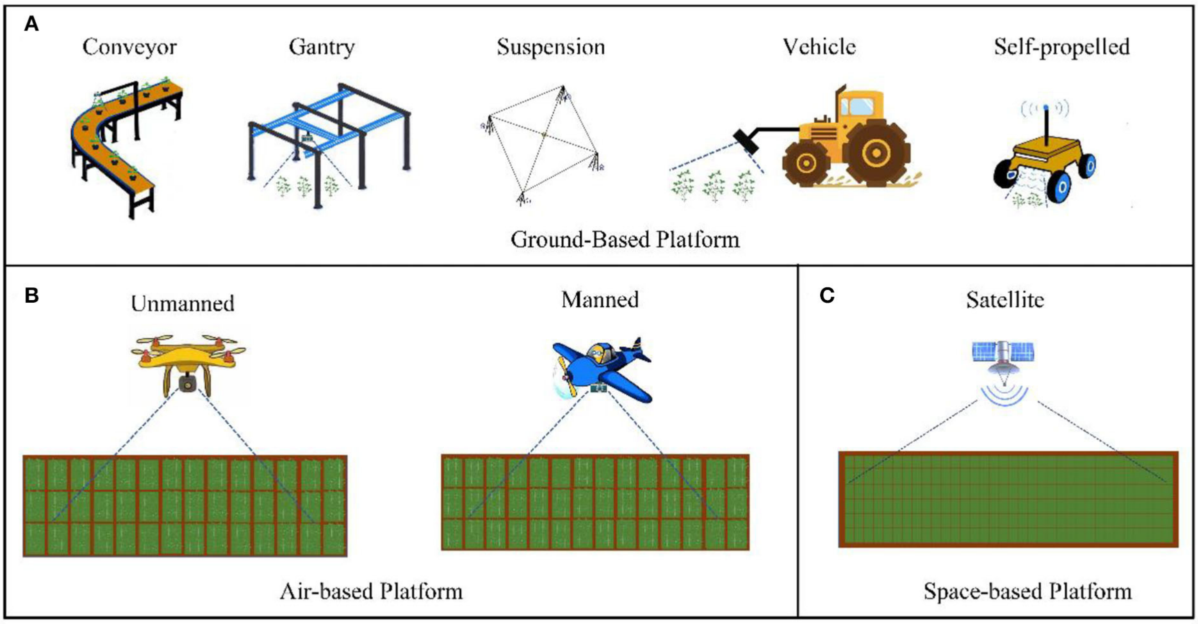

FIGURE 2
Field high-throughput phenotypic information platform. **(A)** Ground-based platforms include conveyor belt types, gantry types, suspension cable types, vehicle types, and self-propelled types. **(B)** Air-based platforms include UAVs or manned aircraft. **(C)** Space-based platforms include satellite remote sensing.

multispectral/hyperspectral cameras, and other sensors. Disease diagnosis (Sugiura et al., 2016), yield estimation (Chang et al., 2021), growth state monitoring and evaluation (Jin et al., 2017; Hu et al., 2018), and analysis of critical phenotypic features have been performed using this type of platform (Ding et al., 2019). Trevisan et al. (2020) used a 3D point cloud derived from UAV images to develop a method for detecting sorghum spikes. The correlation coefficients between the average panicle length and width assessed by UAVs and those measured on the ground were 0.61 and 0.83, respectively. Karthikeyan et al. (2020) used a space-based platform to collect images twice a week and then employed two complimentary convolutional neural networks (CNNs) to forecast soybean maturity. This method can detect the sources of mistakes in maturity forecasting, and its architecture overcomes earlier research limitations and can be used in large-scale commercial breeding initiatives.

When UAVs are employed, it is also important to consider its stability, safety, and controllability.

Space-based platforms

Satellite platforms for monitoring the status of large areas of crops are referred to as a “space-based platforms.” Because they have the highest data flux and lowest accuracy, space-based phenotyping platforms are suited only for a wide spectrum of detection. On the one hand, satellites have a massive payload, and onboard sensors can cover optical, thermal, microwave, and fluorescence frequencies, allowing for the collection of large amounts of data in a short period of time. On the other hand, satellites can provide recurrent information on agricultural conditions at different scales throughout the season (including yield forecasting, field preparation, crop health monitoring, irrigation, and site-specific management) (Zhang et al., 2020). Furthermore, improvements in the spatial (Weiss et al., 2020), spectral, and temporal resolutions of satellite measurements have increased their use in plant breeding (Prey et al., 2020; Weiss et al., 2020). Space-based platforms have become increasingly popular in recent years, and despite their high cost, they are being used in a limited number of agricultural applications. For example, NASA has created the Space Test Station for Thermal Radiation of Ecological Systems, which can be used to monitor the soil moisture content (Entekhabi et al., 2010), drought warnings, and water usage efficiency (Reynolds et al., 2019b). Soil Moisture Active Passive (SMAP) observations of soil moisture and freeze/thaw timing can reduce a major uncertainty in quantifying the global carbon balance by helping to resolve an apparent missing carbon sink on land over the boreal latitudes (Entekhabi et al., 2010). Pleiades-1a and World View-3 have been utilized to detect disease and agricultural water stress (Navrozidis et al., 2018; Salgadoe et al., 2018), promoting the advancement of precision agriculture. On the practical side, Jain and Balwinder-Singh (2019) demonstrated how microsatellite data management can

TABLE 1 Performance comparison of plant phenotypic information collection platforms.

Phenotypic platform	Platform name	Research and development unit	Platform type	Advantages	Limitations	Scanning scale	Practical application
Ground-based Platform	Crop Observer	PhenoVation, Netherlands company	Conveyor belt	Real-time measurement of photosynthetic efficiency, estimation of soil coverage by plant leaves	More suitable for indoor work	1–10 m^2	Experiments in a test field at Wageningen University in the Netherlands
	Field Scan	PhenoVation, Pheno Spex company	Gantry type	Not affected by the environment, the efficiency can reach 5,000 plants/h, and the measurement can be repeated every day	High cost, only a fixed area can be observed	10–50 m^2	Applied to the field phenotyping platform built by Nanjing Agricultural University in 2018
	Field Scanalyzer	Germany, Lemna Tec company	Gantry type	With walking device, automatic control module of mechanical movement, high-precision sensor array, supporting data acquisition and analysis software	High cost, only a fixed area can be observed		Procurement by scientific research institutions such as French Academy of Agricultural Sciences, Chinese Academy of Sciences and DuPont Pioneer (Virlet et al., 2016)
	Breed Vision	University of Applied Technology, Osnabruck, Germany	Gantry type	Mobile darkroom (moving speed 0.5 m/s), equipped with 3D depth camera, color camera, laser ranging sensor, light screen imaging Settings and other optical equipment	High cost, only a fixed area can be observed	1–10 m^2	University of Applied Technology, Osnabruck (Busemeyer et al., 2013)
	Spidercam	University of Nebraska-Lincoln	Suspended cable	Covering a field of 4,000 m^2, a variety of sensors can be mounted on the suspension cable platform	High cost, only a fixed area can be observed	50–100 m^2	Test field use at the University of Nebraska-Lincoln in 2017 (Ge et al., 2019)
	ETH	Swiss ETH Field Phenotyping Platform	Suspended cable	Suspended various sensors	High cost, only a fixed area can be observed	100–1,000 m^2	ETH plant research station Lindau-Eschikon (Kirchgessner et al., 2016)
	Field Scanalyzer	UK, Rothamsted Research Centre	Suspended cable	Equipped with a variety of sensors, the applicability is strong, the system runs smoothly, and is less affected by external interference	High investment cost, high operation and maintenance costs, not suitable for large breeding areas	50–100 m^2	/
	Phenotyping Robot	USA, Iowa State University	Self-propelled	Multiple stereo cameras trigger synchronously, and multiple sets of stereo lenses are superimposed to ensure phenotypic analysis of tall crops	No commercial solution, need to design independently	1–10 m^2	Used in the experimental field of Iowa State University in 2014
	GPheno Vision	University of Georgia	Vehicle	Low cost, can be equipped with a variety of sensors	Fuel power, larger vibration, wider tires, and requirements for row spacing		In 2017, it was used in the experimental field of the University of Georgia, USA (Jiang et al., 2018)

(Continued)

TABLE 1 Continued

Phenotypic platform	Platform name	Research and development unit	Platform type	Advantages	Limitations	Scanning scale	Practical application
Air-based Platform	Helipod	CSIRO	UAV	Equipped with thermal imager and RGB camera to obtain canopy temperature and RGB images	Limited load capacity, regulated altitude, short flight time, and affected by the environment	100–2,000 m^2	Intensive phenotyping experiments in Canberra, Australia
	LiAir	Beijing Digital Green Earth Technology Co., Ltd.		Wide field of vision, daily measurement 2 km^2			In 2012, it has been applied to the field of agroforestry phenotyping
Space-based Platform	The Pleiades−1A and Worldview-3	/	Satellite	The detection area is the largest, which is convenient for macro-control	Highest cost, relatively low accuracy, only suitable for large area inspection	>10,000 m^2	Disease and Crop Water Stress Detection

ETH, Ethiopia; UK, Britain; CSIRO, Commonwealth Scientific and Industrial Research Organisation; UAV, unmanned aerial vehicle.
The short line (-) indicates that the platform is not mentioned in the article.

have a substantial impact on agricultural sustainability in underdeveloped nations.

In summary, many crop phenotyping platforms in the field have distinct properties. Ground-based platforms can analyze the largest number of species and are well-established. Their price is reasonable; however, the vision height is limited, and the data throughput is modest. Two types of space-based platforms are available: manned and unmanned. Unmanned platforms can quickly acquire macrolevel information in a specific area, with broad vision and enormous data throughput, but their cost is significant. Space-based platforms, which offer the widest observation area, mostly rely on satellite remote sensing. However, they cannot perform small-scale or refined crop detection and are infrequently employed in agriculture due to their high cost. The use of space-based platforms in agriculture is projected to become more common as science and technology advance. The properties of many types of field phenotyping platforms are shown in Table 1. When employing phenotyping platforms, platforms that are reasonable for the circumstances must be chosen and developed, taking into account actual requirements such as mobility, ease of operation, data flux and accuracy, and costs (Lee et al., 2015).

Research status of high-throughput phenotypic information of dicots in the field

Morphological indicators

Plant morphology has essential biological implications in agricultural production, and it is a key component of plant science research. Traditional plant identification and classification approaches rely on professional experience, which is subjective and inaccurate, to examine plant morphological traits such as appearance, shape, texture, and color (Liu et al., 2016). Using machine vision, picture segmentation, and big data processing technologies to reliably gather and analyze crucial plant traits is an important technical means for the development of contemporary agriculture, with significant guiding value for crop management and genetic breeding (Granier and Vile, 2014; Li et al., 2021). Scholars have conducted field studies on the morphological indicators of dicotyledonous crops, including stem height (Paproki et al., 2012), plant height (Sun et al., 2017), leaf width (Paproki et al., 2012), leaf length (Paproki et al., 2012), number of leaves (Dobrescu et al., 2020), canopy coverage (Kirchgessner et al., 2016; Borra-Serrano et al., 2020; Wan et al., 2021; Xu et al., 2021), canopy height (Kirchgessner et al., 2016; Borra-Serrano et al., 2020), canopy roughness (Herrero-Huerta et al., 2020), and flowers (Xu et al., 2017; Jiang et al., 2020).

Stems and leaves are the most frequently utilized factors for crop morphological indication, and RGB values are commonly used by researchers to extract these parameters. For example,

TABLE 2 Statistics of field phenotype research on dicotyledonous crops.

Classification of indicators	Crop category	Type of data	Phenotypic analysis method	Phenotypic parameters	Accuracy %	R^2	Shooting scale	Year	Author
Morphological indicators	Cotton	RGB	3D reconstruction	Stem height, leaf width, leaf length	91.66, 94.25, 91.22	–	Single	2012	Paproki et al., 2012
	Soybean	Thermal, Multispectral	Machine learning	Canopy coverage, canopy height	–	0.86, 0.99	Single	2016	Kirchgessner et al., 2016
	Cotton	RGB	CNN	Number of flowers	Error = −4∼3	–	Single	2017	Xu et al., 2017
	Rapeseed	Multispectral, RGB	Machine learning	Canopy coverage	–	0.79	Group	2021	Wan et al., 2021
	Soybean	RGB	Machine learning	Canopy coverage, canopy height	90.4, 99.4	–	Group	2020	Borra-Serrano et al., 2020
	Cotton	RGB	CNN	Flowering patterns	–	0.88	Single		Jiang et al., 2020
	Soybean	RGB	SFM	Canopy roughness	–	>0.5	Group		Herrero-Huerta et al., 2020
	Cotton	RGB	Metashape, Python	Canopy coverage	93.4	–	Group	2021	Xu et al., 2021
	Arabidopsis	RGB	CNN	Number of leaves	–	0.92		2020	Dobrescu et al., 2020
	Cotton	Lidar	3D point cloud	Plant height	–	1	Single	2017	Sun et al., 2017
Physiological and biochemical indicators	Soybean	RGB	Machine learning	Leaf iron deficiency chlorosis	>81, 96	–	Regional	2018	Bai et al., 2018
								2017	Naik et al., 2017
	Cotton	Near Infrared Spectroscopy	/	Leaf macro and micronutrients	87.3, 86.6	–	Organ	2021	Prananto et al., 2021
	Soybean	Hyperspectral	DNN	Fresh biomass of above ground	–	0.91	Group	2021	Yoosefzadeh-Najafabadi et al., 2021
	Cotton	Hyperspectral	/	Coverage, water use efficiency	–	–	Group	2018	Thorp et al., 2018
	Soybean	Spectral Scanner	Modeling	εe, εc	–	0.68	Organ	2021	Keller et al., 2021
Biotic/Abiotic Stress	Rapeseed	RGB	CNN	Oilseed rape pests	77.14		Regional	2019	He et al., 2019
	Rapeseed	RGB	Machine learning	Fruiting bodies of *Leptosphaeria maculans*	–	0.87	Regional	2019	Bousset et al., 2019
	Soybean	RGB	DCNN	Nonbiological	–	–	Regional	2018	Ghosal et al., 2018
	Soybean	RGB	Machine learning	Leaf iron deficiency chlorosis	96%	–	Single	2018	Naik et al., 2017
	Soybean	Multispectral, Infrared	Machine learning	Flood	–	0.9	Organ	2021	Zhou et al., 2021
Yield	Soybean	RGB	/	Canopy coverage	–	0.4–0.7	Regional	2016	Bai et al., 2016
	Soybean	RGB	Machine learning	Yield and maturity	–	0.51, 0.82	Group	2020	Borra-Serrano et al., 2020
	Soybean	RGB	/	Yield/canopy cover	–	0.75	Group	2019	Moreira et al., 2019
	Soybean	Hyperspectral	DNN (EB)	Yield	–	0.76, 0.77	Group	2021	Yoosefzadeh-Najafabadi et al., 2021

RGB, an abbreviation for the three primary colors; CNN, convolutional neural network; DCNN, deep convolutional neural network; SFM, multiview structure from motion; EB, integrated baggies εe, photochemical energy; εc, biomass.
The slash (/) indicates the ratio.
The short line (–) indicates that it is not mentioned in the article.

Paproki et al. (2012) created a cotton plant model by capturing RGB images of cotton plants and extracting indicators such as the cotton stem height, leaf width, and leaf length. When compared to manual measurements, the average absolute error was 9.34, 5.75, and 8.78%, respectively, while the correlation coefficients were 0.88, 0.96, and 0.95, respectively. Dobrescu et al. (2020) used deep learning to analyze the number of Arabidopsis leaves in RGB photos, and the $R^2 = 0.92$ when compared to manual measurements. The approach of collecting crop morphological data from RGB images is quite accurate.

The extraction of crop canopy information is useful in the study of crop data. Previous research has demonstrated that thermal imaging, multispectral imaging, and RGB imaging can be utilized to monitor soybean canopy coverage and canopy height with an accuracy of >90% (Sun et al., 2017; Borra-Serrano et al., 2020), and an $R^2 > 0.5$ was found after linear fitting using the values measured in the field (Herrero-Huerta et al., 2020). Moreover, similar research has been conducted on cotton, rape, and other crops. Xu et al. (2021) created a UAV system with three cameras (RGB, multispectral, and thermal) and a lidar sensor to identify cotton canopy coverage and canopy height, with an average relative error of only 6.6%. The approach of collecting crop morphological data from RGB images is quite accurate. Using a UAV platform fitted with an RGB and multispectral camera, Wan et al. (2021) obtained rape canopy images. The PROSAIL-GP model was used to invert rapeseed vegetation coverage and the $R^2 = 0.79$. The resilience of the proposed method was confirmed in cotton (*Gossypium hirsutum* L.), and a better retrieval accuracy was obtained.

Many experiments have been conducted to analyze cotton flowering utilizing high-throughput phenotyping approaches. Color RGB images obtained by a UAV system and a CNN were used to detect the number of cotton blossoms in the original image, with an error of just $-4\sim3$ (Xu et al., 2017). Scanning cotton with a tractor-mounted lidar had an $R^2 = 0.98$ compared with that of manual measurements (Sun et al., 2017). Moreover, cotton flowering status can be recognized using multiview color imaging and deep learning, with an $R^2 = 0.88$ and an RMSE = 0.79 (Jiang et al., 2020).

Previous research has indicated that the use of a high-throughput phenotyping platform to obtain crop morphological indicators is nearing maturity. Researchers are more likely to use a ground-based platform equipped with an RGB camera as the primary research tool in the study of crop leaves and stalks. Canopy information can be extracted using UAVs equipped with RGB, hyperspectral, and radar sensors, but the accuracy is slightly lower than that obtained in leaf and stem studies. In terms of flower counting, UAVs and vehicle-mounted platforms outfitted with RGB cameras and lidar are commonly used, and the accuracy is acceptable. Thus, it is not surprising that the choice of a high-throughput phenotyping platform is closely related to the specific indicators being studied.

Physiological and biochemical indicators

Crop physiological and biochemical indices include chlorophyll, photosynthetic rate, water stress, biomass, salt tolerance, and leaf water content. These indices can accurately reflect crop growth, health, and resistance. Crop physiology and biochemistry studies involving the use of a high-throughput phenotyping platform have primarily focused on the leaf color (Bai et al., 2018), element content (Naik et al., 2017; Prananto et al., 2021), biomass (Yoosefzadeh-Najafabadi et al., 2021), and water use efficiency (Thorp et al., 2018).

To score iron deficiency chlorosis, RGB images of soybean plants in the field were collected, which revealed an overall accuracy of >81% (Naik et al., 2017; Bai et al., 2018). Prananto et al. (2021) used a ground-based platform equipped with a near-infrared spectrometer (wavelength range 1,350–2,500 nm) to estimate different macro- and micro-elements in cotton leaf tissues, with accuracies of 87.3 and 86.6%, respectively. The fitting degree of aboveground fresh biomass can be as high as 0.91 (Yoosefzadeh-Najafabadi et al., 2021) when combining hyperspectral photography with deep neural network (DNN) analysis for biomass acquisition and water use efficiency. Multispectral images can be used to determine the crop canopy coverage, which is then used to estimate the coefficient of basic crops to improve the crop water use efficiency (Thorp et al., 2018). Previous studies have shown that by acquiring high-throughput phenotypes, crop nutrients can be estimated in the field, farmers can proactively manage nutrition to avoid yield losses or environmental impacts, and evidence is provided for crop selection.

In short, physiological and biochemical indices have received less attention than morphological indices have. The platforms are mainly based on the ground and in space, and the sensor types are more complicated and varied. This research will help with nutrient decisions and the breeding of new varieties.

Biotic/abiotic stress indicators

Pests and diseases are the primary causes of crop yield reductions in terms of biological stress. Abiotic stress refers to all the factors that negatively affect crop growth and development as a result of an unsuitable external environment, which mainly includes light, temperature, water, and fertilizer. Crops are increasingly subjected to biotic/abiotic stress during growth as the global climate changes. The goal of smart agricultural plant protection is to locate the type of stress and determine the degree of stress through accurate identification before crops are stressed and irreparable damage is caused to protect plant operations.

The traditional method for evaluating the tolerance of crops to external stress in terms of the field conditions is to judge the damage level visually, but this method is labor intensive and susceptible to subjective error. This problem can be

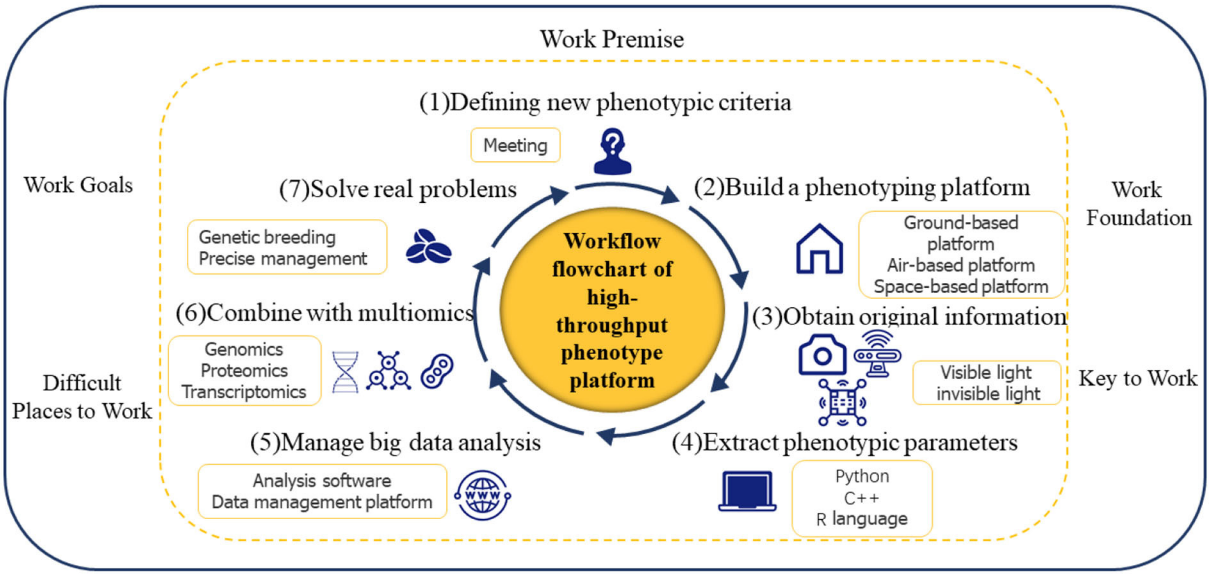

FIGURE 3
High-throughput phenotype workflow flowchart.

effectively resolved by utilizing high-throughput phenotyping. He et al. (2019) used RGB images of rapeseed to judge rapeseed insect pests with an accuracy of 77.14% using CNN processing and analysis. Naik et al. (2017) and Ghosal et al. (2018) used high-throughput phenotypes to evaluate soybean under abiotic stress and obtained promising results. Soybean field images were captured using a UAV equipped with a multispectral and infrared thermal imager, and five image features were extracted, including the canopy temperature, normalized difference vegetation index, canopy area, canopy width, and canopy length. The damage level was evaluated by a deep learning model, with an accuracy of 0.9 based on these features. The method proposed in this paper appears to be very promising for soybean breeding, and it is expected to replace an abundance of manual operations and more efficiently assess the level of waterlogging disasters (Zhou et al., 2021). High-throughput phenotypes have enormous potential for measuring crop traits and detecting crop responses to biological or nonbiological stresses.

Yield indicators

Crop yield estimation in the field is regarded as the foundation of food security. In recent years, remote sensing information and crop growth models have been coupled to resolve a variety of agricultural problems, such as crop growth detection and yield prediction.

Bai et al. (2016) collected soybean field traits *via* a self-propelled platform outfitted with five sensor modules (ultrasonic distance sensor, thermal infrared radiometer, normalized difference vegetation index (NDVI) sensor, portable spectrometer, and RGB network camera). The results of the analysis and processing revealed that the traits obtained by the sensors were highly correlated with the final grain yield in both the early and late seasons ($r = 0.41–0.55$, and $r = 0.55–0.70$). For example, Moreira et al. (2019) attached an RGB camera to a UAV to collect soybean production and canopy coverage data and continued the analysis to yield | ACC with an actual output correlation of 0.75. Yoosefzadeh-Najafabadi et al. (2021) used the hyperspectral vegetation index (HVI) collected by a UAV equipped with hyperspectral sensors to predict soybean yields in conjunction with two artificial intelligence algorithms integrated baggies (EB) and DNN and obtained determination coefficients (R^2) of 0.76 and 0.77, respectively.

We suggest that to acquire a yield index, we must first acquire multi-index information. Because different researchers utilize different predictors, different high-throughput phenotypic platforms and sensors can be used. In general, the use of UAVs equipped with RGB cameras is the most common method. Yield prediction is beneficial for shortening the breeding time of varieties, reducing the cost of yield measurements, and enhancing the yield measurement efficiency, all of which are vital in crop research and development. Table 2 provides statistics on the field phenotypic information of dicotyledons.

High-throughput phenotyping and genetic breeding of dicotyledonous crops in the field

Crop breeding has gone through three generations, with the first being artificial screening as the primary method, the second being hybridization as the primary method, and the third being molecular markers and genome-wide association analysis as the primary and auxiliary methods. The fourth generation of intelligent-assisted breeding with big data, supported by multidisciplinary and multiomics data, is currently underway (Wallace et al., 2018). The incorporation of phenotypic and genomic data, as well as proteome, transcriptome, metabolome, and other omics data, is required for the fourth generation. Utilizing genome-wide association studies (GWASs), quantitative trait loci (QTL) analysis, and other technical methods, a large number of candidate genes and candidate molecular markers have been identified. Models, such as breeding information simulation, parental selection recommendation, breeding path recommendation, and breeding variety prediction, have been established to form the ultimate intelligent breeding decision system (Wang and Xu, 2019).

The high-throughput phenotyping platform, which enables the accurate assessment of a large number of field plots with a variety of measures in a short period of time, simplifies the routine quantification of crop development, physiology, and phenological characteristics (White et al., 2012; Araus and Cairns, 2014). These data provide a useful framework for addressing phenotypic bottlenecks in plant breeding (Furbank and Tester, 2011; Araus and Cairns, 2014; Kumar et al., 2015). Crop dwarfing has contributed to the growth of yields in the Green Revolution (Hammer et al., 2009; Swaminathan, 2014), and the fourth generation of intelligent-assisted breeding with big data could be the next breakthrough in accelerating the genetic harvest of crops in the field. Heritability and genetic gain potential will improve with high-throughput and precise phenotypes (Araus et al., 2018). Numerous successful results have been obtained in many crops by incorporating genomic and phenotypic data. The function of a large number of unknown genes, for example, has been quickly decoded, thereby improving the understanding of G-P maps (Raman, 2017). The water conditions of soybeans with different genotypes have been isolated (Braga et al., 2020), mutant and wild types have been effectively classified (Dobrescu et al., 2020), and flowering patterns in plants with complex canopy structures (such as cotton) have been identified (Jiang et al., 2020). Phenotypic indicators with strongly inherited traits are being investigated. Furthermore, phenotypic and genetic variation can be interpreted using optical sensing-based phenotyping (OSP) data analysis (Xavier et al., 2017; Sun et al., 2021).

High-throughput phenotyping and precise management of dicotyledonous crops in the field

Because agriculture is currently facing resource shortages and serious farmland environmental pollution, the implementation of precision agriculture demonstrations and research is critical. High-throughput phenotyping platforms can be used to obtain crop image traits and conduct modeling to estimate the yield and quality of a crop (Xu et al., 2021) and to analyze the relationship between crop growth and environmental factors, thereby enabling more precise management (Maimaitijiang et al., 2019).

In particular, high-throughput phenotypic data can be used to analyze the factors influencing yield differences among plots, treat different plots differently, and implement "prescription farming" based on positions, regulations, and needs. Making full use of information acquisition means analyzing the crop nutrition status and the spatial and temporal changes in pests and diseases to make tillage and field management decisions, as well as investing in agricultural resources such as water and fertilizer based on local conditions. This approach can ensure that the crop production potential is fully realized and avoid the serious consequences of the overuse of chemical fertilizers and pesticides, such as increased production costs, the pollution of farmland soil and water environments, and a decline in the quality of agricultural products. To achieve the best effect and the lowest cost, agricultural outputs can be increased, the quality can be enhanced, costs can be decreased, resources can be conserved, pollution can be reduced, and the environment can be protected. As a result, precision agriculture can produce significant economic and ecological benefits, which are vital for maximizing the production potential of cultivated land, efficiently using agricultural production factors, and preserving the farmland environment.

Development direction of high-throughput phenotypic information research on dicotyledonous field crops

The development of a high-throughput phenotype must follow a certain workflow. As shown in Figure 3, from the determination of phenotypic concepts to the establishment of phenotypic platforms, the acquisition of original information, the extraction of phenotypic parameters, the analysis, processing and mining of big data, and joint analysis with multiple omics, practical problems can finally be solved. In fact, industry experts must decide on new phenotypic criteria because the step of "determination of unified new phenotypic criteria" is a premise for high-throughput phenotypic work; the demands of researchers for high-quality data, particularly in terms of resolution and accuracy, vary depending on the distinct objective features they are pursuing. Therefore, the key to collecting original information is to "develop a high-performance infrastructure platform," but doing so is difficult. For better trait selection in breeding programs, more effective field management in agricultural operations, and the eventual augmentation of the germplasm of grain, the "construction of a knowledge map of phenotypic big data" stage is crucial but also difficult. The process of "combining with multiomics" is critical for finding functional genes and speeding up breeding.

Determination of new unified phenotypic criteria

Healthy, sustainable development must be based on consistent standards. Mendel, the father of genetics, began to define and evaluate phenotypes as early as 1866. He described seven pairs of relative characteristics of peas in his famous paper "Plant Hybridization Experiments," including round and wrinkled seeds, tall stems vs. short stems, green pods vs. yellow pods, and so on. In 1911, Wilhelm Johannsen, a Danish geneticist, established the concept of a biological phenotype, claiming that an organism's phenotype was the consequence of a complex interaction between the genotype and environmental circumstances (Johannsen, 1911). In the 1990s, Nicholas Schoork, an epidemiology and biostatistics expert at Case Western Reserve University, was the first to propose the concept of physics as a counterpart to genomics (Zhao et al., 2019). Since then, studies on single phenotypes or series of phenotypes of humans, animals, and plants have piqued public interest (Siebner et al., 2009), and such studies have gradually evolved into an important branch of biology (Bilder et al., 2009; Houle et al., 2010; Tester and Langridge, 2010). Plant phenotyping research began at the end of the 20th century with the goals of obtaining high-quality and repeatable shape data and quantitatively analyzing the interactions between genotypes and environmental types and the effects on yields, quality, stress tolerance, and other related main traits (Ribaut et al., 2010). Fiorani and Schurr (2013) proposed a new definition of the plant phenotype in 2013, describing it as a collection of methods and protocols for accurately measuring the growth, structure, and composition of plants at various scales. In Zhao (2019) updated the definition of a phenotype, stating that it is a physical, physiological, and biochemical mechanism that can reflect the structural and functional characteristics of plant cells, tissues, organs, plants, and populations. In essence, a phenotype is the three-dimensional sequential expression of plant gene maps, regional differentiation characteristics, and intergenerational evolution. The phenotype concept is constantly being redefined. As a result, in the context of the rapid development of phenotyping platforms, the definition of new phenotypic concepts must be determined as soon as possible, and a consistent standard is necessary for correct phenotypic research by scientists.

Development of a high-performance infrastructure platform

With the widespread adoption of sequencing technology, an increasing number of plant genome sequences have been released, but few functional genes have been identified due to a lack of phenotypic data. Because of leaf occlusion, a substantial amount of information (such as the leaf number, main stem morphology, branch number, branch morphology, fruit number, and fruit morphology) has not been collected during the late growth stage of dicotyledons. The first step in achieving the comprehensive acquisition of high-throughput phenotypic information is to address the loss of original information, which is also the core challenge faced by the high-throughput phenotyping platform. How do you address the issue of lost data? Due to the nature of high-throughput phenotypic information gathering, all of the information that can be extracted is displayed in the original image. Some medical techniques, including computed tomography (CT), magnetic resonance imaging (MRI), and ultrasound, can be used to recover information that has been lost due to leaf occlusion. Unfortunately, because these technologies are both environmentally and financially demanding, they are rarely applied in agriculture.

After more than 10 years of development, crop phenotyping systems have the following characteristics: a high information acquisition efficiency, the use of non-invasive sensors, high-latitude information acquisition, and a resolution that decreases as the information acquisition area expands. As science and technology advance, future high-throughput phenotyping platforms will be able to combine the flux, resolution, dimension, load, robustness, and working height to obtain a large amount of original information efficiently and quickly. Resolution includes both temporal (from seconds to days to months) and spatial (very small, such as for cells, to large, such as for fields and natural environments) dimensions, denoting the variety of phenotypic features acquired by phenotyping systems under various time, space, and scale conditions. The load refers to the maximum weight that a phenotyping platform can carry; notably, in air-based platforms, the load capacity severely restricts the number and variety of sensors that can be used. Therefore, appropriately enhancing the load capacity of a phenotyping platform can promote the diversification of phenotypic data acquisition. The adaptability of phenotyping platforms to work in the field is referred to as robustness. Harsh field conditions pose significant challenges to the normal operation of phenotyping platforms, and enhancing the robustness of a platform can ensure that the platform operates properly. The working height is vital in obtaining phenotypic regions; the obtained regions increase as the working height increases, while the resolution decreases. The key issue for researchers to overcome is how to organically combine the aforementioned factors.

Furthermore, cost control is a critical link, and scientists have been working to determine how to achieve high performance at a low cost. Existing field phenotyping platforms are frequently unable to combine low cost and high performance, failing to meet the needs of most plant phenotype research institutes. As a result, obtaining fast and precise field phenotypic information at a low cost is a bottleneck in the development of a high-throughput phenotyping platform. This necessitates the gathering of talent from various fields, such as machinery, network communication, and sensors, to cross disciplines and contribute to the development of a high-throughput phenotyping platform in the field.

Construction of a knowledge map of phenotypic big data

Plants are dynamic, complex systems. Plant phenotypes, such as shape, size, color, posture, and texture, will change as they grow. Plants of different varieties have a wide range of appearances at the same time, resulting in the typical 3V characteristics of traditional big data in plant genome big data, that is, data volume, variety, and velocity. A large amount of data is mainly due to the rapid increase in phenotypic data obtained by advanced technology phenotyping equipment based on intelligent equipment and artificial intelligence technology. The diversity and heterogeneity of plant individuals and data types determine data polymorphism. The data are timely because of the dynamic and swift generation of large phenotypic data in the form of data flow.

At the same time, big plant phenomics data exhibit 3H characteristics: high dimension, high complexity, and high uncertainty primarily because plant genomic big data include text data and a large number of images, spectra, and cloud point data, resulting in a wide range of data. The high complexity of phenotypic information is determined by the diversity of genetic information and environmental differences. Phenotypic data have low repeatability and uncertainty because they are affected by many factors, and data acquisition criteria are not uniform. Dicotyledons have more complex plant types and higher 3V and 3H characteristics as a result of genetic diversity and geographical environmental resources, making dicotyledon phenotypic data analysis more difficult. How does one screen for key features under this premise? Big data analysis and in-depth mining must be improved.

After overcoming numerous obstacles to obtain phenotypic data, we are unable to extract such data in depth, resulting in a massive waste of data resources. Phenomic studies are more akin to point-like studies. On the one hand, phenotypic studies are carried out by organizations all over the world, but there is little cooperation between nations and institutions. Currently, only two national-level collaborations (with the US as the sole center and Germany, France, and the United Kingdom as common centers) and four institutional-level collaborations exist (with the United States Department of Agriculture and Cornell University as the centers; China Agricultural University, University of Queensland, Chinese Academy of Sciences, and Chinese Academy of Agricultural Sciences; University of Nottingham and University of Bonn; Wageningen University, French Agricultural Research Institute, and French Scientific Research Center). On the other hand, plant phenotypic databases are limited, and the main data contents vary greatly. For example, the Distributed Phenotypic Data Acquisition and Information Management System (Crop Sight), which primarily includes plant phenotypic data and environmental data (Reynolds et al., 2019a), the phenotypic mixed information system (PHIS), which primarily includes multisource and multiscale information in plant phenomics (Neveu et al., 2019), and the plant genome and phenotypic data sharing platform, primarily consists of data information on plant traits, phenotypes, gene functions, and gene expression of 95 plant taxa (Cooper et al., 2018); the Crop Phenotyping Center of Huazhong Agricultural University, which primarily consists of phenotype data and QTL data (Zhang et al., 2017); and the plant phenotype and genomics data publishing platform. Plant phenotypic data, genome data, mass spectrometry data, and data visualization and analysis software data are mainly included in the PGP Repository (Arend et al., 2016). This phenomenon will result in complex and variable phenotypic data formats, a lack of unified standards, and a significant reduction in the role of data. As a result, we urge countries and institutions to work together to strengthen collaborations, establish phenotype databases, share information, and hold joint discussions.

Combining with multiomics

The rapid development of high-throughput sequencing, mass spectrometry, and chromatography has facilitated the study of genomics, transcriptomics, proteomics, and metabolomics. Dicotyledons are characterized by complex plant types and a wealth of phenotypic data. When combined with multimers, dicotyledons can unlock more functional genes and facilitate plant genomics research. In breeding practice, high-throughput phenotyping combined with a variety of other omic techniques can be applied to crops in different growth periods and at different scales (cells, tissues, organs, groups) in research on the comprehensive analysis of the calculated crop regulation network of life activity, revealing the biological characteristics of crops. Certain studies on monocotyledons have been conducted in conjunction with multiple omics, such as the study by Leiboff et al. (2015), who used high-throughput image processing technology to determine the size of the shoot apical meristem (SAM) in a natural population of maize and discovered some new candidate genes controlling the SAM size through GWAS analysis. The link between the SAM morphology and trait-related SNP variants was verified after researchers looked into possible genes involved in hormone transport, cell division, and cell size. Xin et al. (2021) employed wild populations of 384 significant wheat varieties (lines) as the basis for a genome-wide association analysis that included phenotypes from three settings and 55K SNP chip typing data. The findings revealed that 142 SNPs were strongly related to the number of spikelets, with phenotypic variance ranging from 3.27 to 6.09%. Using the same strategy, Guo et al. (2018) discovered a novel drought tolerance gene in rice. For dicotyledons, few relevant studies have been conducted: Bac-Molenaar et al. (2015) used the PHENOPSIS phenotype platform to analyze high-throughput images of 324 Arabidopsis cultivars from the top view and, combined with genome-wide association analysis, identified some QTLs related to specific periods and growth rates, revealing a new perspective on the genetic structure of Arabidopsis dynamic development.

The ability to integrate metabolomics approaches into the current HTP phenotypic platform has significant potential to add value (Hall et al., 2022). Metabolites can be divided into volatile and nonvolatile categories, but they all play multiple roles in the plant life cycle. For example, they can be continuously present, having a protective function through antiinsect or antimicrobial activity (Lubes and Goodarzi, 2017; Maurya, 2020). The nonvolatile metabolome represents rich information reflecting past (e.g., slow turnover metabolites accumulated in response to past stress), present (e.g., high turnover metabolic intermediates), and future (e.g., precursors of biomass under construction) events. Accordingly, a growing number of top-down studies have shown that this metabolome can be correlated with performance in panels of genetic diversity (Meyer et al., 2007; Riedelsheimer et al., 2012). Until recently, cost issues have limited metabolomics applications in large-scale phenotyping. However, using high-resolution MS [TOF-MS, Orbitrap, and Fourier transform ion cyclotron resonance mass spectrometry (FT-ICR-MS)] to distinguish different structures with the same nominal mass alongside ultrafast chromatography now makes it possible to combine HTP with a high resolution (Fekete et al., 2014). Systems biology approaches and the use of large numbers of samples have become possible, and increased observations will enable the development of new prebreeding strategies based on predictive models (Fernandez et al., 2021).

We have reason to believe that plant genomics will advance faster with the establishment of relevant research institutions, the improvement of research facilities, the development of software, the convening of international academic conferences, and the formation of relevant academic teams.

The workflow of the high-throughput phenotyping platform is divided into seven steps. The first step is to determine the new phenotypic criteria. The second step is to build a phenotyping platform, including ground-based platforms, air-based platforms, and space-based platforms. The third step is to obtain raw information using visible and invisible sensors. The fourth and fifth steps are the extraction, analysis, and mining of phenotypic information. The next step is to combine phenotypic information with multi-omics. Finally, we aim to solve real problems (including genetic breeding and precision management).

Author contributions

XL, XX, and MC jointly wrote the article and prepared the figures and tables. MX, WW, CL, LY, and WY provided overall guidance and some references. WL helped to modify and improve the article. All authors contributed to the article and approved the submitted version.

Funding

This work was supported by the Molecular mechanism of relay intercropping light environment regulating shade-tolerant plant architecture formation in soybean (3217150631), the Physiological mechanism of light regulating branch development in relay intercropping soybean (31871570), the physiology and regulation technology of high quality and high yield of soybean (2018YFD1000905), and the study and demonstration of corn—legume strip compound planting and mixed silage technology in Plateau Tibetan area (2020YFN0021).

Acknowledgments

We would like to thank Teachers MX and WW for their help in the work. We apologize to those colleagues who could not be quoted due to space limitations.

Conflict of interest

The authors declare that the research was conducted in the absence of any commercial or financial relationships that could be construed as a potential conflict of interest.

Publisher's note

References

Amoo, O., Li-Min, H., Yun-Gu, Z., Chu-Chuan, F., and Yong-Ming, Z. (2022). Regulation of shoot branching by BRANCHED1 in *Brassica napus* based on gene editing technology. *Biotechnol. Bull.* 38, 1–9. doi: 10.13560/j.cnki.biotech.bull.1985.2021-1344

Andrade-Sanchez, P., Gore, M. A., Heun, J. T., Thorp, K. R., Carmo-Silva, A. E., French, A. N., et al. (2013). Development and evaluation of a field-based high-throughput phenotyping platform. *Funct. Plant Biol.* 41, 68–79. doi: 10.1071/FP13126

Araus, J. L., and Cairns, J. E. (2014). Field high-throughput phenotyping: the new crop breeding frontier. *Trends Plant Sci.* 19, 52–61. doi: 10.1016/j.tplants.2013.09.008

Araus, J. L., Kefauver, S. C., Zaman-Allah, M., Olsen, M. S., and Cairns, J. E. (2018). Translating high-throughput phenotyping into genetic gain. *Trends Plant Sci.* 23, 451–466. doi: 10.1016/j.tplants.2018.02.001

Arend, D., Junker, A., Scholz, U., Schüler, D., Wylie, J., and Lange, M. (2016). PGP repository: a plant phenomics and genomics data publication infrastructure. *Database.* 33, 1–10. doi: 10.1093/database/baw033

Bac-Molenaar, J. A., Vreugdenhil, D., Granier, C., and Keurentjes, J. J. (2015). Genome-wide association mapping of growth dynamics detects time-specific and general quantitative trait loci. *J. Exp. Bot.* 66, 5567–5580. doi: 10.1093/jxb/erv176

Bai, G., Ge, Y., Hussain, W., Baenziger, P. S., and Graef, G. (2016). A multi-sensor system for high throughput field phenotyping in soybean and wheat breeding. *Comput. Electron. Agric.* 128, 181–192. doi: 10.1016/j.compag.2016.08.021

Bai, G., Jenkins, S., Yuan, W., Graef, G. L., and Ge, Y. (2018). Field-Based scoring of soybean iron deficiency chlorosis using RGB imaging and statistical learning. *Front. Plant Sci.* 9, 1002. doi: 10.3389/fpls.2018.01002

Bilder, R. M., Sabb, F., Cannon, T., London, E., Jentsch, J., Parker, D. S., et al. (2009). Phenomics: the systematic study of phenotypes on a genome-wide scale. *Neuroscience.* 164, 30–42. doi: 10.1016/j.neuroscience.2009.01.027

Bodner, G., Alsalem, M., and Nakhforoosh, A. (2021). "Root system phenotying of soil-grown plants via RGB and hyperspectral imaging," in *Crop Breeding* (Springer), 245–268. doi: 10.1007/978-1-0716-1201-9_17

Borra-Serrano, I., De Swaef, T., Quataert, P., Aper, J., Saleem, A., Saeys, W., et al. (2020). Closing the phenotyping gap: high resolution UAV time series for soybean growth analysis provides objective data from field trials. *Remote Sens.* 12, 1644–1665. doi: 10.3390/rs12101644

Bousset, L., Palerme, M., Leclerc, M., and Parisey, N. (2019). Automated image processing framework for analysis of the density of fruiting bodies of Leptosphaeria maculans on oilseed rape stems. *Plant Pathol.* 68, 1749–1760. doi: 10.1111/ppa.13085

Braga, P., Crusiol, L. G. T., and Nanni, M. R. (2020). Vegetation indices and NIR-SWIR spectral bands as a phenotyping tool for water status determination in soybean. *Precis. Agric.* 22, 249–266. doi: 10.1007/s11119-020-09740-4

Busemeyer, L., Mentrup, D., Möller, K., Wunder, E., Alheit, K., Hahn, V., et al. (2013). BreedVision—a multi-sensor platform for non-destructive field-based phenotyping in plant breeding. *Sensors.* 13, 2830–2847. doi: 10.3390/s130302830

Casagrande, C. R., Sant'ana, G. C., Meda, A. R., Garcia, A., Souza Carneiro, P. C., Nardino, M., et al. (2022). Association between UAV high-throughput canopy phenotyping and soybean yield. *Agron. J.* 23, 1–18. doi: 10.1002/agj2.21047

Chang, A., Jung, J., Yeom, J., Maeda, M. M., Landivar, J. A., Enciso, J. M., et al. (2021). Unmanned aircraft system-(UAS-) based high-throughput phenotyping (HTP) for tomato yield estimation. *J. Sensor.* 2021, 1–14. doi: 10.1155/2021/8875606

Chuanji, G. (1982). Two taxonomic systems of angiosperms. *Collect.* 1, 17–18.

Comar, A., Burger, P., De Solan, B., Baret, F. D. R., Daumard, F., and Hanocq, J. O. (2012). A semi-automatic system for high throughput phenotyping wheat cultivars in-field conditions: description and first results. *Funct. Plant Biol.* 39, 914–924. doi: 10.1071/FP12065

Cooper, L., Meier, A., Laporte, M.-A., Elser, J. L., Mungall, C., Sinn, B. T., et al. (2018). The Planteome database: an integrated resource for reference ontologies, plant genomics and phenomics. *Nucleic Acids Res.* 46, D1168–D1180. doi: 10.1093/nar/gkx1152

Ding, G., Xu, H., Wen, M., Chen, J., Wang, X., and Zhou, J. (2019). Developing cost-effective and low-altitude UAV aerial phenotyping and automated phenotypic analysis to measure key yield-related traits for bread wheat. *J. Agric. Big Data.* 1, 19–31. doi: 10.19788/j.issn.2096-6369.190202

Dobrescu, A., Giuffrida, M. V., and Tsaftaris, S. A. (2020). Doing more with less: a multitask deep learning approach in plant phenotyping. *Front. Plant Sci.* 11, 141. doi: 10.3389/fpls.2020.00141

Entekhabi, D., Njoku, E. G., O'neill, P. E., Kellogg, K. H., Crow, W. T., Edelstein, W. N., et al. (2010). The soil moisture active passive (SMAP) mission. *Proc. IEEE.* 98, 704–716. doi: 10.1109/jproc.2010.2043918

Fan, S., Zhang, L., Tang, M., Cai, Y., Liu, J., Liu, H., et al. (2021). CRISPR/Cas9-targeted mutagenesis of the BnaA03. BP gene confers semi-dwarf and compact architecture to rapeseed (*Brassica napus* L.). *Plant Biotechnol. J.* 19, 2383–2385. doi: 10.1111/pbi.13703

Fekete, S., Schappler, J., Veuthey, J.-L., and Guillarme, D. (2014). Current and future trends in UHPLC. *TrAC Trends Anal. Chem.* 63, 2–13. doi: 10.1016/j.trac.2014.08.007

Fernandez, O., Millet, E. J., Rincent, R., Prigent, S., Pétriacq, P., and Gibon, Y. (2021). "Plant metabolomics and breeding," in *Advances in Botanical Research* (Elsevier), 207–235. doi: 10.1016/bs.abr.2020.09.020

Fiorani, F., and Schurr, U. (2013). Future scenarios for plant phenotyping. *Annu. Rev. Plant Biol.* 64, 267–291. doi: 10.1146/annurev-arplant-050312-120137

Furbank, R. T., Silva-Perez, V., Evans, J. R., Condon, A. G., Estavillo, G. M., He, W., et al. (2021). Wheat physiology predictor: predicting physiological traits in wheat from hyperspectral reflectance measurements using deep learning. *Plant Methods* 17, 1–15. doi: 10.1186/S13007-021-00806-6

Furbank, R. T., and Tester, M. (2011). Phenomics—technologies to relieve the phenotyping bottleneck. *Trends Plant Sci.* 16, 635–644. doi: 10.1016/j.tplants.2011.09.005

Ge, Y., Atefi, A., Zhang, H., Miao, C., Ramamurthy, R. K., Sigmon, B., et al. (2019). High-throughput analysis of leaf physiological and chemical traits with VIS-NIR-SWIR spectroscopy: a case study with a maize diversity panel. *Plant Methods* 15, 66–78. doi: 10.1186/s13007-019-0450-8

Ghosal, S., Blystone, D., Singh, A. K., Ganapathysubramanian, B., Singh, A., and Sarkar, S. (2018). An explainable deep machine vision framework for plant stress phenotyping. *Proc. Natl. Acad. Sci. U. S. A.* 115, 4613–4618. doi: 10.1073/pnas.1716999115

Granier, C., and Vile, D. (2014). Phenotyping and beyond: modelling the relationships between traits. *Curr. Opin. Plant Biol.* 18, 96–102. doi: 10.1016/j.pbi.2014.02.009

Guo, Z., Yang, W., Chang, Y., Ma, X., Tu, H., Xiong, F., et al. (2018). Genome-wide association studies of image traits reveal genetic architecture of drought resistance in rice. *Mol. Plant.* 11, 789–805. doi: 10.1016/j.molp.2018.03.018

Hall, R. D., D'auria, J. C., Ferreira, A. C. S., Gibon, Y., Kruszka, D., Mishra, P., et al. (2022). High-throughput plant phenotyping: a role for metabolomics? *Trends Plant Sci.* 27, 549–563. doi: 10.1016/j.tplants.2022.02.001

Hammer, G. L., Dong, Z., McLean, G., Doherty, A., Messina, C., Schussler, J., et al. (2009). Can changes in canopy and/or root system architecture explain historical maize yield trends in the US corn belt? *Crop Sci.* 49, 299–312. doi: 10.2135/cropsci2008.03.0152

He, Y., Zeng, H., Fan, Y., Ji, S., and Wu, J. (2019). Application of deep learning in integrated pest management: a real-time system for detection and diagnosis of oilseed rape pests. *Mobile Inf. Syst.* 2019, 1–14. doi: 10.1155/2019/4570808

Herrero-Huerta, M., Bucksch, A., Puttonen, E., and Rainey, K. M. (2020). Canopy roughness: a new phenotypic trait to estimate aboveground biomass from unmanned aerial system. *Plant Phenomics.* 2020, 6735967–6735983. doi: 10.34133/2020/6735967

Houle, D., Govindaraju, D. R., and Omholt, S. (2010). Phenomics: the next challenge. *Nat. Rev. Genet.* 11, 855–866. doi: 10.1038/nrg2897

Hu, P., Chapman, S. C., Wang, X., Potgieter, A., Duan, T., Jordan, D., et al. (2018). Estimation of plant height using a high throughput phenotyping platform based on unmanned aerial vehicle and self-calibration: example for sorghum breeding. *Eur. J. Agron.* 95, 24–32. doi: 10.1016/j.eja.2018.02.004

Huichun, Z., Hongping, Z., Jiaqiang, Z., Yufeng, G., and Yangxian, L. (2020). Research progress and prospect in plant phenotyping platform and image analysis technology. Nongye Jixie Xuebao/Trans. *Chin. Soc. Agric. Mach.* 51, 1–17 doi: 10.6041/j.issn.1000-1298.2020.03.001

Jain, M., and Balwinder-Singh, R. (2019). The impact of agricultural interventions can be doubled by using satellite data. *Nat. Sustain.* 2, 931–934. doi: 10.1038/s41893-019-0396-x

Jiang, Y., Li, C., Robertson, J. S., Sun, S., Xu, R., and Paterson, A. H. (2018). GPhenoVision: a ground mobile system with multi-modal imaging for field-based high throughput phenotyping of cotton. *Sci. Rep.* 8, 1213–1228. doi: 10.1038/s41598-018-19142-2

Jiang, Y., Li, C., Xu, R., Sun, S., Robertson, J. S., and Paterson, A. H. (2020). DeepFlower: a deep learning-based approach to characterize flowering patterns of cotton plants in the field. *Plant Methods* 16, 156–174. doi: 10.1186/s13007-020-00698-y

Jin, X., Liu, S., Baret, F., Hemerlé, M., and Comar, A. (2017). Estimates of plant density of wheat crops at emergence from very low altitude UAV imagery. *Remote Sens. Environ.* 198, 105–114. doi: 10.1016/j.rse.2017.06.007

Johannsen, W. (1911). The genotype conception of heredity. *Am. Nat.* 45, 129–159. doi: 10.1086/279202

Jun, S., Kaifeng, Y., Yuanqiu, L., Jifeng, S., Xiaohong, W., and Lei, Q. (2021). Method for the multiscale perceptual counting of wheat ears based on UAV images. *Trans. Chin. Soc. Agric. Eng.* 37, 136–144. doi: 10.11975/j.issn.1002-6819.2021.23.016

Karthikeyan, L., Chawla, I., and Mishra, A. K. (2020). A review of remote sensing applications in agriculture for food security: crop growth and yield, irrigation, and crop losses. *J. Hydrol.* 586, 124905. doi: 10.1016/j.jhydrol.2020.124905

Keller, B., Zimmermann, L., Rascher, U., Matsubara, S., Steier, A., and Muller, O. (2021). Towards predicting photosynthetic efficiency and biomass gain in crop genotypes over a field season. *Plant Physiol.* 188, 1–17. doi: 10.1093/plphys/kiab483

Kirchgessner, N., Liebisch, F., Yu, K., Pfeifer, J., Friedli, M., Hund, A., et al. (2016). The ETH field phenotyping platform FIP: a cable-suspended multi-sensor system. *Funct. Plant Biol.* 44, 154–168. doi: 10.1071/FP16165

Kumar, J., Pratap, A., and Kumar, S. (2015). *Phenomics in Crop Plants: Trends, Options and Limitations.* Springer, 195–205. doi: 10.1007/978-81-322-2226-2_13

Lee, C. M., Cable, M. L., Hook, S. J., Green, R. O., Ustin, S. L., Mandl, D. J., et al. (2015). An introduction to the NASA Hyperspectral InfraRed Imager (HyspIRI) mission and preparatory activities. *Remote Sens. Environ.* 167, 6–19. doi: 10.1016/j.rse.2015.06.012

Leiboff, S., Li, X., Hu, H.-C., Todt, N., Yang, J., Li, X., et al. (2015). Genetic control of morphometric diversity in the maize shoot apical meristem. *Nat. Commun.* 6, 1–10. doi: 10.1038/ncomms9974

Li, B., Chen, L., Sun, W., Wu, D., Wang, M., Yu, Y., et al. (2020). Phenomics-based GWAS analysis reveals the genetic architecture for drought resistance in cotton. *Plant Biotechnol. J.* 18, 2533–2544. doi: 10.1111/pbi.13431

Li, S., Yan, Z., Guo, Y., Su, X., Cao, Y., Jiang, B., et al. (2021). SPM-IS: an auto-algorithm to acquire a mature soybean phenotype based on instance segmentation. *Crop J.* 5, 1–22. doi: 10.1016/j.cj.2021.05.014

Liu, J., Zhao, C., Yang, G., Yu, H., Zhao, X., Xu, B., et al. (2016). Review of field-based phenotyping by unmanned aerial vehicle remote sensing platform. *Trans. Chin. Soc. Agric. Eng.* 32, 98–106. doi: 10.11975/j.issn.1002-6819.2016.24.013

Lubes, G., and Goodarzi, M. (2017). Analysis of volatile compounds by advanced analytical techniques and multivariate chemometrics. *Chem. Rev.* 117, 6399–6422. doi: 10.1021/acs.chemrev.6b00698

Maimaitijiang, M., Sagan, V., Sidike, P., Maimaitiyiming, M., Hartling, S., Peterson, K. T., et al. (2019). Vegetation index weighted canopy volume model (CVMVI) for soybean biomass estimation from unmanned aerial system-based RGB imagery. *ISPRS J. Photogramm. Remote Sens.* 151, 27–41. doi: 10.1016/j.isprsjprs.2019.03.003

Malambo, L., Popescu, S. C., Murray, S. C., Putman, E., Pugh, N. A., Horne, D. W., et al. (2018). Multitemporal field-based plant height estimation using 3D point clouds generated from small unmanned aerial systems high-resolution imagery. *Int. J. Appl. Earth Obs. Geoinform.* 64, 31–42. doi: 10.1016/j.jag.2017.08.014

Maurya, A. K. (2020). "Application of plant volatile organic compounds (VOCs) in agriculture," in *New Frontiers in Stress Management for Durable Agriculture* (Springer), 369–388.

Meyer, R. C., Steinfath, M., Lisec, J., Becher, M., Witucka-Wall, H., Törjék, O., et al. (2007). The metabolic signature related to high plant growth rate in Arabidopsis thaliana. *Proc. Nat. Acad. Sci. U. S. A.* 104, 4759–4764. doi: 10.1073/pnas.0609709104

Miao, C., Guo, A., Thompson, A. M., Yang, J., Ge, Y., and Schnable, J. C. (2021). Automation of leaf counting in maize and sorghum using deep learning. *Plant Phenome J.* 4, 1–15. doi: 10.1002/ppj2.20022

Mishra, P., Angileri, M., and Woltering, E. (2021). Identifying the best rice physical form for non-destructive prediction of protein content utilising near-infrared spectroscopy to support digital phenotyping. *Infrared Phys. Technol.* 116, 103757. doi: 10.1016/J.INFRARED.2021.103757

Moreira, F. F., Hearst, A. A., Cherkauer, K. A., and Rainey, K. M. (2019). Improving the efficiency of soybean breeding with high-throughput canopy phenotyping. *Plant Methods* 15, 1–9. doi: 10.1186/s13007-019-0519-4

Muharam, F. M., Nurulhuda, K., Zulkafli, Z., Tarmizi, M. A., and Ismail, M. R. (2021). UAV- and Random-Forest-AdaBoost (RFA)-based estimation of rice plant traits. *Agronomy* 11, 915–943. doi: 10.3390/AGRONOMY11050915

Naik, H. S., Zhang, J., Lofquist, A., Assefa, T., Sarkar, S., Ackerman, D., et al. (2017). A real-time phenotyping framework using machine learning for plant stress severity rating in soybean. *Plant Methods* 13, 23–40. doi: 10.1186/s13007-017-0173-7

Navrozidis, I., Alexandridis, T. K., Dimitrakos, A., Lagopodi, A. L., Moshou, D., and Zalidis, G. (2018). Identification of purple spot disease on asparagus crops across spatial and spectral scales. *Comput. Electron. Agric.* 148, 322–329. doi: 10.1016/j.compag.2018.03.035

Neveu, P., Tireau, A., Hilgert, N., Nègre, V., Mineau-Cesari, J., Brichet, N., et al. (2019). Dealing with multi-source and multi-scale information in plant phenomics: the ontology-driven Phenotyping Hybrid Information System. *New Phytol.* 221, 588–601. doi: 10.1111/nph.15385

Pan, Y. (2015). Analysis of concepts and categories of plant phenome and phenomics. *Acta Agron. Sin.* 41, 175–186. doi: 10.3724/sp.J.1006.2015.00175

Paproki, A., Sirault, X., Berry, S., Furbank, R., and Fripp, J. (2012). A novel mesh processing based technique for 3D plant analysis. *BMC Plant Biol.* 12, 63. doi: 10.1186/1471-2229-12-63

Poorter, H., Fiorani, F., Stitt, M., Schurr, U., Finck, A., Gibon, Y., et al. (2012). The art of growing plants for experimental purposes: a practical guide for the plant biologist. *Funct. Plant Biol.* 39, 821–838. doi: 10.1071/FP12028

Prananto, J. A., Minasny, B., and Weaver, T. (2021). Rapid and cost-effective nutrient content analysis of cotton leaves using near-infrared spectroscopy (NIRS). *PeerJ.* 9, 11042–11066. doi: 10.7717/peerj.11042

Prey, L., Hu, Y., and Schmidhalter, U. (2020). High-throughput field phenotyping traits of grain yield formation and nitrogen use efficiency: optimizing the selection of vegetation indices and growth stages. *Front. Plant Sci.* 10, 1672. doi: 10.3389/fpls.2019.01672

Prey, L., and Schmidhalter, U. (2020). Deep phenotyping of yield-related traits in wheat. *Agronomy.* 10, 603. doi: 10.3390/agronomy10040603

Raman, R. (2017). The impact of Genetically Modified (GM) crops in modern agriculture: a review. *GM Crops Food.* 8, 195–208. doi: 10.1080/21645698.2017.1413522

Reuzeau, C., Frankard, V., Hatzfeld, Y., Sanz, A., Van Camp, W., Lejeune, P., et al. (2006). Traitmill$^{\mathrm{TM}}$: a functional genomics platform for the phenotypic analysis of cereals. *Plant Genet. Resour.* 4, 20–24. doi: 10.1079/PGR2005104

Reynolds, D., Ball, J., Bauer, A., Davey, R., Griffiths, S., and Zhou, J. (2019a). CropSight: a scalable and open-source information management system for distributed plant phenotyping and IoT-based crop management. *Gigascience* 8, 1–11. doi: 10.1093/gigascience/giz009

Reynolds, D., Baret, F., Welcker, C., Bostrom, A., Ball, J., Cellini, F., et al. (2019b). What is cost-efficient phenotyping? Optimizing costs for different scenarios. *Plant Sci.* 282, 14–22. doi: 10.1016/j.plantsci.2018.06.015

Ribaut, J., De Vicente, M., and Delannay, X. (2010). Molecular breeding in developing countries: challenges and perspectives. *Curr. Opin. Plant Biol.* 13, 213–218. doi: 10.1016/j.pbi.2009.12.011

Riedelsheimer, C., Czedik-Eysenberg, A., Grieder, C., Lisec, J., Technow, F., Sulpice, R., et al. (2012). Genomic and metabolic prediction of complex heterotic traits in hybrid maize. *Nat. Genet.* 44, 217–220. doi: 10.1038/ng.1033

Salgadoe, A. S. A., Robson, A. J., Lamb, D. W., Dann, E. K., and Searle, C. (2018). Quantifying the severity of phytophthora root rot disease in avocado trees using image analysis. *Remote Sens.* 10, 226–343. doi: 10.3390/rs10020226

Shafiekhani, A., Kadam, S., Fritschi, F. B., and Desouza, G. N. (2017). Vinobot and vinoculer: two robotic platforms for high-throughput field phenotyping. *Sensors.* 17, 214. doi: 10.3390/s17010214

Shao, M., Nie, C., Cheng, M., Yu, X., Bai, Y., Ming, B., et al. (2022). Quantifying effect of tassels on near-ground maize canopy RGB images using deep learning segmentation algorithm. *Precis. Agric.* 23, 400–418. doi: 10.1007/S11119-021-09842-7

Siebner, H. R., Callicott, J. H., Sommer, T., and Mattay, V. S.(2009). From the genome to the phenome and back: linking genes with human brain function and structure using genetically informed neuroimaging. *Neuroscience.* 164, 1–6. doi: 10.1016/j.neuroscience.2009.09.009

Souza, A., and Yang, Y. (2021). High-throughput corn image segmentation and trait extraction using chlorophyll fluorescence images. *Plant Phenomics* 2021, 582–597. doi: 10.34133/2021/9792582

Sugiura, R., Tsuda, S., Tamiya, S., Itoh, A., Nishiwaki, K., Murakami, N., et al. (2016). Field phenotyping system for the assessment of potato late blight resistance using RGB imagery from an unmanned aerial vehicle. *Biosyst. Eng.* 148, 1–10. doi: 10.1016/j.biosystemseng.2016.04.010

Sun, D., Robbins, K., Morales, N., Shu, Q., and Cen, H. (2021). Advances in optical phenotyping of cereal crops. *Trends Plant Sci.* 27, 191–208. doi: 10.1016/j.tplants.2021.07.015

Sun, Q., Xie, Y., Li, H., Liu, J., Geng, R., Wang, P., et al. (2022). Cotton GhBRC1 regulates branching, flowering, and growth by integrating multiple hormone pathways. *Crop J.* 10, 75–87. doi: 10.1016/j.cj.2021.01.007

Sun, S., Li, C., and Paterson, A. (2017). In-field high-throughput phenotyping of cotton plant height using LiDAR. *Remote Sens.* 9, 377–398. doi: 10.3390/rs9040377

Sun, S., Li, C., Paterson, A. H., Jiang, Y., Xu, R., Robertson, J. S., et al. (2018). In-field high throughput phenotyping and cotton plant growth analysis using LiDAR. *Front. Plant Sci.* 9, 16. doi: 10.3389/fpls.2018.00016

Swaminathan, M. (2014). Norman Borlaug and a hunger-free world. *Resonance* 19, 109–115. doi: 10.1007/s12045-014-0014-1

Tardieu, F., Cabrera-Bosquet, L., Pridmore, T., and Bennett, M. (2017). Plant phenomics, from sensors to knowledge. *Curr. Biol.* 27, R770–R783. doi: 10.1016/j.cub.2017.05.055

Tester, M., and Langridge, P. (2010). Breeding technologies to increase crop production in a changing world. *Science* 327, 818–822. doi: 10.1126/science.1183700

Thorp, K., Thompson, A., Harders, S., French, A., and Ward, R. (2018). High-throughput phenotyping of crop water use efficiency via multispectral drone imagery and a daily soil water balance model. *Remote Sens.* 10, 1682–1701. doi: 10.3390/rs10111682

Trevisan, R., Pérez, O., Schmitz, N., Diers, B., and Martin, N. (2020). High-throughput phenotyping of soybean maturity using time series UAV imagery and convolutional neural networks. *Remote Sens.* 12, 214–214. doi: 10.3390/rs12213617

Virlet, N., Sabermanesh, K., Sadeghi-Tehran, P., and Hawkesford, M. J. (2016). Field Scanalyzer: an automated robotic field phenotyping platform for detailed crop monitoring. *Funct. Plant Biol.* 44, 143–153. doi: 10.1071/FP16163

Wallace, J. G., Rodgers-Melnick, E., and Buckler, E. S. (2018). On the road to breeding 4.0: unraveling the good, the bad, and the boring of crop quantitative genomics. *Annu. Rev. Genet.* 52, 421–444. doi: 10.1146/annurev-genet-120116-024846

Wan, L., Zhu, J., Du, X., Zhang, J., Han, X., Zhou, W., et al. (2021). A model for phenotyping crop fractional vegetation cover using imagery from unmanned aerial vehicles. *J. Exp. Bot.* 72, 4691–4707. doi: 10.1093/jxb/erab194

Wang, M., and Xu, S. (2019). Statistical power in genome-wide association studies and quantitative trait locus mapping. *Heredity* 123, 287–306. doi: 10.1038/s41437-019-0205-3

Wanli, Y., Lingfeng, D., and Wanneng, Y. (2021). Deep learning-based extraction of rice phenotypic characteristics and prediction of rice panicle weight. *J. Huazhong Agric. Univ.* 40, 227–235. doi: 10.13300/j.cnki.hnlkxb.2021.01.028

Weiss, M., Jacob, F., and Duveiller, G. (2020). Remote sensing for agricultural applications: a meta-review. *Remote Sens. Environ.* 236, 1–69. doi: 10.1016/j.rse.2019.111402

White, J. W., Andrade-Sanchez, P., Gore, M. A., Bronson, K. F., Coffelt, T. A., Conley, M. M., et al. (2012). Field-based phenomics for plant genetics research. *Field Crops Res.* 133, 101–112. doi: 10.1016/j.fcr.2012.04.003

Wu, H., Ren, Z., Zheng, L., Guo, M., Yang, J., Hou, L., et al. (2021). The bHLH transcription factor GhPAS1 mediates BR signaling to regulate plant development and architecture in cotton. *Crop J.* 9, 1049–1059. doi: 10.1016/j.cj.2020.10.014

Xavier, A., Hall, B., Hearst, A. A., Cherkauer, K. A., and Rainey, K. M. (2017). Genetic architecture of phenomic-enabled canopy coverage in *Glycine max*. *Genetics* 206, 1081–1089. doi: 10.1534/genetics.116.198713

Xiao, F., Li, W., Xiao, M., Yang, Z., Cheng, W., Gao, S., et al. (2021). A novel light interception trait of a hybrid rice ideotype indicative of leaf to panicle ratio. *Field Crops Res.* 274, 108338. doi: 10.1016/J.FCR.2021.108338

Xiaobin, Z., Baoliang, X., Yihang, Z., Kefeng, Z., and Qing, G. (2022). High-throughput phenotype collection and analysis of vegetablesoybean pod based on image processing technology. *J. Nucl. Agric. Sci.* 36, 602–612. doi: 10.11869/j.issn.100-8551.2022.03.0602

Xiaobo, Y., Mingrong, Z., Hsaiying, W., and Wenyu, Y. (2012). Agronomic characters and yield distribution of different shade tolerance soybean under monoculture and relay strip intercropping. *Systems* 05, 757–761. doi: 10.3969/j.issn.1000-9841.2012.05.014

Xie, J., Fernandes, S. B., Mayfield-Jones, D., Erice, G., Choi, M., Lipka, A. E., et al. (2021). Optical topometry and machine learning to rapidly phenotype stomatal patterning traits for maize QTL mapping. *Plant Physiol.* 187, 1462–1480. doi: 10.1093/PLPHYS/KIAB299

Xin, X., De-Hua, Z., Ji-Shun, Z., and Xiao-Jun, L. (2021). Genome-wide association study of grain number per spikelet in bread wheat. *J. Plant Genet. Resour.* 23, 1098–1110. doi: 10.13430/j.cnki.jpgr.20211222001

Xu, R., Li, C., and Bernardes, S. (2021). Development and testing of a UAV-based multi-sensor system for plant phenotyping and precision agriculture. *Remote Sens.* 13, 3517–3545. doi: 10.3390/rs13173517

Xu, R., Li, C., Paterson, A. H., Jiang, Y., Sun, S., and Robertson, J. S. (2017). Aerial images and convolutional neural network for cotton bloom detection. *Front. Plant Sci.* 8, 2235. doi: 10.3389/fpls.2017.02235

Yoosefzadeh-Najafabadi, M., Tulpan, D., and Eskandari, M. (2021). Using hybrid artificial intelligence and evolutionary optimization algorithms for estimating soybean yield and fresh biomass using hyperspectral vegetation indices. *Remote Sens.* 13, 2555–2577. doi: 10.3390/rs13132555

Young, S. N., Kayacan, E., and Peschel, J. M. (2018). Design and field evaluation of a ground robot for high-throughput phenotyping of energy sorghum. *Precis. Agric.* 20, 697–722. doi: 10.1007/s11119-018-9601-6

Yu-Shan, W., Wan-Zhuo, G., Qian-Jun, T., Feng, C., Yan-Ling, W., Wei-Guo, L., et al. (2015). Research on the relationship between agronomic traits and yield of soybean in relay strip intercropping. *Soybean Sci.* 03, 394–401. doi: 10.11861/j.issn.1000-9841.2015.03.0394

Zea, M., Souza, A., Yang, Y., Lee, L., Nemali, K., and Hoagland, L. (2022). Leveraging high-throughput hyperspectral imaging technology to detect cadmium stress in two leafy green crops and accelerate soil remediation efforts. *Environ. Pollut.* 292, 118405. doi: 10.1016/j.envpol.2021.118405

Zelazny, W. R., Chrpová, J., and Hamouz, P. (2021). Fusarium head blight detection from spectral measurements in a field phenotyping setting—a pre-registered study. *Biosyst. Eng.* 211, 97–113. doi: 10.1016/J.BIOSYSTEMSENG.2021.08.019

Zhan, J., Chu, Y., Wang, Y., Diao, Y., Zhao, Y., Liu, L., et al. (2021). The miR164-GhCUC2-GhBRC1 module regulates plant architecture through abscisic acid in cotton. *Plant Biotechnol. J.* 19, 1839–1851. doi: 10.1111/pbi.13599

Zhang, C., Marzougui, A., and Sankaran, S. (2020). High-resolution satellite imagery applications in crop phenotyping: an overview. *Comput. Electron. Agric.* 175, 1–10. doi: 10.1016/j.compag.2020.105584

Zhang, X., Huang, C., Wu, D., Qiao, F., Li, W., Duan, L., et al. (2017). High-throughput phenotyping and QTL mapping reveals the genetic architecture of maize plant growth. *Plant Physiol.* 173, 1554–1564. doi: 10.1104/pp.16.01516

Zhao, C. (2019). Big data of plant phenomics and its research progress. *J. Agric. Big Data* 1, 5–18. doi: 10.19788/j.issn.2096-6369.190201

Zhao, C., Zhang, Y., Du, J., Guo, X., Wen, W., Gu, S., et al. (2019). Crop phenomics: current status and perspectives. *Front. Plant Sci.* 10, 714. doi: 10.3389/fpls.2019.00714

Zhou, J., Mou, H., Zhou, J., Ali, M. L., Ye, H., Chen, P., et al. (2021). Qualification of soybean responses to flooding stress using UAV-based imagery and deep learning. *Plant Phenomics* 2021, 1–13. doi: 10.34133/2021/9892570

Zhou, J., Tardieu, F., Pridmore, T., Doonan, J., Reynolds, D., Hall, N., et al. (2018). Plant phenomics: history, present status and challenges. *J. Nanjing Agric. Univ.* 41, 580–588. doi: 10.7685/jnau.201805100

frontiers | Frontiers in Plant Science

TYPE Methods
PUBLISHED 10 October 2022
DOI 10.3389/fpls.2022.992663

The ÓMICAS alliance, an international research program on multi-omics for crop breeding optimization

Andres Jaramillo-Botero[1,12*], Julian Colorado[2,12], Mauricio Quimbaya[3,12], Maria Camila Rebolledo[4,5,6,12], Mathias Lorieux[6,7,12], Thaura Ghneim-Herrera[8,12], Carlos A. Arango[9,12], Luis E. Tobón[10,12], Jorge Finke[10,12], Camilo Rocha[10,12], Fernando Muñoz[11,12], John J. Riascos[11,12], Fernando Silva[11,12], Ngonidzashe Chirinda[6,12], Mario Caccamo[13], Klaas Vandepoele[14,15] and William A. Goddard III[1]

[1]Chemistry and Chemical Engineering Division, California Institute of Technology, Pasadena, CA, United States, [2]Departamento de Ciencias Naturales y Matemáticas, Facultad de Ingeniería y Ciencias, Pontificia Universidad Javeriana, Cali, Valle del Cauca, Colombia, [3]Facultad de Ingenieŕia y Ciencias, Departamento de Ciencias Naturales y Matemáticas, Pontificia Universidad Javeriana, Cali, Colombia, [4]CIRAD, UMR AGAP, Montpelier, France, [5]AGAP, Univ Montpellier, CIRAD, INRA, Montpellier SupAgro, Montpellier, France, [6]International Center for Tropical Agriculture (CIAT), Cali, Colombia, [7]DIADE, University of Montpellier, CIRAD, IRD, Montpelier, France, [8]Facultad de Ciencias Naturales, Departamento de Ciencias Biológicas, Universidad Icesi, Cali, Colombia, [9]Facultad de Ciencias Naturales, Departamento de Ciencias Qúımicas, Universidad Icesi, Cali, Colombia, [10]Departamento de Ingeniería Electrónica y Ciencias dela Computación, Facultad de Ingeniería y Ciencias, Pontificia Universidad Javeriana, Cali, Valle del Cauca, Colombia, [11]Centro de Investigación de la Caña de Azúcar (CENICAÑA), Florida, Valle del Cauca, Colombia, [12]OMICAS Alliance, Pontificia Universidad Javeriana, Cali, Valle del Cauca, Colombia, [13]National Institute of Agricultural Botany (NIAB), Cambridge, United Kingdom, [14]Department of Plant Biotechnology and Bioinformatics, Ghent University, Ghent, Belgium, [15]Center for Plant Systems Biology, Vlaams Instituut voor Biotechnologie (VIB), Ghent, Belgium

The OMICAS alliance is part of the Colombian government's Scientific Ecosystem, established between 2017-2018 to promote world-class research, technological advancement and improved competency of higher education across the nation. Since the program's kick-off, OMICAS has focused on consolidating and validating a multi-scale, multi-institutional, multi-disciplinary strategy and infrastructure to advance discoveries in plant science and the development of new technological solutions for improving agricultural productivity and sustainability. The strategy and methods described in this article, involve the characterization of different crop models, using high-throughput, real-time phenotyping technologies as well as experimental tissue characterization at different levels of the omics hierarchy and under contrasting conditions, to elucidate epigenome-, genome-, proteome- and metabolome-phenome relationships. The massive data sets are used to derive in-silico models, methods and tools to discover complex underlying structure-

EDITED BY
Urs Schmidhalter,
Technical University of Munich,
Germany

REVIEWED BY
Nisha Singh,
Gujarat Biotechnology University, India
Mumtaz Ali Saand,
Zhejiang University, China
Synan F. AbuQamar,
United Arab Emirates University,
United Arab Emirates
Uday Chand Jha,
Indian Institute of Pulses Research
(ICAR), India
Pankaj Kumar, Dr. Yashwant Singh
Parmar University of Horticulture and
Forestry, India
Stefanie Wienkoop, University of
Vienna, Austria

*CORRESPONDENCE
Andres Jaramillo-Botero
ajaramil@caltech.edu

SPECIALTY SECTION
This article was submitted to
Technical Advances in Plant Science,
a section of the journal
Frontiers in Plant Science

RECEIVED 12 July 2022
ACCEPTED 15 September 2022
PUBLISHED 10 October 2022

CITATION
Jaramillo-Botero A, Colorado J,
Quimbaya M, Rebolledo MC,
Lorieux M, Ghneim-Herrera T,
Arango CA, Tobón LE, Finke J,
Rocha C, Muñoz F, Riascos JJ, Silva F,
Chirinda N, Caccamo M, Vandepoele K
and Goddard WA III (2022) The
ÓMICAS alliance, an international
research program on multi-omics for
crop breeding optimization.
Front. Plant Sci. 13:992663.
doi: 10.3389/fpls.2022.992663

function associations, which are then carried over to the production of new germplasm with improved agricultural traits. Here, we describe OMICAS' R&D trans-disciplinary multi-project architecture, explain the overall strategy and methods for crop-breeding, recent progress and results, and the overarching challenges that lay ahead in the field.

KEYWORDS

Multi-omics, crops breeding, foodomics, nanotechnology, rice and sugarcane, in-silico optimization

1 Introduction

According to the United Nations (UN, 2019), global population will continue to grow throughout the 21st century, to an estimated 10.9 billion by 2100. As a result, food production rates will have to double, which require an unprecedented increase in agricultural productivity, at a rate that has not been seen over the past five decades. Figure 1 illustrates the scenario for the case of grains, which constitutes more than 40% of the daily protein intake and diet of the global population.

Both biotic and abiotic stresses have altered the production of sustainable crops, in some cases critically. Global food security is permanently challenged by different phenomena including climate change, population growth, human conflict, the reduction of the arable land, and the increased livestock area requirements among several others. From this perspective, it is mandatory for plant breeders worldwide to develop new strategies to deliver crop varieties at a faster rate, i.e., increase the genetic gain for each crop.

Here, we describe the OMICAS alliance and its commitment to the design, development, validation and deployment of an interdisciplinary panomics strategy and tool set to address the sustainability of productive agricultural systems and global food security. OMICAS was selected in 2018, as the sole program in the Food category of the Scientific Colombia ecosystem. Its name, was inspired from the Spanish acronym for *Optimización Multiescala In-Silico de Cultivos Agrícolas Sostenibles* that translates into English as *In-Silico Driven*

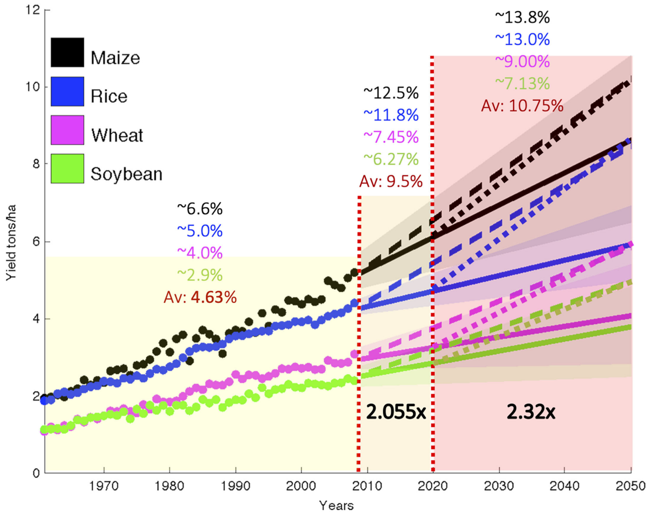

FIGURE 1
Observed area-weighted global yield 1961–2008 shown using closed circles and projections to 2050 using solid lines for maize, rice, wheat, and soybean. Shading shows the 90% confidence region derived from 99 bootstrapped samples. The dashed line shows the yield trend from 2008 needs to double production, on average, for these crops by 2050, without bringing additional land under cultivation starting in the base year of 2008. The dotted lines from 2020 to 2050 show the yield trend needs to increase by more than 2.3 times with respect to 2008. Adapted from (Ray et al., 2013).

Multiscale Optimization of Sustainable Agricultural Crops, also corresponds to the suffix 'omics' in spanish.

A review from different sources, including the United Nations Development Program (UNDP) (UNDP, 2012), the Food and Agriculture Organization of the United Nations (FAO, 2013), and the Organization for Economic Cooperation and Development (OECD) (OECD, 2015), reveals that over the years Colombia's agricultural sector has evolved with critical limitations in terms of production, innovation, and technology implementation. In Colombia, agriculture is the primary economic activity of rural territories, and it has experienced multiple structural crisis, which have resulted in a significant reduction of its contribution to the Gross National Product (GNP) from 27% to 5.4% between 1965 and 2013 (Figure 2. After hitting an inflection minima in 2013, the sector has shown a recovery in GNP participation up until 2020, when the COVID pandemic hit the world.

In 2017, the Colombian Strategic Plan for Science, Technology, and Innovation of the Agricultural Sector (in Spanish PECTIA) (PEC, 2016) was set in motion in an attempt to consolidate the country's National System for Agricultural Innovation (SNIA), in Colombia's post-conflict era. The PECTIA takes into consideration the 3866 Productive Development policy documents from the CONPES (Consejo Nacional de Política Económica y Social, or National Council for Economic and Social Policy) approved in late 2016 (CON, 2015), the recommendations from the Colombian Mission for Rural Transformations, and general orientations provided by the OECD prior to country's admission as a member in 2018. The PECTIA addresses current societal challenges associated to 'best-practices' in agriculture through governance and policy making investment in infrastructure and human resources, as well as financing, planning, tracking, and evaluating strategic projects needed to promote increased productivity and a value-added economy capable of competing in a global market.

The same year PECTIA was unveiled, the Colombian government, through its Ministries of Education, Industry and Tourism, the Colombian Institute of Educational Credit and Technical Studies Abroad (ICETEX), and the Colombian Administrative Department of Science, Technology and Innovation (Colciencias) – now morphed into the Ministry of Science, Technology and Innovation (Minciencias) – created the Colombian Scientific Ecosystem as a two-pronged effort to: 1) promote scientific research and technological development (under the Scientific Colombia program); and 2) graduate-level education abroad (Passport to Science program). Both programs were conceived to prioritize five strategic development areas: Food (Agriculture), Renewable Energy, Health, Society, and Bio-economy, out of which eight international, multi-institutional R&D programs were competitively established. These programs were leveraged by the World Bank through the "Access and Quality in Higher Education Project" (or PACES) program, and anchored at top accredited Colombian Universities.

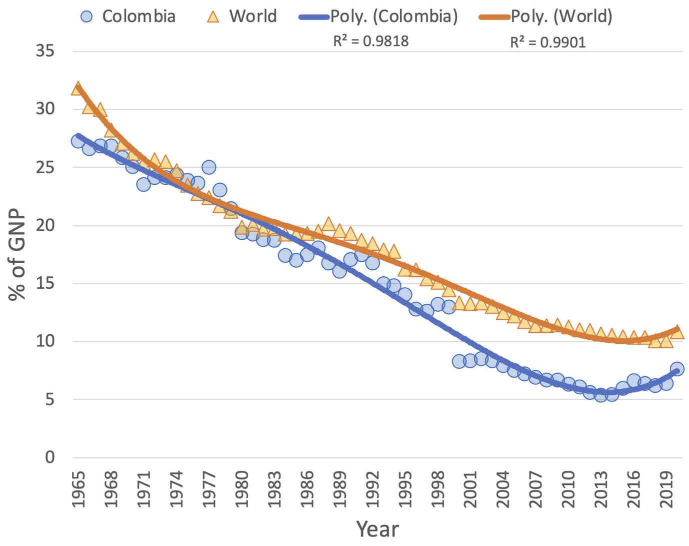

FIGURE 2
Agricultural sector contribution to Colombia's and World's GNP shows a steady decline (faster for the former) in percent contribution since 1965. Includes forestry, hunting and fishing, in addition to growing crops and raising animals. Value added is the net production of the sector, after adding all the products and subtracting the intermediate inputs. It is calculated without making deductions for depreciation of manufactured goods or for depletion and degradation of natural resources. For the countries that count on a value added basis, including Colombia, the gross value added at factor cost is used as the denominator. Source: World Bank National Accounts Data and OECD National Accounts Data Files.

The application of omics technologies for the improvement of plant traits has enabled significant advances in recent years, as summarized in different reviews; (Großkinsky et al., 2017; Zander et al., 2020; Jamil et al., 2020; Yang et al., 2021) which describe, for the most part, partial integrative approaches, the application of different omics levels to address specific plant models and traits (Rasheed et al., 2013; Singh et al., 2020; Yadav et al., 2022), or the use of modeling and simulation to drive discovery and optimization (Matthews and Marshall-Colón, 2021; Marshall-Colon, 2022). The creation of global networks, such as the International Plant Phenotyping Network (IPPN), (IPPN, 2022) is also contributing to the visibility, information sharing, and application of omics science and technology in agriculture.

OMICAS contributes a unique panomics strategy that couples quantifiable parameters and data, from genome to crop, into functional models for multi-objective optimization of agronomic traits. It not only leverages existing characterization resources, but the development of new sensor and phenotyping technologies for real-time non-invasive characterization of analytes in plants, soils, and atmospheres, and of novel computational methods to elucidate complex inter-omics correlations that become the control knobs to reduce the time and costs in plant breeding. It is a holistic approach, being validated on rice and sugarcane models, whilst extensible to any other crop.

The program brings together leading experts from 17 institutions across the globe, including from four world-class foreign universities (California Institute of Technology, University of Illinois at Urbana Champaign, Ghent University, and Tokyo University), 3 world-class agricultural research institutions (NIAB in Cambridge, UK, the International Center of Tropical Agriculture - CIAT [member of the CGIAR global partnership that unites international organizations engaged in research about food security, located in Colombia], and the Colombian Sugar Cane Research Center - Cenicaña], five major private and public Colombian Universities (Pontificia Universidad Javeriana, Universidad de los Andes, Universidad ICESI, Universidad de Ibague, Universidad del Quindio, and Universidad de los Llanos), and three industrial partners (the Federation of Rice Growers - Fedearroz, Intelecto, and Hi-Tech Automation). The team includes professors, scientific researchers, students and technical staff from a variety of disciplines, including molecular and nano-scale science, 'omics' sciences (primarily epigenomics, genomics, transcriptomics, metabolomics, proteomics and phenomics), biology and biotechnology, chemistry, physics, nutrition, computer science, and others, to address the trans-disciplinary challenges associated with sustainable agricultural productivity and food security. This paper presents an outline of OMICAS' multiscale plant breeding optimization strategy, and describes early results and achievements from the alliance members, primarily validated on two crop models - rice and sugarcane (albeit the strategy, methods and tools are extensible to any other crops). Rice was chosen because it is a major global food source, because it the largest cultivated cereal by surface area in Colombia, and because it has an extensively studied genome. On the other hand, we chose sugarcane, because it is third most cultivated crop by surface area in Colombia, after coffee and oil palm, because it is one of the most efficient plants for photosynthesis, and because it has one of the most complex genomes in crop plants due to the extreme level of polyploidy.

2 ÓMICAS R&D architecture

The alliance's multi-disciplinary research plan involves basic science, as well as the design, implementation, validation, and knowledge transfer in the form of technological solutions aimed at contributing to sustainable agricultural productivity and food security. The main thrusts focus on the omics-level characterization of our two model crops to: establish new breeding strategies, methods, and tools; produce plant varieties with increased tolerance to biotic and abiotic stresses, and with improved resource use efficiency; and reduce the overall environmental footprint of agriculture through updated agronomic practices (specifically greenhouse gas emissions).

OMICAS is composed of seven interrelated macro projects, identified in Figure 3 as P1 through P7 and coupled as shown in Figure 4. These projects contribute to the overarching goals of the program, as follows:

1. Development and implementation of an experimental and computational platform for genomic, transcriptomic, and epigenomic plant processing and analysis, and of bioinformatic tools for the analysis and integration of molecular scale data associated with crop productivity,
2. Design, characterization, and fabrication of prototype nanodevices for the detection and measurement of ultra low-concentrations of tissue biomarkers (specifically, primary and secondary metabolites, and aluminum metal Al^{3+} ions in soils), in order to enable early, fast, and high-resolution identification of plant response to stress,
3. Profiling of metabolic pathways for simple sugars, organic acids, phenolics, flavonoids, and dextrans in crops, using targeted and non-targeted metabolomic methods and the high-resolution phenotyping technologies derived from P1, and elucidation of key cell signaling mechanisms from plant cell-membrane receptors, specifically GCR1, to establish their role in stress response,
4. Development and implementation of an integrated low-cost, high-throughput, geographically-distributed multimodal phenotyping platform (fixed, mobile and aerial) that integrates soil-plant-atmosphere variables

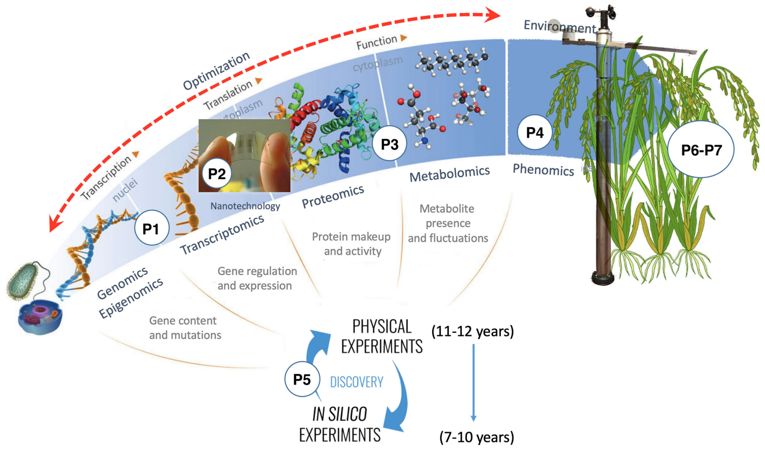

FIGURE 3
The OMICAS program consists of seven highly-coupled projects, each identified in the figure with a number, the first four build the omics characterization layer of the program, the fifth integrates the characterization data through in-silico models for systematic big data analysis, and projects six and seven use the structure-function relationships obtained from the rest of the projects to develop new varieties with improved traits (validated on rice and sugar-cane models).

during meristematic, elongation, and maturation phases of plant growth,

5. Development of computational models and data visualization tools for in-silico analysis and optimization of crops, based on graph theory and big data analytics algorithms, aimed at gene annotation, identification of gene and metabolic circuits associated with productivity and tolerance to stress conditions.
6. Applying the methods and tools developed by P1-P5 to the identification and annotation of genes, the

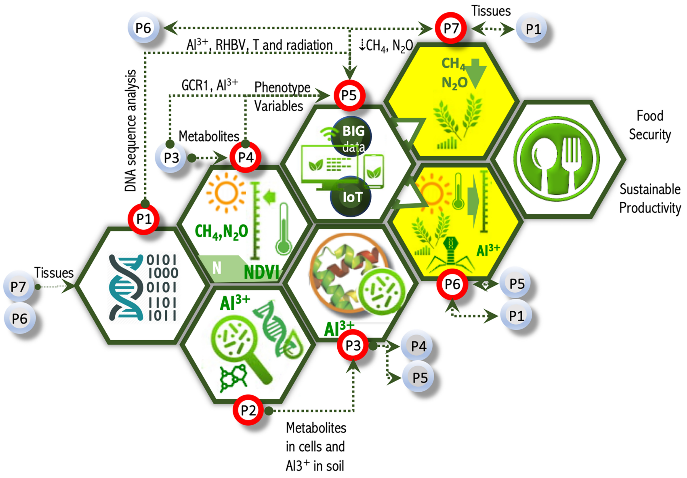

FIGURE 4
OMICAS program architecture, its macroprojects and their parameter-driven couplings. This figure depicts a sub-set of the basic data couplings in the OMICAS strategy. For example, P1 receives plant tissues from P6 and P7, and outputs DNA/RNA sequences for the modeling efforts in P5; P2 validates sensor technologies on metabolomics and ionomics characterized in P3; P3, in turn, contributes metabolomic and ionomic data for the high-throughput phenotyping effort in P4, and for the development of predictive models in P5; P4 uses molecular and elemental information from P2 and P3, and produces continuum-level phenotypic data for the models and codes developed in P5; while P5, integrates the experimental (physical and computational) multi-omics characterizations from P1-P4 into complex models derived from graph- and network theory, machine learning, and other mathematical and computer science methods to produce predictive tools for in-silico analysis and breeding optimization; P6 and P7 contribute breeding of new plant varieties with improved agronomic traits, based on the in-silico results from P5, and feeds tissues, soil and other environmental samples into the characterization and modeling that occur within P1-P5.

development and selection of promising germplasm, and the design of new plant varieties with greater performance in productivity and stability in the presence of diseases (e.g. rice hoja blanca virus), climate changes (i.e. low or high temperatures and radiation), heavy metal soil toxicity (e.g. Al^{3+}), and optimal resource use efficiency (e.g. non-structural carbohydrates).

7. Applying the methods and tools developed by P1-P5 to identify and select plant varieties with reduced greenhouse gas emissions (specifically N_2O and CH_4) that favor soil conservation and minimal environmental footprint.

This alliance is committed to contributing basic, measurable, and transferable solutions to these problems, including but not limited to: new omics characterization and analysis techniques and tools, candidate genome sequences, candidate quantitative trait locus (QTLs) and genes, and optimized germplasm. A key element in OMICAS is the integration of an in-silico and physical experimental optimization cycle, based on epigenomic, genomic, metabolomic, and proteomic data and its correlation with phenomic expression to enable elucidation of complex genotype-phenotype relationships. The in-silico components are meant to improve breeding throughput, and to reduce the cost and time involved in traditional methods. The 'omic' characterization layer allows for multiobjective optimization of agricultural traits, such as, resource use efficiency, nutrient sink-source translocation efficiency, resistance to different biotic and abiotic stresses, and minimization of the environmental footprint. This multiscale characterization approach is essential to elucidate molecular-level structure-function relationships that affect gene expression, metabolic regulation, and an organism's response to its environment.

3 Results and discussion

The use of whole-genome data, derived from high-throughput sequencing technologies, in association with accurate crop phenotyping, has allowed the discovery of genetic traits that control phenotypic variations in crops.

3.1 Epigenetic and genetic characterization of crops

In P1, we have advanced in the implementation of an experimental and computational platform for storage, processing, analysis, and biological interpretation of epigenetic (methylation profiles) and genetic crop data. We have established an epigenomic analysis strategy supported by computational models and experimental methods to characterize yield and differential responses to biotic and abiotic factors in the target crops of rice and sugar-cane. Furthermore, we are developing and validating novel bioinformatics strategies and flows for analysis and visualization of structural and functional genomics.

The focus is placed on the dynamic epigenetic processes that modulate access to DNA in response to upstream signals including DNA methylation, covalent modification of histones, nucleosome remodeling, chromatin interaction with regulatory long noncoding RNAs. These are critical to ultimately understand gene expression.

P1 has established an experimental platform supported by the implementation of computational tools for the analysis of massive omics characterization data. The project integrates a physical layer for handling and processing experimental tissue samples, and a complementary computational high-performance computing (HPC) infrastructure (a GPGPU cluster set up at the alliance's anchor institution) for the storage and analysis of omics data generated. This data will be released to the public domain as the infrastructure grows. Three major computational-experimental efforts are under way between P1 and other projects in OMICAS, one (with P6) meant to identify epigenetic cues associated to reducing the effect of abiotic stresses (specific case of Al^{3+} toxicity from acid soils), a second (again with P6) meant to uncover the genotypic and phenotypic variations underlying sucrose production, and a third (with P5) meant to systematically annotate genes from genome-phenome data using machine learning methods.

For the first case, we are progressing in an epigenomic study to characterize the methylation patterns in four commercial rice cultivars (*Oryza sativa L.* and two accessions of wild rice (*Oryza glumaepatula Steud*, through whole genome bisulfite sequencing. Differential epigenetic marks will be evaluated between rice genotypes with a contrasting response to aluminum stress under controlled conditions. By using this strategy, epigenetic changes will be considered as fixed epigenetic marks. Likewise, the changes in the methylation patterns between the aluminum tolerant and susceptible rice genotypes will be evaluated after being subjected to Al^{3+} toxicity conditions, and the epigenetic changes identified will be considered rapid epigenetic marks in response to aluminum stress. Once the specific differential methylation patterns have been identified, expression levels of genes that had been found to be differentially methylated, between tolerant and susceptible genotypes, will be evaluated by qPCR. With all the epigenetic and transcriptional information, functional enrichment analyzes will be carried and a functional response model to aluminum stress will be developed. This will represent a significant advance in understanding the epigenetic mechanisms in the response to abiotic stresses in plants, in particular to understand the key mechanism in the regulatory response of rice crops to aluminum toxicity. This information will be transferred to different breeding programs worldwide. Our early findings, based on methylation analysis from Nipponbare cultivar (highly tolerant to Al toxicity) and IR64 and Pokkali varieties (susceptible to Al toxicity) indicate that Nipponbare exhibited more methylated sites than the other two varieties (p≤0.01 in an FDR analysis), while IR64 and Pokkali did not show differences in methylation - see Figure 5. These results are particularly interesting, given Nipponbare has been extensively reported as a highly tolerant cultivar to aluminum (Gallo-Franco et al., 2020).

For the second case there were two approaches implemented to identify variations underlying sucrose production. The first one consists of performing the identification of molecular DNA markers throughout the implementation of a genome-wide association analysis (GWAS). To do so, a core collection of 220 sugarcane genotypes, which covers the genetic and commercial diversity from Cenicaña's germplasm bank, were phenotyped during two crop cycles at a field representative from the humid environment of the valle del río Cauca, Colombia. Similarly, each one of the 220 genotypes were sequenced with a high-throughput whole genome sequencing strategy, in order to massively identify Single Nucleotide Polymorphisms (SNPs). Finally, both phenotypic and genotypic information were combined through the QK-mixed linear model (Yu et al., 2006) to find SNPs associated with sucrose production. Preliminary findings indicates the presence of 28 SNPs associated with sucrose content at 13 months after planting, from which only 4 explains between 5 and 10% (R_2>5%) of the total phenotypic variation observed in the 220 genotypes. These results suggest that sucruse production is a quatitative trait that is highly influenced by environmental effects, with several minor QTLs that control its production. To validate the association of each one of the 28 SNPs, we planted a population of 150 sugarcane genotypes, with sucrose production between 5 and 18% in a humid environment. This population will be phenotyped for sucrose production and, at the same time, sequenced with targeted sequencing technologies to look for the allele dossage for each SNP and to confirm the overall impact on sucrose production. The second approach, consists of the quantitative evaluation of the analyzed genotypes by means of the multiscale phenotyping strategy in OMICAS. This involved identifying a set of 4 genotypes with more than 16% sucrose-producing accessions, as high-producing, and with less than 7%, as low-producing. These genotypes were planted in fields from a sugarcane mill in the Valle del Cauca, in Colombia. We will now perform an epigenetic study aimed at finding epi-alleles that could assist the breeding scheme at Cenicaña. Therefore, at harvest time (around 13 months after planting), tissue from the low and high-sucrose-producing genotypes will be collected and sequenced through whole genome bisulfite sequencing. Finally, differentially expressed markers will be evaluated against sucrose production and considered as fixed epigenetic marks or epi-alleles. In this way, not only the genome structural variation will be taken into account to establish direct genotype-phenotype associations with evaluated traits, but also, significant differential epigenetic marks will corroborate and help us elucidate those defined associations.

A major challenge in agriculture is incorporating genomic information into functional plant breeding. A holistic approach is mandatory to directly apply genomics-derived knowledge into agronomy, both at the molecular (genomic through metabolomic) and macroscopic (phenotypic) levels, and for deriving a plant's response under contrasting conditions (i.e.

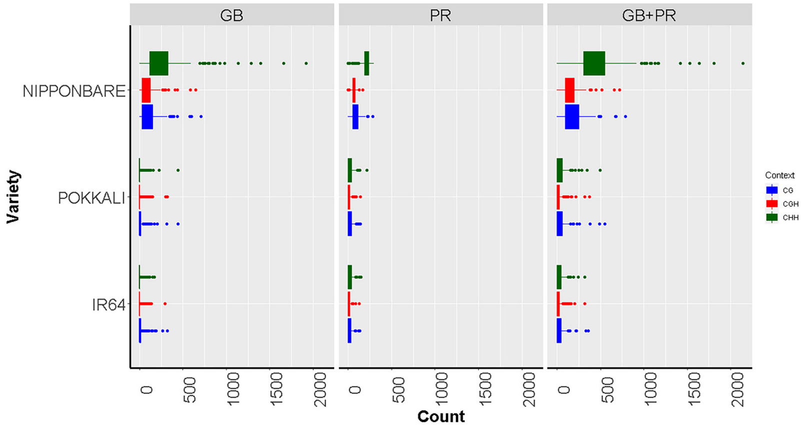

FIGURE 5
Boxplots showing methylated cytosine frequency in three sequence contexts: CG (blue), CHG (red), and CHH (green) among three different rice varieties with contrast responses to aluminum exposure: Nipponbare (Tolerant), Pokkali, and IR64 (Susceptible). The results are discriminated according to the location of the epigenetic mark, either inside the gene body region (GB), the promoter (PR), or both the promoter and inside the gene body region of analyzed genes (PR + GB). From (Gallo-Franco et al., 2020).

normal and stressed). With this goal in mind, we are performing specific phenotype-genotype associations for different agronomic traits, and have developed strategies for the analysis and integration of complex data using comparative genomics approaches, bioinformatics and big data analysis tools. This will generate new pipelines for our model crops and for others. For example, we have now developed a new method for in-silico prediction of functional gene annotations in rice. This approach uses gene annotations from existing knowledge of a given genome in combination with topological properties of its gene co-expression network, to train a supervised machine learning model that is designed to discover unknown annotations. The approach was validated to functionally annotate the Oryza Sativa Japonica genome. It uses any existing body of knowledge about gene annotations for a given genome, and the topological properties of its gene co-expression network, to train a supervised machine learning model that is designed to discover unknown annotations. These results, sumarized in Table 1, revealed that the topological properties derived from co-expression networks improve our predictions for annotating genes (Romero et al., 2020).

We expect that the combined use of traditional genomic and epigenomic characterization strategies, coupled with the use of novel techniques based on holistic analysis, will lead the identification of novel gene/molecular mechanisms aimed at reducing the times to develop agronomically improved varieties.

TABLE 1 Number of genes most frequently annotated as false positives for the 32 annotations by our model, trained from topological metrics extracted from an Oryza Sativa Japonica genome.

ID	Biological process	# Genes	Max FP	# FP
0006807	Nitrogen compound metabolic process	15	41	1
0006289	Nucleotide-excision repair	20	46	1
0006397	mRNA processing	17	48	1
0007017	Microtubule-based process	18	49	1
0070588	Calcium ion transmembrane transport	10	36	1
0006184	GTP catabolic process	49	47	1
0044267	Cellular protein metabolic process	25	49	1
0007186	G-protein coupled receptor protein signaling	11	50	1
0006281	DNA repair	62	50	2
0006754	ATP biosynthetic process	24	49	3
0006904	Vesicle docking involved in exocytosis	11	50	4
0055114	Oxidation-reduction process	870	47	5
0006886	Intracellular protein transport	135	50	19
0006855	Drug transmembrane transport	32	50	21
0006662	Glycerol ether metabolic process	28	50	27
0006888	ER to Golgi vesicle-mediated transport	16	50	29
0006259	DNA metabolic process	15	50	32
0007067	Mitosis	11	48	33
0008652	Cellular amino acid biosynthetic process	18	50	52
0030244	Cellulose biosynthetic process	23	50	64
0034968	Histone lysine methylation	11	50	93
0006812	Cation transport	62	50	96
0045454	Cell redox homeostasis	83	49	103
0006506	GPI anchor biosynthetic process	12	50	284
0007165	Signal transduction	104	50	370
0071805	Potassium ion transmembrane transport	24	50	570
0006357	Regulation of transcription from RNA polymera	12	50	1199
0006396	RNA processing	58	50	1212
0044237	Cellular metabolic process	75	50	1318
0006457	Protein folding	162	50	2358
0006952	Defense response	133	50	2679
0006096	Glycolysis	50	50	2875

The 'Max FP' column summarizes the number of times (out of a total of 50) such an annotation is suggested for a gene, while the 'FP' column identifies the number of genes that are consistently given such an annotation. From (Romero et al., 2020).

3.2 Characterization of plant biomarkers

In P2 we are developing nanoscale sensors for the detection and measurement of bio-markers (primary and secondary metabolites, including non-structural carbohydrates and organic acids) in plants and toxins in soils (Al^{3+}). A plant's response to biotic and abiotic stresses has an early molecular-level expression in the organism's metabolome, which is prior to any phenotypic variations, that can signal proliferation of diseases, compromised productivity, etc. Metabolites provide a direct window into the phenotype, to the physiological state of the plant. These fuel cell signaling and regulate metabolic activity in the plant, so characterizing and associating their concentrations in time with cellular processes, can further our understanding of genome-phenome relationships.

Identifying metabolite-mediated signaling pathways, in real-time, *in-vivo*, selectively (targeted metabolomics), at ultra-low concentrations (pico Moles, pM, or lower), cheaply and without harming the host organism is not only of fundamental importance, but a practical necessity for agriculture. Unfortunately, current technologies for measuring metabolites, such as nuclear magnetic resonance spectroscopy (NMR), high-performance liquid chromatography (HPLC), alone or in tandem with mass spectrometry (HPLC-MS), inductively coupled plasma mass spectrometry (ICP-MS), and enzyme-based methods, fall short of meeting these needs. These lack portability, and tend to be expensive to acquire and operate.

Phenotypic changes in response to biotic and abiotic stresses are reflected early on in an organism's metabolome, hence the need to measure key metabolites for improving early detection of stresses and breeding stress-tolerant species. In our design process, we include both first-principles based in silico screening and experimental prototyping. Our focus is placed on three different sensing platforms:

- Electronic field effect devices (FED): Back-gated transistor devices that translate electronic field effect variations proportional to an analyte's concentration on a functionalized semiconducting channel's surface into changes in transconductance/voltage/current across two or more terminals,
- Colorimetric/optical devices or assays (OD): Functionalized metal nanoparticle systems that fluoresce under UV excitation to produce an intensity signal response proportional, or inversely proportional, to an analyte's concentration in solution, and
- Electrochemical devices (ECD): Functionalized nano-structured electrodes that produce distinguishable voltammetric, impedanciometric or amperometric signals as a function of an analyte's concentration on the electrode's surface (electrochemical sensors).

In our FED designs, the semiconducting channel surface is modified with molecular receptors that are selective to the analyte of interest. The attachment of target analytes to the receptors, result in the depletion or accumulation of charge carriers in the semiconducting channel, analogous to the effect of a transistor base/gate terminal. In (Jaramillo-Botero and Marmolejo-Tejada, 2019), Jaramillo-Botero and Marmolejo demonstrated a low-voltage solution- and back–gated graphene nanoribbon (GNR) field–effect transistor (GFET) sensor design, for the detection and measurement of low-concentration (pM) uridine diphosphate glucose (UDP-glucose), a precursor to sucrose synthesis in a plant cell's cytoplasm and an extracellular signaling molecule capable of activating downstream defense mechanisms, see Figure 6. A self-assembled monolayer (SAM) of 1-pyrenebutyric acid (PyBA) was used to noncovalently functionalize the graphene surface on one end, and to covalently ligate UDP-glucose on its open end,

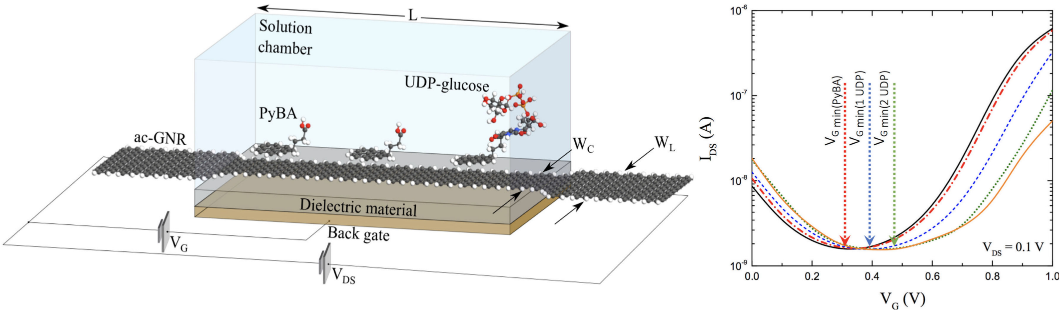

FIGURE 6
(Left) Isometric view of graphene-based FED sensor with solvent box, 3 PyBA SAM molecules, and 1 bound UDP-glucose molecule. A metallic back-gate, with an 8 nm thick separating region with relative dielectric constant of 3.9 (i.e. *SiO2*), lay under the semiconducting junction; (right) Transconductance shows *p*-doping effect of increasing UDP-glucose concentration (at V_{DS}=0.1 V). Figures from (Jaramillo-Botero and Marmolejo-Tejada, 2019).

whilst providing mechanical, chemical and electronic signal sensing stability. The device has a predicted limit of detection (LOD) of *0.997/n* mM/L (where *n* is the number of sensor units in an array configuration), with high transconductance sensitivity, 0.75-1.5 μS for 1-3 UDP-glucose molecules, at low input (V_G=0.9V) and output voltages V_{DS}=0.1V. Thus, a 1000x1000 nanoarray sensor would yield a LOD of *0.997* nM/L. See Figure 6. This low-power, all-armchair g-FET sensor with SAM ligands that may be chosen to bind different biomarkers, provides a unique opportunity for high throughput, real-time, low-cost, high-mobility, and minimal-calibration sensing applications for in-field phenotyping.

Nanoparticle-based fluorescent probes offer an alternative solution to quantify plant analytes directly from exudates or by direct absorption into the tissues. Nanoparticles (NPs) with the proper size (<100nm), composition and surface modifications can be absorbed onto the cell membrane and subsequently internalized into the cytoplasm. Detailed information about the analyte's concentration can be retrieved wirelessly, by modifying the NP's surface with analyte-selective moieties and small molecular weight fluorophores/chromophores to signal the presence or absence of targeted analytes on these sites. The use of NPs has the added benefit of increasing the total surface area available for binding analytes, when compared to a flat electrode surface. We demonstrated a fluorophore-functionalized gold nanoparticles (AuNP) systems for colorimetric detection and quantification of sucrose and other plant analytes as described in (Jaramillo-Botero et al., 2019). Absorption of radiation (typically in the UV spectrum, i.e. relatively high *hv*) promotes an electron from its electronic ground state to an excited state. During the lifetime of the excited electronic state, part of the energy is lost through internal molecular vibration, leading to a longer wavelength of the released/emitted light (Stokes shift). When the fluorophores emit part of this light as radiation, the AuNPs act as a collisional quenchers of the excited state thereby reducing the fluorescence intensity. The fluorophore then returns to the ground state without light emission. The fluorescence wavelength and distribution of the emitting fluorophore is chosen to overlap the absorption spectra of the AuNP, and the length (R_1) of the mercapto-oligomers that connect the fluorophore to the AuNP is chosen to maximize quenching at such a distance. The analyte concentration is therefore inversely proportional to a differential fluorescent signal, with respect to the amount of fluorophores content.

Last, but not least, we have developed disposable carbon-based electrochemical sensors for the detection and quantification of different metabolites in plants, metals in soils, and greenhouse gases. These can be used in the field with a portable instrument or as part of a phenotyping platform, in real-time, and with minimal cost. We are now able to selectively quantify the presence of Al^{3+} ions in dry and acidic soils, as an indicator of its bioavailability. We expect to use the same technology to quantify it in different tissues, in order to study and understand its effect on plant metabolism. Aluminum ion uptake impairs synthesis, cell expansion, and nutrient transfer from plant roots to main stems, affecting their overall metabolism (Barceló and Poschenrieder, 1990). In Camila Ayala et al. (2022), we demonstrate and validated a glassy carbon electrode modified by the electrochemical reduction of bismuth in an acetate buffer, for the detection of Al^{3+} in a cupferron solution, using double-potential pulse chrono-amperometry. The sensor has a linear response in the concentration range of $1.85x10^{10}$ to $3.70x10^{6}$ mol/L and a detection limit of 0.025ppb. Our current technology, uses laser-scribed graphene electrodes, which enable scaling production and tuning the sensor's sensitivity range.

In general, nanostructured electrodes or assays can provide the resolution and accuracy required for detecting and quantifying ultra-low analyte concentrations, from samples captured *via* iontophoresis, natural exudation or gutation processes directly from a plant's leaf, stem or root. Sensors can be tattooed onto the plant surface of interest, in a 'wearable' device configuration, or they can be embedded into other fixed or mobile instruments. These technologies are amenable to industrial scaling and production and are key to improving agroindustrial productivity and safety.

3.3 Characterizing stress signaling through membrane protein complexes

In P3 we are studying G-protein signaling in plants, using a combination of first-principles based membrane protein-structure prediction and experiments on mutants. Stress signalling across the cell membrane remains a fundamental biological question in plant science. Although G protein-coupled receptor (GPCR) analogs in plants have not yet been conclusively determined, we believe G proteins transmit signals by atypical mechanisms in plants (when compared to humans and animals) while effector proteins control growth, cell proliferation, defense, stomatal movements, channel regulation, sugar sensing and some hormone-mediated responses, as shown by Murano et al (Urano et al., 2013) using *Arabidopsis thaliana* and rice (Oryza sativa) models. Genome analysis identified 56 putative GPCRs, including G protein-coupled receptor1 (GCR1), which is reportedly a remote homologue to human class A, B, and E GPCRs (Taddese et al., 2014). Taddesse et al (Taddese et al., 2014). addressed the disparity between genome analysis and biological evidence through a structural bioinformatics study, involving fold recognition methods, from which only GCR1 emerged as a strong candidate. The activation of GPCR analogs in plants defines their function, and it involves multiple distinct conformations that do not follow in step with animal G signalling, as described by Apone et al (Apone et al., 2003).

Moreover, since some G protein components are capable of activating more than one intracellular (IC) signaling pathway, it is essential to identify the multiple active conformations that may be involved with different functions.

To understand the GCR1 activation mechanisms using modeling, accurate three-dimensional (3D) structures are required. However, these are not currently available from crystallographic or NMR experiments, therefore we are leveraging on the first-principles based approach from Goddard et al (Vaidehi et al., 2002; Goddard et al., 2010) to predict and validate the tertiary GCR1 structure from its primary sequence. The predicted structure (see Figure 7 are used in nano-to-micro second molecular dynamics (MD) simulations to determine the potential activation mechanisms and signalling pathways. We are currently supplementing Simulation results using stress-response characterization of *Arabidopsis thaliana* ecotypes and knock-out mutants, and performing gene annotation and analysis to determine stress responses, before moving to a functional validation of a high-performing rice haploid (haplotypes) for particular agronomical traits of interest.

As depicted in Figure 4, P3 is also focused on the characterization of non-structural carbohydrates (NSC), secondary metabolites (e.g. flavonoids), and Al^{3+} ions in acid soils. One major objective was to identify the role of NSC (specifically, sucrose and starch) and secondary metabolites (i.e., phenols and flavonoids) as signaling elements that regulate a plant's performance under biotic and abiotic stresses. On the other hand, toxicity from Al^{3+} affects the absorption ofessential nutrients (such as Ca_{2+}) and restricts the normal growth of its roots. This alters essential physiological processes of a plant, and quenches plant productivity. The phytotoxic effects of aluminium are highly-dependent on the concentration of Al^{3+} and the plant's genotype ability to translocate the metal from source to sink. With P2, we have now demonstrated a rapid, real-time electrochemical sensor for measuring ppm-levels of Al^{3+} in soils; a tool that will undoubtedly contribute to the development of plant varieties with improved tolerance to metal toxicity, accurate selection of crops for acid soils, and to soil remediation strategies (Ayala et al., 2022).

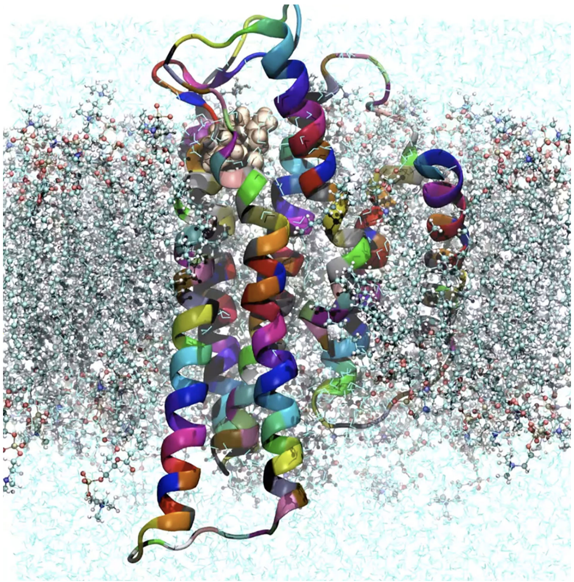

FIGURE 7
Predicted GCR1 3D atomic structure and composition embedded in a bi-lipid cell membrane and in explicit water. The structure was obtained from the primary of *Arabidopsis Thaliana* using a hybrid approach based on homology and our first-principles methods (Hernandez et al. (2022).

3.4 Phenotypic characterization of crops

Increased productivity in agriculture will lead to greater availability and lower costs for both food and non-food products derived from agronomic practices. The efficiency of resource allocation among farmers needs to be characterized through sustainable agriculture. High-performance phenotyping (HTP) strategies and platforms are necessary to optimize the acquisition of data from individual plants and large crop plots. These techniques allow farmers and breeders to access real time data on the status of their crops, improved crop management, and proper selection and optimization of species as a function of microclimate and soil conditions. This involves new sensing technologies capable of resolutions beyond the continuous variables at the macroscopic scale, down to the level of molecules, integrated within low-cost, low-power, massively distributed HTP and new ontologies to facilitate data integration and analysis.

In P4 we are developing a new HTP platform capable of measuring in real-time, among other variables: (i) soil nutrients ($K+$, $NO3-$) and gases ($CO2$, $N2O$), (ii) vegetative indices from individual plant architecture models, and (iii) above-ground biomass (AGB) and leaf nitrogen (N) estimation at crop canopy level (See Figure 8. At the ground-level, a central unit called PhenoAgro, integrates communication through a peer-to-peer wireless LoRa network, wifi communications to data-collecting and processing servers in a cloud configuration, and custom-designed sensors to determine the spatio-temporal evolution of ground, plant, and atmospheric variables. Furthermore, we have own developed our own image-processing and trajectory-control algorithms for commercial unmanned aerial vehicles (UAV), to estimate AGB and N content from canopy-level multispectral imagery.

We have demostrated the UAV platform in spatio-temporal characterization of different morphological and physiological variables in rice crops, specifically leaf nitrogen (N) and biomass production, both of which are good predictors of crop yield and

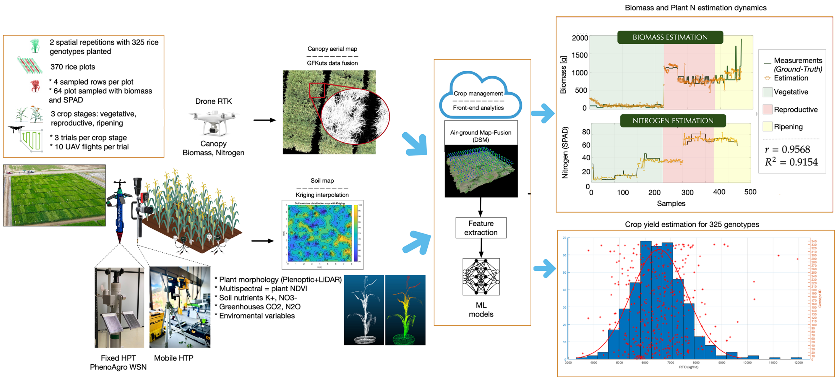

FIGURE 8
The OMICAS alliance has developed, validated and is currently deploying three High-Throughput Phenotyping (HTP) strategies and integrated platforms: aereal, terrestrial-fixed and terrestrial-mobile. From the aereal, drone-based, multispectral imaging platform we are now able to predict leaf-N, NDVI, and other crop data; from the fixed ground-based systems we obtain soil-based nutrients, plant indices (including metabolite profiles) and atmospheric state variables (including greenhouse gas footprints from crops, primarily N_2O and CH_4).

plant health. Our above-ground methods to capture canopy traits, overcome the limitations of traditional destructive methods for biomass sampling, or the use of time-demanding soil plant analysis development chlorophyll meters (SPAD) for the estimation of leaf *N*. Most of the existing body of work uses multispectral aerial images for the calculation of canopy light reflectances at different wavelengths (Mishra et al., 2017; Yue et al., 2019; Maimaitijiang et al., 2019; Zhang et al., 2019b). Several features can be extracted from the aerial imagery to calculate vegetation index (VI) formulas, by associating specific reflectance bandwidths that are highly related to variations in leaf chemical components, leading to a proper estimation of biomass dynamics (Liu et al., 2017; Zhang et al., 2019a) and leaf *N* (Sun et al., 2017; Nigon et al., 2020).

Our UAV systems are equipped with a multispectral sensors (depicted in Figure 8 to capture canopy imagery in the red, green, near-infrared (NIR) and red-edge bands. Images are collected through the entire phenological cycle of the crop, specifically during the vegetative, reproductive, and ripening stages of plant growth. In previous work (Correa et al., 2020), we presented a novel multispectral image segmentation method called GFKuts. The acquired aerial imagery is segmented by optimizing an energy fitness function that enables the proper labeling of texture in the red, green, and near-infrared space (RGN). The resultant RGN image-mask only includes pixel information that accurately represents the vegetation canopy, allowing for the proper extraction of VI-based features.

Several VIs have been proposed to associate specific spectral wavelengths with different crop variables (Lu et al., 2020). Nonetheless, no single set of VIs had been demonstrated across all crop stages and plant varieties, until our recent work (Devia et al., 2019), which identified and characterized a set of VIs suitable for the estimation of both AGB and leaf *N*, namely:

- Normalized Difference Vegetation Index (Kanke et al., 2016)
- Green Normalized Difference Vegetation Index (Prabhakara et al., 2015)
- Difference Vegetation Index (Naito et al., 2017)
- Corrected Transformed Vegetation Index (Naito et al., 2017)
- Soil-Adjusted Vegetation Index (Arroyo et al., 2017)
- Modified SAVI (Gnyp et al., 2014)
- Simple Ratio (Kanke et al., 2016)

The selected VIs exhibit a strong dependence on the NIR reflectance due to leaf chlorophyll absorption, providing an accurate approach for training machine learning models to estimate the accumulated canopy biomass and leaf nitrogen at each crop stage. Figure 8 shows estimation results reported in (Colorado et al., 2020a; Colorado et al., 2020b). Artificial Neural Networks (ANN) are trained with the selected VIs to predict both AGB dynamics and N-to-SPAD correlations during the entire crop phenological stages. Correlations are obtained by comparing the estimations against an assembled ground-truth dataset with biomass and SPAD readings directly measured at ground-level. On average, we have obtained biomass correlations of r=0.9568 with R^2=0.9154, whereas r=0.986 with R^2=0.97 for leaf nitrogen. These are promising results towards the autonomous estimation of rice canopy AGB and N, with the aim of enabling high-resolution genome trait mapping for genomic selection models for plant improvement against abiotic stresses.

3.5 In-silico strategies for improved crop breeding

Plant breeding efforts generally require intensive labor as well as long optimization cycles that can last up to 12 years. Figure 9 illustrates how the in-silico approach strategy in the OMICAS program accelerates traditional approaches, by narrowing down potential candidate species from a large set, based on fitness functions associated to one or more agronomic trait. This reduces the time and cost of experimental breeding and selection. Different components that may complement traditional approaches to plant breeding are grouped together inside the blue box in Figure 9. They take into account omic data representations, mathematical models and optimization algorithms to facilitate the identification of critical features that are present in populations with one (or more) desirable traits. Our goal in OMICAS has been to apply big data and machine learning algorithms on omics data characterized over multiple scales, in order to explore and ultimately uncover the key variables that intervene in stress-response and productivity. For example, an in silico approach may implement a computational environment to simulate critical optimization routes and explore a more ample and complete state/search space at a fraction of the time and cost. In P5, genetic, metabolic, protein, and cellular networks are used to supplement phenotypic traits associated to stress response, and to understand complex interactions and correlations upon which predictions can be based.

Our in-silico approach in OMICAS builds on epigenetic, genetic, metabolic and cellular regulation network models, characterized *via* results from P1-P4 to elucidate some of these complex interactions and correlations. Data analytics algorithms are used to identify and annotate genes associated to phenotypic traits. This in silico optimization cycle reduces the time and costs to breeding optimized agricultural plant varieties. It offers a significant advantages over the traditional labor-intensive scheme, among them:

- Discovering hidden relationships in large collections of data associated with crop productivity traits,
- Understanding the processes underlying the formation of these patterns,
- Quantifying productivity gain traits and their determinants, and
- Minimizing the genetic mutation and crossover space to optimize traits.

One particular path we have taken, addresses a common challenge in deploying new crop varieties, namely gene annotations and correlations. A variety of approaches to identify gene function/s have been proposed over the past years, including Weighted Gene Co-expression Network Analysis (WGCNA) (Langfelder and Horvath, 2008; Wang et al., 2020; Riccio et al., 2020). In (Riccio et al., 2020), for example, we proposed both a generalization and an extension of the original WGCNA, which is applied to rice (*Oryza sativa*. The proposed in silico approach identifies a group of 19 genes which are relevant in the response to salt stress. Such genes are considered target genes for experimental efforts to improve salinity tolerance in rice.

To identify the target genes, the approach relies on the idea of defining specific overlapping network 'communities' of

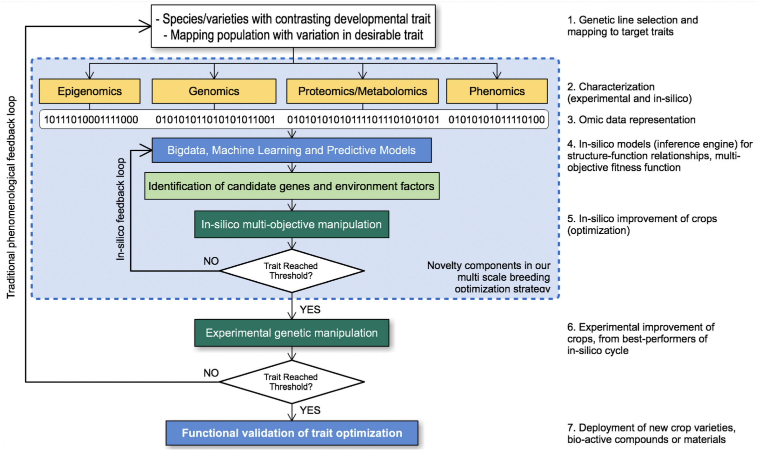

FIGURE 9
In-silico characterization strategy in OMICAS.

genes, which are assumed to underlie the co-expression gene network. In other words, a key hypothesis of the proposed approach is that the overlapping nature of the systems' regulatory domains that generate co-expression can be identified by applying an algorithm that detects modules of overlapping network communities. More specifically, module detection is achieved by using machine learning techniques of hierarchical link clustering. To analyze the phenotypic responses of each gene modules to salt stress, statistical regression analysis based on least absolute shrinkage and selection operator (LASSO) is employed. It is interesting to note that the identified target group is distributed across six classes: three that group together three genes associated to shoot K content; two that group three genes associated to shoot biomass; and finally, there one that groups four genes associated to root biomass. The proposed approach offers a framework to reduce the search-space for target genes that respond to salt stress. It facilitates experimental validation by reducing the number of relevant genes.

Leveraging on the tools, methods and technologies developed in P1 through P5, P6 focuses on optimizing crops through accurate and high-throughput phenotyping, gene and quantitative trait loci (QTL) discovery, molecular marker-assisted elite lines construction *via*, genomic selection (GS) and QTL-based marker-aided selection (MAS). P6 focuses on traits of high importance for the Colombian agricultural sector, and validates these on rice and sugarcane models. The traits are: (1) a biotic stress: *Rice hoja blanca virus* (RHBV) resistance, (2) three abiotic stresses: low radiation, high night temperatures and aluminum toxicity in rice, and (3) two physiological traits: sugar accumulation and nitrogen efficiency in sugarcane. These traits are highly relevant to crops in the region (e.g. RHBV resistance) and to crops worldwide (i.e. abiotic stresses and physiological traits).

3.6 Tolerance to Rice Hoja Blanca virus

The rice hoja blanca (RHB) disease is due to the *Rice hoja blanca virus* (RHBV), which is transmitted by a planthopper insect (see Figure 10, *Tagasodes oryzicolus*. RHB is among the most severe impediments to rice productivity in tropical Americas and the Caribbean Islands (Morales and Jennings, 2010). In Colombia it is the second threat for rice production after rice blast. There is no chemical or biological treatment available to fight the RHB disease, apart from devastating insecticides against its vector. Thus, tapping into diversity of genetic resistance to RHBV is key for a durable, successful, environment- and consumers health-friendly, integrated crop management. In P6 we take advantage of an extensive screening of rice germplasm to map QTLs that control the incidence and the severity of the disease in four diverse resistance donors selected amongst the best performers against the disease (Cruz-Gallego et al., 2018). We also search for possible interactions (epistasis) between the QTLs. And finally we identify candidate genes underlying the QTLs and attempt to validate them using a CRISPR-Cas9-based knock-out approach. The knowledge produced on genes and QTL represents the basis for a modern approach of marker-aided breeding of elite rice lines resistant to RHBV.

Our main result so far is the discovery of a major QTL for resistance to the virus in two Colombian cultivars, FD 50 and FD 2000, as well as two QTLs that control the damages caused by the insect vector (Romero et al., 2014). This QTL for RHBV resistance, renamed as *qHBV4.1*, controls RHBV *incidence*, which is simply the percentage of plants that show symptoms of viral infection, no matter the extent or severity of the symptoms. A local ancestry analysis in the *qHBV4.1* region showed that both resistant cultivars share the same temperate Japonica origin, although FD 50 and FD 2000 are mostly Indica

FIGURE 10
(left) Infected rice panicle showing planthopper insect and larvae, which transmits RHBV, and (right) physically damaged rice leaves.

germplasm. Thus, there is a high risk of resistance breakdown by a mutation in the virus RNA, due to a very poor diversity in resistant alleles in the cultivated germplasm. Recent observations of RHBV outbreaks even in the resistant FD 2000 near Cúcuta (Colombia) in FEDEARROZ plots tend to confirm the imminence of the threat. Other QTLs have been discovered by Genome-Wide Association Study (GWAS) but still need to be confirmed by bi-parental mapping (Cruz-Gallego et al., 2018). Incidence is the primary parameter to look at for the epidemics of a disease. Yet, its *severity* is certainly as important as incidence: if severity is low, a high incidence might have no significant impact on plant viability, panicle development, or grain yield. Additional to RHBV incidence, we thus designed new experiments to decipher the genetic control of RHBV resistance seen as symptoms severity. Through meta-QTL analysis using MapDisto v2 (Lorieux 2012; Heffelfinger et al., 2017) we found a new QTL, *qHBV11.1*, that controls HBV severity in three of the four crosses analyzed. Looking at the rice genome annotation (RAP-DB IRGSP v1) we also found an interesting candidate gene in the QTL region. This gene, STV11, was found to bring resistance to a cousin virus, the *Rice stripe virus* (Wang et al., 2014). We are currently investigating if STV11 in underlying the *qHBV11.1* QTL using *stv11* mutants created by CRISPR-Cas9 knock-out.

Using joint- and meta-QTL approaches, we could refine the *qHBV4.1* position. In the narrowed region of *qHBV4.1* we found a putative gene that encodes for the AGO-4 Argonaute protein (LOC-Os04g06770). Argonaute proteins, in addition to participating in the regulation of endogenous gene expression, also play a critical role in the defense against viruses through small interference RNA of viral origin which bind to Argonaute and serve as a guide for it to cut new viral RNA particles (Mallory and Vaucheret, 2010). This system is a common defense mechanism against pathogens, so AGO-4 may also be associated with resistance to RHBV. We investigated the action of *qHBV4.1* using *stv11* mutants created by CRISPR-Cas9 knock-out in the resistant genetic background FD-2000. We found a mutant that showed higher RHB incidence than the wild FD-2000, indicating that AGO-4 is a major factor of resistance to RHBV.

3.7 Low radiation and high noctural temperature tolerance in rice crops

Studies on climate variability impact on rice yield showed that low radiation is an important yield limiting factor (Sheehy et al., 2006; Yang et al., 2014). Low radiation constrained yield with about 40 to 50% yield loss in rice grown in India and south east asia countries (Viji et al., 1997; Sekhar et al., 2019) and Colombia (Delerce et al., 2016). Furthermore, the lack of optimal windows for farmers to sow either due to climatic or management constrains increases the probability of rice crops to find low radiation conditions at the end of the cycle. Plant traits related to source: sink interaction as carbon partition to grains rather than plant traits related to source activity (photosynthesis) are related to rice plant tolerance to low radiation during grain filling conditions (Shao et al., 2019; Shao et al., 2021). Our project, will look for traits and genes that allow to discriminate low radiation tolerant plants. Field phenotyping in two sites in Colombia of two populations (MAGIC indica and Diversity indica panel) and GBS genotyping will allow us to find out stable QTLs confering tolerance to low radiation to rice.

Despite being a mainly tropical crop, rice is heat sensitive but avoids daytime heat stress *via* transpirational cooling. This works less well at night, resulting in yield reductions through reduced grain filling rates and duration, smaller endosperm cell number and loosely stacked starch. The latter causes chalkiness, an important parameter for grain quality. These High Night Temperature (HNT) effects result from impeded grain development (sink formation) and 'starvation' (source limitation). Possibly, massive increases in panicle respiration are insufficiently offset by increased photosynthesis and reserve mobilization. Evidence is building that HNT causes significant yield reductions in some tropical environments, and this is expected to be aggravated by global warming: Night temperatures rise faster than day temperatures (Davy et al., 2017). Late-season HNT caused 40% yield loss locally in LA and the Caribbean (Delerce et al., 2016) and Asia (Welch et al., 2010). Tolerance to HNT is uncommon among high-yielding rices and has not been explicitly bred for. New phenotyping platforms and the search for traits, tolerant genotypes and favorable alleles in heat stress responsive genes during OMICAS will provide opportunities to develop cultivars tolerant to heat. Tolerant varieties as N22, the most heat tolerant genotype known (Jagadish et al., 2015), is a poor trait donor due to undesirable agronomic traits and genetic distance to the genetic background of high-yielding cultivars. New sources of tolerance are needed. Donors for HNT tolerance may also be sought in distant genomes. A major QTL for thermotolerance was identified and cloned in African rice (Oryza glaberrima). Thermo-tolerance 1 (TT1) encodes an $\alpha 2$ subunit of the 26S proteasome involved in the degradation of ubiquitinated proteins. The OgTT1 allele of heat-tolerant cv. CG14, expressed in a sensitive cultivar, eliminated cytotoxic denatured proteins. Overexpression of OgTT1 was associated with enhanced thermotolerance in rice, A. thaliana and Festuca (Li et al., 2015), although effects on grain quality remain unknown. Some genetic variation for HNT tolerance exists within sativa rice. Some QTLs and genes associated with HNT tolerance were characterized but have not yet been field-validated and introduced to breeding (Janni et al., 2020). More multidisciplinary translational research is needed to develop high-yielding varieties adapted to HNT tolerance and climate change. The grain filling stage in rice is the most sensitive stage to a reduction in radiation. From a physiological angle low radiation can reduce the source of carbon (Wang et al., 2015) but can also affect sink number and activity (Cantagallo et al., 2004). The impact on sink, has not been demonstrated in rice and deserves further studies. The difficulty to find a relevant trait related to low radiation tolerance during grain filling in previous studies generates also on the lack of genetic diversity studied and the difficulty to phenotype large and diverse panels for a stress during a specific phonological phase (Wang et al., 2015).

For low radiation tolerance during grain filling, we carried out phenotype-genotype evaluation on a rice diversity panel using whole genome association studies (GWAS). An Indica panel (300 accessions) was evaluated in the field, during two consecutive years. Grain yield, fertility, 1000 Grain weight, stem-leaf ratio, source:sink relation (SSR) and the number of filled grains per panicle were significantly reduced by low radiation and significantly different across genotypes. A total of 108 QTLs (Quantitative trait loci) with a log 10^{-4} significance, were associated with 20 variables evaluated in the high and low radiation treatments. For low radiation conditions, two common QTLs were found. The OSGRAS19 gene associated in previous studies with grain size (Sink size) and light interception (Source activity) was identified in the LD region of the QTL associated for a proxy trait measured in plants as an indicator of the ability of the plant source organs to fill the grains. A validation of the candidate gene in a MAGIC indica population and the introgration into elite breeding material is ongoing. Concurrently, we will perform a functional analysis of the QTL using tools from P1. During the first two years of the project we have evaluated a set of 30 heat temperature genotypes in a hot spot for hight temperatures in Colombia (Saldaña). However, due to la Niña, we only got one year with real HNT. Hot spot sites are relevant to screen materials, however the stresses are difficult to control and need multi-year trials to find out trend similarities. In order to impose HNT treatment at key developmental stages, we installed controlled heat tents at CIAT to maintain an elevated temperature only through the night. Currently, we are evaluating 140 genotypes (with the 30 genotypes evaluated at Saldaña). This evaluation will allow us to validate the platform for HNT and to suggest candidate parental lines to the breeding program. Along with P4, we are adapting phenotypic tools to continuously sense plants temperature at night within this platform.

3.8 Al^{3+} plant toxicity in acid soils

High concentrations of free aluminum (Al^{3+}) and drought are the main constraints to rice productivity in the Llanos Orientales of Colombia, the most important rice-producing area in the country, in terms of extension. The genetic improvement of drought and aluminum toxicity tolerance has been intensively studied worldwide, with major advances in identifying the genes that regulate these responses and even with the release of rice varieties with high tolerance to these stresses. However, few studies address the impact of the simultaneous occurrence of drought and aluminum toxicity on rice yield, and even fewer focus on identifying the best gene/allele combinations to increase tolerance to these stresses. In the Omicas program, we study these stresses by focusing on: 1) identifying genes/alleles associated with increased cross-tolerance, 2) establishing the regulatory mechanisms, including epigenetics, that determine the difference in tolerance between rice genotypes, and 3) supporting the release of rice varieties adapted to the conditions of the Llanos Orientales of Colombia. For the discovery of genes and allelic variants, we are exploiting the robustness of a synthetic population developed by CIRAD and CIAT for the upland rice-breeding program for Latin America and the Caribbean. Gene discovery is based on GBS-GWAS over the entire synthetic population (some 300 lines). To accelerate the release of tolerant rice varieties, we have selected advanced lines from this synthetic population, which have already been evaluated under the environmental conditions prevailing in the Llanos Orientales and exhibited variability in grain yield and root system characteristics. These advanced lines will be used to identify allelic variants through targeted sequencing of genes with a major influence on the response to aluminum and drought (*Nrat1, STAR1, STAR2, FRDL4, ARS5, ART1, Dro1*, qQTY 2.2, 4.1). If stable favorable haplotypes are identified through these approaches, molecular markers will be developed for use in marker-assisted selection (MAS) and introgression into elite varieties *via* marker-assisted backcrossing (MABC). Epigenetic regulation will be evaluated by sequencing the methylomes of genotypes with contrasting tolerance levels.

3.9 Greenhouse gas emissions from agricultural crops

Nitrogen comprises 78% of the earth's atmosphere and its oxides (nitrous and nitric oxide, $N20$ and NO, respectively) play an important role in the biogeochemical cycle of N but its emission from the ground also has a great environmental impact. Nitrous oxide is not only a powerful greenhouse gas, it is the most depleting substance in stratospheric ozone. According to the Fifth Assessment Report of the Intergovernmental Panel on Climate Change (IPCC, 2013), cultivated soils and natural vegetation contribute 5.0–13.8 Tg $N2O$-N annually (Yao et al, 2020). In soils, $N2O$ emissions are closely linked to the microbial processes of nitrification and denitrification, but nitrification rarely produces more than 1% of the $N2O$ emission from agricultural soils, leaving denitrification, especially in soils with high moisture content, as the major source of $N2O$ in agricultural soils (SYL, 1999). The knowledge of the emission rate from different agricultural production systems will allow to fine-tune their management in order to minimize the emission of $N2O$.

Brazil, followed by Australia, are the countries where the largest number of studies have been carried out to evaluate the emission of $N2O$ from sugarcane. In other countries of Central and South America, including Colombia, these studies have been very scarce (Valencia et al, in preparation). In recent years, according to the Third National Communication on Climate Change, Colombia went from emitting 0.37% of global emissions to 0.46% (11 metric tons of $CO2$), ranking 5th out of32 countries in Latin America and the Caribbean. Sugarcane is one of the most important agro-industrial crops in Colombia, but unfortunately there is not enough information about the emission of GHG from this production system, so our work in the Omicas program will provide a first quantitative view of $N2O$ emissions from this crop under agroindustrial production conditions in the Cauca river valley.

In P7, we implemented a study to quantify the emission of $N2O$ in fields of commercial sugarcane production in two contrasting environments in terms of soil moisture, humid environment, where evapotranspiration is less than precipitation, and a dry environment, where evapotranspiration is greater than precipitation. Our preliminary results show that, in consistency with similar studies in other countries, soil moisture and nitrogen fertilization are the main factors that determine the intensity of $N2O$ emission. After nitrogen fertilization, an increase in the emission of $N2O$ is observed, while the emission decreases over time, after fertilization increases.

3.10 Convergence and future prospects

The OMICAS program brings a trans-disciplinary approach into crops breeding. It couples theory, lab, field and computational experiments within a multiscale omics characterization strategy that enables breeding and validation of new varieties with improved agronomical traits; with higher precision, and in a cost-effective and timely manner. Within three years of its launch, the OMICAS team has, among others:

- uncovered epigenetic differences from four commercial rice cultivars and two accessions of wild rice associated to Al^{3+} toxicity tolerance,
- developed and validated novel graph-theory and machine learning tools to annotate genes using topological properties from co-expression networks, Identified 13 SNP biomarkers and 20 candidate genes associated to sucrose production in sucarcane,
- designed, developed and validated new nano-sensors for the detection and quantification of biomarkers (primary and secondary metabolites) related to a plant organism's health, heavy metals (Al^{3+}) that compromise nutrient absorption, and gases (methane and nitrous oxide) that contribute to the greenhouse footprint of agriculture,
- predicted the tertiary structure of a key membrane protein for stress signaling in plants, from which we are currently studying the plausible signaling pathways through two plant hormones (Abscisic acid [ABA] and gibberellins [GA1]),
- designed, developed and validated a high-throughput phenotyping platform that integrates real-time data from fixed, mobile terrestrial with aerial devices to characterize soil, plant, atmosphere and crop variables,
- identified different rice genes that confer tolerance to RHBV, high nocturnal temperatures, low-radiation, and to aluminum toxicity,
- applied gene-editing technologies (mainly site-specific nuclease (SSN) with CRISPR/Cas) to produce experimental rice crops with enhanced stress response to RHBV, and improved resource use efficiency (Nitrogen and water) and higher yields for both rice and sugarcane, and
- quantified and mapped the emission of nitrous oxide, methane and carbon dioxide from commercial sugarcane production in contrasting environments in Colombia.

We expect the OMICAS strategy, methods and tools will continue to have an incremental impact on breeding of new varieties, beyond rice and sugarcane, and on general agricultural practices. As epigenome and genome-wide characterizations studies lead to function discovery, and our understanding of stress signaling pathways and identification of response mechanisms progresses, we expect a move from editing single or a few nucleotides, to full allele replacement, and ultimately new functional gene insertions.

Such a broad and in-depth characterization effort poses enormous challenges, in terms of the combinatorial explosion of datum, the inherent complexity of deep/hidden interrelationships, and of the non-deterministic nature of multi-objective optimizations will require new processing and interpretation capabilities that are discipline-agnostic. Notwithstanding, this strategy will lead, not only to crops that can resist pests and thrive in difficult climates, but to significant nutritional value improvements, all of which contributes to food security, sustainable productivity, and to the democratization of food production, which disproportionately affects the poorest and most vulnerable people today.

Data availability statement

The original contributions presented in the study are included in the article/Supplementary Material. Further inquiries can be directed to the corresponding author.

Author contributions

All authors contributed to writing and revising the manuscript. AJ-B conceived the program's multiscale strategy and integrated omics architecture. JC, LT, MC and AJ-B contributed directly to phenotyping platforms and sensors, MQ and KV contributed to plant epigenomics and genomics analysis, MR and TG-H to studies on rice abiotic stress tolerance, ML to RHBV stress tolerance, AJ-B, WG and CA to GCR1 structure prediction and function in stress tolerance, JF and CR to computational strategies for gene annotation, FM, NC and AJ-B to GHG characterization of crops, and FS and JR contributed to sugarcane genomic characterization. All authors contributed to the article and approved the submitted version.

Funding

This work was partially funded by the "OMICAS program: Optimización Multiescala In-silico de Cultivos Agrícolas Sostenibles (Infraestructura y validación en Arroz y Caña de Azúcar)" Scientific Ecosystem belonging to the Scientific Colombia Program, sponsored by The World Bank, The Ministry of Science, Technology and Innovation (MinCiencias), ICETEX, the Colombian Ministry of Education and the Colombian Ministry of Commerce, Industry and Turism, under GRANT ID: FP44842-217-2018, Award ID: 792-61187.

Acknowledgments

The authors would like to recognize all the students and technical staff sponsored by the program, from the different institutions involved, for their dedication and contributions to the work reported here, including: Juan M. Marmolejo, Jhonattan de la Roche, Mauricio Peñuela, Jenny Gallo, Chrystian Sosa, Gustavo Lara, Sammy Perdomo, Pedro M. Hernández, David Jimenez, Miguel A. Romero, Nicolás López, Camila Riccio, Sandra Loaiza, Manuel Valencia, Vanessa Reyes, and Juliana Chaura. The authors would also like to thank Dr. Edison Suarez, Ana Claudia Gordillo, and Sandra Losano from Minciencias, father Luis F. Gomez, S.J., Carlos Monthermoso, Ingrid Schuler, Jaime Aguilar, Leidi Rojas, Yaneth Rodríguez, Alejandra Catano, and Michael Hernández from the PUJC, and the alliance's board members Joe Tohme from CIAT-CGIAR, Rodomiro Ortiz from the Swedish University of Agricultural Sciences, José H. Bahamón from Universidad Icesi, Jorge H. Victoria, Patricia Guzmán from Fedearroz, Juan Manuel Chaves from REDDI, and Marcela Arrivillaga from PUJC.

Conflict of interest

Publisher's note

References

Apone, F., Alyeshmerni, N., Wiens, K., Chalmers, D., Chrispeels, M. J., and Colucci, G. (2003). The G-protein-coupled receptor GCR1 regulates DNA synthesis through activation of phosphatidylinositol-specific phospholipase C. *Plant Physiol.* 133 (2), 571–9. doi: 10.1104/pp.103.026005

Arroyo, J. A., Gomez-Castaneda, C., Ruiz, E., Munoz de Cote, E., Gavi, F., and Sucar, L. E. (2017). "Uav technology and machine learning techniques applied to the yield improvement in precision agriculture," in *2017 IEEE Mexican Humanitarian Technology Conference (MHTC)*. NY: IEEE. 137–143. doi: 10.1109/MHTC.2017.80064108006410

Ayala, M. C., Lopez, L. L., Jaramillo-Botero, A., and Valencia, D. P. (2022). Electrochemical electrode with bismuth film for ultrasensitive determination of aluminum (iii). *Under Rev. J. Electroanalytical Chem* 919, p. 116552. doi: 10.1016/j.jelechem.2022.116552

Barceló, J., and Poschenrieder, C. (1990). Plant water relations as affected by heavy metal stress: A review. *J. Plant Nutr.* 13, 1–37. doi: 10.1080/01904169009364057

Camila Ayala, M., Lorena López, L., Jaramillo-Botero, A., and Valencia, D. (2022). Electrochemical modified electrode with bismuth film for ultrasensitive determination of aluminum (iii). *J. Electroanalytical Chem.* 919, 116552. doi: 10.1016/j.jelechem.2022.116552

Cantagallo, J. E., Medan, D., and Hall, A. J. (2004). Grain number in sunflower as affected by shading during floret growth, anthesis and grain setting. *Field Crops Res.* 85, 191–202. doi: 10.1016/S0378-4290(03)00160-6

Colorado, J. D., Calderon, F., Mendez, D., Petro, E., Rojas, J. P., Correa, E. S., et al. (2020a). A novel nir-image segmentation method for the precise estimation of above-ground biomass in rice crops. *PloS One* 15, 1–20. doi: 10.1371/journal.pone.0239591

Colorado, J. D., Cera-Bornacelli, N., Caldas, J. S., Petro, E., Rebolledo, M. C., Cuellar, D., et al. (2020b). Estimation of nitrogen in rice crops from uav-captured images. *Remote Sens.* 12, 3396. doi: 10.3390/rs12203396

CON. (2015). *El Campo Colombiano: un camino hacia el bienestar y la paz. Misión para la Transformación del Campo*. Colombian National Planning Department. Available at: https://colaboracion.dnp.gov.co/cdt/agriculturapecuarioforestal%20y%20pesca/el%20campo%20colombiano%20un%20caminio%20hacia%20el%20bienestar%20y%20la%20paz%20mtc.pdf

Correa, E. S., Calderon, F., and Colorado, J. D. (2020). "Gfkuts: a novel multispectral image segmentation method applied to precision agriculture," in *2020 Virtual Symposium in Plant Omics Sciences (OMICAS)*. NY: IEEE. 1–6. doi: 10.1109/OMICAS52284.2020.9535659

Cruz-Gallego, M., Rebolledo, C., Cuasquer, J., Cruz, D., Peña-Fernández, A. L., Quintero, C., et al. (2018). Identification of new sources of resistance to RHBV- rice hoja blanca virus. *Acta Agronomica* 67, 368–374. doi: 10.15446/acag.v67n2.61334

Davy, R., Esau, I., Chernokulsky, A., Outten, S., and Zilitinkevich, S. (2017). Diurnal asymmetry to the observed global warming. *Int. J. Climatol.* 37, 79–93. doi: 10.1002/joc.4688

Delerce, S., Dorado, H., Grillon, A., Rebolledo, M. C., Prager, S. D., Patiño, V. H., et al. (2016). Assessing weather-yield relationships in rice at local scale using data mining approaches. *PloS One* 11, e0161620. doi: 10.1371/journal.pone.0161620

Devia, C. A., Rojas, J. P., Petro, E., Martinez, C., Mondragon, I. F., Patino, D., et al. (2019). High-throughput biomass estimation in rice crops using uav multispectral imagery. *J. Intelligent Robotic Syst.* 96, 573–589. doi: 10.1007/s10846-019-01001-5

Gallo-Franco, J. J., Sosa, C. C., Ghneim-Herrera, T., and Quimbaya, M. (2020). Epigenetic control of plant response to heavy metal stress: A new view on aluminum tolerance. *Front Plant Sci.* 11, 602625. doi: 10.3389/fpls.2020.602625

Gnyp, M. L., Miao, Y., Yuan, F., Ustin, S. L., Yu, K., Yao, Y., et al. (2014). Hyperspectral canopy sensing of paddy rice aboveground biomass at different growth stages. *Field Crops Res.* 155, 42–55. doi: 10.1016/j.fcr.2013.09.023

Goddard, W. A., Kim, S.-K., Li, Y., Trzaskowski, B., Griffith, A. R., and Abrol, R. (2010). Predicted 3d structures for adenosine receptors bound to ligands: Comparison to the crystal structure. *J. Struct. Biol.* 170, 10–20. doi: 10.1016/j.jsb.2010.01.001

Großkinsky, D. K., Syaifullah, S. J., and Roitsch, T. (2017). Integration of multi-omics techniques and physiological phenotyping within a holistic phenomics approach to study senescence in model and crop plants. *J. Exp. Bot.* 69, 825–844. doi: 10.1093/jxb/erx333

FAO. (2013). *Global state of agriculture and nutrition. Food systems for a better nutrition.* United Nations Development Programme. Available at: https://www.fao.org/3/i3300e/i3300e.pdf

Heffelfinger, C., Fragoso, C. A., and Lorieux, M. (2017). Constructing linkage maps in the genomics era with MapDisto 2.0. *Bioinformatics* 33, 2224-2225.

Hernandez, P., Arango, A., Kim, S., Jaramillo-Botero, A., and III, W. G. (2022). *Predicted 3d structure of the gcr1 putative gpcr in plants and its binding to abscisic acid and gibberellin a1. in prep for submission to the journal of the American chemical society under submission.*

IPPN (2022). *International plant phenotyping network (ippn) IPPN.*

IPCC (2013). *Climate Change 2013: The Physical Science Basis. Contribution of Working Group I to the Fifth Assessment Report of the Intergovernmental Panel on Climate Change*. Eds. T. F. Stocker, D. Qin, G. K. Plattner, M. Tignor, S. K. Allen, J. Boschung, et al. Cambridge University Press, Cambridge, United Kingdom and New York, NY, USA, 1535 pp.

Jagadish, S. V. K., Murty, M. V. R., and Quick, W. P. (2015). Rice responses to rising temperatures–challenges, perspectives and future directions. *Plant Cell Environ.* 38 9, 1686–1698. doi: 10.1111/pce.12430

Jamil, I. N., Remali, J., Azizan, K. A., Nor Muhammad, N. A., Arita, M., Goh, H.-H., et al. (2020). Systematic multi-omics integration (moi) approach in plant systems biology. *Front. In Plant Sci.* 11. doi: 10.3389/fpls.2020.00944

Janni, M., Gullì, M., Maestri, E., Marmiroli, M., Valliyodan, B., Nguyen, H. T., et al. (2020). Molecular and genetic bases of heat stress responses in crop plants and breeding for increased resilience and productivity. *J. Exp. Bot.* 71, 3780–3802. doi: 10.1093/jxb/eraa034

Jaramillo-Botero, A., Hermith, D. P., and Hernandez, P. (2019). *Synthesis of functionalised gold nanoparticles and nanocompounds containing same for measuring sucrose or starch in cells.*

Jaramillo-Botero, A., and Marmolejo-Tejada, J. M. (2019). All-armchair graphene nanoribbon field-effect uridine diphosphate glucose sensor: First-principles in-silico design and characterization. *IEEE Sens. J.* 19, 3975–3983. doi: 10.1109/JSEN.2019.2896448

Kanke, Y., Tubaña, B., Dalen, M., and Harrell, D. (2016). Evaluation of red and red-edge reflectance-based vegetation indices for rice biomass and grain yield prediction models in paddy fields. *Precis. Agric.* 17, 507–530. doi: 10.1007/s11119-016-9433-1

Langfelder, P., and Horvath, S. (2008). WGCNA: an r package for weighted correlation network analysis. *BMC Bioinf.* 9, 559. doi: 10.1186/1471-2105-9-559

Li, X.-M., Chao, D.-Y., Wu, Y., Huang, X., Chen, K., Cui, L., et al. (2015). Natural alleles of a proteasome $\alpha 2$ subunit gene contribute to thermotolerance and adaptation of african rice. *Nat. Genet.* 47, 827–833. doi: 10.1038/ng.3305

Liu, X., Ferguson, R. B., Zheng, H., Cao, Q., Tian, Y., Cao, W., et al. (2017). Using an active-optical sensor to develop an optimal ndvi dynamic model for high-yield rice production (yangtze, china). *Sensors* 17, 672. doi: 10.3390/s17040672

Lu, J., Yang, T., Su, X., Qi, H., Yao, X., Cheng, T., et al. (2020). Monitoring leaf potassium content using hyperspectral vegetation indices in rice leaves. *Precis. Agric.* 21, 324–348. doi: 10.1007/s11119-019-09670-w

Lorieux, M. (2012). MapDisto: fast and efficient computation of genetic linkage maps. *Molecular Breeding* 30, 1231–1235.

Maimaitijiang, M., Sagan, V., Sidike, P., Maimaitiyiming, M., Hartling, S., Peterson, K. T., et al. (2019). Vegetation index weighted canopy volume model (cvmvi) for soybean biomass estimation from unmanned aerial system-based rgb imagery. *ISPRS J. Photogrammetry Remote Sens.* 151, 27–41. doi: 10.1016/j.isprsjprs.2019.03.003

Mallory, A. C., and Vaucheret, H. (2010). Form, function, and regulation of argonaute proteins. *Plant Cell* 22, 3879–3889. doi: 10.1105/tpc.110.080671

Marshall-Colon, A. (2022). *Crops insilico*.

Matthews, M., and Marshall-Colón, A. (2021). Multiscale plant modeling: from genome to phenome and beyond. *Emerg. Top. Life Sci.* 5(2), 231-237. doi: 10.1042/ETLS20200276

Mishra, P., Asaari, M. S. M., Herrero-Langreo, A., Lohumi, S., Diezma, B., and Scheunders, P. (2017). Close range hyperspectral imaging of plants: A review. *Biosyst. Eng.* 164, 49–67. doi: 10.1016/j.biosystemseng.2017.09.009

Morales, F., and Jennings, P. (2010). *Rice hoja blanca: a complex plant–virus–vector pathosystem. perspectives in agriculture, veterinary science, nutrition and natural resources MOR2010.*

Naito, H., Ogawa, S., Valencia, M. O., Mohri, H., Urano, Y., Hosoi, F., et al. (2017). Estimating rice yield related traits and quantitative trait loci analysis under different nitrogen treatments using a simple tower-based field phenotyping system with modified single-lens reflex cameras. *ISPRS J. Photogrammetry Remote Sens.* 125, 50–62. doi: 10.1016/j.isprsjprs.2017.01.010NAITO201750

Nigon, T. J., Yang, C., Dias Paiao, G., Mulla, D. J., Knight, J. F., and Fernández, F. G. (2020). Prediction of early season nitrogen uptake in maize using high-resolution aerial hyperspectral imagery. *Remote Sens.* 12, 1234. doi: 10.3390/rs12081234rs12081234

OECD. (2015). Economic studies of the OECD: Colombia. OECD. Available at: http://www.oecd.org/eco/surveys/Overview_Colombia_ESP.pdf

PEC. (2016). *The Strategic Plan for Colombia's Agricultural Science, Technology and Innovation – PECTIA (2017-2027).* Colombian Ministry of Agriculture, CorpoICA, Colciencias. Available at: https://minciencias.gov.co/sites/default/files/upload/noticias/pectia-2017-actualizado.pdf

Prabhakara, K., Hively, W. D., and McCarty, G. W. (2015). Evaluating the relationship between biomass, percent groundcover and remote sensing indices across six winter cover crop fields in maryland, united states. *Int. J. Appl. Earth Observation Geoinformation* 39, 88–102. doi: 10.1016/j.jag.2015.03.002PRABHAKARA201588

Rasheed, A., Mahmood, T., Gul, A., and Mujeeb-Kazi, A. (2013). An overview of omics for wheat grain quality improvement. In K. Hakeem, P. Ahmad and M. Ozturk Eds. *Crop Improvement*. Boston, MA: Springer. 307–344. doi: 10.1007/978-1-4614-7028-1_10

Ray, D. K., Mueller, N. D., West, P. C., and Foley, J. A. (2013). Yield trends are insufficient to double global crop production by 2050. *PloS One* 8, 1–8. doi: 10.1371/journal.pone.0066428

Riccio, C., Finke, J., and Rocha, C. (2020). *Using overlapping communities and network structure for identifying reduced groups of stress responsive genes.*

Romero, M., Finke, J., Quimbaya, M., and Rocha, C. (2020). "In-silico gene annotation prediction using the co-expression network structure," in *Complex networks and their applications VIII*. Eds. H. Cherifi, S. Gaito, J. F. Mendes, E. Moro and L. M. Rocha (Cham: Springer International Publishing), 802–812.

Romero, M., Finke, J., Quimbaya, M., and Rocha, C. (2014). "In-silico gene annotation prediction using the co-expression network structure," in *Complex networks and their applications VIII*. Eds. H. Cherifi, S. Gaito, J. , F. Mendes, E. Moro and L. M. Rocha (Springer International Publishing), 802–812.

Sekhar, S., Panda, D., Kumar, J., Mohanty, N., Biswal, M., Baig, M. J., et al. (2019). Comparative transcriptome profiling of low light tolerant and sensitive rice varieties induced by low light stress at active tillering stage. *Sci. Rep.* 9 (1), 5753. doi: 10.1038/s41598-019-42170-5

Shao, L., Liu, Z., Li, H., Zhang, Y., Dong, M., Guo, X., et al. (2021). EnglishThe impact of global dimming on crop yields is determined by the source–sink imbalance of carbon during grain filling. *Global Change Biol.* 27, 689–708. doi: 10.1111/gcb.15453

Shao, L., Li, G., Zhao, Q., Li, Y., Sun, Y., Wang, W., et al. (2019). The fertilization effect of global dimming on crop yields is not attributed to an improved light interception. *Global Change Biol* 26 (3), 1697–1713. doi: 10.1111/gcb.14822

Sheehy, J. E., Mitchell, P. L., and Ferrer, A. B. (2006). Decline in rice grain yields with temperature: Models and correlations can give different estimates. *Field Crops Res.* 98, 151–156. doi: 10.1016/j.fcr.2006.01.001

Singh, N., Rai, V., and Singh, N. K. (2020). Multi-omics strategies and prospects to enhance seed quality and nutritional traits in pigeonpea. *Nucleus-India* 63, 249–256. doi: 10.1007/s13237-020-00341-0

Sun, J., Yang, J., Shi, S., Chen, B., Du, L., Gong, W., et al. (2017). Estimating rice leaf nitrogen concentration: Influence of regression algorithms based on passive and active leaf reflectance. *Remote Sens.* 9, 951. doi: 10.3390/rs9090951

SYL. (1999). "Fundamentals and applications of arbuscular mycorrhizae: A biofertilizer perspective," in *In Soil Fertility, Biology, and Plant Nutrition Interrelationships*. Eds. J. O. Siqueira, et al. Vicosa: SBCS, Lavras: UFLA/DCS. 705–723.

Taddese, B., Upton, G. J. G., Bailey, G. R., Jordan, S. R. D., Abdulla, N. Y., Reeves, P. J., et al. (2014). Do plants contain G protein-coupled receptors? *Plant Physiol.* 164, 287–307. doi: 10.1104/pp.113.228874

UN. (2019). *World Population Prospects 2019*. United Nations Department of Economic Affairs, Population division. Available at: http://www.unpopulation.org

UNDP. (2012). *Human Development Report: Rural Colombia, Reasons for Hope.* United Nations Development Programme. Available at: https://info.undp.org/docs/pdc/Documents/CO L/00056950_2Anexo%20sobre%20proceso%20 de%20difusión%20INDH%20- %20Informe%20a%20Embajada%20de%20Sue cia%20(2).pdf

Urano, D., Chen, J.-G., Botella, J. R., and Jones, A. M. (2013). Heterotrimeric G protein signalling in the plant kingdom. *Open Biol.* 3, 120186–120186. doi: 10.1098/rsob.120186

Vaidehi, N., Floriano, W. B., Trabanino, R., Hall, S. E., Freddolino, P., Choi, E. J., et al. (2002). Prediction of structure and function of g protein-coupled receptors. *Proc. Natl. Acad. Sci.* 99, 12622–12627. doi: 10.1073/pnas.122357199

Viji, M. M., Thangaraj, M., and Jayapragasam, M. (1997). Low irradiance stress tolerance in rice (Oryza sativa l.). *Biol. Plantarum* 39, 251–256. doi: 10.1023/A:1000353206366

Wang, Q., Liu, Y., He, J., Zheng, X., Hu, J., Liu, Y., et al (2014). STV11 encodes a sulphotransferase and confers durable resistance to rice stripe virus. *Nature Communications* 5

Wang, L., Deng, F., and Ren, W.-J. (2015). Shading tolerance in rice is related to better light harvesting and use efficiency and grain filling rate during grain filling period. *Field Crops Res.* 180, 54–62. doi: 10.1016/j.fcr.2015.05.010

Wang, Q., Zeng, X., Song, Q., Sun, Y., Feng, Y., and Lai, Y. (2020). Identification of key genes and modules in response to cadmium stress in different rice varieties and stem nodes by weighted gene co-expression network analysis. *Sci. Rep.* 10, 2045–2322. doi: 10.1038/s41598-020-66132-4

Welch, J. R., Vincent, J. R., Auffhammer, M., Moya, P. F., Dobermann, A., and Dawe, D. (2010). Rice yields in tropical/subtropical asia exhibit large but opposing sensitivities to minimum and maximum temperatures. *Proc. Natl. Acad. Sci.* 107, 14562–14567. doi: 10.1073/pnas.1001222107

Yadav, B., Kaur, V., Narayan, O. P., Yadav, S. K., Kumar, A., and Wankhede, D. P. (2022). Integrated omics approaches for flax improvement under abiotic and biotic stress: Current status and future prospects. *Front. Plant Sci.* 13. doi: 10.3389/fpls.2022.931275

Yang, Y., Saand, M., Huang, L., Abdelaal, W., Zhang, J., Wu, Y., et al. (2021). Applications of multi-omics technologies for crop improvement. *Front. Plant Sci.* 3. doi: 10.3389/fpls.2021.563953

Yang, J., Xiong, W., Guang Yang, X., Cao, Y., and Zhi Feng, L. (2014). Geographic variation of rice yield response to past climate change in china. *J. Integr. Agric.* 13, 1586–1598. doi: 10.1016/S2095-3119(14)60803-0

Yao, Y., Tian, H., and Shi, H. (2020). Increased global nitrous oxide emissions from streams and rivers in the Anthropocene. *Nat. Clim. Chang.* 10, 138–142. doi: 10.1038/s41558-019-0665-8

Yue, J., Yang, G., Tian, Q., Feng, H., Xu, K., and Zhou, C. (2019). Estimate of winter-wheat above-ground biomass based on uav ultrahigh-ground-resolution image textures and vegetation indices. *ISPRS J. Photogrammetry Remote Sens.* 150, 226–244. doi: 10.1016/j.isprsjprs.2019.02.022

Yu, J., Pressoir, G., Briggs, W. H., Vroh Bi, I., Yamasaki, M., Doebley, J. F., et al. (2006). A unified mixed-model method for association mapping that accounts for multiple levels of relatedness. *Nat. Genet.* 38, 203–208. doi: 10.1038/ng1702

Zander, M., Lewsey, M. G., Clark, N. M., Yin, L., Bartlett, A., Guzman, J. P. S., et al. (2020). Integrated multi-omics framework of the plant response to jasmonic acid. *Nat. Plants* 6, 290+. doi: 10.1038/s41477-020-0605-7

Zhang, K., Ge, X., Shen, P., Li, W., Liu, X., Cao, Q., et al. (2019a). Predicting rice grain yield based on dynamic changes in vegetation indexes during early to mid-growth stages. *Remote Sens.* 11, 387. doi: 10.3390/rs11040387

Zhang, K., Liu, X., Tahir Ata-Ul-Karim, S., Lu, J., Krienke, B., Li, S., et al. (2019b). Development of chlorophyll-meter-index-based dynamic models for evaluation of high-yield japonica rice production in yangtze river reaches. *Agronomy* 9, 106. doi: 10.3390/agronomy9020106

frontiers | Frontiers in Plant Science

TYPE Original Research
PUBLISHED 13 December 2022
DOI 10.3389/fpls.2022.998803

OPEN ACCESS

EDITED BY
Sindhuja Sankaran,
Washington State University,
United States

REVIEWED BY
René Gislum,
Aarhus University, Denmark
Kang Yu,
Technical University of Munich,
Germany
Chongyuan Zhang,
Purdue University, United States

*CORRESPONDENCE
Daisuke Ogawa
Daisuke.Ogawa@affrc.go.jp

SPECIALTY SECTION
This article was submitted to
Technical Advances in Plant Science,
a section of the journal
Frontiers in Plant Science

RECEIVED 20 July 2022
ACCEPTED 28 November 2022
PUBLISHED 13 December 2022

CITATION
Taniguchi S, Sakamoto T, Imase R, Nonoue Y, Tsunematsu H, Goto A, Matsushita K, Ohmori S, Maeda H, Takeuchi Y, Ishii T, Yonemaru J-i and Ogawa D (2022) Prediction of heading date, culm length, and biomass from canopy-height-related parameters derived from time-series UAV observations of rice.
Front. Plant Sci. 13:998803.
doi: 10.3389/fpls.2022.998803

Prediction of heading date, culm length, and biomass from canopy-height-related parameters derived from time-series UAV observations of rice

Shoji Taniguchi[1,2], Toshihiro Sakamoto[3], Ryoji Imase[2], Yasunori Nonoue[2], Hiroshi Tsunematsu[2], Akitoshi Goto[1,2], Kei Matsushita[2], Sinnosuke Ohmori[2], Hideo Maeda[2], Yoshinobu Takeuchi[2], Takuro Ishii[2], Jun-ichi Yonemaru[1,2] and Daisuke Ogawa[2]*

[1]Research Center for Agricultural Information Technology, National Agricultural and Food Research Organization (NARO), Tsukuba, Japan, [2]Institute of Crop Science, National Agricultural and Food Research Organization (NARO), Tsukuba, Japan, [3]Institute for Agro-Environmental Sciences, National Agricultural and Food Research Organization (NARO), Tsukuba, Japan

Unmanned aerial vehicles (UAVs) are powerful tools for monitoring crops for high-throughput phenotyping. Time-series aerial photography of fields can record the whole process of crop growth. Canopy height (CH), which is vertical plant growth, has been used as an indicator for the evaluation of lodging tolerance and the prediction of biomass and yield. However, there have been few attempts to use UAV-derived time-series CH data for field testing of crop lines. Here we provide a novel framework for trait prediction using CH data in rice. We generated UAV-based digital surface models of crops to extract CH data of 30 Japanese rice cultivars in 2019, 2020, and 2021. CH-related parameters were calculated in a non-linear time-series model as an S-shaped plant growth curve. The maximum saturation CH value was the most important predictor for culm length. The time point at the maximum CH contributed to the prediction of days to heading, and was able to predict stem and leaf weight and aboveground weight, possibly reflecting the association of biomass with duration of vegetative growth. These results indicate that the CH-related parameters acquired by UAV can be useful as predictors of traits typically measured by hand.

KEYWORDS

UAV, canopy height, rice, heading date, biomass, time-series, BLUP

Introduction

Phenotyping is a fundamental procedure in field testing of crops and is typically done laboriously by hand. To make phenotyping more effective, various methods using unmanned aerial vehicles (UAVs) have been developed for measuring crop physical parameters, especially in the field (Furbank and Tester, 2011; Ninomiya, 2022). UAVs can carry several types of cameras, including RGB (red–green–blue), multispectral, and thermal infrared, to take images of crops (Yang et al., 2017; Sakamoto et al., 2022). From RGB images, the 2D vegetation fraction and vertical canopy height (CH) can be extracted (Ogawa et al., 2021a; Ogawa et al., 2021b). Vegetation indices, obtained by spectral analysis, such as the Normalized Difference Vegetation Index (NDVI), have been used for estimating nitrogen use efficiency (Liang et al., 2021), drought resistance (Jiang et al., 2021), and lodging (Yadav et al., 2017; Singh et al., 2019), and for predicting biomass and yield (Yue et al., 2017; Gong et al., 2018; Di Gennaro et al., 2019; Duan et al., 2019; Wang et al., 2019a). These attempts indicate the usefulness of UAVs for high-throughput phenotyping of crops in the field.

Rice is a staple food, especially in Asia (Muthayya et al., 2014). Crucial to increased and sustainable rice production, yield and biomass are complex traits affected by plant shape and size (Peng et al., 2008; Xing and Zhang, 2010; Ikeda et al., 2013). Culm length (CL), panicle length (PL), and panicle number (PN), values of which reflect the genetic architecture of rice, are roughly related to yield and biomass (Zhao et al., 2011). Breeding for longer culms led to the selection of a rice line with higher grain yield and plant weight (Nomura et al., 2019). A rice line carrying *OsglHAT1*, which encodes a new-type GNAT-like protein that harbors intrinsic histone acetyltransferase activity, had increased plant size and grain length and width, with increased yield and biomass (Song et al., 2015). Panicle length (PL) and panicle number (PN) are strongly related to rice yield (Agata et al., 2020; Liu et al., 2022). Growth period also influences rice yield and biomass (Endo-Higashi and Izawa, 2011; Gao et al., 2014), and days to heading (DTH) is generally used to evaluate the transition from vegetative to reproductive stage. Conventionally, CL, PL, PN, and DTH are measured by hand at high cost. For rice breeding and examining the cultivation competence of cultivars at lower cost, a practical high-throughput phenotyping system to estimate these traits in the field is required.

In our previous study, rice CH estimated from UAV images was highly correlated with CL (Ogawa et al., 2021b), making it a potential predictor of yield and biomass. A promising approach to make the most of UAV-based CH data for rice phenotyping is time-series monitoring, in which remote sensing has an advantage by being non-invasive and non-destructive. Estimation of plant height in maize inbred lines at four growth stages by UAV showed that temperate lines grew faster at early growth stages, but tropical lines grew faster at later growth stages (Wang et al., 2019b). Time-series observations of rice CH with UAV correlated highly with CH measured by hand, and revealed growth patterns and differences in functional stages of quantitative trait loci for CH (Ogawa et al., 2021b). Use of a cable-suspended phenotyping platform allowed the temperature response of CH in wheat lines to be clarified (Kronenberg et al., 2021). These studies revealed time-series CH dynamism as a new feature different from one-off CH measurement and led to the hypothesis that time-series CH analysis could reveal genetic and phenological characteristics of rice cultivars and predict yield-related traits usually measured by hand.

One of the important challenges in time-series data analysis is handling time-series changes to allow comparison (Giorgino, 2009; Sugihara et al., 2012; Maziarz, 2015). Many time-series models have been proposed for analyzing crop phenology. Such models include shape-model fitting (Sakamoto et al., 2013; Zhou et al., 2020), random regression with the Legendre polynomial (Campbell et al., 2018; Campbell et al., 2019), segmented linear regression (Toda et al., 2021), and non-linear growth curves (Chang et al., 2017; Grados et al., 2020; Poudel et al., 2022). Anderson et al. (2019) applied a three-parameter logistic model (S-shape non-linear curve) to maize CH time-series data measured by UAV over 1 year, applied a linear mixed effects (LME) model to the logistic parameters, decomposed the parameter variance into genetic and environmental effects: they showed that some of the parameters could be used as predictors of grain yield. Borra-Serrano et al. (2020) and Chang et al. (2017) applied similar S-shape non-linear curves to, respectively, soybean and sorghum CH time-series data measured by UAV. In contrast to these crops, in which CH increases with plant growth, rice CH decreases in the reproductive stage. Therefore, it is necessary to develop a new model to incorporate the effects of the CH decrease and its timing, and to apply it to CH time-series data covering various rice lines.

In this study, we aimed at revealing how UAV-derived time-series CH data are useful for predicting yield and biomass and related traits such as DTH, CL, PL and PN. We developed a novel time-series model incorporating both CH increase and decrease during the growth period, unlike previous models developed for maize, soybean, and sorghum. To develop our model, we used data covering 3 years and 30 cultivars, enabling us to evaluate its robustness and to analyze the cultivar effects by LME models. Through this analysis, we developed a practical and high-throughput method for the prediction of rice traits from CH-related parameters.

Materials and methods

Growing of rice cultivars

Seeds of 30 rice cultivars in Japan, including those developed for high grain yield, lodging resistance, disease resistance, and brown rice quality (Supplementary Table 1), were sown in seedling medium on 17 April 2019, 20 April 2020, and 20 April 2021. We transplanted 3 seedlings per hill at a density of 22.2 plants/m^2 into a paddy field in Tsukubamirai city (36°00′33″N, 140°01′20″E), Japan, on 17 May 2019, 15 May 2020, and 13 May 2021. The paddy field was divided into 60 plots, two per cultivar (Figure 1). The size of each plot was 2.7 m^2. The plants were grown in the field for about 5 months.

UAV-based aerial photography

Aerial observations were made about once a week as in our previous studies (Ogawa et al., 2019; Ogawa et al., 2021a; Ogawa et al., 2021b). We used a Phantom 4 Pro UAV (P4P; DJI, Shenzhen, China) to capture RGB images with an onboard 20-megapixel camera that flew automatically at 1.0 m/s over the paddy field at an altitude of 10.3 m. DJI GS Pro software controlled the flight path and set the following photogrammetry conditions: capture mode, time interval; front overlap ratio, 80%; side overlap ratio, 80%; gimbal pitch angle, −90°, white balance, cloudy; aperture, auto; shutter, auto. Each flight took 150–200 images covering the field, each measuring 5472 × 3648 pixels. To set the focus, the P4P was manually raised to 10.3 m, the camera was focused automatically on a region of the canopy, and then the focus mode was changed to manual. We placed seven ground control point (GCP) markers on the ground around the test field. We obtained the altitude, longitude, and latitude of each GCP by real-time kinematic positioning using a DG-PRO1RWS receiver (BizStation Corp., Matsumoto, Japan).

Generation of digital surface model and quantification of CH

As previously, Agisoft MetaShape Professional v. 1.6.5 software (Agisoft, St. Petersburg, Russia) generated a digital surface model (DSM) from each image set (150–200 images per set) by the date of photogrammetry in the following procedure: (1) align photos (high accuracy), (2) import GCPs, (3) optimize camera, (4) build dense cloud, (5) build digital elevation model (source data to be dense cloud), and (6) export the digital elevation model. The coordinate system was set to UTM zone 54N (WGS-84) and the resolution to 2 mm/pixel. Next, QGIS (3.20.0) software (QGIS Development Team) cut out the area of the paddy field from each DSM image and identified the position of each plot to create shape files. Finally, a script written in Python (3.9.7: Python Software Foundation) cut out the portion in the DSM images corresponding to each plot in reference to the shape files. The computer was an AMD Ryzen Threadripper 2990WX (32-Core Processor, 3.00 GHz, 128 GB RAM, GeForce RTX 2080 Ti GPU) running the 64-bit Windows 10 Pro operating system.

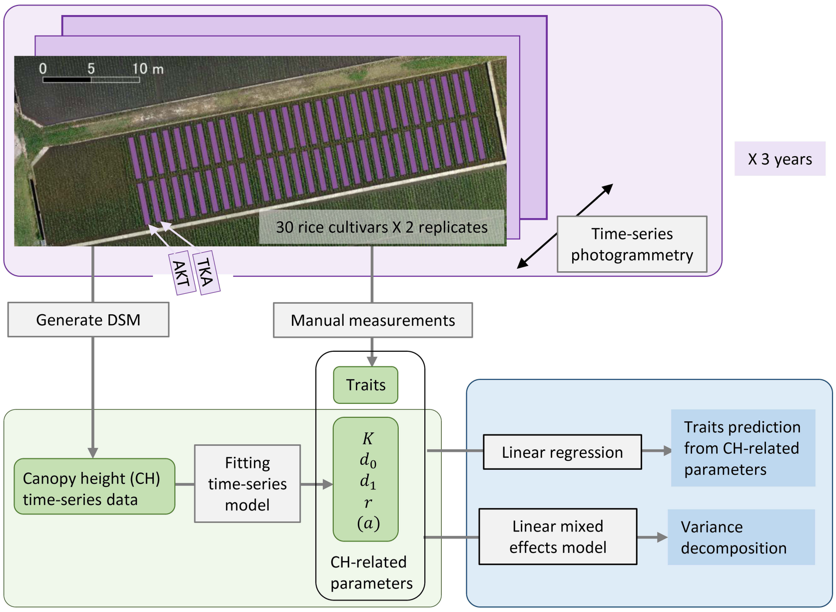

FIGURE 1
Framework of our analysis for the traits prediction from CH-related parameters. Thirty rice cultivars including AKT and TKA were grown with 2 replicates in 2019, 2020, and 2021. Aerial photogrammetry was conducted weekly. CH time-series data were obtained by generating a DSM and CH-related parameters were calculated. Several traits were measured by hand. Statistical analysis included linear regression for the traits prediction and linear mixed effects modeling for the variance decomposition of the traits and CH-related parameters.

We defined the canopy position as the 95th percentile in the cut-out DSMs corresponding to each plot. CH was defined as the difference between canopy position and ground level. We defined ground level as the 2nd percentile just after transplanting in the cut-out DSMs corresponding to each plot.

Fitting time-series model to the CH data

For the statistical modeling of the CH time-series data, we adopted a three-parameter logistic as the typical model for the S-shape plant growth (Paine et al., 2012). Since the logistic asymptotically approaches the maximum saturation value K, we modified it to incorporate the CH decrease in the late growth phase to develop the following time-series model:

$$CH = \begin{cases} \frac{K}{1+\exp(r(d_0-x))} \ (when \ \ x \le d_1), \\ \frac{K}{1+\exp(r(d_0-x))} - a(x-d_1)^2 \ (when \ \ x > d_1), \end{cases} \tag{1}$$

where x is days after sowing, d_0 is the time point at the highest growth rate, d_1 is the time point at the maximum CH, r is the growth rate, and a is the CH decrease rate from the logistic S-shape curve in the late growth phase (Figure 2).

For parameter estimation, we used a two-step procedure to prevent false convergence in the estimation algorithm. First, we calculated K and d_1, taking the maximum value in each CH time-series data set as K. We fitted a cubic polynomial to each data set and obtained d_1 as the time point when the cubic polynomial was at its maximum. We applied the following cubic polynomial:

$$CH = \beta_0 + \beta_1 x + \beta_2 x^2 + \beta_3 x^3 \ . \tag{2}$$

Second, we fitted equation 1 given the values of K and d_1. Except for K, all parameters were obtained by means of the nonlinear least squares method implemented in R (R Core Team, 2021). For parameter estimation for equation 1, we used the R function *nls*, adopting the nl2sol algorithm and setting the initial values to d_0=50 , r=0.05 , and a=1.0 × 10^{-4} .

Manual measurement of traits related to yield

Heading date was defined as the date when panicles emerged from about half of the stems in each plot. DTH (days) was the period from the sowing date to the heading date. CL (m) and PL (cm) of the longest culm of each plant were measured and PN was counted once from 2 to 4 weeks after heading. CL was defined as the length from the ground to the panicle base, and PL was defined as the length from there to the tip of the spikelet. Mean values from 10 plants per cultivar were used for CL, PL, and PN. For aboveground dry weight (ADW; g), 50 plants per plot at maturity were harvested from the ground and air-dried for more than 2 weeks before the measurement. Stem and leaf weight (SLW; g) was obtained as ADW − grain weight (GW; g). These traits were measured in each plot. All trait names are listed in Table 1.

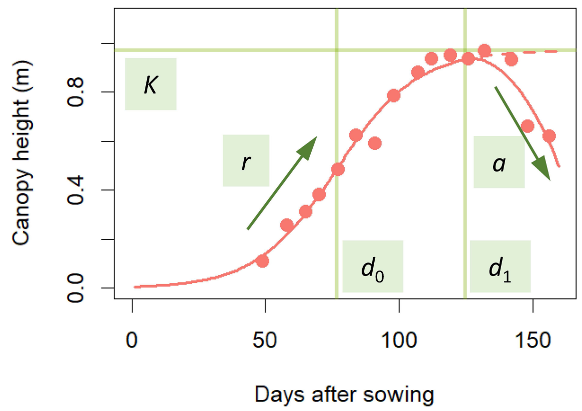

FIGURE 2
Fitting time-series model to CH time-series data. Red points are CH data obtained by UAV. The time-series model applied to the data is the red S-shaped curve. The model was prescribed by 5 parameters: K, the maximum saturation value; r, growth rate; a, CH decrease in the late growth phase; d_0, time point at the highest growth rate; d_1, time point at maximum CH. This curve was described in equation (1).

Statistical analysis of traits and parameters

To decompose the traits and CH-related parameters into cultivar, year, and cultivar × year interaction effects, we applied the linear mixed effects (LME) model:

$$X_{lyb} = \mu_X + X_l + X_y + X_{ly} + \epsilon, \tag{3}$$

where X_{lyb} is a parameter or trait of cultivar l in year y and plot b; μ_X is the fixed effect for the average value; $X_l \sim N(0, \sigma_l^2)$, $X_y \sim N(0, \sigma_y^2)$, and $X_{ly} \sim N(0, \sigma_{ly}^2)$ are random effects of cultivar, year, and cultivar × year interaction, respectively; and $\epsilon \sim N(0, \sigma_\epsilon^2)$ is the residual. We defined heritability as the ratio of cultivar variance to the total variance:

$$h^2 = \frac{\sigma_l^2}{\sigma_l^2+\sigma_y^2+\sigma_{ly}^2+\sigma_\epsilon^2} \ . \tag{4}$$

The R package *lme4* (Bates et al., 2015) estimated the parameters and the best linear unbiased predictors (BLUPs) of the LME model by the REML method. Total variance was calculated as follows:

$$\sigma_{All}^2 = \sigma_l^2 + \sigma_y^2 + \sigma_{ly}^2 + \sigma_\epsilon^2$$

We used the linear regression model to predict the yields from the CH-related parameters and evaluated whether the phenology

TABLE 1 Traits and their abbreviations.

Abbreviation	Trait
ADW	Aboveground dry weight
CL	Culm length
DTH	Days to heading
GW	Grain weight
PL	Panicle length
PN	Panicle number
SLW	Stem and leaf weight

data contained enough information about yield. To reveal what CH-related parameters are useful for the prediction of traits, we examined Pearson's correlations (cor). Since multicollinearity impairs the accuracy of regression coefficients, we used backward variable selection to prevent it. We calculated the variance inflation factor in the R package *car* (Fox and Weisberg, 2019) for variable selection and adopted four parameters as predictors without multicollinearity (variance inflation factor< 5): K, d_0, d_1, and r (Supplementary Table 2). All four predictors were standardized to have a mean of 0 and standard deviation of 1. Next, we constructed linear regression models by the ordinary least squares method to predict CL, DTH, ADW, GW, and SLW. The prediction accuracies were evaluated by cross-validation (CV), splitting data by year and by cultivar (Figure 3). Finally, the regression coefficients were estimated from all data (n = 180). As measures of accuracy, we used cor and root-mean-square error (RMSE) between observed and predicted values of test data. RMSE evaluates the accuracy of predicting the exact values, and cor evaluates the accuracy of predicting the magnitude of correlation.

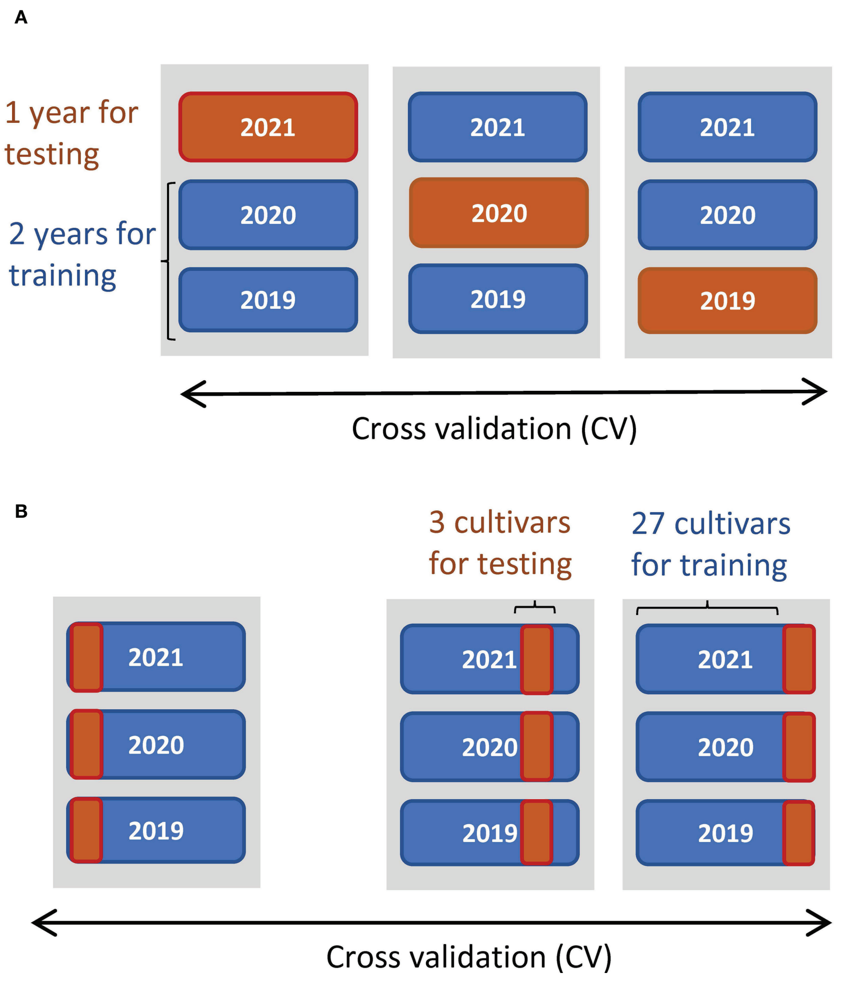

FIGURE 3
Schemes of CV to predict manually measured traits. **(A)** Threefold CV, where data were split by year: two years were used for training data and the other as test data. **(B)** Tenfold CV, where data were split by cultivar: 27 cultivars as training data and the other 3 as test data.

Influence of accumulated daily mean temperature on CH-related parameters d_0 and d_1

We transformed d_0 and d_1 values to accumulated temperature d_0^{temp} and d_1^{temp}, starting from the planting date to the date of d_0 or d_1:

$$d_0^{temp} = \sum_{d=d_p+1}^{d_0} T_d$$

$$d_1^{temp} = \sum_{d=d_p+1}^{d_1} T_d$$

where T_d is the mean temperature of day d and d_p is the date of planting. The base temperature was set to 0°C. We used the LME model in equation 2. Daily mean temperature (°C) in the paddy field is shown in Supplementary Data 1-3.

Results

Relationships between manually measured traits and CH-related parameters in 30 rice cultivars

We characterized phenotype data of 30 Japanese rice cultivars (Supplementary Table 1) in 2019, 2020, and 2021 from the aspect of genetics and examined how to use the CH data for the prediction of traits usually measured by hand (Figure 1).

The sizes of interannual differences in phenotypic distribution depended on trait (Figure 4; Table 2; Supplementary Table 3). Distributions of DTH, CL, PL, and PN were highly overlapped among years, and heritability was high: that of DTH was 0.80, CL 0.81, PL 0.90, and PN 0.63 (Table 2). On the other hand, the phenotypic distribution of GW was wider than that of SLW, especially between 2021 and the other 2 years (Figure 4). Consistent with this, heritability of GW was 0.29, much lower than that of SLW at 0.77. Therefore, GW was more susceptible to year effect than SLW (Table 2). ADW is SLW + GW, and its heritability (0.70) was positioned between theirs.

We collected 2834 CH data of the 30 Japanese cultivars over the 3 years (Supplementary Table 4). Given the huge size of the dataset, we obtained CH-related parameters by applying time-series curves to the CH data by plot (Supplementary Figure 1). The range of phenotypic distributions tended to differ by year (Figure 4; Supplementary Table 3). Heritabilities of K (0.54) and d_1 (0.63) were higher than those of r (0.21) and d_0 (0.29), suggesting that r and d_0, parameters of vegetative growth, might also be more susceptible to year effects than K and d_1, parameters of the reproductive stage (Table 2).

We obtained correlation plots between the parameters and traits (Figure 5; Supplementary Figure 2). K was positively correlated with CL. This result is consistent with our previous data showing high correlation between CH and CL in several rice lines (Ogawa et al., 2021b). d_1 was positively correlated with DTH, ADW, and SLW. These results motivated us to use K and d_1 to predict traits.

Prediction of CL and DTH from CH-related parameters

CV indicated the accuracy of predicting CL and DTH from CH-related parameters (Table 3). In predicting the magnitudes of CL, $\text{cor}_{\text{year}} = 0.82$ and $\text{cor}_{\text{cultivar}} = 0.68$; and of DTH, $\text{cor}_{\text{year}} = 0.89$ and $\text{cor}_{\text{cultivar}} = 0.85$. The scatter plots between observed and predicted CL and DTH were highly correlated (Figure 6). In predicting the exact values of CL, $\text{RMSE}_{\text{year}} = 0.05$ m and $\text{RMSE}_{\text{cultivar}} = 0.04$ m; and of DTH, $\text{RMSE}_{\text{year}} = 5.2$ days and $\text{RMSE}_{\text{cultivar}} = 4.2$ days (Table 3). These RMSE values were smaller than the total standard deviations, the square root of the total variances (Table 2). These results indicate that the CH-related parameters had information that could be used to predict CL and DTH.

We calculated the regression coefficients in the regression models. Since all predictors were standardized, the importance of each parameter in the model was quantified as the absolute value of each coefficient. The regression model to predict CL was

$$CL = 0.84 + 0.06K + 0.01d_0 + 0.01d_1 + 0.01r \tag{5}$$

and the coefficient of determination was R^2=0.684. The model to predict DTH was

$$DTH = 108.6 + 0.1K + 1.3d_0 + 6.8d_1 + 1.1r \tag{6}$$

and $R^2 = 0.794$

In predicting CL, the coefficient of K (0.06, significant by t-test at 0.1%; Supplementary Table 5) had the largest absolute value, more than 4× the second largest one, that of d_0 (0.01). In predicting DTH, the coefficient of d_1 (6.82, significant by t-test at 0.1%; Supplementary Table 5) had the largest absolute value, more than 5× the second largest one, that of d_0 (1.34). Therefore, in the linear regression model, K was the most important predictor of CL, and d_1 was the most important predictor of DTH.

The linear regression models based on CH-related parameters explained the total variances of the manually measured traits, but it was still uncertain whether the relations between the two were derived from the characteristics of each cultivar. The LME model, which decomposed the total variance into cultivar, year, cultivar × year interactions, and residual, extracted the cultivar effects as the BLUPs from the whole data. First, the high heritabilities of CL (0.81) and DTH (0.80) imply that a large proportion of the total variance derived from cultivar

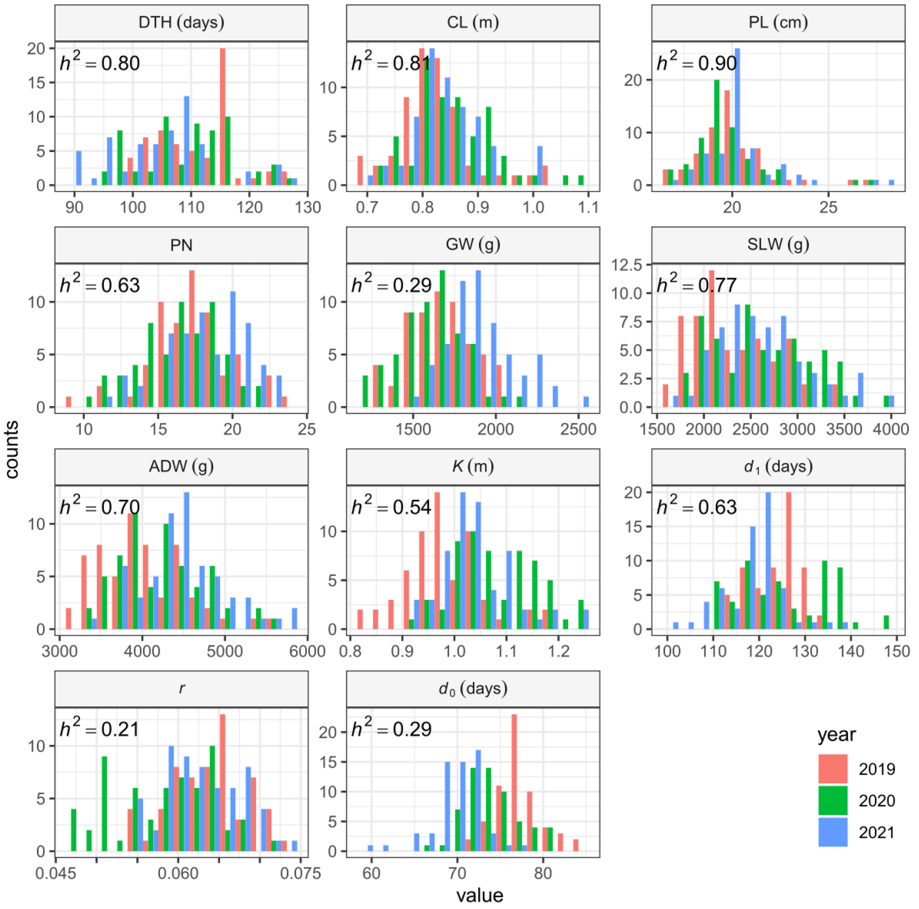

FIGURE 4
Frequency distributions of manually measured traits and CH-related parameters, shown as histograms.

TABLE 2 Summary statistics of CH-related parameters and traits obtained by the linear mixed effects model.

Trait	Heritability	Mean	σ_{All}^{2} [a]	σ_{l}^{2} [b]	σ_{y}^{2} [c]	σ_{ly}^{2} [d]	σ_{ϵ}^{2} [e]
DTH	0.80	108.6	7.3×10	5.9×10	1.2×10	1.8	2.6×10^{-1}
CL	0.81	840.3×10^{-3}	5.2×10^{-3}	4.3×10^{-3}	2.0×10^{-4}	1.8×10^{-4}	5.9×10^{-4}
PL	0.90	200.4×10^{-1}	3.7	3.4	1.0×10^{-1}	5.1×10^{-2}	2.2×10^{-1}
PN [f]	0.63	173.2×10^{-1}	8.2	5.2	6.5×10^{-1}	0.0	2.4
GW	0.29	173.0×10	6.5×10^{4}	1.9×10^{4}	2.3×10^{4}	1.2×10^{4}	1.2×10^{4}
SLW	0.77	252.4×10	2.7×10^{5}	2.1×10^{5}	2.3×10^{4}	1.3×10^{4}	2.7×10^{4}
ADW	0.70	425.4×10	3.3×10^{5}	2.3×10^{5}	5.2×10^{4}	5.5×10^{3}	4.2×10^{4}
K	0.54	103.5×10^{-2}	8.0×10^{-3}	4.3×10^{-3}	2.3×10^{-3}	8.1×10^{-4}	6.1×10^{-4}
d_1	0.63	122.8	7.6×10	4.8×10	1.5×10	1.2×10	7.4×10^{-1}
r	0.21	617.2×10^{-4}	3.7×10^{-5}	7.7×10^{-6}	8.9×10^{-6}	1.8×10^{-5}	2.4×10^{-6}
d_0	0.29	737.3×10^{-1}	2.3×10	6.8	1.4×10	1.7	4.8×10^{-1}
a	0.61	385.6×10^{-6}	3.1×10^{-8}	1.9×10^{-8}	1.4×10^{-9}	9.7×10^{-9}	1.1×10^{-9}

[a] Total variance.
[b] Variance of cultivars.
[c] Variance of years.
[d] Variance of cultivar × year interaction.
[e] Variance of residuals.
[f] Note that the result of PN was singular.

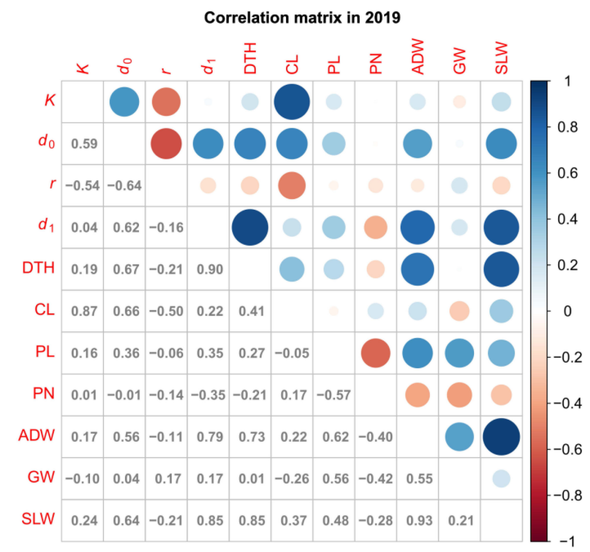

FIGURE 5
Correlation plot of parameters and traits in 2019. Values are correlation coefficients (cor); circles present them by color and size.

effects. Note that heritability is the ratio of cultivar effect to the total variance. Second, the cultivar effects of CL, DTH, K, and d_1, quantified as the BLUPs of each cultivar, showed a clear tendency that the cultivars with smaller K had a smaller CL, and those with smaller d_1 had a smaller DTH (Figure 7). The correlation of cultivar BLUPs between K and CL was cor = 0.89, and that of d_1 and DTH was cor = 0.94. These results indicate that the total variances of CL and DTH were largely prescribed by the cultivar effects of K and d_1, respectively.

Prediction of ADW, GW, and SLW from CH-related parameters

As it did for DTH and CL, our CV method gave the accuracy of prediction of ADW, GW, and SLW (Table 3). In predicting the magnitudes of ADW, cor_{year} = 0.72 and $\text{cor}_{\text{cultivar}}$ = 0.62 and of SLW, cor_{year} = 0.81 and $\text{cor}_{\text{cultivar}}$ = 0.74 (Figure 6). These values were better than predicting the magnitude of GW: cor_{year} = 0.00 and $\text{cor}_{\text{cultivar}}$ = 0.31. The scatter plots between observed and predicted SLW and ADW were highly correlated. In predicting the exact values of ADW, cross-validation by year ($\text{RMSE}_{\text{year}}$ = 406.7 g) had better accuracy than that by cultivar ($\text{RMSE}_{\text{cultivar}}$ = 638.6 g), as had that of SLW (Table 3). The CH-related parameters contained information with which to predict ADW and SLW, but yearly fluctuations could increase RMSE. By contrast, as shown in the scatter plot between observed and predicted GW (Figure 6), the slopes were almost flat and the model explained little of the GW variance. Therefore, CH-related parameters held little information with which to predict GW, at least under our linear regression model.

The regression coefficients indicated the importance of each parameter in our regression models. (All predictors were standardized.) The regression model to predict ADW was

$$ADW = 4254 + 176K - 242d_0 + 518d_1 + 132r \tag{7}$$

and R^2=0.475 . The model to predict SLW was

$$SLW = 2524 + 165K - 199d_0 + 541d_1 + 105r \tag{8}$$

and R^2=0.684 . In predicting ADW and SLW, all four parameters were significant by t-test at 0.1%, and d_1 had the largest absolute values (Supplementary Table 5). For ADW, the coefficient of d_1 was 518, more than 2× the absolute value of d_0 (−242), the second largest. Similarly, for SLW, the coefficient of d_1 was 540, more than 2× the absolute value of d_0 (−198). Therefore, d_1 was the most important predictor of ADW and SLW.

The results of the LME model uncovered the effect of each cultivar on the total variance of ADW and SLW. The high heritabilities of ADW (0.70) and SLW (0.77) imply that a large proportion of total variance derived from cultivar effects. The cultivar effects of ADW, SLW, and d_1, quantified as the BLUPs of each cultivar, showed a clear tendency in which cultivars with smaller d_1 had smaller ADW and SLW (Figure 7C). On the other hand, the cultivar BLUPs of GW had little relation with those of d_1. The correlations of cultivar BLUPs of d_1 with SLW (cor = 0.93) and ADW (cor = 0.87) were higher than that with GW (cor = −0.05). The cultivar effects of d_1 clearly reflected those of SLW. As ADW = SLW + GW, since the low correlation indicates that the cultivar effects of d_1 and GW were almost independent, the

TABLE 3 Prediction accuracy of five traits evaluated by CV by year and by cultivar.

	CV by year		CV by cultivar	
	cor_{year}	$\text{RMSE}_{\text{year}}$	$\text{cor}_{\text{cultivar}}$	$\text{RMSE}_{\text{cultivar}}$
CL	0.823	522.9×10^{-4}	0.682	442.3×10^{-4}
DTH	0.890	515.1×10^{-2}	0.851	420.6×10^{-2}
ADW	0.716	638.6	0.620	406.7
GW	0.003	294.6	0.312	232.6
SLW	0.808	437.0	0.743	291.9

cor, Pearson's correlation coefficient; RMSE, root mean square error.

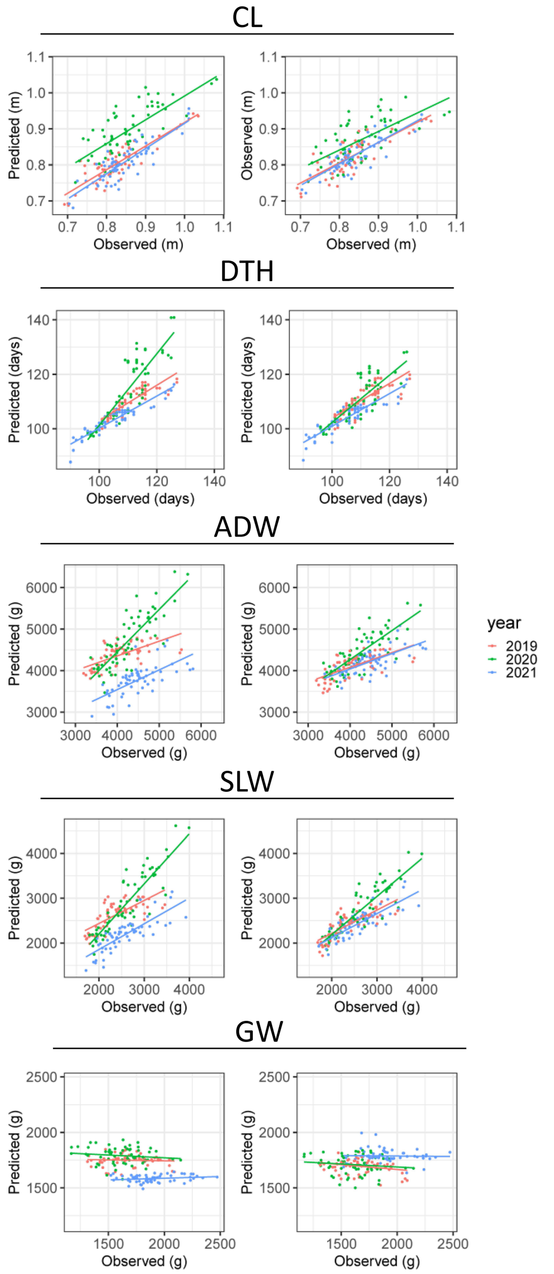

FIGURE 6
Observed and predicted values of CL, DTH, ADW, SLW, and GW. Plots show the results of CV by (left) year and (right) cultivar. The points plot datasets of predicted and observed values, colored by year; the lines are linear regressions applied to them.

result that the cultivar effects of d_1 corresponded to those of ADW derives from the relation of the cultivar effects of d_1 and SLW (Figure 7C; Supplementary Figures 3-5).

Sensitivity of accumulated daily mean temperature to CH data

The frequency distributions of the CH-related parameters differed among years (Figure 4), indicating that those may be influenced by environmental factors. In the developmental rate model, which is well known for the prediction of DTH in rice, daylength and daily mean temperature are explanatory variables (Horie et al., 1995). We asked whether the change of CH is affected by accumulated daily mean temperature instead of daylength, because the former varied among years (Supplementary Data 1-3), whereas daylength was almost constant owing to the similar planting dates. CH-related parameters d_0 and d_1 are based on time-series data, but d_0^{temp} and d_1^{temp} are based on accumulated daily mean temperature. Transforming d_0 into d_0^{temp} increased heritability from 0.29 to 0.58 (Supplementary Table 6) and decreased the year effect from 61% to 21% (Figure 8), meaning that the year effect on d_0 was explained mostly by the accumulated temperature. On the other hand, the heritability of d_1^{temp} (0.62) was almost the same as that of d_1 (Supplementary Table 6; Supplementary Figure 6). These results indicate that the time point at the maximum CH (d_1), which is linked to heading date, is insensitive to accumulated daily mean temperature, but that at the highest CH growth rate (d_0) is sensitive to it.

Discussion

We constructed a time-series model and applied it to the data of 30 rice cultivars in 2019, 2020, and 2021, which were derived from UAV-based time-series aerial photography. In the case of maize (Anderson et al., 2019), soybean (Borra-Serrano et al., 2020) and sorghum (Chang et al., 2017), CH continues to increase, and there is little need to consider the difference of CH growth in between vegetative and reproductive stages. On the other hand, the CH decrease in the reproductive stage is distinct in rice. In our model, we introduced the parameters d_1, the time point at the maximum CH; and a, the rate of CH decrease in the late growth phase, in addition to K, the maximum saturation value; d_0, the time point at the highest growth rate; and r, the growth rate. Our model proved suitable for predicting CL, DTH, SLW, and ADW. The highly heritable CH-related parameters d_1 and K contributed to the prediction of DTH and CL. Notably, d_1 also contributed to the prediction of SLW and ADW, possibly reflecting the association of biomass with duration of vegetative growth. The cultivar effects of traits measured by

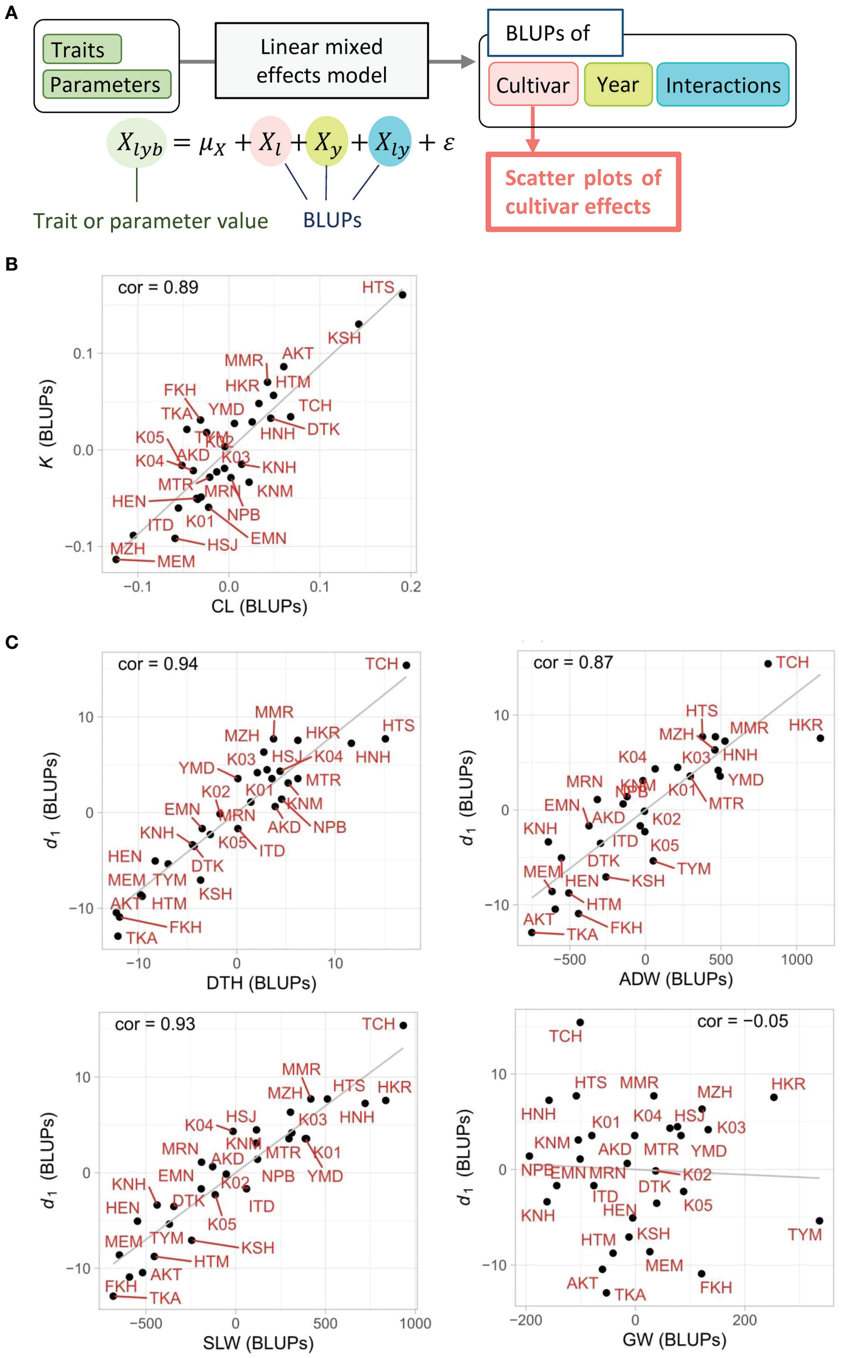

FIGURE 7
Scatter plots of cultivar effects between CH-related parameters and manually measured traits. **(A)** Flow chart of the process to generate scatter plots. The cultivar effect (X_l) on traits and parameters was extracted from the linear mixed effects model as BLUPs from the 3-year experiment. **(B, C)** Plots of cultivar effects showing correlations between **(B)** *K* and CL and between **(C)** d_1 and DTH, ADW, SLW, or GW. Correlation coefficients (cor) are shown in plots. Cultivar name codes are shown in red.

hand (CL, DTH, SLW, and ADW) and their corresponding CH-related parameters were highly correlated. These results indicate that CH-related parameters are useful for the prediction of traits usually measured by hand, reinforcing the significance of time-series monitoring by UAV in high-throughput phenotyping.

Desai et al. (2019) proposed a method to precisely estimate heading date by detecting flowering panicles in RGB images

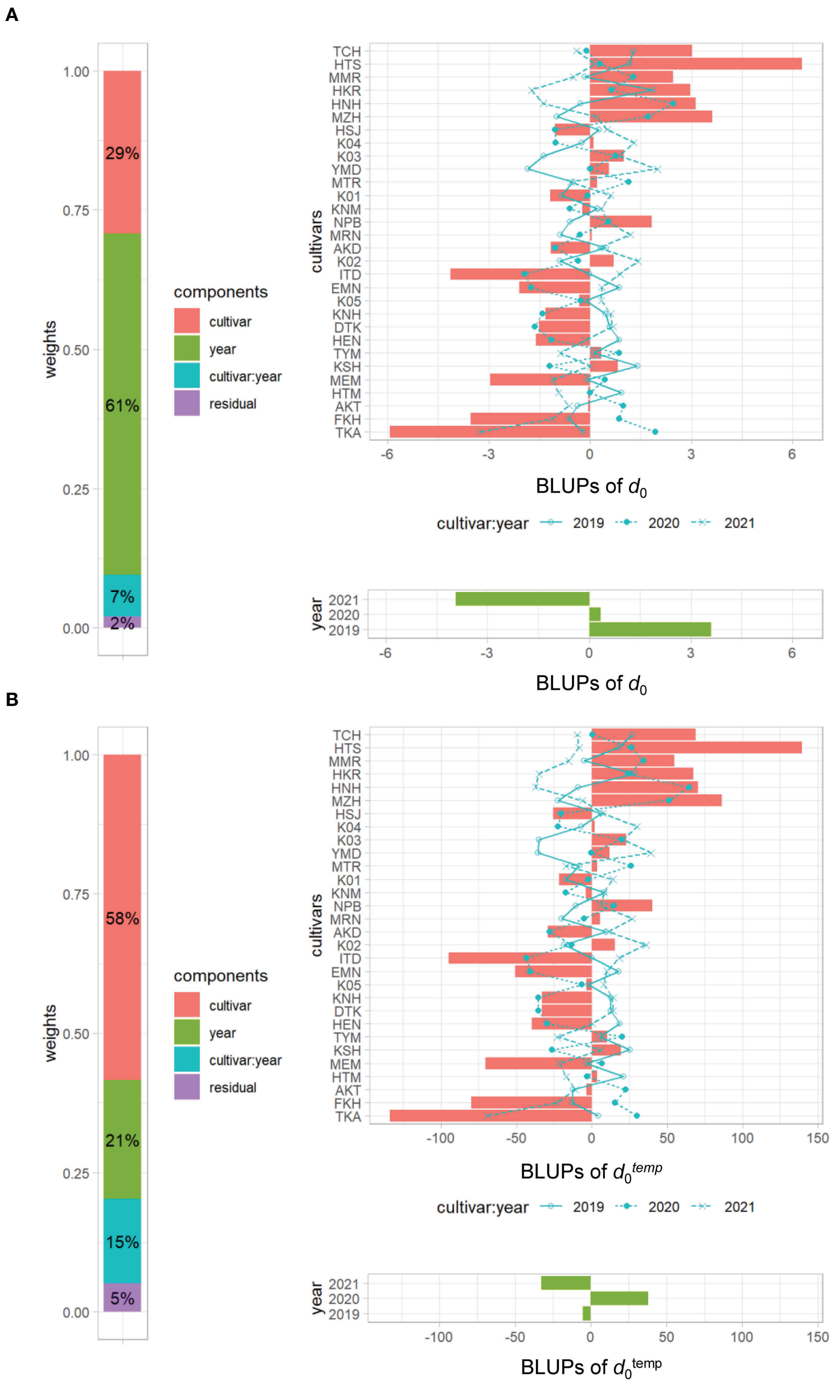

FIGURE 8
Visualization of the linear mixed effects model for **(A)** d_0 and **(B)** d_0^{temp}. Left, proportions of 4 variance components; right top, BLUPs of cultivar and cultivar × year interactions of 30 cultivars; right bottom, BLUPs of 3 years. Cultivars are sorted by d_1. The numbers in cultivar components indicate percentage heritability.

taken with a fixed camera every 5 min. Their method has the advantage of directly detecting panicles but is unsuitable for use by UAV because it requires a higher shooting frequency and a lower shooting altitude. On the other hand, our UAV method enabled us to predict DTH by focusing on the features of time-series CH changes in images taken weekly. Similarly, Zhao et al. (2021) proposed a method to predict wheat heading date by applying a logistic curve to growth data obtained by UAV, extracting the date when the second derivative is minimum. Our and their studies indicate that time-series models derived from UAV data can reveal developmental changes in crops in the field.

Our approach relies on applying a time-series model to CH data spanning crop growth from the vegetative stage to the reproductive stage in the field, and uses CH-related parameters as summary statistics of each trajectory. Time-series or longitudinal trait data have been modeled in several ways, including random regression with the Legendre polynomial. Although this polynomial can be incorporated into the expectation-maximization algorithm (Yang et al., 2006) and kernel methods (Campbell et al., 2018; Campbell et al., 2019), it is difficult to interpret the coefficients in the models. The coefficients of our CH-related parameters, on the other hand, have explicit meaning in the context of phenology and allow better interpretability.

The LME models decomposed each CH-related parameter into cultivar, year, and cultivar × year interaction effects. We considered year effect as an environmental effect and examined the influence of accumulated daily mean temperature on CH data. Our results indicate that d_0, a CH-related parameter in the vegetative stage, is sensitive to the accumulated daily mean temperature, but d_1, in the reproductive stage, is not. It is possible that DTH, associated with d_1, is regulated by daylength, but growth is affected by temperature. In terms of cultivar effect, we showed strong correlations between K and CL, and between d_1 and DTH, ADW, or SLW, suggesting the high contribution of these CH-related parameters to the prediction of each trait. This analysis can be useful in cultivar characterization. For example, in the case of cultivars "HKR" and "TYM", the BLUPs of ADW with d_1 deviated from linear (Figure 7C), probably reflecting their high yield and biomass.

CV by using cor and RMSE evaluated the robustness of the regression models to predict CL, DTH, ADW, GW, and SLW in an untested year and in untested cultivars. CV using cor estimates the magnitude of the correlation. In predicting CL, DTH, ADW, and SLW, values of cor by both CV methods were high. CV using RMSEs, which estimates the accuracy at predicting exact values of test data, can evaluate model robustness from the viewpoint of model variance, the phenomenon by which the prediction fluctuates with the training data, which results in variance of the predicted values (Bishop, 2006; Hastie et al., 2009). In predicting CL and DTH, RMSEs were similar by both types of CV methods. However, in predicting ADW and SLW, RMSEs of CV by year were about 1.5 times higher than those of CV by cultivar. Therefore, the prediction of ADW and SLW had model variance derived from year.

This study provides a novel method to predict traits that would usually be measured by hand from CH-related parameters extracted from aerial time-series data. The parameters did not prove useful in the prediction of GW, which manually measured data showed was not heritable. This indicates that GW is more sensitive to environment, suggesting the necessity of environmental data for the prediction of GW. We will examine new models for GW prediction from environmental data and other UAV-derived time-series data.

Data availability statement

The raw data supporting the conclusions of this article will be made available by the authors, without undue reservation.

Author contributions

ST, J-iY, and DO conceptualized the research; ST, TS, RI, YN, HT, AG, KM, SO, HM, YT, and TI performed the investigations; ST and TS developed the methodology; YN, AG, KM, SO, HM, YT, and TI provided the resources; ST, TS, RI, and YN curated data; HM, YT, TI, J-iY, and DO helped with funding acquisition; ST and DO wrote the manuscript; TS and JY reviewed and edited the manuscript. All authors contributed to the article and approved the submitted version.

Acknowledgments

We thank Hitoshi Koyano, Takeshi Hayashi, and Hiromi Kajiya-Kanegae for scientific discussion. This study was supported by grants from the Ministry of Agriculture, Forestry and Fisheries of Japan (Smart-breeding System for Innovative Agriculture; grant numbers BAC1003 and BAC2001).

Conflict of interest

The authors declare that the research was conducted in the absence of any commercial or financial relationships that could be construed as a potential conflict of interest.

Publisher's note

Supplementary material

The Supplementary Material for this article can be found online at: https://www.frontiersin.org/articles/10.3389/fpls.2022.998803/full#supplementary-material

SUPPLEMENTARY FIGURE 1
Trajectory of each CH time-series curve. The LME model calculated the cultivar effects of each CH-related parameter, which generated the cultivar-specific time-series curve ("Cultivar E").

SUPPLEMENTARY FIGURE 2
Correlation plot of parameters and traits in **(A)** 2020 and **(B)** 2021. Values are correlation coefficients (cor); circles present them by color and size.

SUPPLEMENTARY FIGURE 3
Visualization of the LME model for GW. Left, proportion of 4 variance components; right top, BLUPs of cultivar and cultivar × year interactions of 30 cultivars; right bottom, BLUPs of 3 years. Cultivars are sorted by d_1.

SUPPLEMENTARY FIGURE 4
Visualization of the LME model for ADW. Left, proportion of 4 variance components; right top, BLUPs of cultivar and cultivar × year interactions of 30 cultivars; right bottom, BLUPs of 3 years. Cultivars are sorted by d_1.

SUPPLEMENTARY FIGURE 5
Visualization of the LME model for SLW. Left, proportion of 4 variance components; right top, BLUPs of cultivar and cultivar × year interactions of 30 cultivars; right bottom, BLUPs of 3 years. Cultivars are sorted by d_1.

SUPPLEMENTARY FIGURE 6
Visualization of the linear mixed effects model for **(A)** d_1 and **(B)** d_1^{temp}. Left, proportion of 4 variance components; right top, BLUPs of cultivar and cultivar × year interactions of 30 cultivars; right bottom, BLUPs of 3 years. Cultivars are sorted by d_1.

References

Agata, A., Ando, K., Ota, S., Kojima, M., Takebayashi, Y., Takehara, S., et al. (2020). Diverse panicle architecture results from various combinations of *Prl5/GA20ox4* and *Pbl6/APO1* alleles. *Commun. Biol.* 3 (1), 1–17. doi: 10.1038/s42003-020-1036-8

Anderson, S. L., Murray, S. C., Malambo, L., Ratcliff, C., Popescu, S., Cope, D., et al. (2019). Prediction of maize grain yield before maturity using improved temporal height estimates of unmanned aerial systems. *Plant Phenome J.* 2 (1), 1–15. doi: 10.2135/tppj2019.02.0004

Bates, D., Machler, M., Bolker, B. M., and Walker, S. C. (2015). Fitting linear mixed-effects models using lme4. *J. Stat. Software* 67 (1), 1–48. doi: 10.18637/jss.v067.i01

Bishop, C. M. (2006). *Pattern recognition and machine learning* (New York: Springer).

Borra-Serrano, I., De Swaef, T., Quataert, P., Aper, J., Saleem, A., Saeys, W., et al. (2020). Closing the phenotyping gap: High resolution UAV time series for soybean growth analysis provides objective data from field trials. *Remote Sens.* 12 (10), 1644. doi: 10.3390/rs12101644

Campbell, M., Momen, M., Walia, H., and Morota, G. (2019). Leveraging breeding values obtained from random regression models for genetic inference of longitudinal traits. *Plant Genome* 12 (2), 180075. doi: 10.3835/plantgenome2018.10.0075

Campbell, M., Walia, H., and Morota, G. (2018). Utilizing random regression models for genomic prediction of a longitudinal trait derived from high-throughput phenotyping. *Plant Direct* 2 (9), e00080. doi: 10.1002/pld3.80

Chang, A. J., Jung, J. H., Maeda, M. M., and Landivar, J. (2017). Crop height monitoring with digital imagery from unmanned aerial system (UAS). *Comput. Electron. Agric.* 141, 232–237. doi: 10.1016/j.compag.2017.07.008

Desai, S. V., Balasubramanian, V. N., Fukatsu, T., Ninomiya, S., and Guo, W. (2019). Automatic estimation of heading date of paddy rice using deep learning. *Plant Methods* 15, 1–11. doi: 10.1186/s13007-019-0457-1

Di Gennaro, S. F., Toscano, P., Cinat, P., Berton, A., and Matese, A. (2019). A low-cost and unsupervised image recognition methodology for yield estimation in a vineyard. *Front. Plant Sci.* 10. doi: 10.3389/fpls.2019.00559

Duan, B., Fang, S. H., Zhu, R. S., Wu, X. T., Wang, S. Q., Gong, Y., et al. (2019). Remote estimation of rice yield with unmanned aerial vehicle (UAV) data and spectral mixture analysis. *Front. Plant Sci.* 10. doi: 10.3389/fpls.2019.00204

Endo-Higashi, N., and Izawa, T. (2011). Flowering time genes *Heading date 1* and *Early heading date 1* together control panicle development in rice. *Plant Cell Physiol.* 52 (6), 1083–1094. doi: 10.1093/pcp/pcr059

Fox, J., and Weisberg, S. (2019). *An r companion to applied regression* (Thousand Oaks, CA: Sage).

Furbank, R. T., and Tester, M. (2011). Phenomics - technologies to relieve the phenotyping bottleneck. *Trends Plant Sci.* 16 (12), 635–644. doi: 10.1016/j.tplants.2011.09.005

Gao, H., Jin, M. N., Zheng, X. M., Chen, J., Yuan, D. Y., Xin, Y. Y., et al. (2014). "*Days to heading 7*, a major quantitative locus determining photoperiod sensitivity and regional adaptation in rice," in *Proceedings of the National Academy of Sciences of the United States of America*, Vol. 111 (46), 18399–18399. doi: 10.1073/pnas.1422341112

Giorgino, T. (2009). Computing and visualizing dynamic time warping alignments in r: the dtw package. *J. Stat. Software* 31 (7), 1–24. doi: 10.18637/jss.v031.i07

Gong, Y., Duan, B., Fang, S. H., Zhu, R. S., Wu, X. T., Ma, Y., et al. (2018). Remote estimation of rapeseed yield with unmanned aerial vehicle (UAV) imaging and spectral mixture analysis. *Plant Methods* 14 (70), 1–14. doi: 10.1186/s13007-018-0338-z

Grados, D., Reynarfaje, X., and Schrevens, E. (2020). A methodological approach to assess canopy NDVI-based tomato dynamics under irrigation treatments. *Agric. Water Manage.* 240, 106208. doi: 10.1016/j.agwat.2020.106208

Hastie, T., Tibshirani, R., and Friedman, J. (2009). *The elements of statistical learning* (New York: Springer).

Horie, T., Nakagawa, H., Centeno, H., and Kropff, M. (1995). "The rice crop simulation model SIMRIW and its testing," in *Modeling the impact of climate change on rice production in Asia*. Eds. R. B. Matthews, M. J. Kropff, D. Bachelet and H. H. van Laar. (Los Banos, Philippines: International Rice Research Institute), 51–66.

Ikeda, M., Miura, K., Aya, K., Kitano, H., and Matsuoka, M. (2013). Genes offering the potential for designing yield-related traits in rice. *Curr. Opin. Plant Biol.* 16 (2), 213–220. doi: 10.1016/j.pbi.2013.02.002

Jiang, Z., Tu, H. F., Bai, B. W., Yang, C. H., Zhao, B. Q., Guo, Z. Y., et al. (2021). Combining UAV-RGB high-throughput field phenotyping and genome-wide association study to reveal genetic variation of rice germplasms in dynamic response to drought stress. *New Phytol.* 232 (1), 440–455. doi: 10.1111/nph.17580

Kronenberg, L., Yates, S., Boer, M. P., Kirchgessner, N., Walter, A., and Hund, A. (2021). Temperature response of wheat affects final height and the timing of stem elongation under field conditions. *J. Exp. Bot.* 72 (2), 700–717. doi: 10.1093/jxb/eraa471

Liang, T., Duan, B., Luo, X. Y., Ma, Y., Yuan, Z. Q., Zhu, R. S., et al. (2021). Identification of high nitrogen use efficiency phenotype in rice (Oryza sativa l.) through entire growth duration by unmanned aerial vehicle multispectral imagery. *Front. Plant Sci.* 12. doi: 10.3389/fpls.2021.740414

Liu, Y. Q., Wang, H. R., Jiang, Z. M., Wang, W., Xu, R. N., Wang, Q. H., et al. (2022). Genomic basis of geographical adaptation to soil nitrogen in rice. *Nature* 590 (7847). doi: 10.1038/s41586-022-05362-0

Maziarz, M. (2015). A review of the Granger-causality fallacy. *J. Philos. Economics* 8 (2), 86–105.

Muthayya, S., Sugimoto, J. D., Montgomery, S., and Maberly, G. F. (2014). An overview of global rice production, supply, trade, and consumption. *Tech. Considerations Rice Fortification Public Health* 1324, 7–14. doi: 10.1111/nyas.12540

Ninomiya, S. (2022). High-throughput field crop phenotyping: current status and challenges. *Breed. Sci.* 72 (1), 3–18. doi: 10.1270/jsbbs.21069

Nomura, T., Arakawa, N., Yamamoto, T., Ueda, T., Adachi, S., Yonemaru, J., et al. (2019). Next generation long-culm rice with superior lodging resistance and high grain yield, monster rice 1. *PLoS One* 14 (8), e0221424. doi: 10.1371/journal.pone.0221424

Ogawa, D., Sakamoto, T., Tsunematsu, H., Kanno, N., Nonoue, Y., and Yonemaru, J. I. (2021a). Haplotype analysis from unmanned aerial vehicle imagery of rice MAGIC population for the trait dissection of biomass and plant architecture. *J. Exp. Bot.* 72 (7), 2371–2382. doi: 10.1093/jxb/eraa605

Ogawa, D., Sakamoto, T., Tsunematsu, H., Kanno, N., Nonoue, Y., and Yonemaru, J. I. (2021b). Remote-sensing-combined haplotype analysis using multi-parental advanced generation inter-cross lines reveals phenology QTLs for canopy height in rice. *Front. Plant Sci.* 12. doi: 10.3389/fpls.2021.715184

Ogawa, D., Sakamoto, T., Tsunematsu, H., Yamamoto, T., Kanno, N., Nonoue, Y., et al. (2019). Surveillance of panicle positions by unmanned aerial vehicle to reveal morphological features of rice. *PLoS One* 14 (10), e0224386. doi: 10.1371/journal.pone.0224386

Paine, C. E. T., Marthews, T. R., Vogt, D. R., Purves, D., Rees, M., Hector, A., et al. (2012). How to fit nonlinear plant growth models and calculate growth rates: an update for ecologists. *Methods Ecol. Evol.* 3 (2), 245–256. doi: 10.1111/j.2041-210x.2011.00155.x

Peng, S. B., Khush, G. S., Virk, P., Tang, Q. Y., and Zou, Y. B. (2008). Progress in ideotype breeding to increase rice yield potential. *Field Crops Res.* 108 (1), 32–38. doi: 10.1016/j.fcr.2008.04.001

Poudel, P., Bello, N. M., Lollato, R. P., and Alderman, P. D. (2022). A hierarchical Bayesian approach to dynamic ordinary differential equations modeling for repeated measures data on wheat growth. *Field Crops Res.* 283, 108549. doi: 10.1016/j.fcr.2022.108549

R Core Team (2021). *R: A language and environment for statistical computing* (Vienna, Austria: R Foundation for Statistical Computing).

Sakamoto, T., Gitelson, A. A., and Arkebauer, T. J. (2013). MODIS-based corn grain yield estimation model incorporating crop phenology information. *Remote Sens. Environ.* 131, 215–231. doi: 10.1016/j.rse.2012.12.017

Sakamoto, T., Ogawa, D., Hiura, S., and Iwasaki, N. (2022). Alternative procedure to improve the positioning accuracy of orthomosaic images acquired with agisoft metashape and DJI P4 multispectral for crop growth observation. *Photogrammetric Eng. Remote Sens.* 88 (5), 323–332. doi: 10.14358/Pers.21-00064r2

Singh, D., Wang, X., Kumar, U., Gao, L. L., Noor, M., Imtiaz, M., et al. (2019). High-throughput phenotyping enabled genetic dissection of crop lodging in wheat. *Front. Plant Sci.* 10. doi: 10.3389/fpls.2019.00394

Song, X. J., Kuroha, T., Ayano, M., Furuta, T., Nagai, K., Komeda, N., et al. (2015). Rare allele of a previously unidentified histone H4 acetyltransferase enhances grain weight, yield, and plant biomass in rice. *Proc. Natl. Acad. Sci. U.S.A.*, 112, 76–81. doi: 10.1073/pnas.1421127112

Sugihara, G., May, R., Ye, H., Hsieh, C. H., Deyle, E., Fogarty, M., et al. (2012). Detecting causality in complex ecosystems. *Science* 338 (6106), 496–500. doi: 10.1126/science.1227079

Toda, Y., Kaga, A., Kajiya-Kanegae, H., Hattori, T., Yamaoka, S., Okamoto, M., et al. (2021). Genomic prediction modeling of soybean biomass using UAV-based remote sensing and longitudinal model parameters. *Plant Genome* 14 (3), e20157. doi: 10.1002/tpg2.20157

Wang, F. L., Wang, F. M., Zhang, Y., Hu, J. H., Huang, J. F., and Xie, J. K. (2019a). Rice yield estimation using parcel-level relative spectra variables from UAV-based hyperspectral imagery. *Front. Plant Sci.* 10. doi: 10.3389/fpls.2019.00453

Wang, X. Q., Zhang, R. Y., Song, W., Han, L., Liu, X. L., Sun, X., et al. (2019b). Dynamic plant height QTL revealed in maize through remote sensing phenotyping using a high-throughput unmanned aerial vehicle (UAV). *Sci. Rep.* 9, 1–10. doi: 10.1038/s41598-019-39448-z

Xing, Y., and Zhang, Q. (2010). Genetic and molecular bases of rice yield. *Annu. Rev. Plant Biol.* 61 (1), 421–442. doi: 10.1146/annurev-arplant-042809-112209

Yadav, S., Singh, U. M., Naik, S. M., Venkateshwarlu, C., Ramayya, P. J., Raman, K. A., et al. (2017). Molecular mapping of QTLs associated with lodging resistance in dry direct-seeded rice (*Oryza sativa* l.). *Front. Plant Sci.* 8. doi: 10.3389/fpls.2017.01431

Yang, G. J., Liu, J. G., Zhao, C. J., Li, Z. H., Huang, Y. B., Yu, H. Y., et al. (2017). Unmanned aerial vehicle remote sensing for field-based crop phenotyping: current status and perspectives. *Front. Plant Sci.* 8. doi: 10.3389/fpls.2017.01111

Yang, R. Q., Tian, Q., and Xu, S. Z. (2006). Mapping quantitative trait loci for longitudinal traits in line crosses. *Genetics* 173 (4), 2339–2356. doi: 10.1534/genetics.105.054775

Yue, J. B., Yang, G. J., Li, C. C., Li, Z. H., Wang, Y. J., Feng, H. K., et al. (2017). Estimation of winter wheat above-ground biomass using unmanned aerial vehicle-based snapshot hyperspectral sensor and crop height improved models. *Remote Sens.* 9 (7), 708. doi: 10.3390/rs9070708

Zhao, L. C., Guo, W., Wang, J., Wang, H. Z., Duan, Y. L., Wang, C., et al. (2021). An efficient method for estimating wheat heading dates using UAV images. *Remote Sens.* 13 (16), 3067. doi: 10.3390/rs13163067

Zhao, K., Tung, C.-W., Eizenga, G. C., Wright, M. H., Ali, M. L., Price, A. H., et al. (2011). Genome-wide association mapping reveals a rich genetic architecture of complex traits in oryza sativa. *Nat. Commun.* 2 (1), 467. doi: 10.1038/ncomms1467

Zhou, M., Ma, X., Wang, K. K., Cheng, T., Tian, Y. C., Wang, J., et al. (2020). Detection of phenology using an improved shape model on time-series vegetation index in wheat. *Comput. Electron. Agric.* 173, 105398. doi: 10.1016/j.compag.2020.105398

Frontiers in Plant Science

TYPE Methods
PUBLISHED 06 March 2023
DOI 10.3389/fpls.2023.1112973

EDITED BY
Sindhuja Sankaran,
Washington State University, United States

REVIEWED BY
Nelson Nazzicari,
Council for Agricultural and Economics Research (CREA), Italy
Max Feldman,
Agricultural Research Service (USDA), United States

*CORRESPONDENCE
Duke Pauli
dukepauli@arizona.edu

SPECIALTY SECTION
This article was submitted to Technical Advances in Plant Science, a section of the journal Frontiers in Plant Science

RECEIVED 30 November 2022
ACCEPTED 14 February 2023
PUBLISHED 06 March 2023

CITATION
Gonzalez EM, Zarei A, Hendler N, Simmons T, Zarei A, Demieville J, Strand R, Rozzi B, Calleja S, Ellingson H, Cosi M, Davey S, Lavelle DO, Truco MJ, Swetnam TL, Merchant N, Michelmore RW, Lyons E and Pauli D (2023) PhytoOracle: Scalable, modular phenomics data processing pipelines.
Front. Plant Sci. 14:1112973.
doi: 10.3389/fpls.2023.1112973

PhytoOracle: Scalable, modular phenomics data processing pipelines

Emmanuel M. Gonzalez[1], Ariyan Zarei[2], Nathanial Hendler[1], Travis Simmons[1], Arman Zarei[3], Jeffrey Demieville[1], Robert Strand[1], Bruno Rozzi[1], Sebastian Calleja[1], Holly Ellingson[4], Michele Cosi[1,5], Sean Davey[6], Dean O. Lavelle[7], Maria José Truco[7], Tyson L. Swetnam[5,8], Nirav Merchant[4,5], Richard W. Michelmore[7,9], Eric Lyons[1,4,5] and Duke Pauli[1,4]*

[1]School of Plant Sciences, University of Arizona, Tucson, AZ, United States, [2]Department of Computer Science, University of Arizona, Tucson, AZ, United States, [3]Department of Computer Engineering, Sharif University of Technology, Tehran, Iran, [4]Data Science Institute, University of Arizona, Tucson, AZ, United States, [5]BIO5 Institute, University of Arizona, Tucson, AZ, United States, [6]Department of Cellular and Molecular Medicine, University of Arizona, Tucson, AZ, United States, [7]The Genome and Biomedical Sciences Facility, University of California, Davis, Davis, CA, United States, [8]School of Natural Resources and the Environment, University of Arizona, Tucson, AZ, United States, [9]Department of Plant Sciences, University of California, Davis, Davis, CA, United States

As phenomics data volume and dimensionality increase due to advancements in sensor technology, there is an urgent need to develop and implement scalable data processing pipelines. Current phenomics data processing pipelines lack modularity, extensibility, and processing distribution across sensor modalities and phenotyping platforms. To address these challenges, we developed PhytoOracle (PO), a suite of modular, scalable pipelines for processing large volumes of field phenomics RGB, thermal, PSII chlorophyll fluorescence 2D images, and 3D point clouds. PhytoOracle aims to (*i*) improve data processing efficiency; (*ii*) provide an extensible, reproducible computing framework; and (*iii*) enable data fusion of multi-modal phenomics data. PhytoOracle integrates open-source distributed computing frameworks for parallel processing on high-performance computing, cloud, and local computing environments. Each pipeline component is available as a standalone container, providing transferability, extensibility, and reproducibility. The PO pipeline extracts and associates individual plant traits across sensor modalities and collection time points, representing a unique multi-system approach to addressing the genotype-phenotype gap. To date, PO supports lettuce and sorghum phenotypic trait extraction, with a goal of widening the range of supported species in the future. At the maximum number of cores tested in this study (1,024 cores), PO processing times were: 235 minutes for 9,270 RGB images (140.7 GB), 235 minutes for 9,270 thermal images (5.4 GB), and 13 minutes for 39,678 PSII images (86.2 GB). These processing times represent end-to-end processing, from raw data to fully processed numerical phenotypic trait data. Repeatability values of 0.39-0.95 (bounding area), 0.81-0.95 (axis-aligned bounding volume), 0.79-0.94 (oriented bounding volume), 0.83-0.95 (plant height), and 0.81-0.95

(number of points) were observed in Field Scanalyzer data. We also show the ability of PO to process drone data with a repeatability of 0.55-0.95 (bounding area).

KEYWORDS

phenomics, morphological phenotyping, physiological phenotyping, distributed computing, high performance computing, image analysis, point cloud analysis, data management

1 Introduction

The world population is expected to reach 10 billion people by 2050 with a projected 50% decrease in global freshwater resources (Searchinger et al., 2019; Gupta et al., 2020). Although existing crop improvement methods have maintained stable increases in crop yields, a continuation of these trends is not sustainable (Grassini et al., 2013). Crop improvement methods continue to rely on subjective, manually collected phenotype data. However, advances in sensor technology have contributed to the emergence of plant phenomics, the study of plant phenotypes, over the last decade (Andrade-Sanchez et al., 2014; Araus and Cairns, 2014; Pauli et al., 2016). Low-cost, user-friendly sensors now enable the collection of objective data at high throughput. The resulting data volumes are substantial and reveal bottlenecks in data processing, data management, and data storage. To date, a variety of phenomics bottlenecks related to data collection have been resolved, but computational bottlenecks related to data volume and velocity have been largely overlooked (Furbank and Tester, 2011). The volume and velocity of plant phenomics data collection makes it difficult to extract phenotypic trait data using existing software at the scale required for breeding programs and basic research. Therefore, addressing bottlenecks in computational throughput would enable the efficient processing of data and, as a result, the study of variation and plasticity of fine-scale traits at high temporal resolution. These high-resolution datasets may improve the elucidation of genetic components controlling agronomic and functional traits (Furbank and Tester, 2011).

Phenotyping, various marker technologies, and statistical methods have enabled the prediction of genotypic values and genetic mapping (Bernardo, 2020). The application of these methods allows for the dissection of the genetic and environmental components of phenotypic trait variance. Such studies require the measurement of quantitative traits that are often collected visually, in the case of observational data, and manually using handheld devices such as PAM fluorometers for chlorophyll fluorescence measurements, spectroradiometers for UV-VIS-NIR, protractors for leaf angle, rulers for plant height, and weight scales for yield. Visual and manual phenotyping are common due to having low initial investment costs, but these approaches lack throughput and reproducibility due to the labor required and subjectivity of measurements (Reynolds et al., 2019). Emerging technologies, such as automated high-throughput plant phenotyping platforms, often have higher initial investment costs compared to traditional phenotype collection, but this is quickly changing. High-throughput platforms are diverse, including robots, drones, phones, and carts (White and Conley, 2013; Bai et al., 2016; Thompson et al., 2018; Thorp et al., 2018; Yuan et al., 2018; Guo et al., 2020; Roth et al., 2020). Compared with traditional methods, these platforms improve data collection throughput, reduce subjectivity through varying levels of automation, and enable higher phenotyping resolution, referred to here as fine-scale phenotyping (Reynolds et al., 2019). The resolution provided by fine-scale phenotyping has enabled studies revealing genetic loci associated with drought resistance (Li et al., 2020), stomatal conductance (Prado et al., 2018), temporal salinity responses (Campbell et al., 2015), and panicle architecture (Rebolledo et al., 2016). Other studies have captured natural variation in photosynthetic efficiency (van Bezouw et al., 2019; Khan et al., 2020) as well as highlighted the feasibility of phenomics selection (Rincent et al., 2018; Parmley et al., 2019; Zhu et al., 2021) based on traits such as stay-green (Rebetzke et al., 2016) and spectral reflectance (Aguate et al., 2017; Lane et al., 2020).

The high temporal and spatial resolution of fine-scale phenotyping using automated plant phenotyping platforms provide new opportunities to study dynamic patterns in phenotype expression in response to varying conditions. For example, the phenotypic effects of induced variation can be assessed in mutant populations and natural variation in diversity panels (Khan et al., 2020), allowing for the detection of temporal fluctuations in trait expression and associations between morphological and physiological phenotypic traits. Future research and development in computational plant phenomics could help improve selection accuracy due, in part, to increasingly precise extraction of fine-scale phenotypes enabled by complementary analytical methods and algorithms. In plant phenomics, the level of extraction required to dissect agronomic and functional traits would involve processing large volumes of image, spectral, and point cloud raw data across thousands of plants and time points to identify unique, obscure patterns of morphophysiological responses to various environments. The integration of these fine scale phenomics datasets within and across projects would further expand our knowledge of traits and aid in hypothesis generation (Coppens et al., 2017).

The data volumes generated by biological sciences research outpace existing computing infrastructure (Chen et al., 2013; Qin et al., 2015;

Stephens et al., 2015; Sivarajah et al., 2017). Additionally, data variety within biological sciences research is widening due to the emergence of phenomics, particularly in plant science research (Furbank and Tester, 2011; Furbank et al., 2019; Harfouche et al., 2019). The increasing availability and diversity of modular, high-quality sensors mounted on automated phenotyping platforms has led to the collection of large volumes of various data types, including morphological and physiological traits (Coppens et al., 2017). These expanding data volumes pose new challenges related to computation, data integration, and data management – a problem that is likely to be exacerbated by continued improvements and widespread use of sensor technology (Kim et al., 2017). In information science, it has long been recognized that existing computational techniques are inadequate in dealing with big data, primarily due to bottlenecks in the extraction of information from large volumes of data and the associated bottlenecks of scalability and data management. The bottleneck in information extraction is actively being addressed through the development of methods including machine learning (ML) and artificial intelligence (AI), while parallel processing is addressing scalability (Chen et al., 2013; Jukić et al., 2015; Sivarajah et al., 2017). Although these methods improve scalability and information extraction, they do not address data management. Parallel computing systems (PCSs) are characterized by the co-location of input data and processing code, representation of processing in terms of data flows and transformations, and scalability. Collectively, these characteristics facilitate the processing of datasets once considered intractable due to previous limitations in computing (Kale, 2020). The required computational resources in PCSs are commonly data-dependent, meaning that each dataset requires a different set of computational resources. To increase processing efficiency and reduce computing costs, PCSs could allow users to tailor CPU/GPU, high-memory/high-processor nodes, and other computational resources to specific datasets. This capability may become increasingly important as expanding data volumes pose a higher cost if computational resources are used inefficiently.

For phenomics data to provide actionable genome-phenome insights in combination with other -omics data, large scale phenomics data must be processed in a scalable and reproducible manner, stored in publicly accessible data stores, and be interoperable with other data types (Coppens et al., 2017; Kim et al., 2017). To address these requisites, a variety of established resources can be leveraged. For example, data management systems such as the CyVerse Data Store, a cloud-based data management system built on the Integrated Rule-Oriented Data System (iRODS), provides storage and cross-platform command line interface (CLI) access to data (Goff et al., 2011; Merchant et al., 2016). Container technologies, such as Docker and Singularity, serve as stand-alone environments with required dependencies pre-installed by software developers for increased extensibility (Kurtzer et al., 2017). High performance computers (HPCs) supply numerous processors, dual in-line memory modules (DIMMs), internal disk, and networking ports to scale up processing tasks. Container technology and data management systems coupled with HPCs provide reproducible and scalable environments, respectively (Devisetty et al., 2016; Kurtzer et al., 2017). Large volume datasets further require advanced PCSs capable of leveraging thousands of computers or cluster nodes for parallel processing on local, cloud, and/or HPC compute resources. A suite of computing tools for deploying scalable applications known as the Cooperative Computing Tools (CCTools) consists of Makeflow and Work Queue, a language and computational resource management framework for distributed computing, respectively (Albrecht et al., 2012). When coordinated, the above-mentioned computational resources can improve the processing and management of raw data and enable large scale analyses of extracted phenomics data.

Several image analysis pipelines exist for morphological and physiological phenotype trait extraction including: ImageHarvest (Knecht et al., 2016); Greenotyper (Tausen et al., 2020); and PlantCV (Fahlgren et al., 2015; Gehan et al., 2017). Most of these software were developed for automated phenotyping platforms in controlled greenhouse environments and would require significant modification for processing field phenomics data due to variations in image illumination and the lack of spacing between plants in field settings. Although some pipelines integrate multi-processing or distributed computing capabilities, there is currently no published pipeline that integrates data management systems, container technologies, PCSs, and multi-system deployment within a single framework. Importantly, many existing image analysis software were not designed to enable customization of computational resources, a critical component for efficiently processing phenomics' expanding data volumes (Kale, 2020).

Here, we present PhytoOracle (PO), a suite of data processing pipelines for phenomics data processing. PhytoOracle combines data management systems, container technologies, distributed computing, and multi-system deployment into a single framework capable of processing phenomics data collected with RGB cameras (RGB), photosystem II chlorophyll fluorescence imagers (PSII), thermal cameras (thermal), structured-light laser scanners (3D). Each pipeline component is containerized and can be removed, replaced, rearranged, or deployed in isolation. PhytoOracle provides advanced PCS and automation capabilities for processing large phenomics datasets across HPC, cloud, and/or local computing environments. The PO suite organizes all processing tasks and computational resource specifications within a single YAML file, which enables customization of computational resources, processing modules, and data management systems. Users can target pipelines to the optimal computational resources whether that be high-memory, high-processor, and/or GPU nodes. The modularity and distributed computing capabilities of PO enable the efficient extraction of time series, individual plant phenotypic trait data from large, multi-modal phenomics datasets. The PCSs like PO improve data analysis and information processing, providing large scale data that can help answer questions that were previously intractable due to data volumes outpacing computing systems' capacities.

2 Materials and methods

2.1 Plant material

For this study, a panel of 241 lettuce genotypes were evaluated at the University of Arizona's Maricopa Agricultural Center (MAC) in Maricopa, Arizona (33°04'24.8" N 111°58'25.7" W). The soil type is a Casa Grande sandy loam (fine-loamy, mixed, superactive, hyperthermic Typic Natrargids). The panel consisted of two subpopulations of lettuce, a diversity panel (147 genotypes) that represented all major market classes of lettuce and a recombinant inbred line (RIL) mapping population (94 genotypes) developed from a cross of the cultivars "Iceberg" and "Grand Rapids." The population was organized in a randomized incomplete block design with three replications of both lettuce panels per irrigation treatment level with common checks used throughout the field. The borders around each irrigation treatment were of the cultivar "Green Towers." The three irrigation treatments were: well-watered (WW), level 1 drought (D1), and level 2 drought (D2) (Supplementary Figure 1). The WW treatment was defined as 24% volumetric soil water content (VSWC) which represents field capacity. To achieve the D1 and D2 conditions, 75% and 50% of the WW irrigation amounts were applied to the plots, respectively. Raised vegetable beds on 1.02 m row spacing were shaped to have a surface width of 0.56 m with two seed lines per bed spaced at 0.31 m; plots were 4.00 m in length. Experimental plots consisted of one of the individual seed lines per raised bed so that two genotypes were planted per raised bed.

The crop was established using sprinkler irrigation for the first 35 days before switching to subsurface drip irrigation. Buried within each bed, at a depth of 0.20 m, was pressure compensated drip tape (Model 06D63613.16-12, Netafim, Tel Aviv, Israel) supplying a constant 0.38 liters per hour of water. Soil moisture conditions were recorded using a neutron probe (Model 503, Campbell Pacific Nuclear, CPN, Martinez, CA, USA) with readings taken at depths of 10, 30, 50, 70, and 90 cm on a weekly basis. Neutron probe access tubes were distributed throughout the field to capture the VSWC across the different irrigation treatments over the growing period. Once plants were established and being irrigated with subsurface irrigation, plots were thinned to a density of 10 equidistant plants to facilitate individual plant phenotyping. After thinning, approximately 26,000 plants were present in the field, with each treatment containing approximately 9,000 plants. Standard cultivation practices and agronomic management for lettuce production in the Southwest were followed. A total of 1,472 plants, one from each plot within the WW and D2 treatments, were harvested and their fresh weights were recorded at the end of the growing period (2020-03-03).

2.2 Phenotyping platforms

The Field Scanalyzer (FS) is a ground-based, automated phenotyping platform that moves along rails that are 394.1 m in length running North-South with 28 m separation between the rails; the area covered by the FS is approximately 1.11 hectares. This area is split into two fields with scannable areas of 0.37 hectare for the north field and 0.46 hectare for the south field; for the purposes of the present research, only the south field was used (Figure 1A). The FS is equipped with a ventilated sensor box that holds multiple imagers and cameras including the following: Allied Vision Prosilica GT3300C stereo RGB cameras (RGB), LemnaTec photosystem II chlorophyll fluorescence prototype imager (PSII), FLIR A615 thermal camera (Thermal), pair of Fraunhofer structured-light laser scanners (3D), and two Headwall HyperSpec Inspector pushbroom hyperspectral imagers (visible to near infrared [VNIR] and short-wave infrared [SWIR]) (Figure 1B and Supplementary Table 1). The sensor box can move vertically from 0.43 to 6.26 m above ground level to accommodate varying scanning distance requirements for each sensor and to maintain a consistent distance from the instrument to plant canopy throughout the growing season.

The FS scanning scheme is controlled by custom operating scripts that specify the scan area, pattern, and scheduling for data collection of each sensor. These operating scripts are set to collect data on specific regions of the field, agricultural plots, or the entire field by the FS operator. The RGB, thermal, and PSII sensors collect binary (BIN) format images, while the 3D laser scanners collect depth and reflectance imagery from which point clouds are generated using manufacturer-provided software (Table 1). Each data collection is accompanied by metadata files in JavaScript Object Notation (JSON) format containing FS variable position, sensor fixed position (location of sensors within sensor box), preset scanning area, and timestamps. Positioning information is collected by a series of barcodes along the rails (X and Y axes) and a string encoder (Z axis) using a right-handed coordinate system (+X South-to-North, +Y East-to-West, and +Z 0.76 cm above soil upwards). Additionally, environmental sensors collect and log information on downwelling irradiance, photosynthetically active radiation, air temperature, relative humidity, brightness, ambient air carbon dioxide concentration, precipitation, and wind velocity and direction all at 5-second intervals in JSON format.

2.2.1 Data collection and management

For this study, the FS scanned the south field during the day and night throughout a growing season, collecting high-resolution, time-series images and point cloud data. The total number of RGB, thermal, PSII, and 3D data collections were 36, 36, 13, and 46, respectively. The RGB, thermal, and 3D laser scanner data collections covered the entire field while PSII data collections covered the center of each bed within a single treatment (Table 1). The FS total raw data sizes for each sensor were as follows: 0.12 terabytes (TBs) for thermal, 1.19 TBs for PSII, 3.20 TBs for RGB, and 8.77 TBs for 3D. Altogether, the FS data collections resulted in 13.36 TBs of raw data for the lettuce trial (Supplementary Figure 2).

In addition to FS data, drone (DR) flights were conducted over the same 0.46-hectare south field on a weekly basis using a DJI Phantom 4 Pro V2 (DJI, Nanshan, Shenzhen, China) and DroneDeploy software (v. 4.2.1; DroneDeploy, San Francisco, CA, USA) installed on an Apple iPad Mini 4 (Model #MK9P2LL/A;

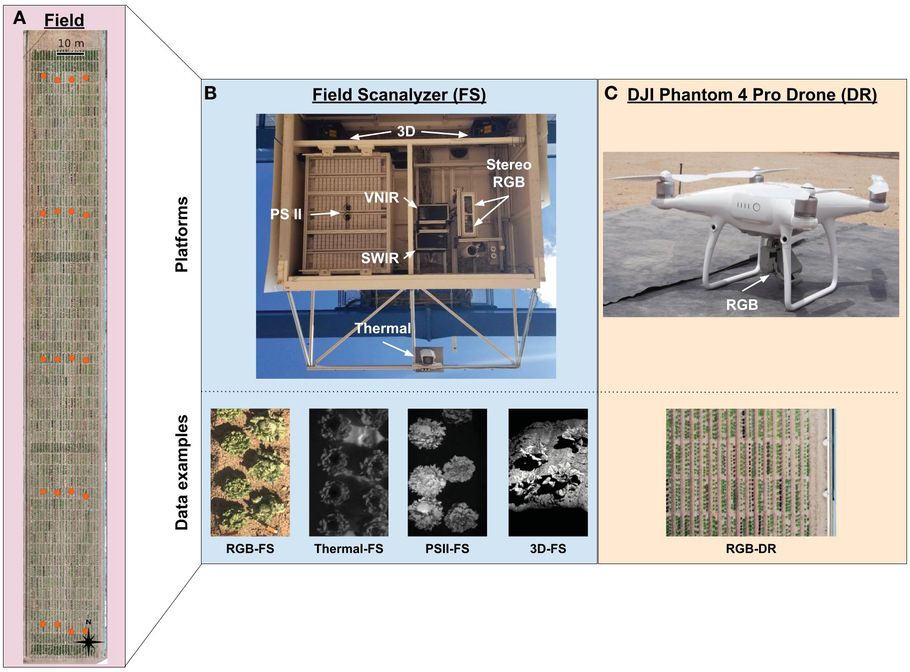

FIGURE 1
Overview of the Field Scanalyzer (FS) and DJI Phantom 4 Pro V2 drone (DR) phenotyping platforms, the components that make up each platform's sensor array and resulting data types. **(A)** An aerial photograph showing the area scanned by the FS which totals 0.63 hectare. Orange dots indicate the ground control point (GCPs) configuration, consisting of five sets of four GCPs running east to west for a total of 20 GCPs. (Top **B**) The FS sensor box contains a photosystem II (PSII) chlorophyll fluorescence imager, stereo RGB cameras, a thermal camera, two pushbroom hyperspectral imagers (visible near-infrared [VNIR] and shortwave near-infrared [SWIR]), a pair of structured-light laser scanners, and environmental sensors. (Botton **B**) Collected data included RGB, thermal, and PSII 2D image data and 3D point cloud data. (Top **C**) The DJI Phantom 4 Pro V2 drone (DR) was equipped with a 20-megapixel RGB camera and flown with automated flight mapping software at an altitude of 15 meters. (Bottom **C**) Collected data included RGB 2D image data.

Apple, Cupertino, CA, USA) (Figure 1). The flight mission settings were as follows: 15 m altitude, 80% front - 80% side overlaps, 0.41 cm/pixel ground sample distance, resulting in approximately 450 images per flight. In total, the DR collections resulted in 0.08 TBs of raw image data for the lettuce trial (Supplementary Figure 2). For a complete list of FS and DR data collection dates, refer to Supplementary Table 2.

2.2.2 Data management

The FS data collections were temporarily stored on a platform-mounted server and transferred to a cache server located at MAC. After a three-day retention period, each data collection was programmatically archived, producing a single ".tar.gz" archive file per data collection (one sensor's scan), and programmatically transferred to the CyVerse Data Store servers located in Tucson, AZ using Internet2. Each DR data collection was uploaded to the CyVerse Data Store manually. The DR and FS archives were placed in a publicly available location in the CyVerse Data Store for general use and CLI access during data processing (Goff et al., 2011) (see Data Availability Statement).

2.3 Parallel computing system

The PO pipelines require ML models for object detection and point cloud segmentation during data processing. Data must be

TABLE 1 Data collection summary for Field Scanalyzer (FS) and drone (DR) phenotyping platforms of data types supported by PhytoOracle.

Data	Collection time	Concurrent scan	Scanning area	Data type	Benchmark data size	Total scans	Total size
RGB-FS	5	Thermal-FS	Full field	BIN	140	36	2.91
Thermal-FS	5	RGB-FS	Full field	BIN	5	36	0.10
PSII-FS	5	–	Paired-plot center	BIN	80	18	1.00
3D-FS	9	–	Full field	PLY	350	32	8.37
RGB-DR	0.5	–	Full field	JPEG	3	19	0.059

The scanning area listed as full field encompassed the south portion of the field (0.63 hectare). Benchmark data size, gigabytes; total size, terabytes.
Collection duration (hours) represents the time from first data capture to final data capture.

annotated, models trained, and performance assessed before data processing can be performed. As such, a description of model training is presented before describing PO processing pipelines in detail. Together with a season-specific GeoJSON containing plot boundaries, a YAML file specifying processing tasks, and computational resources, PO can distribute tasks across processing nodes of an HPC.

2.3.1 Training and assessing performance of machine learning models

2.3.1.1 2D object detection

To prepare image data for manual annotation, RGB and thermal data collections were processed up to the plot clip step to produce plot clipped orthomosaics (Figure 2A, Steps 1-4). Thermal and RGB plot clipped orthomosaics were converted from georeferenced Tag Image File Format (GeoTIFF) to PNG format (GeoTIFFs are not supported by annotation tools). Thermal image pixel values were normalized to the range of 0 to 255 to enhance visible features for manual annotation. Heat map images, with each pixel representing height, were generated from 3D point cloud data. The scripts for each of these steps is publicly accessible (see Code Availability Statement).

To train object detection ML models for RGB and thermal imagery, a total of 2,000 images per sensor type were randomly selected for developing training data (see Code Availability Statement). A total of 200 3D-derived heatmap images were randomly generated to train object detection ML models. The RGB, thermal, and 3D-derived heatmap image datasets were uploaded to Labelbox (http://labelbox.com; Labelbox, San Francisco, CA, USA) and manually labeled with a single bounding box around each plant. All images were manually reviewed to ensure label quality. A JSON file containing label bounding box coordinates for all images in a dataset was programmatically converted to XML files, resulting in one XML

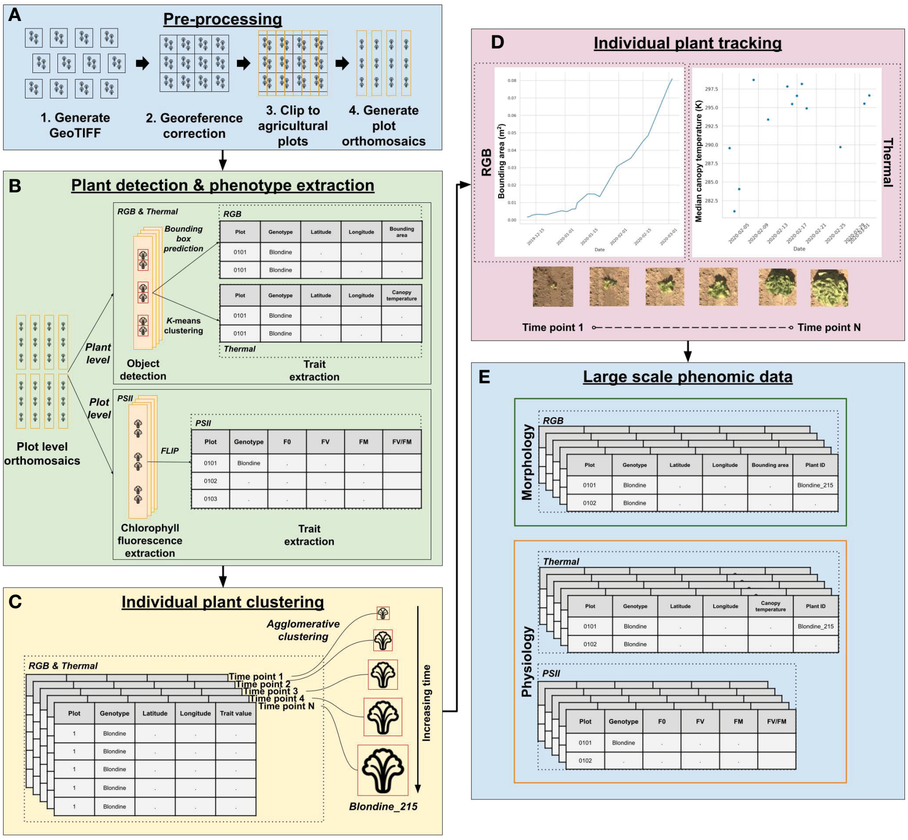

FIGURE 2
PhytoOracle two-dimensional (2D) image processing workflow. **(A)** The 2D pre-processing steps include the conversion of binary (BIN) files (RGB, thermal, PSII chlorophyll fluorescence) to GeoTIFF files, correction of georeferencing information within each GeoTIFF metadata using Megastitch for RGB and thermal data, clipping corrected GeoTIFF images to plots using a GeoJSON file with plot boundary information, and generation of plot level orthomosaics (Zarei et al., 2022). **(B)** RGB & thermal plot level orthomosaics are run through a Faster R-CNN detection model for plant detection and phenotype extraction; PSII images are run through FLIP for extraction of minimum (F_0) and maximum (F_M) fluorescence values, variable fluorescence (F_V), and maximum yield of primary photochemical efficiency (F_V/F_M). **(C)** Upon completion of data processing for a single experiment, individual plant detections from RGB and thermal data are associated over time using agglomerative clustering. Agglomerative clustering uses longitude and latitude to associate multiple plant observations, giving them a shared, unique plant identifier. **(D)** The growth and temperature of individual plants can be tracked and visualized using the unique plant identifier. A merged, full season RGB and thermal data file can then be combined with PSII (plot level) and 3D laser phenotype data using the unique plant/plot identifiers. **(E)** The results of PhytoOracle are time series datasets with plant geographical coordinates of the bounding box predictions and plant centers; bounding area (BA); median and mean canopy temperatures (MEDT and MEAT, respectively); plant height (PH), axis-aligned and oriented bounding box volumes (AABV and OBV, respectively), and convex hull volume (CHV); and plot level F_0, F_V, F_M, and F_V/F_M for each detected plant.

file per image (see Code Availability Statement). The RGB and thermal datasets were each randomly split into training, validation, and test sets (80%, 10%, and 10%, respectively). Transfer learning was employed to train a Faster R-CNN (region-based convolutional neural network) ResNet-50 FPN pre-trained model for RGB, thermal, and 3D-derived image datasets, separately, using the Detecto Python package (v. 1.2.1, http://github.com/alankbi/detecto) (Ren et al., 2017). The models for all data types were trained on a single label ("plant"). Training was performed on a HPC compute node with two AMD Zen2 48-core processors (AMD, Santa Clara, CA, USA), 512 GB of RAM, sixteen 32 GB memory DIMM, 2 TB SSD disk, and a V100S graphics processing unit (GPU) (NVIDIA, Santa Clara, CA, USA) with 32 GB memory. The selected setting of training parameters was 10 epochs, batch size of one, learning rate of 5 x 10^{-3}, 5 x 10^{-4} weight decay (L2 regularization), and step size of three.

Model performance was assessed by calculating Intersection over Union (IoU), recall, precision, and F1 scores for RGB, thermal, and 3D-derived test datasets. To determine model performance more finely across the developmental stages of lettuce, we assessed IoU of randomly selected plots over the course of the season for RGB and thermal models. The IoU values were calculated as follows:

$$IoU = \frac{|A \cap B|}{|A \cup B|} \tag{1}$$

where A is the area of the predicted bounding box, B is the area of the ground truth bounding box, and ∩ is the intersection and ∪ is the union of predicted and ground truth boxes. Detections with an IoU ≥ 0.5 were classified as true positives (TP, correctly detected plant), those with an IoU< 0.5 were classified as false positives (FP, plant is not present but detected), and detections with an IoU = 0 were classified as false negative (FN, plant is present but not detected). Recall, precision, and F1-score were calculated as follows:

$$Recall = \frac{TP}{TP + FN} \tag{2}$$

$$Precision = \frac{TP}{TP + FP} \tag{3}$$

$$F1 = 2 \cdot \frac{Precision \cdot Recall}{Precision + Recall} \tag{4}$$

2.3.1.2 3D segmentation

To train segmentation ML models, a random sample of individual plant point clouds were collected and labeled using a model-assisted labeling (MAL) approach (Model-assisted labeling (MAL); Huxohl and Kummert, 2021). The MAL script fit a plane to each point cloud and resulted in the labeling of two classes: plant and soil (see Code Availability Statement). The results were visualized, and segmentation errors were manually corrected, resulting in a total of 160 annotated individual plant point clouds; plant point clouds were randomly split into train, validation, and test sets (80%, 10%, and 10%, respectively). A Dynamic Graph CNN (DGCNN) was trained on a server with four AMD EPYC 7702 64-Core processors (AMD, Santa Clara, CA, USA), 1 TB of RAM, and three NVIDIA Tesla T4 GPUs (NVIDIA, Santa Clara, CA, USA) (Wang et al., 2019). The following training parameters were selected: 30 epochs, learning rate of 0.01, 1 x 10^{-4}, momentum of 0.9, and batch size of 32. The classes predicted by the DGCNN model for each point were compared with manually annotated data to collect TP, FP, TN, FN values, which were used to calculate the point-wise accuracy as follows:

$$Point - wise\ accuracy = \frac{TP + TN}{TP + FP + TN + FN} \tag{5}$$

2.3.2 Multimodal pipeline deployment

The processing instructions for PO data processing are defined in a Yet Another Markup Language (YAML) file (Ben-Kiki and Evans, 2001). The PO YAML template consists of four sections: "tags", "modules", "workload_manager", and "paths". The "tags" section allows users to define season-specific metadata for documentation purposes. The "modules" section is where users define their processing tasks by specifying the container to be used, the command to be run within the container, and the inputs and outputs. The user can select to run the workflow locally or remotely, that is using existing local cores or remote worker cores. The "workload_manager" key defines computational resource specifications required by pipeline worker nodes including the cores per worker, number of workers, and memory per core. The information provided within the "workload_manager" key is used to request jobs using the Slurm workload manager. Importantly, this allows users to customize the computing system to accommodate datasets of varying levels of processing scales and computational complexities. The "paths" section defines CyVerse Data Store paths for raw data download, including ML models to be used within the processing steps, and output data uploads. At the moment, only CyVerse Data Store paths are supported, but other storage providers can be supported with a few changes to the code. Users can specify their project-specific CyVerse Data Store paths or keep data locally without uploading it onto a data store. Users can select to use data transfer nodes, if running PO on HPC systems. Examples of YAML files for data processing of RGB, PSII, thermal, and 3D phenomics data of lettuce and sorghum are publicly available (see Code Availability Statement).

2.3.2.1 RGB processing pipeline

The full field RGB-FS datasets each consisted of 9,270 BIN files. Each image capture collected two BIN files, one from each RGB camera, and an associated JSON metadata file. Due to the physical arrangement of the stereo RGB cameras and the resulting high image overlap, only one image of each capture was used in this study. The RGB pipeline consisted of four containerized components (Supplementary Table 3 and Supplementary Figure 3). The first container converted BIN files to GeoTIFF images with approximate GPS bounding coordinates calculated from barcode positioning information contained within the JSON metadata file generated by the FS. The second container deployed MegaStitch, which is a software for efficient image stitching of large-scale image datasets (Zarei et al., 2022). Megastitch was run in a non-distributed manner as all images are required for the global optimization stitching method, which generated geometrically corrected GeoTIFFs. The third container clipped GeoTIFFs to plot boundaries using a GeoJSON file that delimits plots within the field. The fourth container deployed a Faster R-CNN model to detect individual plants within each plot-clipped orthomosaic, which output bounding box coordinates. Bounding box coordinates were converted from pixel coordinates to geographic coordinates using the geotransform information of each plot-clipped orthomosaic. All georeferencing was calculated in the World Geodetic System (WGS84) coordinate reference system (Lohmar, 1988). Longitude was calculated as follows:

$$\text{Longitude} = a \cdot x + b \cdot y + a \cdot 0.5 + b \cdot 0.5 + c \qquad (6)$$

where c is the upper left Easting coordinate of the image, a is the E-W pixel spacing, c is the rotation, and x and y are the bounding box image coordinates. Latitude was calculated as follows:

$$\text{Latitude} = d \cdot x + e \cdot y + d \cdot 0.5 + e \cdot 0.5 + f \qquad (7)$$

where d is the rotation, e is the N-S pixel spacing, f is the upper left Northing coordinate, and x and y are the bounding box image coordinates. The four geographical corner coordinates were converted to UTM coordinates and used to calculate plant bounding area (BA) as follows:

$$\text{Plant bounding area} = (SE_e - NW_e) \cdot (SE_n - NW_n) \qquad (8)$$

where SE_e is the southeast corner Easting coordinate of the image, NW_e is the northwest corner Easting coordinate, SE_n is the southeast corner Northing coordinate, and NW_n is the northwest corner Northing coordinate.

The RGB drone (RGB-DR) images from each data collection were processed using Pix4DMapper software (Pix4D S.A., Prilly, Switzerland). For each collection date, the "3D Maps" processing template was used, which generated an orthomosaic, point cloud, and depth maps. The "GCP/MTP Manager" interface was used to load GCP coordinates, co-align GCPs within images to known GCP coordinates, and confirm adequate placement of GCPs within the generated ray cloud. The resulting orthomosaics were processed using PO containers described above starting with the third container that clipped GeoTIFFs to plot boundaries.

2.3.2.2 Thermal processing pipeline

The full field thermal-FS datasets each consisted of 9,270 BIN files. Each image capture collected one BIN file and an associated JSON metadata file. Each pixel within a thermal-FS image represents an uncalibrated digital number (DN), a dimensionless value corresponding to the output of the detector's analog-digital conversion. The thermal pipeline consisted of four components (Supplementary Table 3 and Supplementary Figure 3). The first container converted BIN files to GeoTIFFs with approximate GPS bounding coordinates calculated from barcode positioning information contained within the JSON metadata file. Thermal calibration measurements were applied to each pixel, converting the DN value to Celsius. The second container deployed MegaStitch (Zarei et al., 2022) in a non-distributed manner, which generated geometrically corrected GeoTIFFs. The third container clipped GeoTIFFs to plot boundaries specified within a GeoJSON file. The fourth container deployed a Faster R-CNN model to detect individual plants within each plot clipped GeoTIFF, which outputted bounding box coordinates. To collect individual plant canopy temperatures, each predicted bounding box, representing a single plant, was programmatically cropped from plot level GeoTIFF orthomosaics and K-means clustering was used with $K = 3$ (MacQueen, 1967; Poblete-Echeverría et al., 2017). The median and mean canopy temperatures (MEDT and MEAT, respectively) were collected from the plant pixel clusters for each plant along with corresponding distribution statistics. A 10x10 pixel region of interest (ROI) centered within each plant detection was analyzed for median temperature, referred to as the ROI temperature. The longitude and latitude for each plant detection were calculated using Equations 6, 7 respectively for subsequent plant tracking and multi-modal data association.

2.3.2.3 PSII chlorophyll fluorescence processing pipeline

The PSII-FS datasets each consisted of 39,678 BIN files. Each data capture resulted in a 101-image stack over a 2-second interval along with an associated JSON metadata using a validated chlorophyll fluorescence imaging sensor (Herritt et al., 2020). Unlike RGB and thermal, these images captured the center of each plot instead of the full field. One image was captured shortly before LED light saturation, 50 images during the one-second saturating pulse of light, and 50 images after the pulse of light. The illuminating LED flash has a dominant wavelength in the range of 620-630 nm with an intensity of up to 7,000 µmol photosynthetically active radiation (PAR) at 70 cm from plant canopies. A modified version of the FLuorescence Imaging Pipeline (FLIP) software was used to extract plot level minimum fluorescence (F_0), variable fluorescence (F_V), maximum fluorescence (F_M), and maximum yield of primary photochemical efficiency (F_V/F_M) (Herritt et al., 2021). Modifications included two containers that converted BIN files to GeoTIFF images and clipped GeoTIFF images to plot boundaries using a GeoJSON file. The modification facilitated multi-modal data merging by acquiring geographical coordinates instead of pixel coordinates and enabled the integration of the software into the distributed computing framework. The PSII chlorophyll fluorescence pipeline consists of four components (Supplementary Table 3 and Supplementary Figure 3). The first container converted 101 BIN files to 101 GeoTIFFs with approximate GPS bounding coordinates calculated from barcode positioning information contained within the associated JSON metadata file. The second container clipped GeoTIFFs to plot boundaries specified within a GeoJSON file. The third container segmented each pixel within an image into one of five F_M experimentally derived contribution thresholds (Herritt et al., 2021). The fourth container applied the contribution thresholds to extract F_0 and F_M values for each image pixel, which were used to calculate F_V and F_V/F_M for each stack of 101 images were calculated as follows:

$$F_V = F_M - F_0 \qquad (9)$$

$$F_V/F_M = \frac{(F_M - F_0)}{F_M} \qquad (10)$$

2.3.2.4 3D laser scanner processing pipeline

The 3D-FS datasets consist of 320 pairs of PLY files. A pair of structured-light laser scanners captured depth and reflectance imagery for preprocessing to point clouds, resulting in two PLY files per data capture (640 total PLY files). Pre-processing of image data to point clouds was performed by the manufacturer-provided software PlyWorker before the data was transmitted offsite. The pair of scanners captured the 3D structure of plants from east and west directions, thereby minimizing occlusions. Each pair of PLY files had an associated JSON metadata file. The 3D laser scanner pipeline, utilizing the output of the PlyWorker software as an input, consisted of six components (Supplementary Table 3 and Supplementary Figure 3). The first container corrected the orientation and scale of the point cloud tiles and applied the RANSAC algorithm implemented in the Open3D Python package (v. 0.11.2) to find a simple translation (X and Y axes) to reduce misalignment (Fischler and Bolles, 1981; Choi et al., 2015; Zhou et al., 2018; Zhou et al., 2018) (Figure 3A). The second step co-aligned 3D point clouds to RGB-derived plant detections. A custom graphical user interface (GUI) was developed to download and visualize 3D point cloud data and RGB orthomosaic data on local computers after selecting a scan date to manually georeference (see Code Availability Statement). The purpose of this tool was to co-align 3D and RGB by identifying shared landmark features between 3D point clouds and RGB data. This co-alignment allows for individual plant clipping using RGB-derived plant detections (Figure 3B). Selected features included plot stakes, ground control point (GCP) lids, or distinguishable plants in the field. The GUI (*i*) shows the RGB orthomosaic region, (*ii*) prompts the user to select a landmark feature, (*iii)* displays the point cloud tile region that neighbors the selected landmark feature, (*iv*) prompts the user to select the corresponding landmark feature within the point cloud tile. This process is repeated until an adequate number of landmark features are selected (Figure 3C). After RGB and 3D data are co-registered by the user, an affine transformation is calculated from the correspondences between the selected landmark features. This transformation maps a point in the original space of the 3D point cloud into the space of the georeferenced RGB orthomosaic. This transformation was then saved to a JSON file. The third container applied the calculated transformation to the point cloud tiles, resulting in co-aligned, georeferenced point cloud tiles (Figure 3D). The fourth container used RGB-derived plant detections to clip individual plants from large point clouds tiles (Figure 3E). The fifth container merged multiple tiles containing the same plant using the iterative closest point (ICP) method implemented in the Open3D Python package (v. 0.11.2) (Besl and McKay, 1992; Zhou et al., 2018) (Figure 3F). The sixth container deployed a Faster R-CNN model to localize the focal plant on 3D-derived heat map images (Figure 3G). The seventh container segmented soil and plant points, which allowed for the isolation of plant points within each point cloud (Figure 3H). The eighth container removed any residual neighbor plant points using the DBSCAN clustering algorithm implemented in the Open3D Python package (v. 0.11.2) (Ester et al., 1996; Zhou et al., 2018) (Figure 3I). Lastly, the ninth container created persistence diagrams for a single plant point cloud using the Giotto-tda Python package (v. 0.5.1) (Tauzin et al., 2021), from which the following topological data analysis (TDA) values were collected: persistence entropy and amplitude (with distance functions of landscape, bottleneck, Wasserstein, Betti, silhouette, heat, and persistence image). Plant height (PH) was calculated as follows:

$$\text{Plant height} = Z_{max} - Z_{min} \tag{11}$$

Where Z_{max} is the maximum Z-axis plant point value and Z_{min} is the minimum Z-axis plant point value. In addition, the oriented bounding box volume (OBV), axis-aligned bounding box volume (AABV), and number of points (NP) were calculated using the Open3D Python package (v. 0.11.2) (Zhou et al., 2018) (Figure 3J).

2.3.3 Pipeline benchmarking

The RGB, thermal, and PSII pipelines were benchmarked using a single data collection for each sensor (Table 2). Benchmarking consisted of manager and worker compute nodes using CCTools Makeflow and Work Queue (Albrecht et al., 2012). A single HPC compute node equipped with two AMD Zen2 processors x 48 cores (94 total cores), 512 GB of RAM, sixteen 32 GB memory DIMM, and 2 TB SSD disk served as the manager node. Worker nodes, with the same computational resources mentioned above, were requested on which the command *work_queue_factory* (CCTools v. 7.1.12) was run to request one worker per core, resulting in a total of 94 Work Queue workers per node each with 5 GB of RAM. A Makeflow file containing information for each data input file was created programmatically using the PO automation script, which allowed for parallel distribution of tasks. In addition, this automation script provided a detailed workflow to each worker, specifying the processing step to be performed on each input file using Singularity v3.6 for running containers (Hunt and Larus, 2007; Kurtzer et al., 2017). A single task was performed per worker to allow for maximum distribution of tasks. Importantly, each pipeline differs in its definition of a single task input: RGB and thermal consist of one BIN file; 3D of two PLY files; and PSII of 101 BIN files, each with an associated metadata JSON file. Upon completion of assigned tasks, the manager compute node assigned additional tasks in queue to available workers. The benchmark dataset for RGB, thermal, and PSII sensors was processed over the following range of available workers: 1, 4, 8, 16, 32, 64, 128, 256, 512, and 1024. Each configuration was replicated three times, for a total of 30 benchmark data points per sensor. A log file with information on processing times and number of workers during processing was collected during processing.

2.3.4 Multi-modal data merging and association

To allow for identification of single plants throughout the growing period and across sensor modalities, individual plant detections from each collection date need to be grouped. Two phases were carried out to accomplish this: (*i*) data cleaning to remove any outliers and (*ii*) a series of sequential clustering steps to combine multi-modal datasets and enable individual plant tracking.

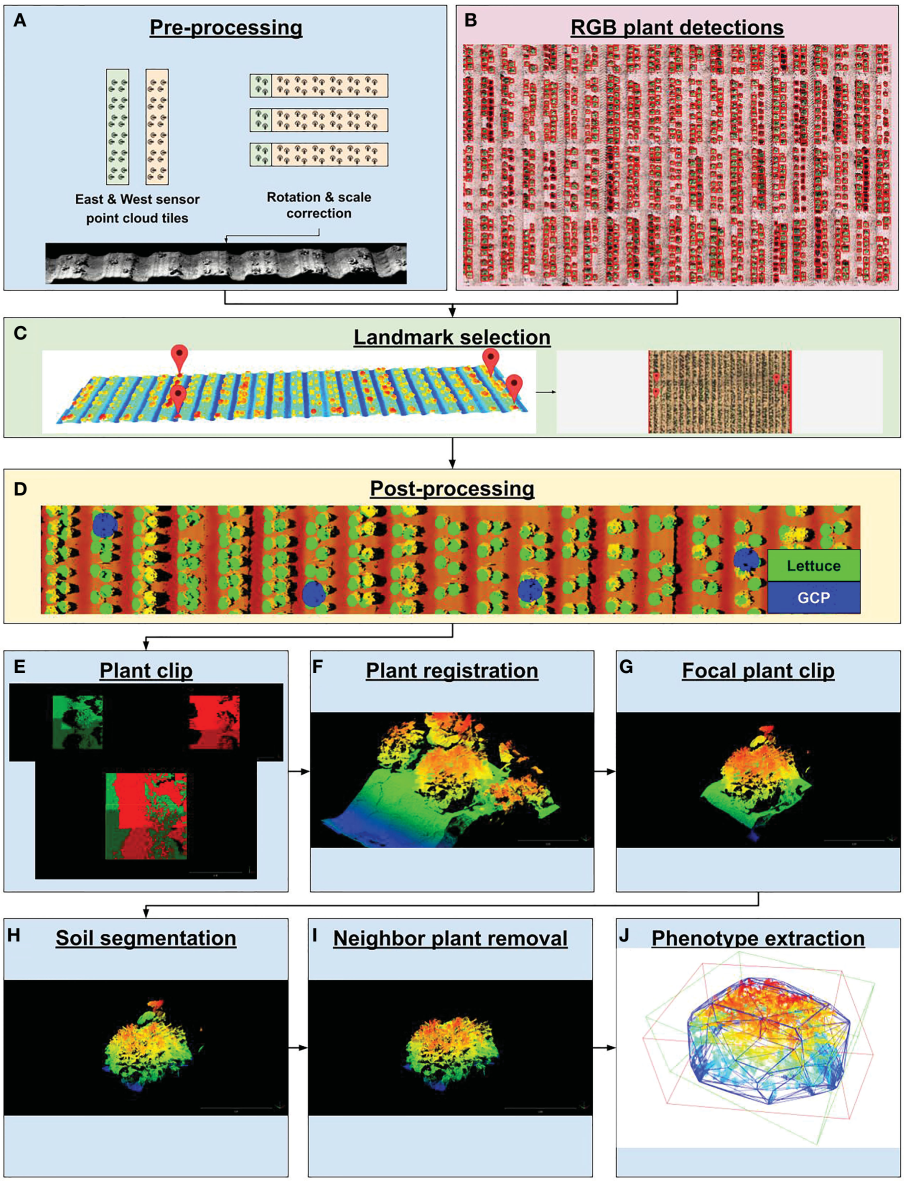

FIGURE 3
PhytoOracle 3D point cloud processing workflow. **(A)** Two raw point cloudscollected simultaneously were rotated, scaled, and georeferenced using positioning information from the Field Scanalyzer (FS) metadata file. **(B)** Time series plant detection from RGB data processing were coregistered with 3D point clouds by landmark selection. **(C)** Landmark selection involved selecting landmark features in point clouds and selecting the same landmark feature in RGB images. This step resulted in the co-registration of 3D point clouds with RGB data types. **(D)** Co-registered point clouds and plant detections were visualized by painting each plant detection with a green dot and ground control points (GCPs) with a blue dot. **(E)** Large point cloud tiles were clipped to known plant locations and **(F)** merged using the iterative closest point (ICP) algorithm. **(G)** Focal plants were further isolated by deploying a trained Faster R-CNN detection model to form a tight bounding box around the focal plant, eliminating neighboring plants. **(H)** Plant and soil points were segmented by deploying a trained DGCNN model on focal plant clips, resulting in a point cloud containing only plant points. **(I)** Residual neighbor plant points were removed by using the DBSCAN unsupervised clustering algorithm, resulting in a point cloud containing only focal plant points. **(J)** Focal plant point clouds were analyzed for morphometric phenotypes such as axis-aligned and oriented bounding box volumes (AABV and OBV, respectively) and convex hull volume (CHV), plant height (PH), and number of points (NP) as well as topological data analysis values calculated from persistence diagrams.

2.3.4.1 Removal of outlier plants

The first phase involved the removal of overlapping plants, hereafter termed outliers, which were the result of two or more plants growing in proximity and merging into what appeared to be a single plant. These outliers resulted in a single plant detection for this pair of plants, leading to errors in subsequent analyses. To remove these outliers, the field was manually assessed at the end of the season for outliers, which were manually marked with spray paint for easy visual identification in imagery collected right before harvesting. A GeoJSON vector layer containing a point for each outlier was manually created on QGIS (www.qgis.org) and the end-of-season orthomosaic containing the marked outlier canopies, which were used to identify these outliers in the multi-modal dataset.

TABLE 2 Information on each benchmarking dataset's collection date, size, and number of images.

Sensor	Date	Start time	End time	Elapsed time	Total size	Image count
RGB	03/03/2020	08:45	13:27	04:42	140.7	9270
Thermal	03/03/2020	08:45	13:27	04:42	5.4	9270
PSII	02/27/2020	19:58	00:37	04:39	86.2	39678
3D laser	03/01/2020	18:59	03:54	08:55	308.5	640

Elapsed time, HH : MM; total size, gigabytes.

2.3.4.2 Grouping plant phenotypes for individual plant tracking

The second phase involved the sequential clustering of phenotypic trait data from various sensor modalities. First, the full season RGB dataset was combined with the GeoJSON file containing manually marked outlier plant points generated in the first phase. Individual plant detections throughout the season were then clustered using agglomerative clustering, a form of hierarchical clustering algorithm implemented in the scikit-learn Python package v0.24.2 (Cox, 1957; Fisher, 1958; Ward, 1963; Pedregosa et al., 2011). Agglomerative clustering requires a threshold value, which was empirically derived based on having the lowest number of outliers grouped into a cluster and reduced fluctuations in growth curves. The optimal threshold value of 6 x 10^{-7} was used to maximize the number of clustered observations of a single plant and minimize the clustering of weeds and/or neighboring plants. The full season RGB plant detections were clustered using the empirically derived threshold value and results were assessed in QGIS. Each cluster, representing a single plant time series, was given a unique identifier denoting the plant's genotype and the clustering number ("genotype"_"cluster number"). All clusters containing an outlier point were given the label 'double' for the identification and exclusion of these data points from subsequent analyses (Supplementary Figure 4). Second, the resulting grouped RGB dataset was then clustered with the full season thermal data. Full season RGB and thermal outputs were merged using the same technique used during clustering of the full season RGB data. This clustering step resulted in a single dataset containing RGB and thermal data with a shared unique plant identified. Third, the merged dataset, containing clustered RGB and thermal phenotypic trait data, was combined with PSII chlorophyll fluorescence and 3D laser full season files using plot numbers and unique plant identifiers, respectively. The final output was a time-series, multi-modal phenotypic trait dataset at the individual plant level for RGB, thermal, and 3D phenotype data and plot level for PSII chlorophyll fluorescence phenotype data.

2.3.5 Analysis of extracted phenotypes

2.3.5.1 Assessing accuracy of plant detection across growing period

To assess plant detection performance, the median IoU throughout various time points were quantified for RGB and thermal image data. Canopy temperature extraction performance was assessed by manually extracting median canopy temperature across all time points of a random sample of 200 selected plots, with each plot containing a minimum of five plants across 19 collection dates resulting in 1,481 data points. We examined the correlation between manually extracted canopy temperature and pipeline extracted MEDT over an entire season for these selected plots. The BA extraction performance was evaluated by assessing its Pearson correlation with harvested, fresh weight biomass for each plot in the field trial. The median individual plant BA was used for correlation assessments. A similar assessment of correlation was conducted for AABV extraction.

2.3.5.2 Assessing grouping of plant phenotypes performance

The results from the proposed clustering association method were visualized across 200 plots as a vector layer overlaid on an end-of-season orthomosaic in which the outliers were marked. Each plot was imaged over 19 time points, resulting in a total of 3,800 images. If an identification was marked and the overlaid detection was identified as an outlier by the clustering algorithm, then the identification was classified as a true positive (TP). If the plant was marked and the overlaid detection was not determined to be an outlier by the clustering script, then the identification was classified as a false negative (FN). If the plant was not marked and the overlaid detection was determined to be an outlier by the clustering script, then the overlaid identification was classified as a false positive (FP). If the plant was not marked and the overlaid detection was determined to not be an outlier by the clustering script, then the overlaid identification was classified as a true negative (TN).

2.3.5.3 Statistical analysis and data visualization

The BA, NP, OBV, AABV, and PH phenotype trait data were analyzed after first checking for residual normality and error variance homogeneity at each collection event. For each trait, collection time points were analyzed separately using the lme4 package (Bates et al., 2015) in the R programming language (R Core Team, 2022). Spatial effects were modeled on a row and column basis. The following linear mixed model was fitted to trait data for the estimation of variance components:

$$y_{ijk} = \mu + g_i + irg_j + g \times irg_{ij} + rep(irg)_{kj} + row(rep \times irg)_{lkj} + col(rep \times irr)_{mkj} + \epsilon_{ijklm} \qquad (12)$$

where y_{ijk} is an individual phenotypic observation; μ is the overall mean; g_i is the effect of the i-th genotype; irg_j is the effect of the j-th irrigation treatment which was either WW, D1 or D2; $g \times$

irg_{ij} is the interaction effect between the i-th genotype and the j-th irrigation treatment; $rep(irg)_{kj}$ is the effect of the k-th replication nested within the j-th irrigation treatment; $row(rep \times irg)_{lkj}$ is the effect of the l-th plot grid row nested with k-th replication within the j-th irrigation treatment; $col(rep \times irr)_{mkj}$ is the effect of the m-th plot grid column nested within the k-th replication within the j-th irrigation treatment; and ε_{ijklm} is the residual effect. The variance component estimates from the full model were used to estimate repeatability (r) as follows:

$$r = \frac{\sigma_g^2}{\sigma_g^2 + \frac{\sigma_{gi}^2}{n_{irg}} + \frac{\sigma_{\in}^2}{n_{plot}}} \tag{13}$$

where σ_g^2 is the genotypic variance due to genotypes, σ_{gi}^2 is the estimated variance with the genotype-by-irrigation treatment variation, and $\sigma_{\in}^2$ and residual variances, respectively. The variable n_{irg} is the number of irrigation treatments in which each genotype was observed and n_{plot} is the number of plots in which the genotype was observed.

All plots presented in this study were generated using the Seaborn, Matplotlib, and Plotly Python packages using Python v3.9 (Hunter, 2007; Hossain, 2019; Waskom, 2021). Pearson correlations presented in the plots were calculated using the SciPy Python package (v0.15.1) (Virtanen et al., 2020).

3 Results

3.1 Environmental conditions during growing period

Weather data mean values for the growing season between 2019-11-13 and 2020-03-03 were: 10.72 °C air temperature, 61.88% relative humidity, 0.62 kPa vapor pressure deficit, and 0.55 MJ/m^2 solar radiation (Supplementary Figure 5). The irrigation treatments resulted in contrasting VSWC, with minimum values at 10 cm of 19.2, 14.7, and 12.8 in irrigation treatments WW, D1, and D2, respectively. At 30 cm, minimum values were 21.3, 21.5, and 17.2 for WW, D1, and D2, respectively (Supplementary Figure 1).

3.2 Model performance metrics

Faster R-CNN models were separately trained to identify single plants in RGB and thermal imagery, each trained and evaluated with 2,000 and 250 images, respectively. Performance was assessed without any prediction confidence threshold, resulting in 2,752 and 1,450 ‘plant’ class detections for RGB and thermal, respectively. The RGB detection model detected plants with a 0.98 recall, 0.93 precision, 0.96 F1-score, and 0.96 overall accuracy when tested on FS (RGB-FS) image data. The RGB detection model performance was further evaluated with a 400-image RGB-DR test dataset and resulted in 0.98 recall, 0.96 precision, 0.97 F1-score, and 0.97 overall accuracy. The thermal detection model performed better than the RGB detection model with a 0.98 recall, 0.99 precision, 0.98 F1-score, and 0.98 overall accuracy. A single DGCNN model was trained to segment points corresponding to plant and soil classes in point clouds containing a single plant. The model was trained and evaluated with 128 point clouds and 16 point clouds, respectively. The DGCNN model was assessed for point-wise accuracy using the test set, which was calculated at 0.98 (Table 3).

The median IoU was calculated separately for each distinct collection time point represented in a 250-image test set to assess temporal effects on bounding box accuracy. Overall, the median IoU was 0.84, 0.84, and 0.88 for RGB-FS, RGB-DR, and thermal-FS, respectively. The median IoU differed between dates, with an increasing trend as time progressed (Figure 4). This trend was stronger in the RGB-FS and RGB-DR data as these data were collected earlier in the season when plants were small with fewer distinguishable features as compared to thermal scans.

3.3 Validation of pipeline-extracted phenotypes and multimodal data association

Across the entire time series clustering test set, the agglomerative clustering method grouped plant detections into individual plant, time-series data with 0.99 recall, 0.93 precision, 0.96 F1-score, and 0.96 overall accuracy. The observed coefficient of determination (r^2) between individual plant fresh weight collected at harvest and pipeline-extracted 3D-FS AABV were 0.29 for Batavia ($p< 0.01$), 0.36 for Butterhead ($p< 0.0001$), 0.55 for Cutting/Crisp ($p< 0.0001$), 0.59 for Iceberg ($p< 0.0001$), 0.61 for Leaf ($p< 0.0001$), and 0.48 for Romaine ($p< 0.0001$) (Supplementary Figure 6). The observed coefficient of determination (r^2) between individual plant fresh weight and pipeline-extracted RGB-FS BA were 0.21 for Batavia ($p< 0.01$), 0.39 for Butterhead ($p< 0.0001$), 0.56 for Cutting/Crisp ($p< 0.0001$), 0.62 for Iceberg ($p< 0.0001$), 0.61 for Leaf ($p< 0.0001$), and 0.29 for Romaine ($p< 0.0001$) (Figure 5). The observed range of r^2 values between manually extracted and pipeline-extracted median canopy temperatures (MEDT) over 12 unique collection dates was 0.43-0.94 (Supplementary Figure 7). The overall observed r^2 was 0.95 when considering all dates ($p< 0.0001$) (Figure 6).

3.4 Collection and processing benchmarks

3.4.1 Field scanalyzer data collection

Benchmark datasets were collected using the FS, with varying operation times depending on the sensor. The file size of benchmark datasets ranged from 5.4 GB to 308.5 GB in size and consisted of 640 to 39,678 files. The data collection of RGB and thermal image data, which occurs simultaneously, took a total of 4 hours and 42 minutes to complete resulting in 9,270 raw images per sensor. The PSII data collection took 4 hours and 39 minutes, resulting in the largest raw file count (39, 678 images).

TABLE 3 Performance metrics for Faster R-CNN detection models for image processing of Field Scanalyzer RGB (RGB-FS), drone RGB (RGB-DR), and Field Scanalyzer thermal (Thermal-FS).

Model	Data	Type	Detections	TP	FP	FN	Recall	Precision	F1-score	Accuracy
A	RGB - DR	Detection	4356	4097	182	77	0.98	0.96	0.97	0.97
A	RGB - FS	Detection	2752	2519	178	54	0.98	0.93	0.96	0.96
B	Thermal - FS	Detection	1450	1404	10	36	0.98	0.99	0.98	0.98
C	3D - FS	Segmentation	–	–	–	–	–	–	–	0.98

FS, Field Scanalyzer; DR, drone; TP, true positive; FP, false positive; and FN, false negative. For the 3D-FS model, the accuracy reported is a point-wise accuracy collected across points within the test dataset, as such values for columns Total detections through F1-score are not presented.

3.4.2 PhytoOracle data processing

The RGB and PSII processing times saw the largest reduction from computational parallelization, at 61% and 95% respectively, at the maximum number of 1024 workers. Thermal processing time saw the smallest reduction of 22% at the maximum number of 1024 workers. At the maximum number of workers tested in this study, RGB and thermal each processed in 235 minutes and PSII in 13 minutes (Figure 7).

3.5 Phenotypic repeatability estimates at individual sampling events

The mean repeatability values for each pipeline are as follows: 0.86 (RGB-DR BA), 0.81 (RGB-FS BA), 0.90 (3D-FS AABV), 0.90 (3D-FS OBV), 0.90 (3D-FS PH), and 0.89 (3D-FS NP) (Table 4). In general, the repeatability of RGB and 3D phenotypic trait data had increasing trends over the growing season (Figure 8).

4 Discussion

The proliferation of phenomics technology has led to large data volumes that need to be processed. Challenges related to computation of phenomics big data reduce its full application and efficacy in providing actionable genome-phenome insights into plant morphophysiological traits. Among the significant bottlenecks in plant phenomics, we address the lack of scalable, modular processing pipelines capable of processing expanding data volumes to extract morphological and physiological phenotypic trait data. Although other pipelines, such as Image Harvest and Greenotyper, have considered and implemented distributed computing systems, these capabilities have not been fully developed for general use on HPC clusters or multiple node deployment. Instead, it is left to the user to undertake that implementation (Knecht et al., 2016; Tausen et al., 2020). The PhytoOracle suite of scalable, modular data processing pipelines addresses critical bottlenecks within plant phenomics including data diversity, scalability, reproducibility, and extensibility. PhytoOracle accomplishes this by integrating distributed computing, container technology, data management systems, and machine learning into a single suite of phenomics data processing pipelines.

4.1 PhytoOracle addresses neglected bottlenecks in phenomics data processing

The PO suite can process data from multiple sensors including RGB, thermal, and PSII chlorophyll fluorescence 2D image data and 3D point cloud data. Except for PSII chlorophyll fluorescence, PO data processing pipelines result in individual plant phenotypic trait data that can be associated using our agglomerative clustering approach (Figure 2 and Supplementary Figure 5). To date, the only other published pipeline capable of handling such diverse data types is PlantCV. However, PlantCV's approach to individual plant

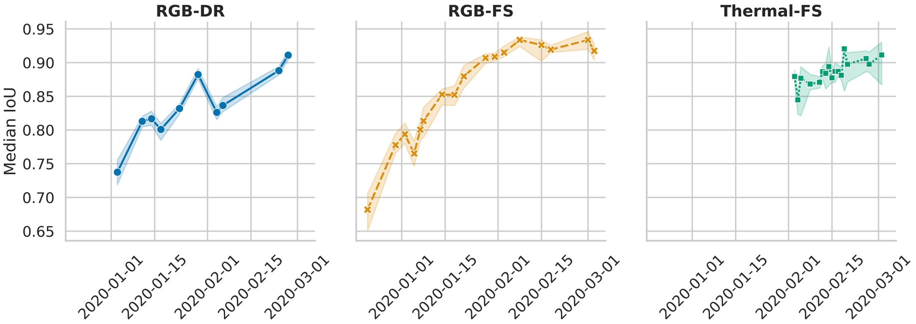

FIGURE 4
Change in median Intersection over Union (IoU) across the collection dates represented in RGB and thermal test data sets for the Field Scanalizer (FS) and Drone (DR) systems. Both RGB Field Scanalyzer scans (RGB-FS) and drone flights (RGB-DR), began earlier than thermal, allowing to capture the temporal effect of collection date, a proxy to plant size, on the median IoU. Error bands represent 95% confidence intervals around the median.

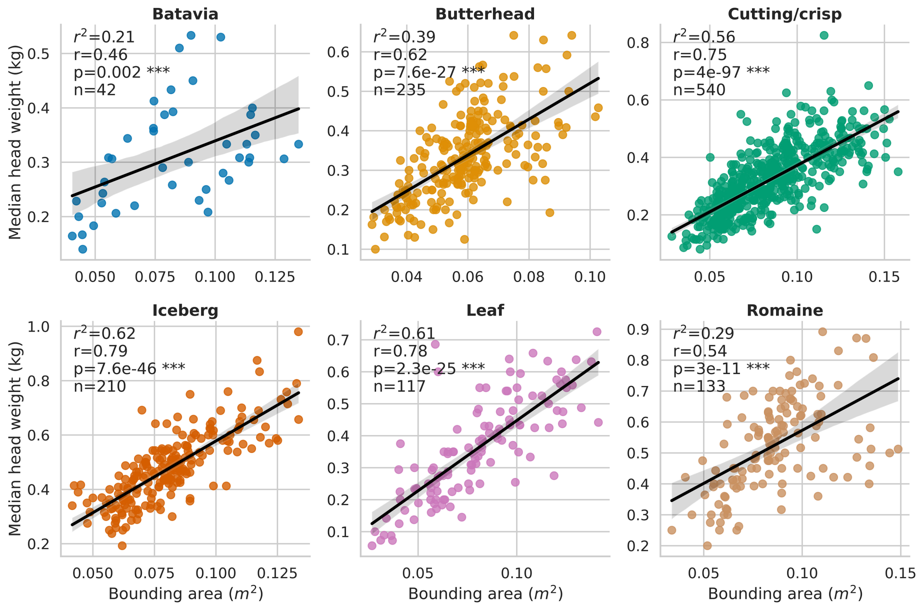

FIGURE 5
Correlation between individual plant fresh weight and pipeline-extracted bounding area (RGB-FS BA, m^2) for all plots in the field trial. Genotypes were grouped by horticultural type, resulting in 6 groups which are Batavia, Butterhead, Cutting/crisp, Iceberg, Leaf, and Romaine. *** = P value $\leq$ 0.001.

phenotyping does not translate well to field phenomics data (Fahlgren et al., 2015; Gehan et al., 2017). In field phenomics data, plant spacing creates challenges for individual plant phenotype extraction. The threshold-based contour approach used by much software, including PlantCV, works well in controlled environments, however, most imaging approaches outside of controlled environments often capture multiple overlapping plants under highly variable lighting conditions. These variable conditions make threshold-based contour approaches difficult to implement in processing field phenomics data. For this reason, PO leverages ML models that are better able to handle overlapping plants and variable lighting conditions.

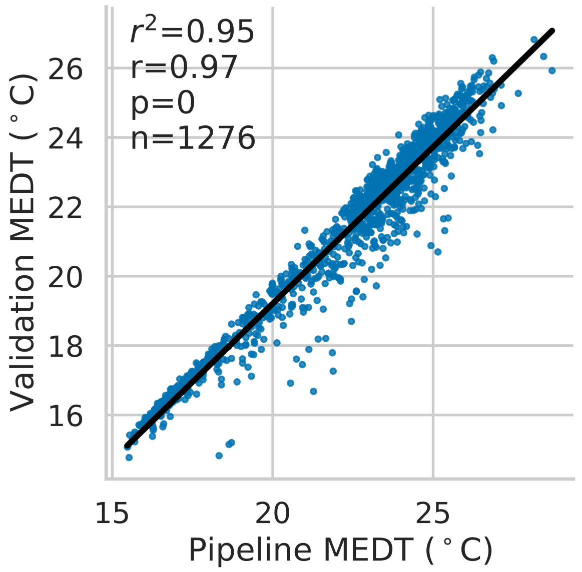

FIGURE 6
Correlation between validation and pipeline-extracted median canopy temperatures (MEDT). Each point represents an individual plant temperature collected at a single time point, with the complete dataset consisting of 12 distinct collection dates.

To resolve time series, multi-plant measurements to the individual plant level, PO leverages ML approaches, such as Faster R-CNN for object detection and DGCNN for point cloud segmentation. These ML models make PO robust and generalizable to other crops. For instance, if a user wants to process a new crop species, a model could be trained and deployed within PO, requiring little to no code development. Furthermore, the ML models presented here can be used by other researchers and/or new models can be trained using our labeled data and existing containers. PO also provides a general use solution to training of Faster R-CNN object detection models.

The PO suite provides scalability through a distributed computing framework leveraging the open-source CCTools' Makeflow and Work Queue software (Albrecht et al., 2012), which provides the language and computational resource management necessary to scale tasks beyond traditional job arrays and local computing resources. Importantly, this enables users to leverage dataset-specific resources across multiple computing environments during data processing, providing a path to maximize and optimize computational resource use. For example, the manager can be launched on an HPC cluster to ensure adequate storage space while workers could be launched on a lab workstation. The benefit of this approach is that computational resources beyond one computer or even one cluster can be leveraged to process thousands of tasks in parallel. Data

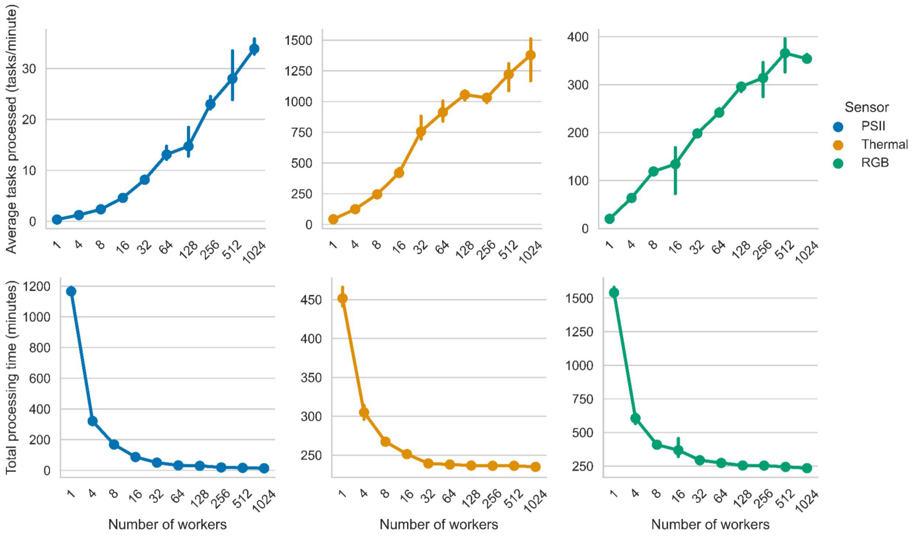

FIGURE 7
Average tasks process per minute and processing times for each PhytoOracle pipeline. (Top) Average tasks processed (tasks/minute) as a function of the number of worker cores. (Bottom) Total processing time (minutes) as a function of the number of workers (one CPU core per work). Available workers ranged from 1 to 1024 and the values represent the average of three runs with the same configuration. Error bars represent 95% confidence intervals.

processing on a single computer or server constrains users to locally available memory and processors, preventing scalability. On the other hand, distributed computing systems allow users to access processors and memory on remote nodes, allowing the system to, in theory, linearly scale the processing task at hand. The PO benchmarking focused on HPC nodes instead of local nodes and cloud-native options, such as XSEDE, due to those resources not having the storage space required to store raw and intermediate data. This is important, as it highlights that computational resources must consider not only CPU/GPU availability but also storage space capabilities as large-scale phenomics data processing results in many intermediate outputs that must be temporarily stored to serve as input to subsequent steps. In the end, these intermediate data can be deleted, but they must be able to be temporarily stored during data processing.

As data volumes increase, scalability will become a higher priority within research fields aimed at extracting relevant insights from big data (Chen et al., 2013; Sivarajah et al., 2017). However, this is likely to exacerbate existing network IO bottlenecks, which prevent linear scaling (Zhang et al., 2020). For example, the presented benchmarking information shows that although the average number of tasks completed continued to increase, the total processing time remained relatively stable after 32 workers. These results highlight limitations in scaling likely associated with network and data transfer bottlenecks. Improving the utilization of local, cloud, or HPC systems is a major concern and area of active research (Tanash et al., 2019). Generally, there are seemingly two options for further improvements to computational throughput: (*i*) identifying the optimal worker configurations per pipeline and/or (*ii*) moving pipelines closer to where the data are collected. An analysis of big data environments using Docker containers found that adding nodes (workers) beyond a certain threshold decreased performance due to an increase in the time for a network request to be sent and received (round trip time), which is similar to the results presented here (China Venkanna Varma et al., 2016). Moving pipelines closer to the data seems more feasible than finding optimal worker configurations as there may not be an optimal worker configuration to mitigate scaling plateaus until network bottlenecks are resolved. Network bandwidth is commonly associated with a lack of linear scaling; oftentimes, the

TABLE 4 Repeatability of pipeline extracted phenotypes collected from Field Scanalyzer (FS) and drone (DR) platforms.

Data	Trait	Min.	Mean	Max.
RGB-DR	Bounding area	0.55	0.86	0.95
RGB-FS	Bounding area	0.39	0.81	0.95
3D-FS	Axis-aligned bounding volume	0.81	0.90	0.95
3D-FS	Oriented bounding volume	0.79	0.90	0.94
3D-FS	Plant height	0.83	0.90	0.95
3D-FS	Number of points	0.81	0.89	0.95

Minimum, Min.; Max., Maximum.

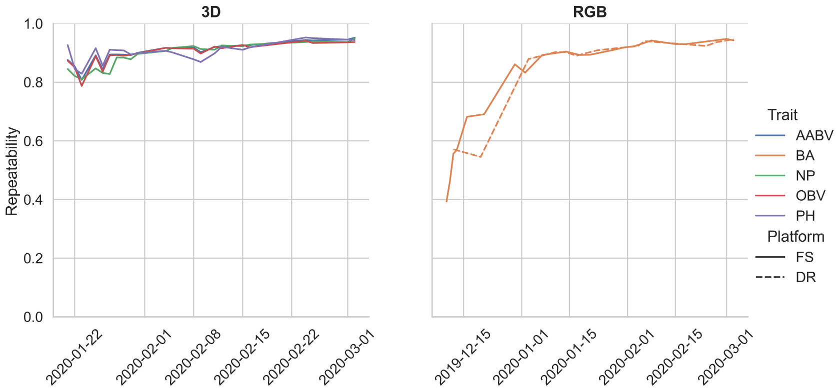

FIGURE 8
Repeatability estimates for pipeline-extracted phenotypes collected during a single year trial. Bounding area, BA; axis-aligned bounding box volume, AABV; number of points, NP; oriented bounding box volume, OBV; plant height, PH; Field Scanalyzer, FS; drone, DR.

processing phase is efficient and would theoretically allow for linear scaling, but the communication phase creates a bottleneck preventing linear scaling (Zhang et al., 2020). In our case, raw data is stored on the CyVerse Data Store due to its volume, velocity, and variety–making it intractable to keep these data on local servers for processing. This results in data being located "far" (CyVerse Data Store servers) from the processing pipeline (HPC), resulting in significant network requests that negatively impact data processing throughput. In the future, improvements to network capabilities may help to further improve processing efficiency.

The PO suite leverages container technology to ensure consistent, immutable data processing. Each PO processing step is containerized using Docker and deployable on HPC, cloud, and local computers on which either Docker or Singularity is installed. As opposed to running non-containerized processing code, containers ensure that each processing step is reproducible by controlling code versions and processing environments. Instead of users having to install over 40 Python packages to run PO, we provide containers that contain these libraries, significantly reducing the barrier to entry (Supplementary Table 4). Additionally, the PO automation script automatically downloads and configures CCTools, and requires no additional third-party Python packages. The only requirements for running PO are Singularity or Docker, iRODS, and Python. These tools are generally found on HPC clusters, except for iRODS which can be installed by system administrators.

The PO suite provides a general use framework through our automation script. Together with our suite of processing containers, this automation script automates the complexity of developing a PCSs, allowing users with little computer programming experience to leverage PO for processing their own phenomics data. The PO suite has four existing YAML files that can be customized by other researchers to process their own data. Users with advanced programming and command line experience can develop their own containers for data processing and integrate them into PO by including each container as a module within the YAML file, specifying the location of raw data on the CyVerse Data Store or local storage, and outlining the expected output files. The use of a generalizable automation script and a customizable YAML file makes it possible for users to run PO on various datasets, allowing researchers to spend more time on analysis than software development and data processing.

4.2 PhytoOracle extracts repeatable phenotypes from distinct platforms

The phenotypic trait data extracted from the FS and DR platforms align with values reported in the literature. Morphological trait repeatability values collected by the 3D-FS sensor align with the range of values reported in wheat (Deery et al., 2019; Walter et al., 2019; Deery et al., 2020). Similar values for 3D-FS phenotypes are reported here: 0.81-0.95 (AABV), 0.79-0.94 (OBV), 0.83-0.95 (PH), and 0.81-0.95 (NP). These values highlight the usefulness and applicability of PO for phenotype extraction, particularly morphological phenotypes. Additionally, similar trends of repeatability values were found across two distinct datasets: 0.55-0.95 and 0.39-0.95 for RGB-DR and RGB-FS platforms, respectively. These overlapping repeatability values demonstrate the applicability of PO to multiple platforms. The lower limit for repeatability for bounding area is an artifact of varying data collection start dates: 2019-12-10 for RGB-FS, 2019-12-12 for RGB-DR, and 2020-01-21 for 3D-FS. These earlier dates had a greater number of plants per plot, lowering the ability to accurately extract individual plant phenotypes due to overlap between plants. The number of plants per plot was reduced to approximately ten on 2020-01-16. Notably, all 3D-FS scans were collected after this date, resulting in a narrower range of repeatability values due to all scans being collected on well-spaced, lower overlap conditions.

Repeatability is dependent on data and algorithms, meaning that any system could result in similar repeatability values as PO. However, an important difference is the ease at which these other systems handle and process large volumes of data to extract those repeatable phenotypic trait values. The PO system addresses this issue by allowing the extraction of highly repeatable traits in a few hours. Furthermore, the PO system also provides extensibility. Each module within PO collectively results in highly repeatable phenotypic traits across sensor data types. Even in cases where scalability is not necessary, such as small volumes of drone data, these repeatability values across sensors and phenotyping platforms highlight PO's wide range of applications. The PO system, therefore, accelerates data processing of diverse data types from across phenotyping platforms, enabling the extraction of highly repeatable phenotypic traits that would otherwise have to be extracted using various, disparate systems or software that make it difficult to analyze, interpret, or combine resulting outputs.

4.3 PO enables deployment of future algorithms across species

The PO suite addresses challenges in scalability and modularity to improve plant phenomics data processing. This was accomplished by leveraging existing and emerging technologies to process large volumes of phenomics data in a scalable, modular manner. Existing technologies include container technology, distributed computing frameworks, and data management systems, while emerging technologies include ML models for trait extraction. By coordinating this combination of technologies, PO processes data in an automated, efficient manner across platforms and sensors. The PO suite serves as a tool for others in plant phenomics to leverage within their research groups. This is made possible by the diverse availability of processing containers which can be deployed on any system on which Docker, Singularity, iRODS, and CCTools are installed. The phenotypic data processed by PO show high repeatability values across platforms, indicating PO's utility within plant science and plant breeding programs. Importantly, the PO suite provides large volumes of phenotypic trait data that can be combined with other -omics data for applications in selection, dissection of functional and adaptive traits, and characterization of temporal patterns in trait expression (Supplementary Figure 8).

As ML methods mature, new models can be implemented within PO due to its customizable YAML configuration file. For example, models for leaf segmentation and extraction of traits such as leaf curling at scale, are the next steps of PO development. Furthermore, the training of these models is possible due to the large volume of intermediate data generated by pipelines like PO, which can serve as (*i*) training data for these next-generation models and (*ii*) as samples for model-generated data to further increase training data sizes. Containers that deploy these next-generation ML models could then be added to existing PO pipelines to provide organ-level phenotypic trait data that complements existing whole plant phenotypic trait data. This volume and diversity of phenomics data would enable fine-scale phenotyping at scale, which may uncover details on the temporal patterns in trait expression.

PhytoOracle addresses many phenomics bottlenecks, but there are outstanding bottlenecks such as enviromic capabilities and multi-species support. Enviromic capabilities are limited within PO, which are important to account for the environmental noise encountered in field phenomics data. In the future, PO pipelines will be further developed to output environmental data directly from the Field Scanalyzer and neighboring weather stations alongside phenotypic trait data. As this would be difficult to generalize across users, we decided not to provide this capability at present. However, the authors understand that these complementing data would enhance interpretability and interoperability of processed phenotypic trait data, therefore, we plan to support these capabilities in the future. Although the present study focuses on lettuce, PO has been refactored to process sorghum phenomics data with the same containers used to process lettuce phenomics data (Supplementary Figure 9). Further research and development will lead to the extraction of species-specific traits, and it is our goal to publish updates on these added functionalities.

5 Conclusion

The scalable, modular PhytoOracle data processing pipelines enable the extraction of large, time-series phenotypic trait data in an automated and reproducible manner, key factors required to process projected data volumes. The resulting traits extracted by PO from both FS and DR platforms show high repeatability, highlighting the usefulness of PO across phenotyping platforms. The intermediate processed data, such as individual plant point clouds, extracted by PO opens new opportunities to extract fine-scale phenotypes at multiple resolutions (plot, plant, and organ levels). Importantly, the PO pipelines can be refactored to process phenomics data from other crops species, as discussed here with sorghum phenomics data. In the future, these time-series datasets may provide biological insight into morphological and physiological responses to drought conditions at the individual plant level across multiple crop species. This information could enable new species-specific targets for genetic improvement based on time-series, fine-scale phenotypic trait data.

Code availability statement

The Python scripts used to prepare RGB training data can be accessed here: http://github.com/phytooracle/automation/blob/main/ml/collect_rgb_data.py. The Python script used to prepare thermal training data can be accessed here: http://github.com/phytooracle/automation/blob/main/ml/collect_flir_data.py. The Python script used to prepare 3D-derived images can be found here: http://github.com/phytooracle/3d_heat_map/blob/main/3d_heat_map.py. The code used to train object detection models can be found here: http://github.com/phytooracle/ezobde. Examples of YAML files used for data processing can be accessed here: http://github.com/phytooracle/automation/tree/main/yaml_files. The automation script and data processing repositories can be accessed at: http://github.com/phytooracle. Each PhytoOracle container built from data processing repositories can be accessed at: http://hub.docker.com/orgs/phytooracle. For a detailed description of each data processing3repository and associated container, refer to the Supplementary Material.

Data availability statement

The datasets presented in this study can be found in online repositories. The names of the repository/repositories and accession number(s) can be found below: https://datacommons.cyverse.org/browse/iplant/home/shared/phytooracle/season_10_lettuce_yr_2020.

Author contributions

EMG conceptualized and developed processing code, analyzed data, and wrote the manuscript. AriZ, NH, TS conceptualized and developed processing code, and contributed to manuscript preparation. ArmZ, MC conceptualized and developed processing code. JD conceptualized and developed code related to data acquisition, oversaw the Field Scanalyzer operation, and contributed to manuscript preparation. HE contributed to the development of processing code and oversaw data labeling. SD conceptualized and developed processing code related to data transfer from Field Scanalyzer to the CyVerse Data Store. DL and MT contributed to the field design, harvesting, and manual collection of ground truth data. RM, TLS, NM, and EL contributed to project conceptualization, overseeing processing code development, and manuscript preparation. DP conceptualized, designed, and oversaw all aspects of the project including acquisition of funds and manuscript preparation. All authors contributed to the review of the manuscript and all authors have read the manuscript.

Funding

This research was supported by the following grants: U.S. Department of Energy Biological and Environmental Research (DE-SC0020401) and Advanced Research Projects Agency - Energy OPEN (DE-AR0001101); National Science Foundation CyVerse project (DBI-1743442); National Science Foundation (IOS-2102120 and IOS-2023310); Cotton Incorporated (18-384, 20-720, and 21-830); and U.S. Department of Agriculture National Institute of Food and Agriculture Specialty Crop Research Initiative (2021-51181-35903).

Acknowledgments

The authors would like to thank numerous members of the Pauli and Michelmore labs for their help in field set up, field management, and harvesting; CyVerse staff including Reetu Tuteja, Ryan Bartelme, Edwin Skidmore, and Tony Edgin for their help in implementing iRODS; UArizona High Performance Computing staff including Blake Joyce, Sara Marie Willis, and Chris Reidy for their help in computation; Pauli lab undergraduate students including Victoria Ramsay, Brenda Esmeralda Jimenez, Hanna April Lawson, Hassan Alnamer, Jordan Pettiford, and Nimet Beyza Bozdag for their help in image annotation, workflow development, and data processing; the Fall 2019 Applied Concepts in Cyberinfrastructure class at the University of Arizona for their participation in the initial development of this project; and Benjamin Tovar, Douglas Thain, and the entire CCTools team for their support in implementing CCTools.

Conflict of interest

The authors declare that the research was conducted in the absence of any commercial or financial relationships that could be construed as a potential conflict of interest.

Publisher's note

Supplementary material

The Supplementary Material for this article can be found online at: https://www.frontiersin.org/articles/10.3389/fpls.2023.1112973/full#supplementary-material

References

Aguate, F. M., Trachsel, S., Pérez, L. G., Burgueño, J., Crossa, J., Balzarini, M., et al. (2017). Use of hyperspectral image data outperforms vegetation indices in prediction of maize yield. *Crop Sci.* 57, 2517–2524. doi: 10.2135/cropsci2017.01.0007

Albrecht, M., Donnelly, P., Bui, P., and Thain, D. (2012). Makeflow: a portable abstraction for data intensive computing on clusters, clouds, and grids. In *Proceedings of the 1st ACM SIGMOD Workshop on Scalable Workflow Execution Engines and Technologies* (Scottsdale, Arizona, USA: Association for Computing Machinery), 1–13. doi: 10.1145/2443416.2443417

Andrade-Sanchez, P., Gore, M. A., Heun, J. T., Thorp, K. R., Carmo-Silva, A. E., French, A. N., et al. (2014). Development and evaluation of a field-based high-throughput phenotyping platform. *Funct. Plant Biol.* 41, 68–79. doi: 10.1071/FP13126

Araus, J. L., and Cairns, J. E. (2014). Field high-throughput phenotyping: The new crop breeding frontier. *Trends Plant Sci.* 19, 52–61. doi: 10.1016/J.TPLANTS.2013.09.008

Model-assisted labeling (MAL). Available at: https://docs.labelbox.com/docs/model-assisted-labeling (Accessed July 3, 2022).

Total data volume worldwide 2010-2025 statista. Available at: https://www.statista.com/statistics/871513/worldwide-data-created/ (Accessed April 25, 2022).

Bai, G., Ge, Y., Hussain, W., Baenziger, P. S., and Graef, G. (2016). A multi-sensor system for high throughput field phenotyping in soybean and wheat breeding. *Comput. Electron. Agric.* 128, 181–192. doi: 10.1016/j.compag.2016.08.021

Bates, D., Mächler, M., Bolker, B., and Walker, S. (2015). Fitting linear mixed-effects models using lme4. *J. Stat. Software* 67, 1–48. doi: 10.18637/jss.v067.i01

Ben-Kiki, O., and Evans, C. (2001) *YAML ain't markup language (YAMLTM) version 1.2.* Available at: http://yaml.org/spec/1.2/spec.html (Accessed October 4, 2022).

Bernardo, R. (2020). Reinventing quantitative genetics for plant breeding: something old, something new, something borrowed, something BLUE. *Heredity* 125, 375–385. doi: 10.1038/s41437-020-0312-1

Besl, P. J., and McKay, N. D. (1992). A method for registration of 3-d shapes. *IEEE Trans. Pattern Anal. Mach. Intell.* 14, 239–256. doi: 10.1109/34.121791

Campbell, M. T., Knecht, A. C., Berger, B., Brien, C. J., Wang, D., and Walia, H. (2015). Integrating image-based phenomics and association analysis to dissect the genetic architecture of temporal salinity responses in rice. *Plant Physiol.* 168, 1476–1489. doi: 10.1104/pp.15.00450

Chen, J., Chen, Y., Du, X., Li, C., Lu, J., Zhao, S., et al. (2013). Big data challenge: a data management perspective. *Front. Comput. Sci.* 7, 157–164. doi: 10.1007/s11704-013-3903-7

China Venkanna Varma, P., Venkata Kalyan Chakravarthy, K., Valli Kumari, V., and Viswanadha Raju, S. (2016). Analysis of a network IO bottleneck in big data environments based on docker containers. *Big Data Res.* 3, 24–28. doi: 10.1016/j.bdr.2015.12.002

Choi, S., Zhou, Q. Y., and Koltun, V. (2015). "Robust reconstruction of indoor scenes," in *Proceedings of the IEEE Computer Society Conference on Computer Vision and Pattern Recognition*, (Boston, MA, USA: IEEE), 07-12-June-2015. 5556–5565. doi: 10.1109/CVPR.2015.7299195

Coppens, F., Wuyts, N., Inzé, D., and Dhondt, S. (2017). Unlocking the potential of plant phenotyping data through integration and data-driven approaches. *Curr. Opin. Syst. Biol.* 4, 58–63. doi: 10.1016/j.coisb.2017.07.002

Cox, D. R. (1957). Note on grouping. *J. Am. Stat. Assoc.* 52, 543–547. doi: 10.1080/01621459.1957.10501411

Deery, D. M., Rebetzke, G. J., Jimenez-Berni, J. A., Bovill, W. D., James, R. A., Condon, A. G., et al. (2019). Evaluation of the phenotypic repeatability of canopy temperature in wheat using continuous-terrestrial and airborne measurements. *Front. Plant Sci.* 10. doi: 10.3389/fpls.2019.00875

Deery, D. M., Rebetzke, G. J., Jimenez-Berni, J. A., Condon, A. G., Smith, D. J., Bechaz, K. M., et al. (2020). Ground-based LiDAR improves phenotypic repeatability of above-ground biomass and crop growth rate in wheat. *Plant Phenomics* 2020, 1–11. doi: 10.34133/2020/8329798

Devisetty, U. K., Kennedy, K., Sarando, P., Merchant, N., and Lyons, E. (2016). Bringing your tools to CyVerse discovery environment using docker. *F1000Research* 5 (1442), 1442. doi: 10.12688/F1000RESEARCH.8935.1

Ester, M., Kriegel, H.-P., and Xu, X. (1996). *A density-based algorithm for discovering clusters in Large spatial databases with noise*. 96(34), 26–231.

Fahlgren, N., Feldman, M., Gehan, M. A., Wilson, M. S., Shyu, C., Bryant, D. W., et al. (2015). A versatile phenotyping system and analytics platform reveals diverse temporal responses to water availability in setaria. *Mol. Plant* 8, 1520–1535. doi: 10.1016/j.molp.2015.06.005

Fischler, M. A., and Bolles, R. C. (1981). Random sample consensus: a paradigm for model fitting with applications to image analysis and automated cartography. *Communications of the ACM* 24(6), 381–395.

Fisher, W. D. (1958). On grouping for maximum homogeneity. *J. Am. Stat. Assoc.* 53, 789–798. doi: 10.1080/01621459.1958.10501479

Furbank, R. T., Jimenez-Berni, J. A., George-Jaeggli, B., Potgieter, A. B., and Deery, D. M. (2019). Field crop phenomics: enabling breeding for radiation use efficiency and biomass in cereal crops. *New Phytol.* 223, 1714–1727. doi: 10.1111/nph.15817

Furbank, R. T., and Tester, M. (2011). Phenomics - technologies to relieve the phenotyping bottleneck. *Trends Plant Sci.* 16, 635–644. doi: 10.1016/j.tplants.2011.09.005

Gehan, M. A., Fahlgren, N., Abbasi, A., Berry, J. C., Callen, S. T., Chavez, L., et al. (2017). PlantCV v2: Image analysis software for high-throughput plant phenotyping. *PeerJ* 5, e4088. doi: 10.7717/peerj.4088

Goff, S. A., Vaughn, M., McKay, S., Lyons, E., Stapleton, A. E., Gessler, D., et al. (2011). The iPlant collaborative: Cyberinfrastructure for plant biology. *Front. Plant Sci.* 2. doi: 10.3389/fpls.2011.00034

Grassini, P., Eskridge, K. M , and Cassman, K. G. (2013). Distinguishing between yield advances and yield plateaus in historical crop production trends. *Nat. Commun.* 4, (1), 2918. doi: 10.1038/ncomms3918

Guo, W., Fukano, Y., Noshita, K., and Ninomiya, S. (2020). Field-based individual plant phenotyping of herbaceous species by unmanned aerial vehicle. *Ecol. Evol.* 10, 12318–12326. doi: 10.1002/ece3.6861

Gupta, A., Rico-Medina, A., and Caño-Delgado, A. I. (2020). The physiology of plant responses to drought. *Science* 368, 266–269. doi: 10.1126/science.aaz7614

Harfouche, A. L., Jacobson, D. A., Kainer, D., Romero, J. C., Harfouche, A. H., Scarascia Mugnozza, G., et al. (2019). Accelerating climate resilient plant breeding by applying next-generation artificial intelligence. *Trends Biotechnol. Regul. Ed* 37, 1217–1235. doi: 10.1016/j.tibtech.2019.05.007

Herritt, M. T., Long, J. C., Roybal, M. D., Moller, D. C., Mockler, T. C., Pauli, D., et al. (2021). FLIP: FLuorescence imaging pipeline for field-based chlorophyll fluorescence images. *SoftwareX* 14, 100685. doi: 10.1016/j.softx.2021.100685

Herritt, M. T., Pauli, D., Mockler, T. C., and Thompson, A. L. (2020). Chlorophyll fluorescence imaging captures photochemical efficiency of grain sorghum (Sorghum bicolor) in a field setting. *Plant Methods* 16, 1-13. doi: 10.1186/s13007-020-00650-0

Hossain, S. (2019). Visualization of bioinformatics data with dash bio. *Proceedings of the 18th Python in Science Conference* (Austin, Texas: Proceedings of the Python in Science Conferences). 126–133. doi: 10.25080/Majora-7ddc1dd1-012

Hunt, G. C., and Larus, J. R. (2007). Singularity: rethinking the software stack. *ACM SIGOPS Oper. Syst. Rev.* 41, 37–49. doi: 10.1145/1243418.1243424

Hunter, J. D. (2007). Matplotlib: A 2D graphics environment. *Comput. Sci. Eng.* 9, 90–95. doi: 10.1109/MCSE.2007.55

Huxohl, T., and Kummert, F. (2021). Model-assisted labeling and self-training for label noise reduction in the detection of stains on images of laundry. *Mathematics* 9 (19), 1–16. doi: 10.3390/MATH9192498

Jukić, N., Sharma, A., Nestorov, S., and Jukić, B. (2015). Augmenting data warehouses with big data. *Inf. Syst. Manage.* 32, 200–209. doi: 10.1080/10580530.2015.1044338

Kale, V. (2020). *Parallel computing architectures and APIs: IoT big data stream processing* (New York: CRC Press). doi: 10.1201/9781351029223

Khan, N., Essemine, J., Hamdani, S., Qu, M., Lyu, M.-J. A., Perveen, S., et al. (2020). Natural variation in the fast phase of chlorophyll a fluorescence induction curve (OJIP) in a global rice minicore panel. *Photosynth. Res* 150, 137-158. doi: 10.1007/s11120-020-00794-z

Kim, S.-L., Solehati, N., Choi, I.-C., Kim, K.-H., and Kwon, T.-R. (2017). Data management for plant phenomics. *J. Plant Biol.* 60, 285–297. doi: 10.1007/s12374-017-0027-x

Knecht, A. C., Campbell, M. T., Caprez, A., Swanson, D. R., and Walia, H. (2016). Image harvest: An open-source platform for high-throughput plant image processing and analysis. *J. Exp. Bot.* 67, 3587–3599. doi: 10.1093/jxb/erw176

Kurtzer, G. M., Sochat, V., and Bauer, M. W. (2017). Singularity: Scientific containers for mobility of compute. *PloS One* 12, e0177459. doi: 10.1371/journal.pone.0177459

Lane, H. M., Murray, S. C., Montesinos-López, O. A., Montesinos-López, A., Crossa, J., Rooney, D. K., et al. (2020). Phenomic selection and prediction of maize grain yield from near-infrared reflectance spectroscopy of kernels. *Plant Phenome J.* 3(1), e20002. doi: 10.1002/ppj2.20002

Li, B., Chen, L., Sun, W., Wu, D., Wang, M., Yu, Y., et al. (2020). Phenomics-based GWAS analysis reveals the genetic architecture for drought resistance in cotton. *Plant Biotechnol. J.* 18, 2533–2544. doi: 10.1111/pbi.13431

Lohmar, F. J. (1988). World geodetic system 1984 — geodetic reference system of GPS orbits. *GPS-Techniques Appl. to Geodesy Survey.*, 476–486. doi: 10.1007/BFB0011360

MacQueen, J. (1967). Some methods for classification and analysis of multivariate observations. *Proc. Fifth Berkeley Symp. Math. Stat. Probab.* 19, 281–297.

Merchant, N., Lyons, E., Goff, S., Vaughn, M., Ware, D., Micklos, D., et al. (2016). The iPlant collaborative: Cyberinfrastructure for enabling data to discovery for the life sciences. *PloS Biol.* 14 (1), e1002342. doi: 10.1371/JOURNAL.PBIO.1002342

Parmley, K., Nagasubramanian, K., Sarkar, S., Ganapathysubramanian, B., and Singh, A. K. (2019). Development of optimized phenomic predictors for efficient plant breeding decisions using phenomic-assisted selection in soybean. *Plant Phenomics* 2019, 1–15. doi: 10.34133/2019/5809404

Pauli, D., Chapman, S. C., Bart, R., Topp, C. N., Lawrence-Dill, C. J., Poland, J., et al. (2016). The quest for understanding phenotypic variation *via* integrated approaches in the field environment. *Plant Physiol.* 172, 622–634. doi: 10.1104/PP.16.00592

Pedregosa, F., Varoquaux, G., Gramfort, A., Michel, V., Thirion, B., Grisel, O., et al. (2011). Scikit-learn: Machine learning in Python. *J. Mach. Learn. Res.* 12, 2825–2830.

Poblete-Echeverría, C., Olmedo, G., Ingram, B., and Bardeen, M. (2017). Detection and segmentation of vine canopy in ultra-high spatial resolution RGB imagery obtained from unmanned aerial vehicle (UAV): A case study in a commercial vineyard. *Remote Sens.* 9, 268. doi: 10.3390/rs9030268

Prado, S. A., Cabrera-Bosquet, L., Grau, A., Coupel-Ledru, A., Millet, E. J., Welcker, C., et al. (2018). Phenomics allows identification of genomic regions affecting maize stomatal conductance with conditional effects of water deficit and evaporative demand. *Plant Cell Environ.* 41, 314–326. doi: 10.1111/pce.13083

Qin, Y., Yalamanchili, H. K., Qin, J., Yan, B., and Wang, J. (2015). The current status and challenges in computational analysis of genomic big data. *Big Data Res.* 2, 12–18. doi: 10.1016/j.bdr.2015.02.005

R Core Team (2022) *R: The r project for statistical computing*. Available at: https://www.r-project.org/ (Accessed October 4, 2022).

Rebetzke, G. J., Jimenez-Berni, J. A., Bovill, W. D., Deery, D. M., and James, R. A. (2016). High-throughput phenotyping technologies allow accurate selection of stay-green. *J. Exp. Bot.* 67, 4919–4924. doi: 10.1093/jxb/erw301

Rebolledo, M. C., Peña, A. L., Duitama, J., Cruz, D. F., Dingkuhn, M., Grenier, C., et al. (2016). Combining image analysis, genome wide association studies and different field trials to reveal stable genetic regions related to panicle architecture and the number of spikelets per panicle in rice. *Front. Plant Sci.* 7. doi: 10.3389/fpls.2016.01384

Ren, S., He, K., Girshick, R., and Sun, J. (2017). Faster r-CNN: Towards real-time object detection with region proposal networks. *IEEE Trans. Pattern Anal. Mach. Intell.* 39, 1137–1149. doi: 10.1109/TPAMI.2016.2577031

Reynolds, D., Baret, F., Welcker, C., Bostrom, A., Ball, J., Cellini, F., et al. (2019). What is cost-efficient phenotyping? optimizing costs for different scenarios. *Plant Sci.* 282, 14–22. doi: 10.1016/j.plantsci.2018.06.015

Rincent, R., Charpentier, J.-P., Faivre-Rampant, P., Paux, E., Le Gouis, J., Bastien, C., et al. (2018). Phenomic selection is a low-cost and high-throughput method based on indirect predictions: Proof of concept on wheat and poplar. *G3 GenesGenomesGenetics* 8, 3961–3972. doi: 10.1534/g3.118.200760

Roth, L., Camenzind, M., Aasen, H., Kronenberg, L., Barendregt, C., Camp, K. H., et al. (2020). Repeated multiview imaging for estimating seedling tiller counts of wheat genotypes using drones. *Plant Phenomics* 2020, 1-20. doi: 10.34133/2020/3729715

Searchinger, T., Waite, R., Hanson, C., Ranganathan, J., Dumas, P., Matthews, E., et al. (2019) *World resources report: Creating a sustainable food future*. Available at: www.SustainableFoodFuture.org.

Sivarajah, U., Kamal, M. M., Irani, Z., and Weerakkody, V. (2017). Critical analysis of big data challenges and analytical methods. *J. Bus. Res.* 70, 263–286. doi: 10.1016/j.jbusres.2016.08.001

Stephens, Z. D., Lee, S. Y., Faghri, F., Campbell, R. H., Zhai, C., Efron, M. J., et al. (2015). Big data: Astronomical or genomical? *PloS Biol.* 13, e1002195. doi: 10.1371/journal.pbio.1002195

Tanash, M., Dunn, B., Andresen, D., Hsu, W., Yang, H., and Okanlawon, A. (2019). Improving HPC system performance by predicting job resources *via* supervised machine learning. *PEARC19* 2019, 69. doi: 10.1145/3332186.3333041. Rise Mach. Learn. July 28-August 1 2019 Chic. Ill. Pract. Exp. Adv. Res. Comput. Conf. 2019 Chic. Il.

Tausen, M., Clausen, M., Moeskjær, S., Shihavuddin, A. S. M., Dahl, A. B., Janss, L., et al. (2020). Greenotyper: Image-based plant phenotyping using distributed computing and deep learning. *Front. Plant Sci.* 11. doi: 10.3389/fpls.2020.01181

Tauzin, G., Lupo, U., Tunstall, L., Perez, J. B., Caorsi, M., Medina-Mardones, A. M., et al (2021). Giotto-tda: A topological data analysis toolkit for machine learning and data exploration. *The Journal of Machine Learning Research* 22(1), 1834–1839.

Thompson, A. L., Thorp, K. R., Conley, M., Andrade-Sanchez, P., Heun, J. T., Dyer, J. M., et al. (2018). Deploying a proximal sensing cart to identify drought-adaptive traits in upland cotton for high-throughput phenotyping. *Front. Plant Sci.* 9. doi: 10.3389/fpls.2018.00507

Thorp, K. R., Thompson, A. L., Harders, S. J., French, A. N., and Ward, R. W. (2018). High-throughput phenotyping of crop water use efficiency *via* multispectral drone imagery and a daily soilwater balance model. *Remote Sens.* 10(1), 1682. doi: 10.3390/rs10111682

van Bezouw, R. F. H. M., Keurentjes, J. J. B., Harbinson, J., and Aarts, M. G. M. (2019). Converging phenomics and genomics to study natural variation in plant photosynthetic efficiency. *Plant J.* 97, 112–133. doi: 10.1111/tpj.14190

Virtanen, P., Gommers, R., Oliphant, T. E., Haberland, M., Reddy, T., Cournapeau, D., et al. (2020). SciPy 1.0: Fundamental algorithms for scientific computing in Python. *Nature methods* 17(3), 261–272.

Walter, J. D. C., Edwards, J., McDonald, G., and Kuchel, H. (2019). Estimating biomass and canopy height with LiDAR for field crop breeding. *Front. Plant Sci.* 10. doi: 10.3389/fpls.2019.01145

Wang, Y., Sun, Y., Liu, Z., Sarma, S. E., Bronstein, M. M., and Solomon, J. M. (2019). Dynamic graph cnn for learning on point clouds. *Acm Transactions On Graphics (tog)*. 38(5), 1–12.

Ward, J. H. (1963). Hierarchical grouping to optimize an objective function. *J. Am. Stat. Assoc.* 58, 236–244. doi: 10.1080/01621459.1963.10500845

Waskom, M. L. (2021). Seaborn: Statistical data visualization. *J. Open Source Software* 6(60), 3021. doi: 10.21105/joss.03021

White, J. W., and Conley, M. M. (2013). A flexible, low-cost cart for proximal sensing. *Crop Sci.* 53, 1646–1649. doi: 10.2135/cropsci2013.01.0054

Yuan, H., Wang, N., Bennett, R., Burditt, D., Cannon, A., and Chamberlin, K. (2018). *Development of a ground-based peanut canopy phenotyping system* (Beijing, China: Elsevier B.V), 162–165. doi: 10.1016/j.ifacol.2018.08.081

Zarei, A., Gonzalez, E., Merchant, N., Pauli, D., Lyons, E., and Barnard, K. (2022). MegaStitch: Robust Large-scale image stitching. *IEEE Trans. Geosci. Remote Sens.* 60, 1–9. doi: 10.1109/TGRS.2022.3141907

Zhang, Z., Chang, C., Lin, H., Wang, Y., Arora, R., and Jin, X. (2020). Is network the bottleneck of distributed training?. In *Proceedings of the Workshop on Network Meets AI & ML* (pp. 8–13).

Zhou, Q.-Y., Park, J., and Koltun, V. (2018) *Open3D: A modern library for 3D data processing*. Available at: http://arxiv.org/abs/1801.09847 (Accessed August 5, 2021). ArXiv180109847 Cs.

Zhu, X., Leiser, W. L., Hahn, V., and Würschum, T. (2021). Phenomic selection is competitive with genomic selection for breeding of complex traits. *Plant Phenome J.* 4, e20027. doi: 10.1002/ppj2.20027

frontiers | Frontiers in Plant Science

TYPE Original Research
PUBLISHED 14 March 2023
DOI 10.3389/fpls.2023.1087239

OPEN ACCESS

EDITED BY
Wei Guo,
The University of Tokyo, Japan

REVIEWED BY
Ruifang Zhai,
Huazhong Agricultural University, China
Fan Shi,
Agriculture Victoria Research, Australia

*CORRESPONDENCE
Scott D. Noble
✉ Scott.noble@usask.ca

SPECIALTY SECTION
This article was submitted to
Technical Advances in Plant Science,
a section of the journal
Frontiers in Plant Science

RECEIVED 02 November 2022
ACCEPTED 14 February 2023
PUBLISHED 14 March 2023

CITATION
Khorsandi A, Tanino K and Noble SD (2023)
The effects of sampling and instrument
orientation on LiDAR data from crop plots.
Front. Plant Sci. 14:1087239.
doi: 10.3389/fpls.2023.1087239

The effects of sampling and instrument orientation on LiDAR data from crop plots

Azar Khorsandi[1], Karen Tanino[2] and Scott D. Noble[3]*

[1]Department of Chemical and Biological Engineering, College of Engineering, University of Saskatchewan, Saskatoon, SK, Canada, [2]Department of Plant Sciences, College of Agriculture and Bioresources, University of Saskatchewan, Saskatoon, SK, Canada, [3]Department of Mechanical Engineering, College of Engineering, University of Saskatchewan, Saskatoon, SK, Canada

Wheat is one of the most widely consumed grains in the world and improving its yield, especially under severe climate conditions, is of great importance to world food security. Phenotyping methods can evaluate plants according to their different traits, such as yield and growth characteristics. Assessing the vertical stand structure of plants can provide valuable information about plant productivity and processes, mainly if this trait can be tracked throughout the plant's growth. Light Detection And Ranging (LiDAR) is a method capable of gathering three-dimensional data from wheat field trials and is potentially suitable for providing non-destructive, high-throughput estimations of the vertical stand structure of plants. The current study considers LiDAR and focuses on investigating the effects of sub-sampling plot data and data collection parameters on the canopy vertical profile (CVP). The CVP is a normalized, ground-referenced histogram of LiDAR point cloud data representing a plot or other spatial domain. The effects of sub-sampling of plot data, the angular field of view (FOV) of the LiDAR and LiDAR scan line orientation on the CVP were investigated. Analysis of spatial sub-sampling effects on CVP showed that at least 144000 random points (600 scan lines) or an area equivalent to three plants along the row were adequate to characterize the overall CVP of the aggregate plot. A comparison of CVPs obtained from LiDAR data for different FOV showed that CVPs varied with the angular range of the LiDAR data, with narrow ranges having a larger proportion of returns in the upper canopy and a lower proportion of returns in the lower part of the canopy. These findings will be necessary to establish minimum plot and sample sizes and compare data from studies where scan direction or field of view differ. These advancements will aid in making comparisons and inform best practices for using close-range LiDAR in phenotypic studies in crop breeding and physiology research.

KEYWORDS

wheat, LiDAR, phenomics, phenotyping, spatial sampling

1 Introduction

With an increasing global population, providing enough food to satisfy needs is a big challenge. Plant breeding has effectively increased agricultural productivity over the past century (Evenson and Golin, 2003). Connecting genotypes with their phenotypes and selecting high-yield and stress-tolerant plants can help crop breeders keep pace with population growth (Rahaman et al., 2015).

High-quality phenotypic data are vital to plant breeders' decision-making process to realize genetic improvements (Chapman et al., 2014; Bai et al., 2016). Phenotyping methods are able to evaluate plants according to their different traits, such as physiology, yield, development, and tolerance to environmental stresses (Li et al., 2014; Rahaman et al., 2015). Some morphological traits that are often used to evaluate plant growth and characterize the canopy structure include canopy biomass (Hansen and Schjoerring, 2003; Ehlert et al., 2009), height (Zhang and Grift, 2012; Bendig, 2015), and leaf area index (LAI) (Baret et al., 2010; Béland et al., 2011; Béland et al., 2014; Verger et al., 2014; Zhao et al., 2015). Studies have shown that these morphological traits have a strong relationship with plant genotype, cultivars, growth rate and yield (Sharma and Ritchie, 2015; Friedli et al., 2016; Sun et al., 2018).

Biomass measurement is a good indicator of crop growth and growth rate, leaf area, organ size and partitioning and morphological characteristics. These data can be used to calculate radiation use efficiency and metabolite analysis (Pask et al., 2012). Biomass production can be reduced dramatically by stresses, resulting in a reduced ability of the crop to intercept solar radiation and a decrease in the photosynthesis rate and/or radiation use efficiency. Identifying genotypes that are able to maintain their biomass production during stress conditions is an essential key to finding the better-adapted lines (Pask et al., 2012).

Plant height has been used as a proxy for plant biomass (Madec et al., 2017) and can be a trait for phenotyping. Studies showed stress conditions affect the stem height that defines plant height (Ota et al., 2015; Tilly et al., 2015). Some individual traits, such as plant height and stem solidness, both have a beneficial relationship with plant yield and harvest index. (Pask et al., 2012). Blonquist et al. (2009) used height as one of the model's inputs to evaluate the water stress condition in plants. These traits are good for breeders to screen large plant populations (Pask et al., 2012).

Traditional methods to measure such phenotypic traits are focused on single time points and therefore do not consider the developmental dynamics of these traits. The limited sampling possible for human evaluators is insufficient to capture the variation within plots (Guan et al., 2018). Using modern technologies to develop high-throughput phenotyping methods is a way to overcome traditional manual methods' temporal and sampling limitations.

One technology that can provide 3D canopy data for estimating plant traits is LiDAR. LiDAR uses the phase shift between an emitted signal and the reflected return signal (or signals) to estimate the distance between the instrument (zero point) and a target. While the application of LiDAR for estimation of height and above-ground biomass has been well-established in forestry (Lucas et al., 2008; Eitel et al., 2013; Kankare et al., 2013; Greaves et al., 2015), the use of this technology in field crops is much less mature. Recent studies established the LiDAR scanning approach to estimate the number of spikes and crop density (Saeys et al., 2009). In most studies, LiDAR data are often presented in the form of a meshed, 3D reconstruction of the scanned surface. They have focused on extracting and estimating a variety of canopy information such as height, canopy biomass, leaf area, leaf shape, leaf inclination angle, leaf area index (LAI) and leaf area density (LAD) from these data (Ehlert et al., 2010; Gebbers et al., 2011; Tilly et al., 2014; Jimenez-Berni et al., 2018; Qiu et al., 2019; Su et al., 2019; Walter et al., 2019; Maesano et al., 2020).

However, some work has represented plot data using relatively simple histograms, representing the canopy vertical profile (CVP) (Jimenez-Berni et al., 2018; Furbank et al., 2019). To determine the histogram of the vertical height of points with respect to the ground, the distance between the ground and the LiDAR sensor must first be determined. One approach is to consider the peak of the histogram (i.e., mode) as the ground elevation for a given plot, assuming that some ground is visible through the canopy or at the plot edge (Jimenez-Berni et al., 2018). Evaluating the CVP of crop plots is a promising approach for providing information about plant processes and development, especially if these traits can be tracked throughout the growing season. In this study, LiDAR data from a canopy were height corrected, combined across an area of interest (plot), and presented as a CVP plot of height versus a normalized number of returns. One of the main questions here is how CVP or LiDAR histogram data can be affected by instrumental adjustments and data acquisition approach.

The main objective of this study was to evaluate factors that could impact the consistency of LiDAR data for creating repeatable CVPs for wheat. The particular objectives were completed as described below.

1) Find the minimum sample size to consistently capture the CVP characteristics of a wheat genotype per plot.
2) Ascertain the effect of the angular FOV of LiDAR on the resulting CVP, and
3) Determine the impact of scan line orientation with respect to the row direction.

2 Methodology

This study was conducted in two parts. Part one was a field experiment (2019) to investigate the spatial sampling and FOV effects on LiDAR data. Part two was a container experiment (2020) to investigate the repeatability and effect of direction of travel on LiDAR data.

2.1 Area of study

This study was carried out in Saskatoon, Saskatchewan. Data were collected in separate experiments in 2019 and 2020. The 2019 experiment included four wheat varieties (Stettler, Superb, AC Sadash and Acadia) planted on May 24, 2019, in well-watered and drought treatment blocks with three replicate plots of each variety (24 plots total). Due to rainfall patterns, these treatments were not substantially different. The plots were 2.5 m long and 1 m wide, and each plot contained five rows of wheat plants with a row spacing of 0.2 m.

The 2020 experiment consisted of a single replicate of two wheat varieties (Stettler and Superb) planted in three rows on July 26, 2020, under two irrigation treatments (well-watered and drought). These varieties were planted at the same time in 45-litre containers 56 cm long × 41 cm wide × 33 cm deep.

2.2 Data acquisition

In the 2019 experiment, the LiDAR scanner was mounted in the instrument payload on a two-wheeled cart consisting of a lightweight extruded aluminium frame that was pushed by an operator, manually (Figures 1A, C, E). In this experiment, the distance between the LiDAR scanner and the ground was inconsistent during data acquisition due to instabilities in the two-wheeled cart used. The 2019 experimental plots were organized in field layouts of columns and rows. Each data acquisition experiment included six scanning passes in the planting direction. Data were acquired in a single direction of travel. In this experiment, LiDAR scanning was conducted on 53 and 83 days after planting (DAP) when wheat varieties were at anthesis -Zadoks growth scale 61 [ZGS 61 (Zadoks et al., 1974)]- and ripening -ZGS 91-, respectively.

In the 2020 experiment, the instrument payload was mounted on the University of Saskatchewan Field Phenotyping System (UFPS) which is a portable cart consisting of a lightweight extruded aluminium frame with four wheels that was better able to maintain a consistent distance above the plants (Figures 1B, D, F). In this experiment, UFPS was pushed manually by the operator. Three data acquisition passes (replicates) were conducted for each canopy orientation (rows parallel and rows perpendicular to the direction of travel) on September 9, 10 and 11, 2020 (45, 46 and 47 DAP, respectively) when wheat varieties were at anthesis (ZGS 61). In both the 2019 and 2020 experiments, the operator pushed the cart.

The LiDAR sensor used (model SICK LMS 400-1000, SICK AG, Waldkrich, Germany) was a line scanning type. In this study, the FOV of the LiDAR was adjusted to 60°, and the scanning rate was 360 Hz with an angular resolution of 0.1°. The LiDAR working range was from 0.7 to 3 meters. The average speed of the cart carrying the LiDAR sensor was 0.23 m/s, resulting in an average interval between each scan line of 0.6 mm. The UFPS PhenoDAQ software was used for data acquisition.

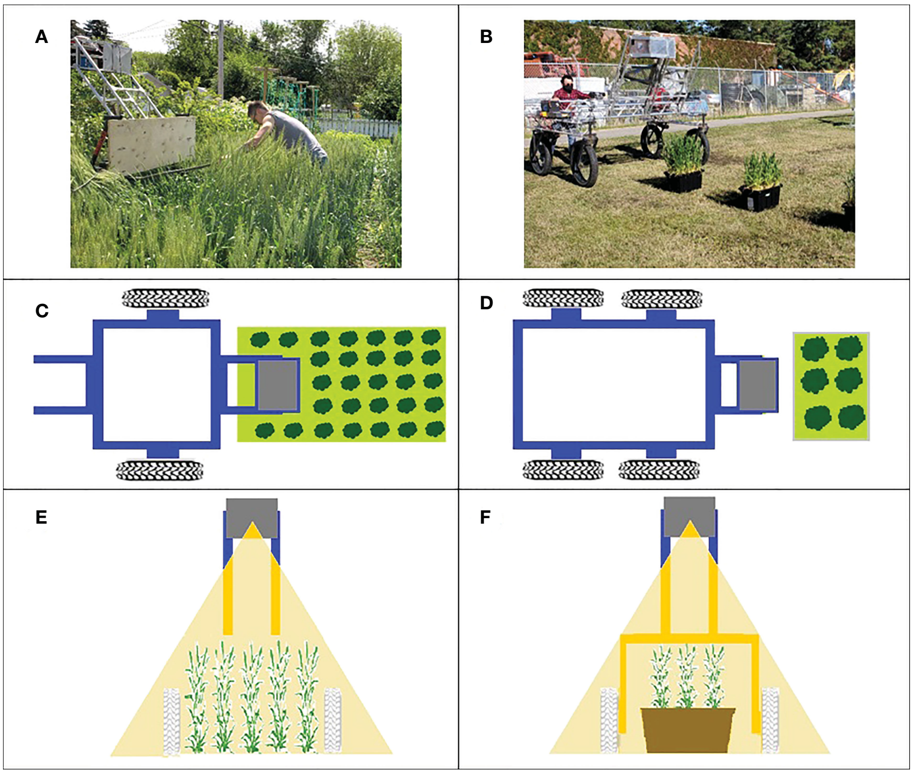

FIGURE 1
Data acquisition platform. Left column **(A, C, E)** shows the system used in 2019 experiment, right column **(B, D, F)** shows the 2020 system. Top row: photographs of the systems in use. Middle row: a top view diagram of data acquisition for the year. Bottom row: Front view showing the plane of the LiDAR scan.

2.3 Pre-processing

Raw data from the LiDAR were stored in HDF5 format on the payload computer. LiDAR scans contain information on range and return intensity (remittance) with 240 data points per scan line. The number of scan lines for each plot varied with the speed of travel and small variances in the lengths of plots.

The processing code was written in MATLAB (MATLAB R2018a). In the first step, raw LiDAR data were transformed from polar coordinates into Cartesian coordinates. In this step, each point comprises X, Y and Z coordinates, where X is the position along the direction of travel, Y is the position across the plot width (scan line orientation), and Z is the vertical position of each point.

The LiDAR data were collected in the LiDAR frame of reference; part of pre-processing is to convert data to a ground frame of reference. When the variation in the distance between the instrument and the ground was slight, the ground elevation for a given plot was considered the histogram mode (Jimenez-Berni et al., 2018). Subtracting the mode from the histogram data (and multiplying by -1), the histogram is transformed into a ground, rather than instrument, frame of reference. This step was called height correction pre-processing, and the resulting graph was the histogram of distances from the ground. To make this histogram comparable between different sample size, normalization with the number of return points were conducted, and the resulting graph was named CVP.

When the distance between the ground and the instrument is inconsistent, the peak at the ground distance is less distinct when data are observed in aggregate for a plot. This issue was corrected by applying the height correction pre-processing to small numbers of contiguous scan lines at a time and aggregating them post-correction. This process was called ground correction pre-processing. In this pre-processing, it was assumed that variation of payload height with respect to the ground was negligible over a time of 1 second. The data collection frequency in this study was 360 Hz which means 360 lines were scanned with the LiDAR sensor within each second. Figure 2 shows the effect of the different numbers of contiguous scan lines for applying height correction pre-processing on appearing ground peak elevation on CVP data compared with uncorrected CVP data. As can be seen in Figure 2, the raw height corrected aggregate CVP data ground peak is broad, having been spread out by variations in instrument height. Applying the height correction pre-processing on every 360 contiguous scan lines and then aggregating these post-correction resulted in a more distinct ground peak. Applying the same process on a larger number of contiguous lines did not produce the sharp ground peak seen in the ground correction using 360-scan line blocks. As it takes several seconds to collect 1000 scan lines, there may be more variation in instrument height over that more prolonged time, resulting in a less defined peak. Negative height values in these CVP graphs were created due to the instrument uncertainty and the variation in the surface profile and instrument height (Figure 2).

2.4 Impacts of LiDAR spatial sampling

The number of LiDAR data points is influenced by the size of the plot, LiDAR scan rate, angular resolution, and travel speed. A practical question for high-throughput phenotyping with LiDAR is how large a sample (both in terms of data points and area) is required to consistently capture the CVP characteristics of a larger plot. These sampling questions were studied using LiDAR data from the 2019 field data.

In the 2019 experiment, each treatment was planted in triplicate with a plot size of 2.5 m^2. Plant growth in these plots

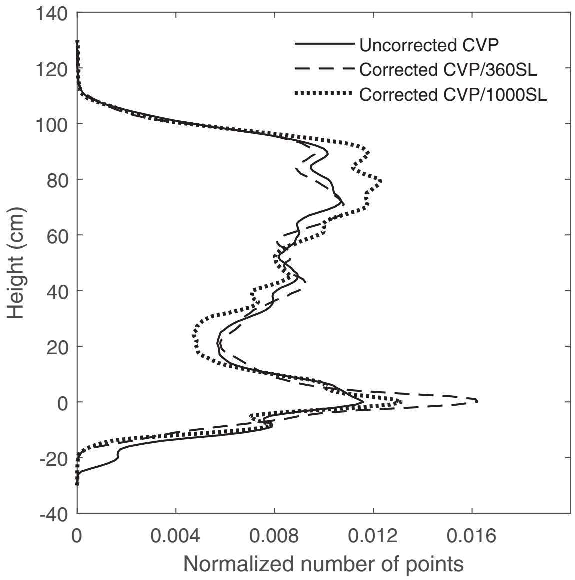

FIGURE 2
The effect of the different number of contiguous scan lines for applying height correction pre-processing on ground peak elevation on CVP.

was observed to be relatively uniform. Thus, the data were combined for each variety yielding four aggregate plots per treatment. Each aggregate plot was equivalent to 7.5 m^2 containing roughly 375 wheat plants in five rows with approximately 12,000×240 LiDAR points. The CVP obtained from this aggregate plot was considered the reference CVP for the variety. Each wheat plant in these aggregate plots occupied an average of 0.02 m^2 of space. These data were subsampled in two ways: random points and contiguous blocks.

To find the minimum number of randomly sampled points required to accurately estimate the CVP of an entire plot, random subsamples were taken, and CVP's compared to the CVP from the entire plot. Subsamples were taken using numbers of points ranging from 24×10^3 (equal to 100 scan lines) to 24×10^5 (equal to 10000 scan lines) and CVPs were constructed. This was repeated three times for each number of points. The resulting CVPs were normalized with the number of points, and then their standard deviations across the canopy height were investigated. In the next step, each CVP was compared to that made by using the entire population in terms of the root mean squared error (RMSE).

For the spatially contiguous subsets, blocks of scan lines were selected from the total population based on the nominal in-row space required for between one and 12 plants along the rows. Like the random selection case, the resulting CVPs were visually compared to the aggregate plot CVP and used the root mean squared error (RMSE).

2.5 Field of view in LiDAR and its effect on CVP

It was hypothesized that the angular FOV of the LiDAR influences the resulting CVP of a scanned canopy. In the 2019 experiment, each plot contained five rows of wheat scanned with the LiDAR FOV of 60° (Figure 3). These data were used to create three FOV scenarios: 12°, 36°, and the entire 60° FOV. These roughly equated to scanning only the middle row of the plot, the centre three rows, and the whole plot, respectively (Figure 3). The resulting data were processed for each of the 24 plots, and then compared.

2.6 Repeatability and Orientation

To investigate the repeatability of the CVP of the scanned canopy, an experiment was conducted with four containers of wheat planted in rows. Two containers were planted with "Superb" and the other two with "Stettler". One container of each variety was designated as a well-watered treatment and the other as a water-stressed (deficiency) treatment. Plants in the well-watered group were regularly watered in the days prior to measurements, while the water-stressed group was allowed to dry out. The containers were placed in a line with their rows aligned and scanned with the LiDAR scanner. Then each container was turned 90°, so their rows were perpendicular to the cart's travel direction, and they were scanned again. Rotating the containers

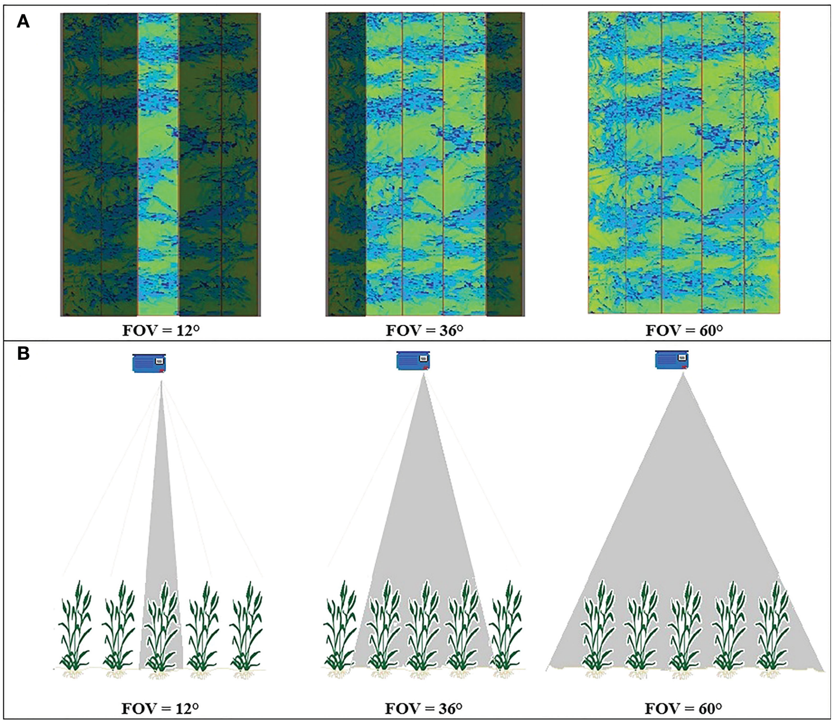

FIGURE 3
(A) the LiDAR images obtained from a typical plot on 15/08/2019, highlighting the scanned region covered by different angular FOV. **(B)** a representation of the FOV geometry viewed perpendicularly from the scanning plane.

90° and scanning them was repeated six times. In total, three passes of LiDAR measurements were made for the rows aligned with the cart's travel direction and three passes were made for the rows perpendicular to the cart's travel direction. This experiment was repeated on September 9, 10 and 11, 2020, with both treatments being thoroughly watered following scanning on September 9. The CVP of each container and measurement replication was obtained from the LiDAR data and compared to observe the repeatability of LiDAR canopy measurements and the effect of row orientation on the CVP data.

3 Results and discussion

3.1 Pre-processing

After converting the LiDAR data from polar coordinates to Cartesian coordinates, the histogram of distance from the LiDAR sensor was provided (Figure 4). One typical result on 15/08/2019 for one Acadia wheat plot (Figure 4A) showed that, in this plot where payload height with respect to the ground was consistent, the ground elevation peak could be clearly seen in the histogram of distance from

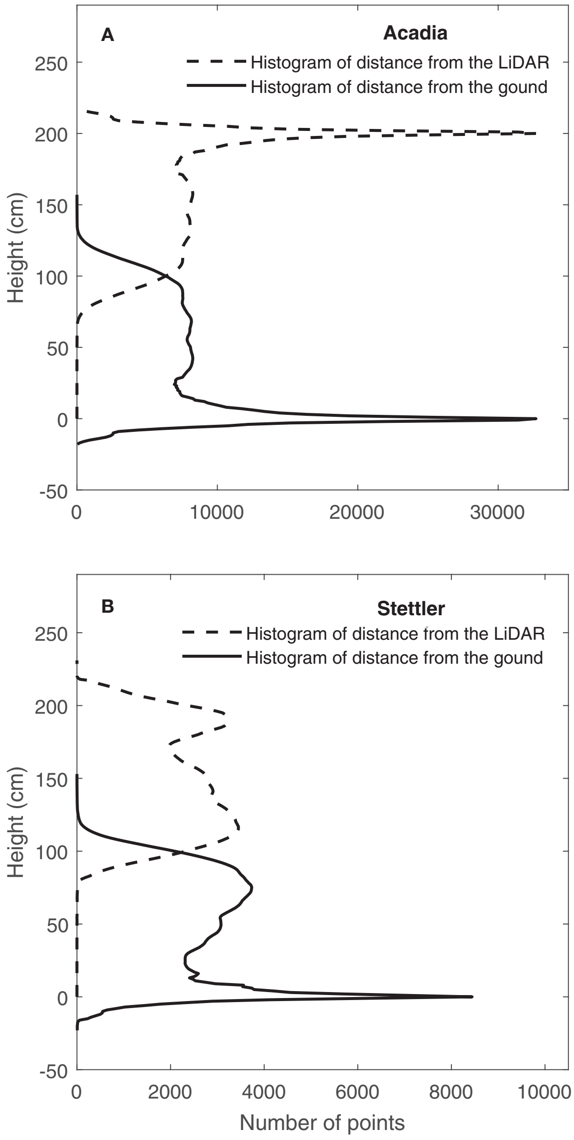

FIGURE 4
Determination of ground elevation from LiDAR data on 15/08/2019. Histogram of distance from the LiDAR and CVP after distance correction and height correction pre-processing were applied for a typical plot **(A)** (Acadia) when the distance between LiDAR and ground was consistent and **(B)** (Stettler) when there was variation in payload height with respect to the ground.

the LiDAR (Jimenez-Berni et al., 2018). Figure 4A shows that in this typical case, the ground correction process did not affect the shape of the histogram, but height correction pre-processing corrected the height of points in the histogram of distance from the ground.

In contrast, results on the same date but for a typical Stettler wheat plot lacked a distinct ground peak, indicating an inconsistent distance between the LiDAR and the ground (Figure 4B). In this case, the ground correction process's effect can be observed in Figure 4B. In general, results showed that after this pre-processing, the ground elevation peak was significant and sharp on the histogram of distance from the ground (Figure 4B). Overall, after doing ground correction pre-processing, height correction pre-processing was conducted, and CVP for the plots was determined.

3.2 Impacts of LiDAR spatial sampling

A comparison of CVP graphs obtained from different numbers of random points showed a lot of variation around the ground peak area. Figure 5 is one case that shows the standard variation of the normalized number of points for an average of 10 CVPs obtained from 192000-point random samples (equal to 800 scanlines). The most considerable standard deviations in the CVP graphs were related to the ground peak, and its neighborhood (-10 to +10 cm) shows the variations of obtained CVPs around the ground peak are much larger than those across the canopy height. This might happen due to the uneven ground surface or the existence of dead leaves or litter on the ground surface. Including or excluding data from the ground peak region on the overall RMSE when comparing a subsampled CVP to a reference may be critical to evaluating subsampling performance. This was assessed as part of the determination of minimum subsample size.

Figure 6 shows the calculated RMSEs between each CVP graph and the reference CVP made using the entire population. With the majority of subsample variance occurring in the region of the ground peak, this analysis was conducted both including and excluding the ground-peak region (± 10cm). A stronger relationship between RMSE and the number of random subsample points was found for CVP's with the ground peak excluded ($R^2 = 0.95$) than with these data included ($R^2 = 0.87$). In addition, Figure 6 shows that most outlier points disappeared by removing the ground peak neighborhood points from the RMSE calculation process. Figure 6 illustrates the RMSE decreased with a power relationship with an increasing number of random points in the subsample. The incremental improvement in CVP representation with increasing subsample size decreases rapidly. Comparisons of selected subsample CVPs with the whole-plot reference are shown in Figure 7.

As seen in Figure 6, RMSE related to the 144000 random points (equal to 600 scan lines) is near the shoulder in the curve, and below this amount of random points, RMSE increased rapidly. Figure 7 shows that the CVP obtained from 144000 random points was very similar to that obtained from the whole plot area. In contrast, the CVP obtained from 48000 random points (equal to 200 scan lines) had lots of variation and could not follow the reference CVP. For this reason, 144000 random points were selected as the minimum random subsample points to capture the CVP characteristics of a larger plot.

Similarly, Figure 8 shows that with increasing the number of plants per row scanned by the LiDAR scanner, RMSE also decreased with a power relationship. Reducing the number of plants below three, RMSE changed dramatically from 0.0015 to 0.003, suggesting three plants as the minimum sample extent for predicting changes in the CVP of the whole population scanned by LiDAR. In addition, Figure 9 shows that the CVP of scanned

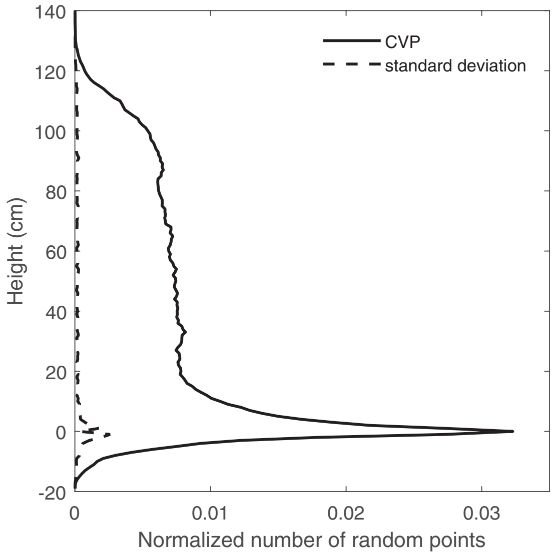

FIGURE 5
The average of 10 CVPs obtained from 800×240 random points and the standard deviation of these CPV graphs- in different canopy heights.

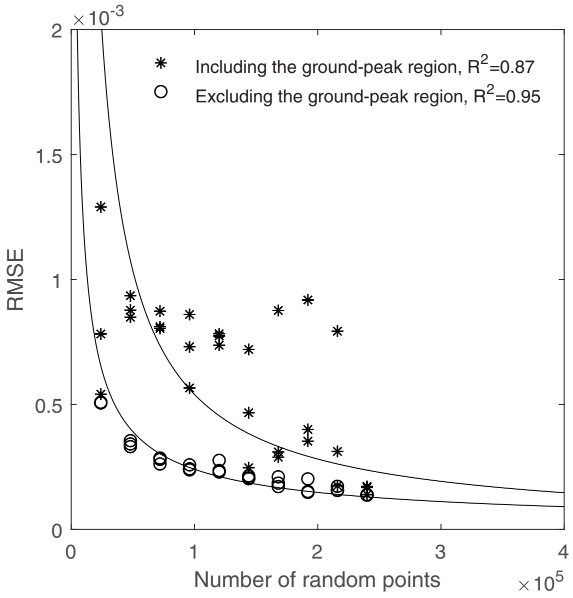

FIGURE 6
The relationship between the number of random points used and RMSE compared to using the whole area points, including and excluding the ground-peak region.

data with three plants per row could follow the shape of the CVP provided by the whole plot data. The average number of normalized points on each height for the area with the entire population, three-plant length section and one plant length section was 0.006. It was concluded that the area containing three or more plants per row was adequate to characterize the overall CVP of the aggregate plots.

3.3 The effect of LiDAR field of view on CVP

A comparison of the CVPs for three FOVs of 12, 36 and 60° showed changes in the shapes of CVPs with FOV (Figure 10). It was observed that responses varied with the angular range of the LiDAR data, with narrow ranges having a more significant proportion of

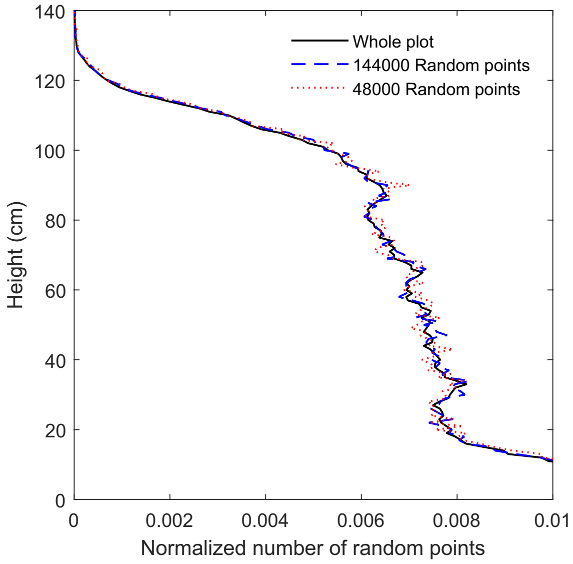

FIGURE 7
The CVP obtained from LiDAR data provided with 48000, 144000 and whole plot data.

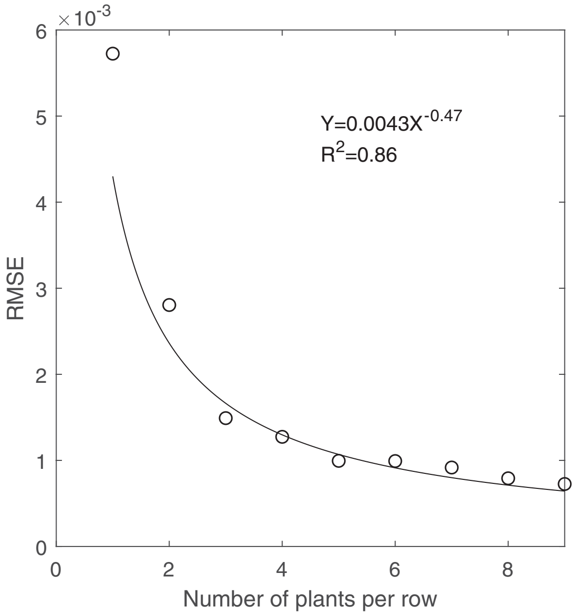

FIGURE 8
The correlation between areas containing the different number of plants per row and RMSE.

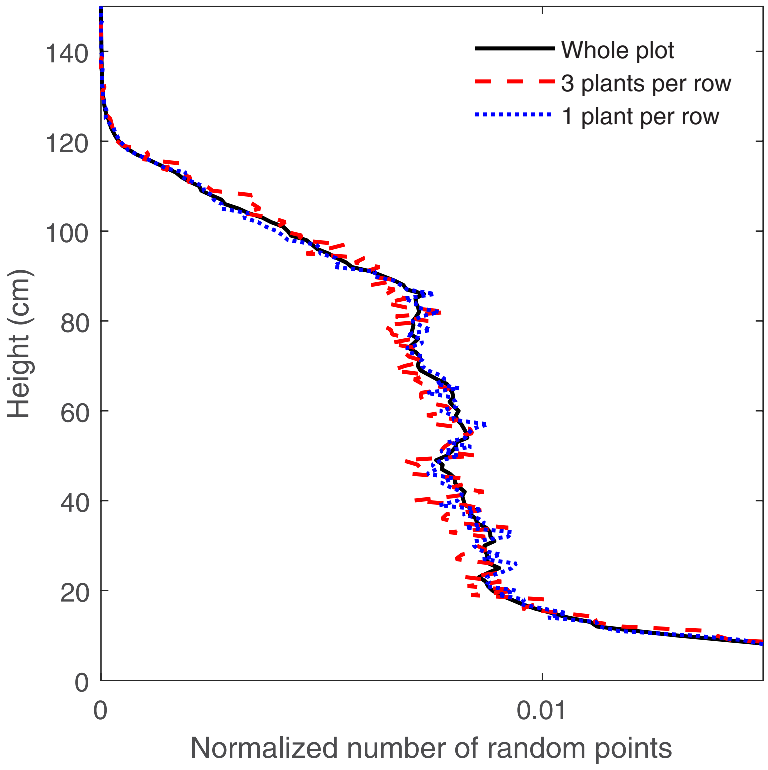

FIGURE 9
The CVP obtained from LiDAR data provided with three different numbers of plants per row.

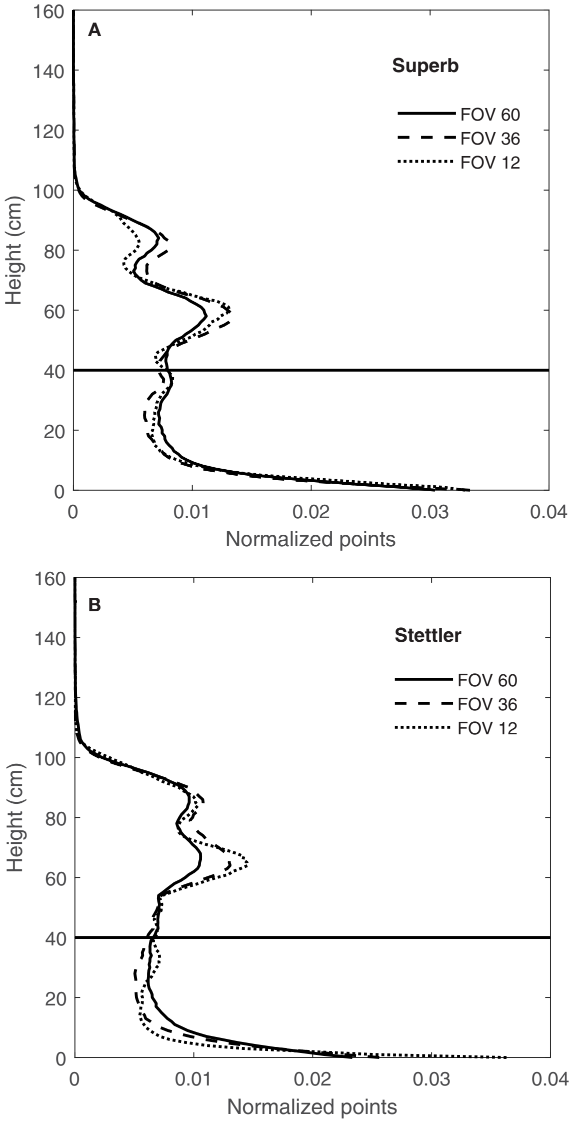

FIGURE 10
CVPs for FOV of 12, 36 and 60° for wheat genotype Superb **(A)** and for the wheat genotype of Stettler **(B)** on 15/08/2019 and the difference in the proportion of areas for FOV 12 and 60° for height greater than 40 cm.

returns in the upper canopy and a lower proportion of returns in the lower part of the canopy.

This difference in normalized CVPs with the number of points at different FOV might be due to the direction of LiDAR's rays hitting the canopy. As shown in Figure 3, at the narrow 12° FOV, the LiDAR was more-or-less directly over the middle row of the plot, so the middle 12° of the scan primarily sees the top of the row. In this case, the upper parts of the canopy block the path of the rays and prevent them from penetrating the lower parts of the canopy. Therefore, the proportion of points related to the upper levels of the canopy is greater at this FOV and lower in the bottom half of the canopy (Figures 10A, B). With a wider 60° FOV, the inter-row space helps make a gap in the canopy allowing off-nadir rays to penetrate deeper into the canopy (Figure 3). This results in more information being collected from the sides of the plants compared to a narrower FOV. This increases the proportion of the CVP area lower in the canopy (Figures 10A, B). The 36° FOV acted more like a narrow FOV, and the proportion of points related to the upper levels of the canopy was greater at this FOV and lower in the bottom half of the canopy (Figures 10A, B).

3.4 Repeatability results

Figure 11 shows the variation in CVPs obtained by LiDAR from well-watered Superb wheat grown in a container and scanned with

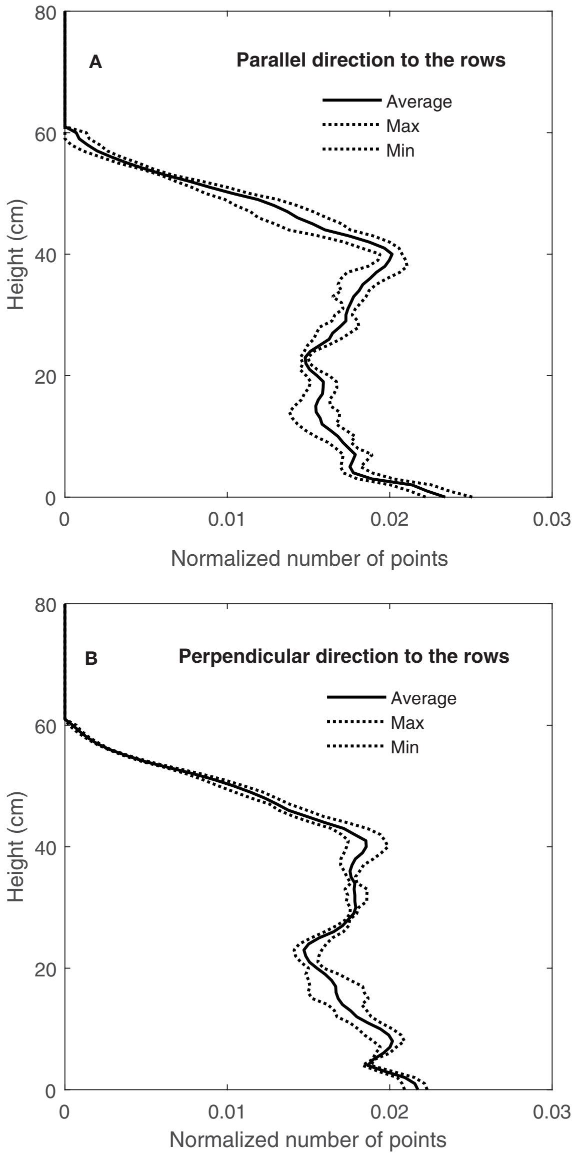

FIGURE 11
Variation of normalized CVP for two directions of travel **(A)** parallel to (or with) the rows and **(B)** perpendicular to (across) the rows.

the direction of travel parallel to the rows (Figure 11A) and direction of travel perpendicular to the rows (Figure 11B). Both directions of travel (parallel to and perpendicular to the rows) showed a similar amount of CVP variation. Similar results were observed in CVPs obtained from other containers on September 9, 10 and 11, 2020.

Figure 12A shows the comparison of three scans, obtained from travelling parallel to the rows (parallel 1, 2 and 3), and Figure 12B shows the comparison of orthogonal scans, one with a travel direction parallel to the rows (parallel 1) and the other two with travel direction perpendicular to the rows (perpendicular 1 and 2). Results showed that CVPs obtained from parallel directions of travel (Figure 12A) and perpendicular directions of travel, were followed each other in peaks and height. Similar results were observed in other containers on consecutive days (September 9, 10 and 11). These results showed the repeatability of LiDAR data in two perpendicular directions of travel for the same containers.

Figures 13A, B show the repeatability of CVPs on consecutive days (September 9, 10 and 11) again for the well-watered Superb container by plotting CVP pairs against each other. Comparing the same travel direction (with respect to the rows), the linear regression slope coefficients were near one, and the intercepts were near zero (Figure 13A). However, comparing orthogonal travel directions (parallel 1 and perpendicular 1) in Figure 13B, scanned data showed much greater variation with a lower linear regression coefficient than the same directions. Similar results were observed for the other three containers on September 9, 10 and 11. Walter et al. (2019) conducted an experiment to investigate the repeatability of LiDAR measurements. Their results showed that the repeatability of LiDAR measurements was higher in the same directions of travel than in opposite directions of travel.

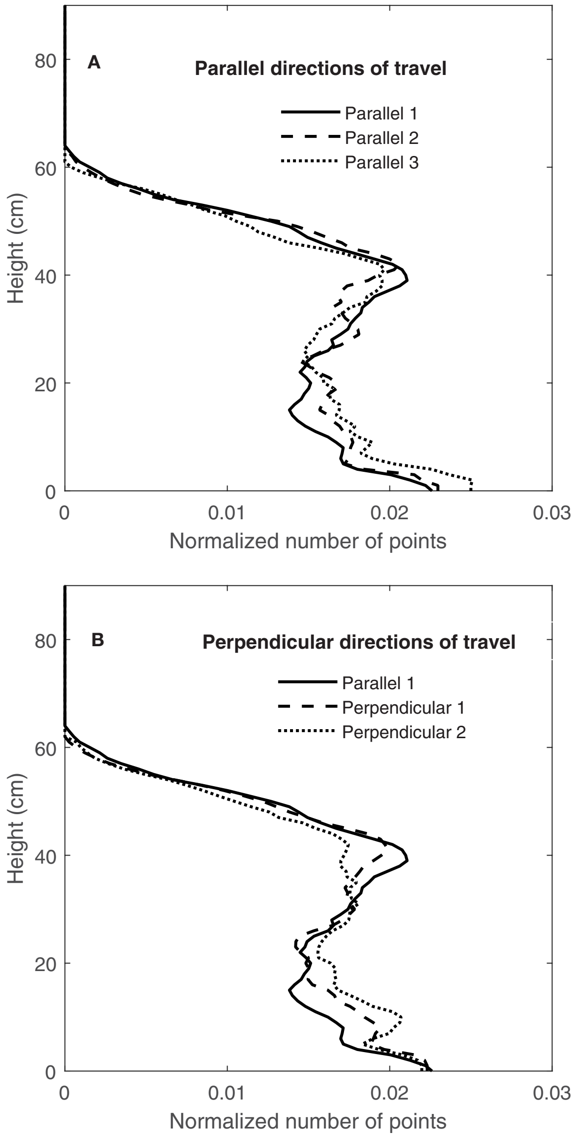

FIGURE 12
Comparing the CVP obtained from **(A)** the same directions of travel and **(B)** the perpendicular directions of travel from one container on 09/09/2020.

4 Conclusion

In this study a ground-based LiDAR system was used to collect data from wheat plots, from which histograms of height vs normalized number of points were constructed and referred to as the canopy vertical profile (CVP). Height correction pre-processing and normalization with a number of return points were two main steps to convert histogram data to CVP and make them ready and comparable for the subsequent analysis. However, when the distance between the ground and the instrument was inconsistent, applying ground correction pre-processing to small numbers of contiguous lines (360) at a time and aggregating them post-correction was a solution to convert the LiDAR data from an unsteady sensor to the ground frame of reference.

This study showed that the CVP of a scanned, uniform plot could be represented by a subset of at least 144000 random points (600 scan lines). In addition, analysis of the impact of LiDAR spatial sampling showed that areas containing at least three plants per row are needed to consistently capture the CVP characteristics of wheat genotype per plot.

Investigating the impact of LiDAR FOV \ on CVP graphs showed differences between narrow and wide fields of view. The narrow 12° FOV of the scan rays primarily sees the top of the canopy in a row directly below, preferentially returning top-of-canopy points. In wider FOVs, the off-nadir rays can penetrate deeper into the canopy profile and provide more information from the lower parts of the canopy due to the inter-row space and the gaps that happened in the canopy. This observation confirms that

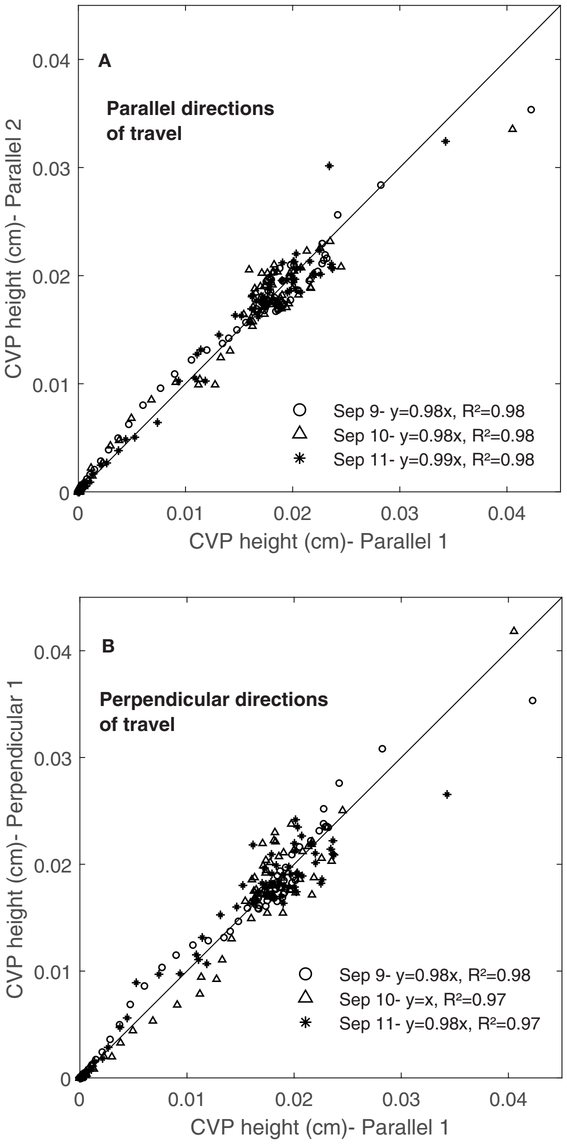

FIGURE 13
The Repeatability of CVP graphs obtained in three consequence days. Comparing scans collected **(A)** from the same directions of travel and **(B)** from the perpendicular directions of travel during three days (9, 10 and 11 of September 2020) from the same container.

LiDAR FOV influenced the CVP graph and should be considered during data acquisition and comparing results from different instruments or scan settings.

Multiple measurements of CVP of the same canopy were shown to be repeatable when collected from the parallel or perpendicular travel directions with respect to the rows. These advancements may help plant breeders to compare data from studies where scan direction, FOV, or sample sizes differ. This combination of findings demonstrates the ability of LiDAR to provide repeatable information about the vertical profile of wheat plants in field conditions. In future studies, the ability of CVP as a phenotypic trait can be investigated by comparing the relationship between the CVPs obtained from different plant genotypes with other plant traits.

Data availability statement

The original contributions presented in the study are included in the article/supplementary material. Further inquiries can be directed to the corresponding author.

Author contributions

AK: author, design of the work, analysis, interpretation of data, and drafting of the work. KT: co-author and funding. SDN: author, design of the work, interpretation of data, and revising. All authors contributed to the article and approved the submitted version.

Funding

The authors acknowledge the financial support of the Dean's Scholarship and from the College of Graduate and Postdoctoral Studies (CGPS), University of Saskatchewan., the Saskatchewan Ministry of Agriculture, the Western Grains Research Foundation, the Saskatchewan Wheat Development Commission, and the Canada First Research Excellence Fund *via* the P2IRC project.

Acknowledgments

We also thank undergraduate students Krista Jenke and Craig Gavelin for their work collecting data.

Conflict of interest

The authors declare that the research was conducted in the absence of any commercial or financial relationships that could be construed as a potential conflict of interest.

Publisher's note

References

Bai, G., Ge, Y., Hussain, W., Baenziger, P. S., and Graef, G. (2016). A multi-sensor system for high throughput field phenotyping in soybean and wheat breeding. *Comput. Electron. Agric.* 128, 181–192. doi: 10.1016/j.compag.2016.08.021

Baret, F., De Solan, B., Lopez-Lozano, R., Ma, K., and Weiss, M. (2010). GAI estimates of row crops from downward looking digital photos taken perpendicular to rows at 57.5 zenith angle: Theoretical considerations based on 3D architecture models and application to wheat crops. *Agric. For. Meteorol.* 150 (11), 1393–1401. doi: 10.1016/j.agrformet.2010.04.011

Beland, M., Widlowski, J., Fournier, R. A., Cote, J., and Verstraete, M. M. (2011). Estimating leaf area distribution in savanna trees from terrestrial LiDAR measurements. *Agric. For. Meteorol.* 151 (9), 1252–1266. doi: 10.1016/j.agrformet.2011.05.004

Beland, M., Baldocchi, D. D., Widlowski, J., Fournier, R. A., and Verstraete, M. M. (2014). On seeing the wood from the leaves and the role of voxel size in determining leaf area distribution of forests with terrestrial LiDAR. *Agric. For. Meteorol.* 184, 82–97. doi: 10.1016/j.agrformet.2013.09.005

Bendig, J. V. (2015). "Unmanned aerial vehicles (UAVs) for multi-temporal crop surface modelling," in *A new method for plant height and biomass estimation based on RGB-imaging* (Cologne, Germany: Doctoral dissertation, University of Cologne).

Blonquist, J. M., Norman, J. M., and Bugbee, B. (2009). Automated measurement of canopy stomatal conductance based on infrared temperature. *Agric. For. Meteorol.* 149 (11), 1931–1945. doi: 10.1016/j.agrformet.2009.06.021

Chapman, S. C., Merz, T., Chan, A., Jackway, P., Hrabar, S., Dreccer, M. F., et al. (2014). Phenocopter: A low-altitude, autonomous remote-sensing robotic helicopter for high-throughput field-based phenotyping. *Agronomy* 4 (2), 279–301. doi: 10.3390/agronomy4020279

Ehlert, D., Adamek, R., and Horn, H.-J. (2009). Laser rangefinder-based measuring of crop biomass under field conditions. *Precis. Agric.* 10 (5), 395–408. doi: 10.1007/s11119-009-9114-4

Ehlert, D., Heisig, M., and Adamek, R. (2010). Suitability of a laser rangefinder to characterize winter wheat. *Precis. Agric.* 11 (6), 650–663. doi: 10.1007/s11119-010-9191-4

Eitel, J. U. H., Vierling, L. A., and Magney, T. S. (2013). A lightweight, low cost autonomously operating terrestrial laser scanner for quantifying and monitoring ecosystem structural dynamics. *Agric. For. Meteorol.* 180, 86–96. doi: 10.1016/j.agrformet.2013.05.012

Evenson, R. E., and Golin, D. (2003). Assessing the impact of the green revolution 1960 to 2000. *Science* 300, 758–762. doi: 10.1126/science.1078710

Friedli, M., Kirchgessner, N., Grieder, C., Liebisch, F., Mannale, M., and Walter, A. (2016). Terrestrial 3D laser scanning to track the increase in canopy height of both monocot and dicot crop species under field conditions. *Plant Methods* 12 (1), 1–15. doi: 10.1186/s13007-016-0109-7

Furbank, R. T., Jimenez-Berni, J. A., George-Jaeggli, B., Potgieter, A. B., and Deery, D. M. (2019). Field crop phenomics: Enabling breeding for radiation use efficiency and biomass in cereal crops. *New Phytol.* 223 (4), 1714–1727. doi: 10.1111/nph.15817

Gebbers, R., Ehlert, D., and Adamek, R. (2011). Rapid mapping of the leaf area index in agricultural crops. *Agron. J.* 103 (5), 1532–1541. doi: 10.2134/agronj2011.0201

Greaves, H. E., Vierling, L. A., Eitel, J. U.H., Boelman, N. T., Magney, T. S., Prager, C. M., et al. (2015). Estimating aboveground biomass and leaf area of low-stature Arctic shrubs with terrestrial LiDAR. *Remote Sens. Environ.* 164, 26–35. doi: 10.1016/j.rse.2015.02.023

Guan, H., Liu, M., Ma, X., and Yu, S. (2018). Three-dimensional reconstruction of soybean canopies using multisource imaging for phenotyping analysis. *Remote Sens.* 10 (8), 1206. doi: 10.3390/rs10081206

Hansen, P. M., and Schjoerring, J. K. (2003). Reflectance measurement of canopy biomass and nitrogen status in wheat crops using normalized difference vegetation indices and partial least squares regression. *Remote Sens. Environ.* 86 (4), 542–553. doi: 10.1016/S0034-4257(03)00131-7

Jimenez-Berni, J. A., Deery, D. M., Rozas-Larraondo, P., Condon, A. G., Rebetzke, G. J., James, R. A., et al. (2018). High throughput determination of plant height, ground cover, and above-ground biomass in wheat with LiDAR. *Front. Plant Sci.* 9, 1–18. doi: 10.3389/fpls.2018.00237

Kankare, V., Holopainen, M., Vastaranta, M., Puttonen, E., Yu, X., Hyyppa, J., et al. (2013). Individual tree biomass estimation using terrestrial laser scanning. *ISPRS J. Photogrammetry Remote Sens.* 75, 64–75. doi: 10.1016/j.isprsjprs.2012.10.003

Li, L., Zhang, Q., and Huang, D. (2014). A review of imaging techniques for plant phenotyping. *Sensors (Switzerland)* 14 (11), 20078–20111. doi: 10.3390/s141120078

Lucas, R. M., Lee, A. C., and Bunting, P. J. (2008). Retrieving forest biomass through integration of CASI and LiDAR data. *Int. J. Remote Sens.* 29 (5), 1553–1577. doi: 10.1080/01431160701736497

Madec, S., Baret, F., De Solan, B., Thomas, S., Dutartre, D., Jezequel, S., et al. (2017). High-throughput phenotyping of plant height: Comparing unmanned aerial vehicles and ground lidar estimates. *Front. Plant Sci.* 8, 1–14. doi: 10.3389/fpls.2017.02002

Maesano, M., Khoury, S., Nakhle, F., Firrincieli, A., Gay, A., Tauro, F., et al. (2020). UAV-based LiDAR for high-throughput determination of plant height and above-ground biomass of the bioenergy grass arundo donax. *Remote Sens.* 12 (20), 1–20. doi: 10.3390/rs12203464

Ota, T., Ogawa, M., Shimizu, K., Kajisa, T., Mizoue, N., Yoshida, S., et al. (2015). Aboveground biomass estimation using structure from motion approach with aerial photographs in a seasonal tropical forest. *Forests* 6 (11), 3882–3898. doi: 10.3390/f6113882

Pask, A., Pietragalla, J., Mullan, D., and Reynolds, M. P. (Eds.). (2012). *Physiological Breeding II: A Field Guide to Wheat Phenotyping.* (Mexico, D.F.: CIMMYT). Available at: http://onlinelibrary.wiley.com/doi/10.1002/cbdv.200490137/abstract.

Qiu, Q., Sun, N., Bai, H., Wang, N., Fan, Z., Wang, Y., et al. (2019). Field-based high-throughput phenotyping for maize plant using 3d LIDAR point cloud generated with a "phenomobile. *Front. Plant Sci.* 10, 1–15. doi: 10.3389/fpls.2019.00554

Rahaman, M. M., Chen Di., , Gillani, Z., Klukas, C., and Chen, M. (2015). Advanced phenotyping and phenotype data analysis for the study of plant growth and development. *Front. Plant Sci.* 6, 1–15. doi: 10.3389/fpls.2015.00619

Saeys, W., Lenaerts, B., Craessaerts, G., and De Baerdemaeker, J. (2009). Estimation of the crop density of small grains using LiDAR sensors. *Biosyst. Eng.* 102 (1), 22–30. doi: 10.1016/j.biosystemseng.2008.10.003

Sharma, B., and Ritchie, G. L. (2015). High-throughput phenotyping of cotton in multiple irrigation environments. *Crop Sci.* 55 (2), 958–969. doi: 10.2135/cropsci2014.04.0310

Su, Y., Wu, F., Ao, Z., Jin, S., Qin, F., Liu, B., et al. (2019). Evaluating maize phenotype dynamics under drought stress using terrestrial lidar. *Plant Methods* 15 (1), 1–16. doi: 10.1186/s13007-019-0396-x

Sun, S., Li, C., Paterson, A. H., Jiang, Y., Xu, R., Robertson, J. S., et al. (2018). In-field high throughput phenotyping and cotton plant growth analysis using LiDAR. *Front. Plant Sci.* 9, 1–17. doi: 10.3389/fpls.2018.00016

Tilly, N., Aasen, H., and Bareth, G. (2015). Fusion of plant height and vegetation indices for the estimation of barley biomass. *Remote Sens.* 7 (9), 11449–11480. doi: 10.3390/rs70911449

Tilly, N., Hoffmeister, D., Cao, Q., Huang, S., Lenz-Wiedemann, V., Miao, Y., et al. (2014). Multitemporal crop surface models: Accurate plant height measurement and biomass estimation with terrestrial laser scanning in paddy rice. *J. Appl. Remote Sens.* 8 (1), 83671. doi: 10.1117/1.jrs.8.083671

Verger, A., Vigneau, N., Cheron, C., Gilliot, J., Comar, A., and Baret, F. (2014). Green area index from an unmanned aerial system over wheat and rapeseed crops. *Remote Sens. Environ.* 152, 654–664. doi: 10.1016/j.rse.2014.06.006

Walter, J., Edwards, J., McDonald, G., Kuchel, H., Mayer, J. E., and Walter, J. D. C. (2019). Estimating biomass and canopy height with LiDAR for field crop breeding. *Front. Plant Sci.* 10. doi: 10.3389/fpls.2019.01145

Zadoks, J. C., Chang, T. T., and Konzak, C. F. (1974). A decimal code for the growth stages of cereals. *Weed Res.* 14 (6), 415–421. doi: 10.1111/j.1365-3180.1974.tb01084.x

Zhang, L., and Grift, T. E. (2012). A LIDAR-based crop height measurement system for miscanthus giganteus. *Comput. Electron. Agric.* 85, 70–76. doi: 10.1016/j.compag.2012.04.001

Zhao, K., Garcia, M., Liu, S., Guo, Q., Chen, G., Zhang, X., et al. (2015). Terrestrial lidar remote sensing of forests: Maximum likelihood estimates of canopy profile, leaf area index, and leaf angle distribution. *Agric. For. Meteorol.* 209, 100–113. doi: 10.1016/j.agrformet.2015.03.008

frontiers | Frontiers in Plant Science

TYPE Original Research
PUBLISHED 03 April 2023
DOI 10.3389/fpls.2023.1063983

OPEN ACCESS

EDITED BY
Andreas Hund,
ETH Zürich, Switzerland

REVIEWED BY
Nicolas Virlet,
Rothamsted Research, United Kingdom
Freddy Mora-Poblete,
University of Talca, Chile
Javier Fernandez,
The University of Queensland, Australia

*CORRESPONDENCE
Marta S. Lopes
✉ marta.dasilva@irta.cat

SPECIALTY SECTION
This article was submitted to Technical Advances in Plant Science, a section of the journal Frontiers in Plant Science

RECEIVED 07 October 2022
ACCEPTED 16 March 2023
PUBLISHED 03 April 2023

CITATION
Gracia-Romero A, Rufo R, Gómez-Candón D, Soriano JM, Bellvert J, Yannam VRR, Gulino D and Lopes MS (2023) Improving in-season wheat yield prediction using remote sensing and additional agronomic traits as predictors. *Front. Plant Sci.* 14:1063983. doi: 10.3389/fpls.2023.1063983

Improving in-season wheat yield prediction using remote sensing and additional agronomic traits as predictors

Adrian Gracia-Romero[1], Rubén Rufo[1], David Gómez-Candón[2], José Miguel Soriano[1], Joaquim Bellvert[2], Venkata Rami Reddy Yannam[1], Davide Gulino[1] and Marta S. Lopes[1]*

[1]Field Crops Program, Institute for Food and Agricultural Research and Technology (IRTA), Lleida, Spain, [2]Efficient Use of Water in Agriculture Program, Institute for Food and Agricultural Research and Technology (IRTA), Lleida, Spain

The development of accurate grain yield (GY) multivariate models using normalized difference vegetation index (NDVI) assessments obtained from aerial vehicles and additional agronomic traits is a promising option to assist, or even substitute, laborious agronomic in-field evaluations for wheat variety trials. This study proposed improved GY prediction models for wheat experimental trials. Calibration models were developed using all possible combinations of aerial NDVI, plant height, phenology, and ear density from experimental trials of three crop seasons. First, models were developed using 20, 50 and 100 plots in training sets and GY predictions were only moderately improved by increasing the size of the training set. Then, the best models predicting GY were defined in terms of the lowest Bayesian information criterion (BIC) and the inclusion of days to heading, ear density or plant height together with NDVI in most cases were better (lower BIC) than NDVI alone. This was particularly evident when NDVI saturates (with yields above 8 t ha^{-1}) with models including NDVI and days to heading providing a 50% increase in the prediction accuracy and a 10% decrease in the root mean square error. These results showed an improvement of NDVI prediction models by the addition of other agronomic traits. Moreover, NDVI and additional agronomic traits were unreliable predictors of grain yield in wheat landraces and conventional yield quantification methods must be used in this case. Saturation and underestimation of productivity may be explained by differences in other yield components that NDVI alone cannot detect (e.g. differences in grain size and number).

KEYWORDS

wheat, grain yield, prediction models, UAV, NDVI, plant height, phenology

1 Introduction

Wheat yield progress has been achieved at more than 1% *p. a.* in Europe and other parts of the world (Fischer et al., 2022; Lopes, 2022). Yield progress depends on direct experimental testing of novel agronomic practices and improved germplasm. Moreover, efficient research and innovation require modern, fast, accurate, and cost-effective tools to identify the most productive and sustainable wheat production strategies using large sets of experimental trials (several thousand plots) that can be readily transferred and adopted by producers as quickly as possible. For field evaluations, it is prevalent to find applications of high-throughput methodologies based on remote sensing; in particular, the use of unmanned aerial vehicles has become a popular topic for supporting crop breeding (Yang et al., 2017) owing to its high capacity for screening large populations rapidly and the moderate costs in comparison to traditional phenotyping procedures (Araus and Cairns, 2014). Among all the indices used, the versatility and simplicity of the normalized difference vegetation index (NDVI) across crop species (Gao et al., 2020; Tenreiro et al., 2021) and the possibility of measurement across a variety of platforms (Araus et al., 2021) have prompted the widespread use of NDVI for phenotyping purposes. However, even if a close relationship between grain yield and vegetation indices has been demonstrated under a wide range of growing conditions, these approximations are not considered universal solutions, as some limitations have been reported. Challenges are mainly attributed to the saturation effect during dense canopy assessment (Duan et al., 2017). In contrast to NDVI, LiDAR is not affected by saturation at high ground cover and might be an alternative for biomass (Jimenez-Berni et al., 2018); however, these models still have limitations in predicting grain yield, and alternatives are necessary to increase the accuracy and precision of vegetation indices.

Alternative models have been explored and reported in the literature using plant height (PH) together with NDVI in herbaceous crops, such as perennial ryegrass, to estimate biomass (Gebremedhin et al., 2019). Other candidate traits, such as phenology, may provide important information regarding how wheat genotypes perform in a given environment (Lafitte et al., 2003) and can assist in-season selection. The measurement of wheat PH (Rebetzke and Richards, 2000) and phenology (Lopes et al., 2018) helps in understanding the sensitivity of crop production to fluctuating seasonal conditions, as the duration of developmental phases is a key determinant of genetic adaptation to the environment. Among the wheat yield components, ear density per unit of ground area has been considered an important agronomic trait (Pask et al., 2012) that can be easily measured with image analysis (Fernandez-Gallego et al., 2018) and may improve the accuracy of yield prediction models. The development of new grain yield (GY) prediction models, including NDVI together with additional easy-to-measure agronomic traits, has the potential to address the NDVI saturation issues described, and eventually improve yield predictions. To explore this hypothesis, two case studies were used and carefully selected to demonstrate and investigate the mechanisms associated with NDVI saturation. The first case study consisted of a set of data obtained from landraces and modern varieties, whereas the second case study was characterized by trials under various agronomic testing conditions and a wide range of GY variation. For these two case studies, calibration curves or training sets were developed using various model combinations of GY, NDVI, and other easy-to-measure traits, including phenology, PH, and ear density (EARS), using a reduced number of plots. These calibrations were then used to predict the yield of the remaining plots (validation sets) and the correlations between the predicted and observed yields obtained for the various sets to select the best and most universal model.

2 Materials and methods

2.1 Site description, plant material, and experimental design

2.1.1 Case study 1

Field experiments were conducted at an experimental station in Gimenells, Lleida, Spain 41°38′N, 00°22′E, 260 m a.s.l) in 2017 and 2018 under rainfed conditions. The environmental conditions of the study area are characterized by a temperate semi-arid climate with cool, wet winters, and dry and hot spring to summer seasons. The average annual precipitation is approximately 370 mm. The month with the lowest precipitation on average is July, with an average of 12.7 mm. The trials were sown on 21/11/2016 and 15/11/2017. In 2017 trial, after soil analysis, N, P and K were applied (pre-planting) to reach 50 kg of N/ha, 98 kg P/ha and 108 kg K/ha in the form of Calcium nitrate (NAC 27%), KCl and $Ca(H_2PO_4)_2$. At tillering, 150 kg N/ha in the form of Calcium nitrate (NAC 27%) were additionally applied. In 2018 trial, N content in the soil was more than 200 kg/ha and only P and K were applied at the same rates used in 2017. The experiments followed a non-replicated augmented design with two replicated checks ('Anza' and 'Soissons') and plots of 3.6 m^2 (1.2 m wide and 3 m long) with eight rows spaced 0.15 m apart. The seed rate was adjusted to 250 seeds per m^2 and the plots were kept free of weeds and diseases. The germplasm assessed in Case Study 1 comprised 365 bread wheat (*Triticum aestivum* L.) genotypes from a diverse panel of landraces and modern wheat varieties (Rufo et al., 2019). This dataset obtained from landraces was of particular interest in this study to determine the limitations and challenges in predicting yield using the NDVI; Wheat landraces have high biomass (similar or even higher than that of modern wheat varieties), and consequently, high NDVI; however, this type of plant material has low GY and low harvest index, creating a bias towards yield predictions when using NDVI and additional agronomic traits (see Supplementary Figure 1). The GY ranges for each germplasm and the growing season are listed in Table 1.

2.1.2 Case study 2

Field experiments were conducted at the experimental stations in Sucs, Lleida, Spain (41°38′N 00°22′E, 260 m a.s.l) in 2021, which

TABLE 1 Grain yield (GY, t ha_{-1}) means and standard deviation, number of plots, the minimum and maximum GY, and heritability (calculated only in replicated trials, H_2) evaluated for each germplasm set, group of varieties, and growing conditions.

Case Study	Year	Exp.	Water treatment	Date of sowing	Gen.	N	Mean GY	Lowest GY	Highest GY	H^2
1	2017	1	Rainfed	21/11/2016	354	Landrace, 170	5.10 ± 0.91	2.97	8.48	
						Modern, 184	9.48 ± 1.01	6.54	11.80	
	2018	1	Rainfed	15/11/2017	354	Landrace, 170	5.63 ± 0.82	3.65	8.99	
						Modern, 184	9.94 ± 0.98	6.93	12.40	
2	2021	1	Rainfed	27/12/2020	10	30	5.33 ± 1.61	1.87	9.00	0.688
		2	Irrigated	27/12/2020	10	30	8.87 ± 1.77	5.41	12.70	0.885
		3	Rainfed	03/12/2020	10	30	7.86 ± 2.17	3.77	11.83	0.776
		4	Irrigated	03/12/2020	10	30	10.32 ± 1.90	6.20	13.44	0.903
		5	Irrigated	03/12/2020	22	66	11.87 ± 1.54	8.05	14.64	0.678
		6	Irrigated	03/12/2020	22	66	10.55 ± 1.02	7.62	12.83	0.664
		7	Rainfed	03/12/2020	16	96	4.14 ± 1.09	2.17	7.18	0.697

is very close to the experimental station where Case Study 1 was conducted. A set of seven wheat experimental trials (with a total of 300 plots) conducted under rainfed and well-irrigated conditions with variable sowing dates and a diverse set of 39 modern wheat varieties were used to determine yield predictions. In all trials, after soil analysis, nitrogen contents in the soil were above 200 kg N/ha with no additional N requirements for optimal crop growth. Moreover, P and K were applied (pre-planting) to reach 98 kg P/ha and 108 kg K/ha with the same formulations used in case study 1. The experiments followed a replicated alpha-lattice design and plots of 9.6 m^2 with eight rows spaced 0.15 m apart. The seed rate was adjusted to 250 seeds per m^2, and the plots were kept free of weeds and diseases, as appropriate. This dataset is characterized by a wide range of GY variations retrieved from plots grown under various agronomic test conditions and sets of germplasm (all containing modern cultivated wheat varieties). This helped explore one of the limiting factors to NDVI prediction ability due to saturation. The GY ranges for each germplasm set and the growing season aspects are listed in Table 1.

2.2 Data acquisition and processing

In 2017 and 2018, remote sensing image acquisition was performed using a Parrot Sequoia multispectral camera onboard a hexacopter unmanned aerial vehicle. The Parrot Sequoia (Parrot, Paris, France) has a 1.2 mega-pixel sensor, yielding a resolution of 1280 × 960 pixels. The camera included four individual image sensors with filters centered at wavelengths and full-width half-maximum bandwidths (FWHM) of 550 ± 40 (green), 660 ± 40 (red), 735 ± 10 (red edge), and 790 ± 40 nm (near infrared). A Micasense RedEdge-M multispectral camera (Micasense, Seattle, Washington, USA) was used in 2021. This camera captured images at five spectral bands located at wavelengths of 475 ± 20 nm (blue), 560 ± 20 nm (green), 668 ± 10 nm (red), 717 ± 10 nm (red edge), and 840 ± 40 nm (near-infrared), and a field of view (FOV) of 47.2°. Image acquisition for all years was performed coinciding with the crop developmental stages of anthesis the 21/04/2017, 17/04/2018 and the 19/04/2021 (when more than 90% of the varieties reached anthesis). All flights were conducted at ~12:00 h solar time and at 40–50 m above ground level (agl), capturing images ground sampling distance of 50 m. The flight plan had an 80/60 frontal and side overlap. During image acquisition, *in situ* measurements were conducted for different targets to correct for atmospheric contributions to the signal. Radiometric calibration of the multispectral sensor was conducted using an external incident light sensor that measured the irradiance levels of light at the same bands as those of the camera. In addition to the radiometric corrections made by the internal solar irradiance sensor, corrections were conducted through *in situ* spectral measurements with black-and-white ground calibration targets, bare soil, and wheat plots using a JAZ-3 Ocean Optics STS VIS spectrometer (Ocean Optics, Inc., Dunedin, FL) with a wavelength response from 350 to 800 nm and an optical resolution of 0.3 to 10.0 nm. During spectral data collection, spectrometer calibration measurements were recorded with a reference panel (white color Spectralon^{TM}) and dark current before and after taking readings from the radiometric calibration targets. Geometric correction was conducted using ground control points. The position of each ground control point was acquired using a handheld global positioning system (Geo7x, Trimble GeoExplorer series, Sunnyvale, CA). All images were mosaicked using Agisoft Photoscan Professional version 1.6.2 (Agisoft LLC., St. Petersburg, Russia) software and geometric and radiometric terrain correction was performed using QGIS 3.4.15 (QGIS Development Team, Gossau, Switzerland). The NDVI values from each plot were calculated according to the equation shown below [1]:

$$NDVI = \frac{(R790 - R660)}{(R790 + R660)} \qquad [1]$$

The following agronomic traits were measured: phenology (days to heading, DH), plant height (PH), ear density (EARS), and GY (t ha^{-1}). Days to heading was measured as the number of days between sowing and the day when 50% of spikes emerged in a plot (Zadoks Stage 59, Zadoks et al., 1974). Plant height was measured near maturity in 10 main stems per plot from the tillering node to the top of the spike, excluding the awns. The EARS was measured by counting the number of ears in one linear meter in the middle of each plot and calculating the number of ears per unit area (1 m^2). Plots were mechanically harvested at ripening, and grain yield was calculated at 12% moisture.

2.3 Statistical analysis

Statistical analysis was performed using the open-source software R and RStudio 1.0.44 (R Foundation for Statistical Computing, Vienna, Austria), and all statistical analyses were equally applied in case studies 1 and 2. The strength of the relationships between the individual parameters DH, PH, EARS, NDVI and GY was examined using the Pearson correlation test. Broad sense heritability (H^2) was estimated for each trait individually in each environment (only for replicated trials) as:

$$H^2 = \frac{\sigma_g^2}{\left[\sigma_g^2 + \left(\frac{\sigma^2}{r}\right)\right]}$$

where r=number of repetitions, σ^2=error variance and $\sigma^2 g$ =genotypic variance.

A multivariate approach was used to develop yield predicting models and procedures are illustrated in the flowchart shown in Figure 1. Multivariate ridge regression was selected as a model-tuning method to overcome multicollinearity among traits (Hoerl and Kennard, 2000). More complex models as Artificial Neural Networks were also considered, reporting very similar prediction accuracies (data not shown). However, we decided to perform the data analysis with Ridge Regression as is less likely to overfit the data and it provides a direct interpretation of feature importance. To perform the Ridge Regression, we used the functions from the glmnet package (Friedman et al., 2010). First, the lambda value that produces the lowest test mean squared error (MSE) was identified by k-fold cross validation using k = 10 folds.

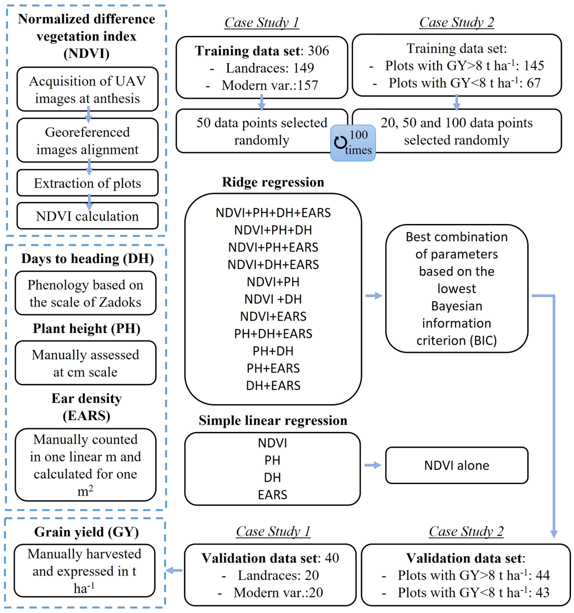

FIGURE 1
Flowchart of data acquisition and model elaboration. DH, days to heading; PH, plant height; NDVI, normalized difference vegetation index; EARS, ear density; UAV, unmanned aerial vehicle.

2.4 Calibration of the yield prediction models

In order to find the best parameter combination, all possible 15 different models were developed to predict yield, including: (i) NDVI, PH, DH and EARS, (ii) NDVI, PH and DH, (iii) NDVI, PH and EARS, (iv) NDVI, DH and EARS, (v) NDVI and PH, (vi) NDVI and DH, (vii) NDVI and EARS, (viii) PH, DH and EARS, (ix) PH and DH, (x) PH and EARS, (xi) DH and EARS, (xii) NDVI, (xiii) PH, (xiv) DH and (xv) EARS.

First, data was split into training data sets, used to build the models, and validation data sets, not included in the training data set to evaluate model accuracy. In Case Study 1, for each of the two growing seasons evaluated, a total of 40 plots (20 landraces and 20 modern varieties) were randomly selected for the validation set. In Case Study 2, the validation data sets were comprised by the experimental conditions 2, 3 and 4 (Table 1); and the other two were used as two independent validations set: the experimental condition 1 (rainfed and late-planting) as low yielding plots and the experimental condition 5 (irrigation and normal planting) as high yielding plots (Table 1). For Case Study 1, multiple and simple regression models were constructed using 50 randomly selected plots from the training data sets, whereas for Case Study 2, models were constructed using 20, 50 and 100 randomly selected plots from the training data sets. For each model, 100 iterations were performed and, in each iteration, random plots were used to develop models. The best performing models were selected based on the lowest Bayesian information criterion (BIC) in each calibration subset. The best multiple regression model together with the best simple NDVI regression was used to directly predict yield of the validation data sets. The coefficients of determination

(R^2), equation parameters, and associated probabilities were calculated for each yield multiple and simple regression models.

3 Results

3.1 Grain yield correlations with NDVI, PH, DH, and EARS

To assess the correlation between NDVI and grain yield (GY), Pearson correlation coefficients were calculated (Figure 2). Significant correlations were reported across the complete set of plots (R^2 = 0.259, R^2 = 0.239, and R^2 = 0.795; $p< 0.0001$), for the 2017, 2018 and 2021 growing seasons, respectively. For Case Study 1, significant correlations were only reported for modern varieties (R^2 = 0.116, and R^2 = 0.212; $p< 0.0001$) but not in landraces. For Case Study 2, these correlations were also significant, however, NDVI saturated and did not change when plots showed yields above 8 t ha^{-1} (Figure 2C). When NDVI-GY correlation was tested for the two groups (below and above 8 t ha^{-1}), regressions using data from plots with yields below 8 t ha^{-1} showed higher R^2 (R^2 = 0.548; $p< 0.0001$) than regression obtained from plots with yields above 8 t ha^{-1} (R^2 = 0.152; $p< 0.0001$). To determine if yield prediction models would improve with the inclusion of additional agronomic traits when NDVI saturates, modelling and validations were calculated in the two groups of plots separately (below and above 8 t ha^{-1}).

Likewise, correlations between plant height (PH), phenology (DH), and ear density (EARS) and grain yield (GY) were calculated (Figure 3). Significant correlations were reported between DH–GY (R^2 = 0.228, R^2 = 0.261, and R^2 = 0.356; $p< 0.0001$), and PH–GY (R^2 = 0.719, R^2 = 0.600, and R^2 = 0.510; $p< 0.0001$) across the complete set of plots for the 2017, 2018, and 2021 growing seasons, respectively. The correlation between EARS and GY was also significant in 2017 (R^2 = 0.055, $p< 0.0001$) and in 2021 (R^2 = 0.49, $p< 0.0001$) (Figure 3).

3.2 Development and validation of simple and multiple regression models to predict grain yield

The objective of this step was to determine the minimum number of plots required for accurate grain-yield predictions. Data from Case Study 2 was used in this step and models were built within the groups set in the Results section 3.1 of plots yielding over and below 8 t ha^{-1} (threshold yield for NDVI saturation). For the models developed using plots with yields over 8 t ha^{-1}, the best combination with the lowest Bayesian information criterion (BIC) was NDVI+DH (Supplementary Table 1). When models were trained using yields below 8 t ha^{-1}, the best model was the combination of NDVI+PH+DH+EARS when 20 data points were used as training sets and the combination of NDVI +DH+EARS with the 50 data point training sets. In that case, R^2 was improved and the RMSE reduced as the training sets were increased (Supplementary Table 1).

3.3 Development and validation of models to predict grain yield in various wheat genetic resources (landraces and modern varieties): Case study 1

Prediction models using all possible trait combinations were constructed with data from Case Study 1 within landraces, within

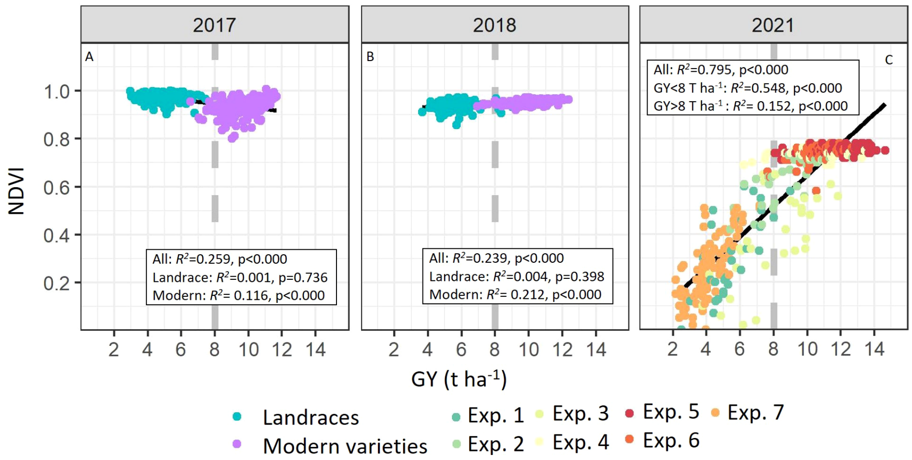

FIGURE 2
Linear relationships between grain yield (GY, t ha-1) with the normalized difference vegetation index (NDVI) measured at anthesis in Case Study 1 (**A**, 2017; **B**, 2018) and 2 (**C**, 2021). In case study 1 correlations were calculated separately in modern wheat varieties and landraces. In case study 2, correlations were also calculated separately in plots with yields below and above 8 t ha-1. Coefficients of determination (R2) and associated probabilities are shown. Dashed line represents the GY after which NDVI saturates. R2 within experimental conditions from case study 2 were 0.581 for Exp.1, 0.563 for Exp.2, 0.493 for Exp.3, 0.030 for Exp.4, 0.076 for Exp.5, 0.226 for Exp.6 and 0.549 for Exp.7.

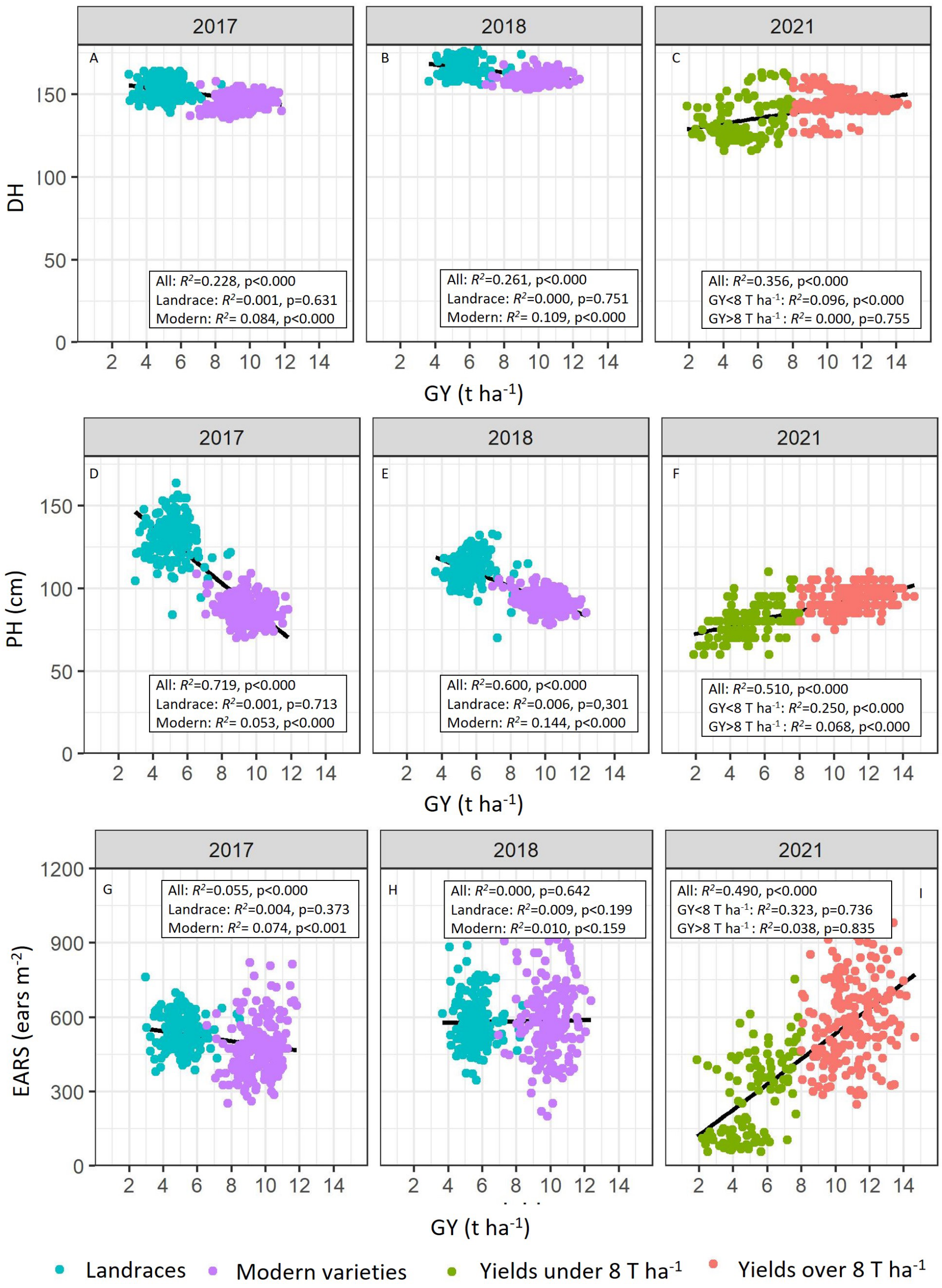

FIGURE 3

Linear relationships between grain yield (GY, t ha-1) and the number of days to heading (DH) (**A**, 2017; **B**, 2018; **C**, 2021), plant height (PH, cm) (**D**, 2017; **E**, 2018; **F**, 2021), and ear density (EARS, ears m-2) (**G**, 2017; **H**, 2018; **I**, 2021). Coefficients of determination (R2) and associated probabilities are shown.

modern varieties and across the combination of both (Supplementary table 2). Yield prediction models obtained from modern varieties were significant, however in Landraces neither multiple nor single regressions were significant (Supplementary Table 2). The best yield prediction models obtained from modern wheat varieties with the lowest BIC included NDVI+DH (R^2 =0.24 and RMSE=0.86) in 2017 and NDVI in 2018 (R^2 =0.20 and RMSE=0.88). When GY predictions were modeled using both landraces and modern varieties, best model with the lowest BIC included single regression with PH (R^2 =0.71) in 2017 and multiple regression of NDVI+PH+EARS (R^2 =0.69) in 2018, reporting the highest model accuracies in terms of R^2 but the highest RMSE (RMSE=1.29 and RMSE=1.31, respectively).

Given the challenge of predicting landrace yields with the proposed parameters (with non- significant regressions), only models developed using modern varieties were validated. For the validation, the best model with the lowest BIC (using 50 data points) was selected and its accuracy to predict yield was compared with the accuracy of the NDVI simple regression (Figure 4), considered herein the benchmark model. For each

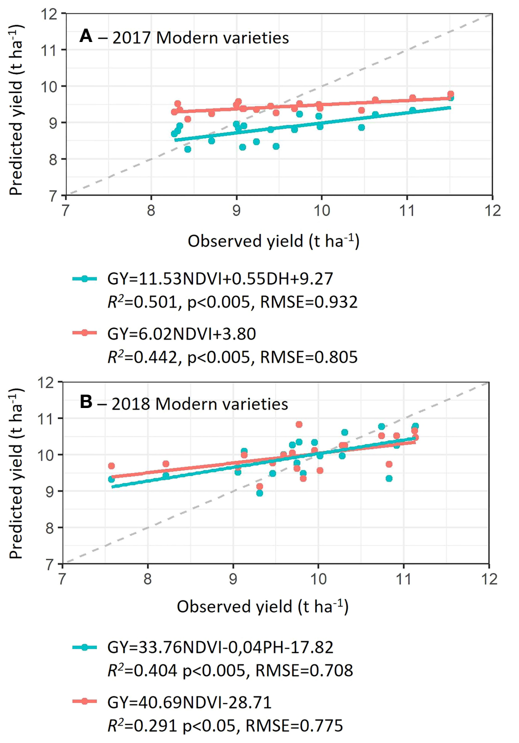

FIGURE 4
Prediction accuracies (coefficients of determination, R^2), root means square root (RMSE) and probability of models developed with 50 data points from Case Study 1 using modern varieties in 2017 **(A)** and 2018 **(B)**. Predicted yield values were calculated in 20 plots not used in the development of models (irrigated and optimal sowing date). Dashed line indicates a 1:1 correlation.

validation, one model from all the 100 runs calculated was selected by sorting all the BIC values and selecting a model with the median BIC. For both growing seasons, the addition of agronomic parameters together with NDVI, to predict yield improved the prediction accuracies in comparison to simple NDVI models (Figures 4A, B).

3.4 Development and validation of models to predict grain yield of wheat variety testing trials with yield below and above 8 t ha^{-1}: Case study 2

Following the same procedure as in Case Study 1, best parameter combination was assessed to predict GY in the validation sets while comparing its accuracy with simple NDVI models (Figure 5). When plots with yields over 8 t ha^{-1} were evaluated, the model combining NDVI with DH significantly improved the yield prediction (R^2 =0.595, $p<0.05$) compared to the model using solely NDVI (R^2 =0.150, ns). For the selection of plots with yields under 8 t ha^{-1}, even if the NDVI model reported a significant yield prediction (R^2 =0.536), the addition of DH and EARS improved yield predictions to R^2 =0.651 (Figure 5).

4 Discussion

4.1 Contributions of additional agronomic traits to improve remote sensing-based yield prediction models

Originally, NDVI was found to be an adequate indicator of plant biomass, chlorophyll content and N content (Stone et al., 1996; Babar et al., 2006; Tremblay et al., 2009; Hassan et al., 2019). Moreover, dynamic monitoring of NDVI in wheat trials to predict yield was later confirmed by direct correlations between NDVI and yield particularly at anthesis (Duan et al., 2017; Goodwin et al., 2018). Biomass, chlorophyll and Nitrogen content are physiological components of yield, however, biomass partition to yield may vary and higher biomass, chlorophyll and N may not result in higher yields. Herein, two case studies were used to determine the accuracy and reliability of the yield prediction ability of NDVI with agronomic traits such as DH, PH, and EARS. Overall, in both case studies, NDVI was, at least in plots with yields below 8 T ha^{-1} and using cultivated modern wheat varieties, an adequate predictor of yield (with prediction accuracies of up to R^2 =0.536; Figure 5B). The addition of agronomic traits such as DH to NDVI, in multiple regression models to predict yield improved prediction accuracies by up to 75% in plots with yields above 8 T ha^{-1} as compared to simple regression NDVI models. However, the accuracy obtained from multiple regression models (NDVI+DH+EARS was the best model with lowest BIC) to predict yields below 8 t ha^{-1} was 18% higher than simple regression models using NDVI. These results, support the hypothesis that the addition of simple to measure additional agronomic traits to NDVI in yield prediction models increased prediction acuracy. Moreover, phenology, i.e. (days to heading, DH), plant height (PH), ear density (EARS) are agronomic traits which all have the potential to be measured non-destructively in high throughput using proximal and aerial sensing devices. Potentially, in the future, yields will be accurately predicted using functions that model contributions of these various traits reducing harvest costs of breeding programs.

4.2 Mechanisms of NDVI saturation and underestimation of productivity

The assumptions of a linear relationship between GY and NDVI are not always fulfilled because of the reduced sensitivity of this vegetation index to large biomass (Huete et al., 1985). One of the most prominent and discussed limitations of remote-sensing-based studies is the saturation found with dense canopies, which underestimates productivity (Chen et al., 2006; Gu et al., 2013). Herein, saturation at high NDVI values is clearly demonstrated in case studies 1 and 2. In Case Study 1, yield in wheat landraces was weakly correlated with NDVI and additional easy-to-measure agronomic traits, such as DH, PH, and EARS. Moreover, yield prediction models using these traits in landraces were never adequate showing non-significant R^2. Compared to semi-dwarf

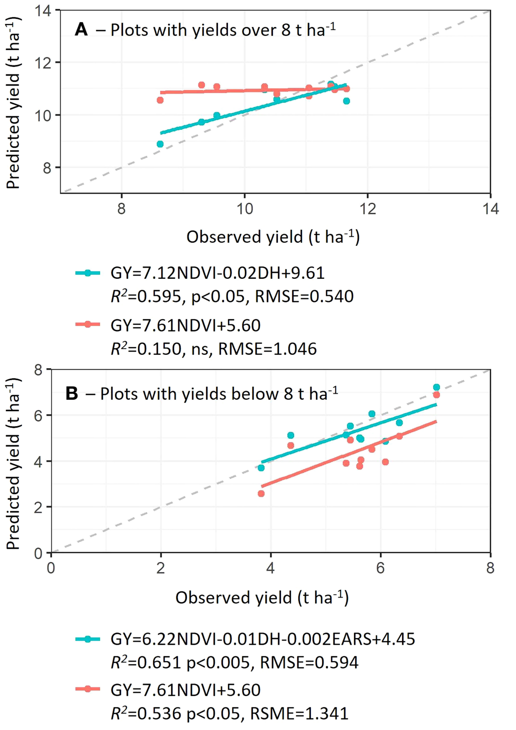

FIGURE 5
Prediction accuracies (coefficients of determination, R^2), root means square root (RMSE) and probability of models developed with 50 data points from Case Study 2 using plots with yields over and below 8 t ha^{-1} **(A, B)**, respectively. Predicted yield values were calculated in 10 plots not used in the development of models (rainfed and late sowing). Dashed line indicates a 1:1 correlation.

cultivars with a high harvest index, landraces show relatively high biomass and high or similar NDVI (see Figures 2A, B), whereas yields and harvest index are low (Jaradat, 2013; Lopes et al., 2015 and Supplementary Figure 1) resulting in poor correlation and prediction ability. It has been previously reported that reductions in plant height and biomass associated with the Rht-B1b (formerly Rht1) and Rht-D1b (formerly Rht2) alleles in modern varieties increased grain yield, spike dry matter, grains m^{-2} and harvest index (Gale and Youssefian, 1985; Flintham et al., 1997) at the expense of stem dry matter (Fischer, 1985). The mechanisms underlying this trade-off are yet to be discovered, however, the results observed by Fischer (1985) and Flintham et al. (1997) support our observations that biomass in tall landraces (and high NDVI) is increased at the expense of yield loss. As such, higher biomass and NDVI in the landraces did not result in higher yields in this set of germplasm. It is concluded that the yield of landraces must be assessed directly and traditionally harvested and weighted due to a lack of yield prediction accuracy from models developed with NDVI and additional agronomic traits.

Further evidence of productivity saturation underestimation was observed in Case Study 2, where NDVI and yield prediction models were less robust, at yields above 8 t ha^{-1} and NDVI above 0.75. This can be explained by differences in grain yield components in high-yielding plots, including grain number and size (Sukumaran et al., 2018) which NDVI alone cannot detect. However, when DH was included in the prediction models, the accuracies were considerably improved (to R^2 =0.595). These results highlight the importance of developing new and more sensitive indices (Huete et al., 2002; Gracia-Romero et al., 2019) to improve performance predictions under high-yielding conditions together with the inclusion of easy to measure additional agronomic traits in prediction models.

4.3 Can NDVI measurements replace machine-harvested and seed-weighted yield determination in experimental wheat field trials?

The development of accurate yield prediction models is of key importance to facilitate the adoption of new wheat varieties and best agronomic practices. If sufficiently solid algorithms with reduced error in assessing GY are achieved, it might be possible to avoid the harvest of the whole panel of experimental plots, reducing the costs and efforts of the selection process. The actual replacement of labor-intensive harvested yields determined by machine harvest and seed weight in the field with yields predicted from NDVI and agronomic trait based models would be particularly useful for multi-location trials where seed recovery is not essential. Most countries worldwide perform regional evaluations of value for cultivation and use testing, and these networks would benefit from accurate yield prediction models.

The methodology proposed in this study suggests using a reduced number of wheat plots in experimental field trials to calibrate an optimized model to predict the yield of the remaining plots. A similar evaluation of the calibration and training size was presented by Tehseen et al. (2021), who demonstrated the effect of different population sizes of landraces in developing genome prediction methods and assisting the selection of rust-resistant wheat genotypes. Herein, the larger the training sets were, the more robust the models were, however, mean accuracies were very similar among the dataset sizes evaluated as the loss of predictive accuracy was reasonably small when the number of replicates sampled for the training set was reduced to 20 in comparison to the sets with 100 plots. Thus, following a plot selection criterion based on NDVI and additional agronomic traits, could help reduce the number of field plots to be machine harvested for calibration of the model. Moreover, to avoid NDVI saturation at high yielding growth conditions, calibration models must be developed separately according to data obtained from different treatments either with optimal crop management or with yield limiting factors (e.g. drought, heat or others) requiring separate model training.

To date, many studies have used different empirical models developed using NDVI to successfully predict wheat GY. However, most of the highest predictions are based on using accumulated NDVI values across crop development stages and collecting data across different years (as Aranguren et al. (2020) with R^2 = 0.89 and n = 204) or combining information from different study sites and using satellite information (as Lopresti et al. (2015) with R^2 = 0.56 and n = 90). In similar evaluations (data across a single growing season and from a unique experimental field) when GY differences are evaluated among genotypes grown under irrigated (i.e., high-yielding conditions), prediction accuracies are limited (as Naser et al. (2020) r = 0.47 and n = 72). Given the reported improvements achieved with the addition of DH, PH, and EARS to the models, opportunities to find proxies capable of evaluating those parameters directly from NDVI and high-throughput platforms will help to better select varieties in a cost-effective manner.

5 Conclusions

The proposed models combining NDVI with additional agronomic traits improved GY prediction of wheat varieties compared to models using NDVI as the sole predictor. These demonstrations will benefit the application of remote sensing in breeding programs, thereby providing more confidence in the selection of varieties using proxies. Remote sensing-based models showed a high potential to discriminate between wheat genotypes within a field, but only at GY lower than 8 t·ha^{-1}, after which the GY prediction models were less robust. Similarly, the accuracy was reduced when landraces were assessed. Accuracy reduction was associated with NDVI saturation owing to (i) high biomass and low harvest index in landraces and (ii) under high yielding conditions when wheat varieties share high biomass but differ in other yield components (grain size and number). Therefore, using conventional harvest is advisable when testing landraces and adaptation to yield potential conditions (high yield with optimal agronomic management), at least until novel or improved models are available.

Data availability statement

The raw data supporting the conclusions of this article will be made available by the authors, without undue reservation.

Author contributions

AG-R analyzed the data and wrote the manuscript. RR collected and processed the data. DG-C collected and processed the data and reviewed and edited the manuscript. JS reviewed and edited the manuscript. JB collected and processed the data and reviewed and edited the manuscript. VRRY reviewed and edited the manuscript. DG reviewed and edited the manuscript. MSL designed the study and prepared the manuscript. All authors contributed to the article and approved the submitted version.

Funding

This study was funded by the projects AGL2015-65351-R, PID2019-109089RB-C31 and TED2021-131606B-C21 of the Spanish Ministry of Economy and Competitiveness. AG-R was funded by a Margarita Salas post-doctoral contract from the Spanish Ministry of Universities affiliated to the Research Vice-Rector of the University of Barcelona. VRRY was funded by a pre-doctoral contract from the Spanish Ministry of Economy and Competitiveness (PRE2020-092369). The funders had no role in the study design, data collection and analysis, decision to publish, or manuscript preparation.

Acknowledgments

The authors acknowledge the contribution of the CERCA Program (Generalitat de Catalunya). The authors acknowledge Andrea Lopez, Ezequiel Arqué, Jordi Companys, and Josep Millera for their technical contributions to the experimental setup of field trials.

Conflict of interest

The authors declare that the research was conducted in the absence of any commercial or financial relationships that could be construed as a potential conflict of interest.

Publisher's note

Supplementary material

The Supplementary Material for this article can be found online at: https://www.frontiersin.org/articles/10.3389/fpls.2023.1063983/full#supplementary-material

References

Aranguren, M., Castellón, A., and Aizpurua, A. (2020). Wheat yield estimation with NDVI values using a proximal sensing tool. *Remote Sens* 12(17), 2749. doi: 10.3390/rs12172749

Araus, J. L., and Cairns, J. E. (2014). Field high-throughput phenotyping: The new crop breeding frontier. *Trends Plant Sci.* 19, 52–61. doi: 10.1016/j.tplants.2013.09.008

Araus, J. L., Kefauver, S. C., Díaz, O. V., Gracia-Romero, A., Rezzouk, F. Z., Segarra, J., et al. (2021). Crop phenotyping in a context of global change: What to measure and how to do it. *J. Integr. Plant Biol.* 64, 592–618. doi: 10.1111/jipb.13191

Babar, M. A., Reynolds, M. P., van Ginkel, M., Klatt, A. R., Raun, W. R., and Stone, M. L. (2006). Spectral reflectance to estimate genetic variation for in-season biomass, leaf chlorophyll, and canopy temperature in wheat. *Crop Sci.* 46, 1046–1057. doi: 10.2135/cropsci2005.0211

Chen, P.-Y., Fedosejevs, G., Tiscareño-López, M., and Arnold, J. (2006). Assessment of MODIS-EVI, MODIS-NDVI and vegetation-NDVI composite data using agricultural measurements: an example at corn fields in western Mexico. *Environ. Monit. Assess* 119, 69–82. doi: 10.1007/s10661-005-9006-7

Duan, T., Chapman, S. C., Guo, Y., and Zheng, B. (2017). Dynamic monitoring of NDVI in wheat agronomy and breeding trials using an unmanned aerial vehicle. *F Crop Res.* 210, 71–80. doi: 10.1016/j.fcr.2017.05.025

Fernandez-Gallego, J. A., Kefauver, S. C., Gutiérrez, N. A., Nieto-Taladriz, M. T., and Araus, J. L. (2018). Wheat ear counting in-field conditions: High throughput and low-cost approach using RGB images. *Plant Methods* 14, 22. doi: 10.1186/s13007-018-0289-4

Fischer, R. A. (1985). Number of kernels in wheat crops and the influence of solar radiation and temperature. *J. Agric. Sci.* 105, 447–461. doi: 10.1017/S0021859600056495

Fischer, T., Ammar, K., Monasterio, I. O., Monjardino, M., Singh, R., and Verhulst, N. (2022). Sixty years of irrigated wheat yield increase in the yaqui valley of Mexico: Past drivers, prospects and sustainability. *F Crop Res.* 283, 108528. doi: 10.1016/j.fcr.2022.108528

Flintham, J. E., Borner, A., Worland, A. J., and Gale, M. D. (1997). Optimizing wheat grain yield: effects of rht (gibberellin-insensitive) dwarfing genes. *J. Agric. Sci.* 128, 11–25. doi: 10.1017/S0021859696003942

Gale, M. D., and Youssefian, S. (1985). "Dwarfing genes in wheat," in *Progress in plant breeding*. Ed. G. E. Russell (London, United Kingdom: Butterworths), 1–35.

Gao, L., Wang, X., Johnson, B. A., Tian, Q., Wang, Y., Verrelst, J., et al. (2020). Remote sensing algorithms for estimation of fractional vegetation cover using pure vegetation index values: A review. *ISPRS J. Photogramm Remote Sens* 159, 364–377. doi: 10.1016/j.isprsjprs.2019.11.018

Gebremedhin, A., Badenhorst, P., Wang, J., Giri, K., Spangenberg, G., and Smith, K. (2019). Development and validation of a model to combine NDVI and plant height for high-throughput phenotyping of herbage yield in a perennial ryegrass breeding program. *Remote Sens* 11(21), 2494. doi: 10.3390/rs11212494

Goodwin, A. W., Lindsey, L. E., Harrison, S. K., and Paul, P. A. (2018). Estimating wheat yield with normalized difference vegetation index and fractional green canopy cover. *Crop Forage Turf Man* 4 (1), 1–6. doi: 10.2134/cftm2018.04.0026

Gracia-Romero, A., Kefauver, S. C., Fernandez-Gallego, J. A., Vergara-Díaz, O., Nieto-Taladriz, M. T., and Araus, J. L. (2019). UAV and ground image-based phenotyping: A proof of concept with durum wheat. *Remote Sens* 11(10), 1244. doi: 10.3390/rs11101244

Gu, Y., Wylie, B. K., Howard, D. M., Phuyal, K. P., and Ji, L. (2013). NDVI saturation adjustment: A new approach for improving cropland performance estimates in the greater platte river basin, USA. *Ecol. Indic* 30, 1–6. doi: 10.1016/j.ecolind.2013.01.041

Hassan, M. A., Yang, M., Rasheed, A., Yang, G., Reynolds, M., Xia, X., et al. (2019). A rapid monitoring of NDVI across the wheat growth cycle for grain yield prediction using a multi-spectral UAV platform. *Plant Sci.* 282, 95–103. doi: 10.1016/j.plantsci.2018.10.022

Hoerl, A. E., and Kennard, R. W. (2000). Ridge regression: Biased estimation for nonorthogonal problems. *Technometrics* 42, 80–86. doi: 10.1080/00401706.2000.10485983

Huete, A., Didan, K., Miura, T., Rodriguez, E. P., Gao, X., and Ferreira, L. G. (2002). Overview of the radiometric and biophysical performance of the MODIS vegetation indices. *Remote Sens Environ.* 83, 195–213. doi: 10.1016/S0034-4257(02)00096-2

Huete, A. R., Jackson, R. D., and Post, D. F. (1985). Spectral response of a plant canopy with different soil backgrounds. *Remote Sensing of Environment* 17, 37–53. doi: 10.1016/0034-4257(85)90111-7

Jaradat, A. A. (2013). Wheat landraces: A mini review. *Emirates J. Food Agric.* 25, 20–29. doi: 10.9755/ejfa.v25i1.15376

Jimenez-Berni, J. A., Deery, D. M., Rozas-Larraondo, P., Condon, A. T. G., Rebetzke, G. J., James, R. A., et al. (2018). High throughput determination of plant height, ground cover, and above-ground biomass in wheat with LiDAR. *Front. Plant Sci.* 9, 1–18. doi: 10.3389/fpls.2018.00237

Lafitte, R., Blum, A., and Atlin, G. (2003) *Using secondary traits to help identify drought-tolerant genotypes*. Available at: http://books.irri.org/9712201899_content.pdf#page=44%5Cnhttp://books.google.de/books?hl=de&lr=&id=eiuo-UrnItMC&oi=fnd&pg=PA37&dq=breeding+rice+for+drought-prone+environments&ots=tqNxcTFOB4&sig=7E0E2LfZnSXOwHMYsuR2LgKPLAc.

Lopes, M. S. (2022). Will temperature and rainfall changes prevent yield progress in Europe? *Food Energy Secur* 11, 1–12. doi: 10.1002/fes3.372

Lopes, M. S., El-Basyoni, I., Baenziger, P. S., Singh, S., Royo, C., Ozbek, K., et al. (2015). Exploiting genetic diversity from landraces in wheat breeding for adaptation to climate change. *J. Exp. Bot.* 66, 3477–3486. doi: 10.1093/jxb/erv122

Lopes, M. S., Royo, C., Alvaro, F., Sanchez-Garcia, M., Ozer, E., Ozdemir, F., et al. (2018). Optimizing winter wheat resilience to climate change in rain fed crop systems of Turkey and Iran. *Front. Plant Sci.* 9, 1–14. doi: 10.3389/fpls.2018.00563

Lopresti, M. F., Di Bella, C. M., and Degioanni, A. J. (2015). Relationship between MODIS-NDVI data and wheat yield: A case study in northern Buenos Aires province, Argentina. *Inf. Process Agric.* 2, 73–84. doi: 10.1016/j.inpa.2015.06.001

Naser, M. A., Khosla, R., Longchamps, L., and Dahal, S. (2020). Using NDVI to differentiate wheat genotypes productivity under dryland and irrigated conditions. *Remote Sens* 12(5), 824. doi: 10.3390/rs12050824

Pask, A., Pietragalla, J., Mullan, D., and Reynolds, M. P. W. (2012). "Physiological breeding II: A field guide to wheat phenotyping," in *Encyclopedic dictionary of polymers*. (Mexico: CIMMYT)

Rebetzke, G. J., and Richards, R. A. (2000). Gibberellic acid-sensitive dwarfing genes reduce plant height to increase kernel number and grain yield of wheat. *Aust. J. Agric. Res.* 51, 235–246. doi: 10.1071/AR99043

Rufo, R., Alvaro, F., Royo, C., and Soriano, J. M. (2019). From landraces to improved cultivars: Assessment of genetic diversity and population structure of Mediterranean wheat using SNP markers. *PloS One* 14 (7), e0219867. doi: 10.1371/journal.pone.0219867

Stone, M. L., Solie, J. B., Raun, W. R., Whitney, R. W., Taylor, S. L., and Ringer, J. D. (1996). Use of spectral radiance for correcting in-season fertilizer nitrogen deficiencies in winter wheat. *Trans. ASAE* 39 (5), 1623–1631. doi: 10.13031/2013.27678

Sukumaran, S., Lopes, M., Dreisigacker, S., and Reynolds, M. (2018). Genetic analysis of multi-environmental spring wheat trials identifies genomic regions for locus-specific trade-offs for grain weight and grain number. *Theor. Appl. Genet.* 131, 985–998. doi: 10.1007/s00122-017-3037-7

Tehseen, M. M., Kehel, Z., Sansaloni, C. P., Lopes, M., da, S., Amri, A., et al. (2021). Comparison of genomic prediction methods for yellow, stem, and leaf rust resistance in wheat landraces from afghanistan. *Plants* 10, 1–15. doi: 10.3390/plants10030558

Tenreiro, T. R., García-Vila, M., Gómez, J. A., Jiménez-Berni, J. A., and Fereres, E. (2021). Using NDVI for the assessment of canopy cover in agricultural crops within modelling research. *Comput. Electron. Agric.* 182. doi: 10.1016/j.compag.2021.106038

Tremblay, N., Wang, Z., Ma, B. L., Belec, C., and Vigneault, P. (2009). A comparison of crop data measured by two comercial sensors for variable-rate nitrogen application. *Precis. Agric.* 10, 145–161. doi: 10.1007/s11119-008-9080-2

Yang, G., Liu, J., Zhao, C., Li, Z., Huang, Y., Yu, H., et al. (2017). Unmanned aerial vehicle remote sensing for field-based crop phenotyping: Current status and perspectives. *Front. Plant Sci.* 8. doi: 10.3389/fpls.2017.01111

Zadoks, J. C., Chang, T. T., and Konzak, C. F. (1974). A decimal code for the growth stages of cereals. *Weed Res.* 14, 415–421. doi: 10.1111/j.1365-3180.1974.tb01084.x

Frontiers in Plant Science

TYPE Perspective
PUBLISHED 16 May 2023
DOI 10.3389/fpls.2023.1114670

OPEN ACCESS

EDITED BY
Sindhuja Sankaran,
Washington State University, United States

REVIEWED BY
Afef Marzougui,
University of California, Davis, United States

*CORRESPONDENCE
Urs Schulthess
u.schulthess@cgiar.org

RECEIVED 02 December 2022
ACCEPTED 12 April 2023
PUBLISHED 16 May 2023

CITATION
Pinto F, Zaman-Allah M, Reynolds M and Schulthess U (2023) Satellite imagery for high-throughput phenotyping in breeding plots.
Front. Plant Sci. 14:1114670.
doi: 10.3389/fpls.2023.1114670

Satellite imagery for high-throughput phenotyping in breeding plots

Francisco Pinto[1], Mainassara Zaman-Allah[2], Matthew Reynolds[1] and Urs Schulthess[3]*

[1]Global Wheat Program, International Maize and Wheat Improvement Center (CIMMYT), Texcoco, Mexico, [2]Global Maize Program, International Maize and Wheat Improvement Center (CIMMYT), Southern Africa Regional Office, Harare, Zimbabwe, [3]CIMMYT-China Wheat and Maize Joint Research Center, Agronomy College, Henan Agricultural University, Zhengzhou, China

Advances in breeding efforts to increase the rate of genetic gains and enhance crop resilience to climate change have been limited by the procedure and costs of phenotyping methods. The recent rapid development of sensors, image-processing technology, and data-analysis has provided opportunities for multiple scales phenotyping methods and systems, including satellite imagery. Among these platforms, satellite imagery may represent one of the ultimate approaches to remotely monitor trials and nurseries planted in multiple locations while standardizing protocols and reducing costs. However, the deployment of satellite-based phenotyping in breeding trials has largely been limited by low spatial resolution of satellite images. The advent of a new generation of high-resolution satellites may finally overcome these limitations. The SkySat constellation started offering multispectral images at a 0.5 m resolution since 2020. In this communication we present a case study on the use of time series SkySat images to estimate NDVI from wheat and maize breeding plots encompassing different sizes and spacing. We evaluated the reliability of the calculated NDVI and tested its capacity to detect seasonal changes and genotypic differences. We discuss the advantages, limitations, and perspectives of this approach for high-throughput phenotyping in breeding programs.

KEYWORDS

high-throughput phenotyping, satellite, wheat, maize, breeding, normalized difference vegetation index, optimized soil adjusted vegetation index

1 Introduction

Climate change causes widespread changes in weather patterns and therefore poses new challenges for plant breeders (Stamp and Visser, 2012; Xiong et al., 2022). To strategically plan for future crop genetics, plant breeders must consider how to assess germplasm performance in locations that better represent their future environments – i.e. climate analogue sites – which are likely further from their research stations and possibly in another country or continent, where frequent data collection may be challenged by the availability of trained personnel, travel, logistics and equipment. In addition, multi-environment trials (METs) are needed to enable prediction of genotype reaction-norms (van Eeuwijk et al., 2019; Cooper and Messina, 2021). These prediction models tend to be based on markers, big data and machine learning approaches, and they strongly rely on a standardized, quality-controlled set of data from many different environments. Since the contribution of a gene to a trait can vary depending on environmental conditions, the results of genomic selection, genome wide association studies (GWAS) and other genomics-driven breeding and research methods will be more precise and relevant if run using phenomic data from numerous locations representing the diversity among growing environments (Korte and Ashley, 2013; Jarquín et al., 2014).

Accurately linking genotypes to phenotypes requires large populations of replicated genotypes, which can be costly to evaluate, especially at multiple locations (Furbank and Tester, 2011). Furthermore, bias due to differences in specifications of instruments or their handling, human error, as well as poor plot quality due to irregular emergence and soil heterogeneity can render big data analyses useless. These challenges limit the scalability of current phenotyping techniques across diverse environments, especially when linking the phenomic data to genomic data. Genetics-based breeding technologies, such as genomic selection, speed breeding and gene editing (CRISPR/CAS), offer ways to accelerate breeding, but their value is limited by the quality and relevance of phenotypic data. Consequently, standardized phenotyping of experiments or nurseries grown at different locations has remained a bottleneck for the use of phenomic data in genomic analyses (Crossa et al., 2021).

High resolution satellites may contribute to address this bottleneck, and have been recently tested for monitoring small plots (Tattaris et al., 2016; Sankaran et al., 2020; Sankaran et al., 2021). However, apart from being relatively costly, the resolution of the multispectral bands used to be coarser than 1 m. This changed with the launch of the Pleiades (Airbus, 2022) and SkySat (Planet, 2022a) constellations. The fleet of 21 high resolution (0.5 m) SkySat satellites became fully operational in the fall of 2020. Daily acquisitions attempts are now guaranteed, resulting in at least one cloud free image every 7 to 10 days for most regions on Earth. This opens up the opportunity to monitor and phenotype breeding plots across diverse environments over an entire growing season with identical measurement protocols.

2 Perspective: harnessing multi-temporal high resolution satellite images for monitoring breeding plots in diverse environments

Many of the variables collected in crop phenotyping can potentially be generated from satellite images. The SkySat sensors have 4 spectral bands: blue, green, red and infrared. They can be used to calculate the normalized difference vegetation index (NDVI), which is a measure of the amount of vegetation and its greenness, and other bio-physical parameters, including plot establishment, and various canopy traits, such as ground cover (fCover), leaf area and chlorosis (Jin et al., 2021). Using a time series of standardized images, date of emergence, end of leaf growth (which is an approximation of heading or tasseling date), and senescence or maturity can also be estimated (Jönsson and Eklundh, 2004; Pérez-Valencia et al., 2022). From a series of images covering the entire growing period, the performance of selected lines can be evaluated under specific weather conditions around the time that they occur, such as cold or dry spells and heat waves. In this context, satellite-generated phenotypic data from METs can be easily complemented with information on the dynamics of the environments retrieved from weather station networks or the global ECMWF Reanalysis products AgERA5 (Boogaard et al., 2020) and ERA5 (Hersbach et al., 2018). These products provide daily or hourly weather data at a resolution of either 10 or 30 km in close to real time, allowing better enviromics for the optimization of prediction models within the framework of the modern plant breeding triangle (Crossa et al., 2021; Resende et al., 2021).

Satellite images would enable breeders and researchers to monitor their field-plots in a single time-point (for each image), across a time-span (multiple images), and collect performance data on germplasm throughout a season at locations around the globe. In addition, since each satellite image covers an entire research field, genotypes across a field trial can be effectively compared without the potentially confounding effect of time (compared to physically carrying a hand-held tool to each plot in the field while ambient conditions are drifting). Plot level data collected by satellites can also be used to compare plot quality and to perform statistical correction for spatial heterogeneity in the field that can otherwise confound the expression of yield and other traits. They also allow for quality control and verification of reported data, such as date of sowing and management of the plots according to protocol. The use of satellite data will ultimately allow for the inclusion of larger nurseries (more lines) and more locations. Biases due to differences in instruments, human or other experimental errors will be reduced, resulting in standardized, multi-temporal data sets that allow for comparisons among sites in close to real time.

However, nursery plots for wheat and maize, as well as for other crops, tend to be relatively small. Plots tend to measure 2 or more meters in length, but plot width might be a bottleneck for the use of satellite images. For maize, breeders plant 1 or 2 rows, whereas for wheat, plots usually consist of 2 to 6 rows. This results in plots that tend to be between 0.7 m (one row of maize) to 1.2 to 1.6 m wide, which may pose some challenges for the use of 0.5 m satellite data to capture pure vegetation pixels and avoid mixed pixels affected by the signal from soil surfaces or neighboring plots. The native resolution, or ground sampling distance (GSD) of SkySat images depends on the view angle of the satellite among others. The resolution of the multispectral bands at nadir is 0.81 m for SkySat-3 to 15 and 0.72 m for SkySat-16 to 21 (Planet, 2022b). To align the satellite images with each other, they need to be orthorectified (Leprince et al., 2007). During the orthorectification process, the images are being resampled to a standard resolution of 0.5 m. Thus, a SkySat, or any other pixel of a satellite image, is not an exact representation of the area it covers on the ground (Saunier et al., 2022). Other technical factors such as radiometric calibration, atmospheric correction and the point spread function of the sensor can also affect the quality of the data, being especially relevant when using time series and multi-environment comparisons. To assess the potential and limitations of the use of SkySat images for phenotyping, we conducted separate field campaigns in Mexico and Zimbabwe.

3 Case study

We used time series of SkySat imagery to estimate the NDVI ($NDVI_{SAT}$) from wheat breeding plots. The $NDVI_{SAT}$ values were evaluated in terms of their reliability—i.e. capacity to detect genotypic differences, and how observed seasonal changes were related to crop phenology—and how they are affected by the plot size and spacing; all this while comparing $NDVI_{SAT}$ to NDVI calculated from a UAV ($NDVI_{UAV}$) at different moments during the growing cycle in wheat and maize, respectively.

A dedicated wheat experiment for assessing the effect of plot size and spacing in $NDVI_{SAT}$ was planted at CIMMYT headquarters, Texcoco, Mexico (19.5338° N, 98.8428° W, 2,278 masl), under optimal growing conditions. A spring wheat panel comprising 10 genotypes from the Roots Anatomy panel was planted in six treatments resulting from the combination of two plot widths of 0.8 and 1.6 m (referred as small and big plots) and three spacings between plots of 0.5, 0.75 and 1.5 m in all directions (Figures 1A, B). The small and big plots had two and six rows of plants, respectively, and the same plot length of 2.5 m. Each treatment had an α-lattice design with two replicates, resulting in twenty plots per treatment. This experimental design is commonly used in breeding trials. The experiment was sown on 27 May and harvested on 5 October 2021. Aerial high-resolution multispectral images (GSD ~ 0.017 m) were collected at 25 m altitude using a RedEdge (Micasense, USA) multispectral camera mounted on a UAV (Matrice 100, DJI, China). The images were georeferenced using ground control points distributed along the field, and the spectral reflectance was calculated using a calibration target (Micasense, USA). A commercial software (Pix4D, Switzerland) was used to mosaic the images from which $NDVI_{UAV}$ was extracted for each plot. The UAV images were collected across the cycle as close as possible to the satellite acquisitions (Supplementary Table S1).

Time series of SkySat multispectral images were collected over the wheat experiments starting from canopy closure. The acquisitions targeted a revisit frequency of 7 to 10 days. In order to limit BRDF effects (Royer et al., 1985) and distortion in GSD, maximum view angle was restricted to 16°. $NDVI_{SAT}$ was calculated using the RED and NIR bands from the SkySat surface reflectance product (Planet, 2022b). Additionally, the Optimized Soil Adjusted Vegetation Index (OSAVI, Rondeaux et al., 1996) was calculated to mitigate the potential impact that soil brightness can have on NDVI, especially with larger plot spacing. A total of six satellite acquisitions were obtained during the cycle (Supplementary Table S1). For the extraction of NDVI and OSAVI, we first manually drew the plot boundaries based on an accurately geo-referenced UAV image. Using ArcGIS georeferencing tool, we then shifted the satellite images so that they would align with the plot boundaries. For this we employed sharp edges in the scenery as references, such as road corners and trial boundaries. After applying a 15 cm in-side buffer to the plot boundaries, we extracted the NDVI values with the R-library raster v3.6.3 using the normalizeWeights option, which accounts for the proportion of each pixel that falls in a polygon. The best linear unbiased estimators (BLUEs; Bernal-Vasquez et al., 2016) of the remote sensing data were calculated for each genotype using the R-package “asreml-R” version 4.1.0.160.

We also collected satellite images over maize breeding nurseries located in Muzarabani, Zimbabwe (16.3972° S, 31.0160° E, 498 masl). Three images were collected over the cycle starting from mid vegetative stage. However, UAV measurements were not available on site and satellite data could only be compared to NDVI readings measured with a hand-held optical sensor with adjustable arm (GreenSeeker, Trimble, USA). Therefore, details on the maize experiment and results are presented as supplementary material (Supplementary Figure S1).

A visual assessment of satellite images indicates that individualization of plots represents one of the challenges for extracting quality phenotypic data. Wheat plot boundaries were visually evident only for plots with a spacing of 0.75 m and 1.5 m (Figure 1B). In general, the increase of plot size and plot spacing resulted in higher and more significant correlations between satellite and UAV data, possibly due to better plot individualization (Figures 1C, D). In maize, plots were sown without spacing in between, hindering the visualization of plot boundaries. But the ranges as well as the edges of the experiment were clearly visible (Supplementary Figure S1B).

Given the satellite resolution and plot size, $NDVI_{SAT}$ is expected to be affected by mixed pixels. The values of $NDVI_{SAT}$ were much lower and showed a larger range between treatments in comparison to $NDVI_{UAV}$ in all the dates (Figure 1C). While $NDVI_{UAV}$ showed values close to saturation after canopy closure, $NDVI_{SAT}$ ranged between 0.45 and 0.65, suggesting a degradation of the signal due to contamination from the neighboring bare soil. The $OSAVI_{SAT}$ also showed lower values than $OSAVI_{UAV,}$ except for the treatments with 0.5 inter-plot spacing where values were within the same range (Figure 1D). When plot spacing was increased, $OSAVI_{SAT}$ decreased considerably to values much lower than those calculated from the UAV. A small inter-plot spacing facilitates the pollution of pixels by neighboring plots in the satellite data, which could explain the higher $NDVI_{SAT}$ and $OSAVI_{SAT}$ in plots with 0.5 m distance compared to wider plot spacing. In contrast, adding space between plots may imply a larger mixing of vegetation and bare soil spectra, decreasing the $NDVI_{SAT}$ and $OSAVI_{SAT}$. Conversely, the higher resolution of the UAV imagery can help avoid the effect of mixed pixels. However, increasing the plot spacing also decreased the values of both $NDVI_{UAV}$ and $OSAVI_{UAV}$ (although to a lesser extent than for $NDVI_{SAT}$ and $OSAVI_{SAT}$, respectively; Figures 1C, D). This suggests that mixed pixels may not be the only factor affecting the spectral signature when increasing the distance between plots. One possibility is that the larger spacing changes the illumination conditions within the plot due to more lateral light penetration.

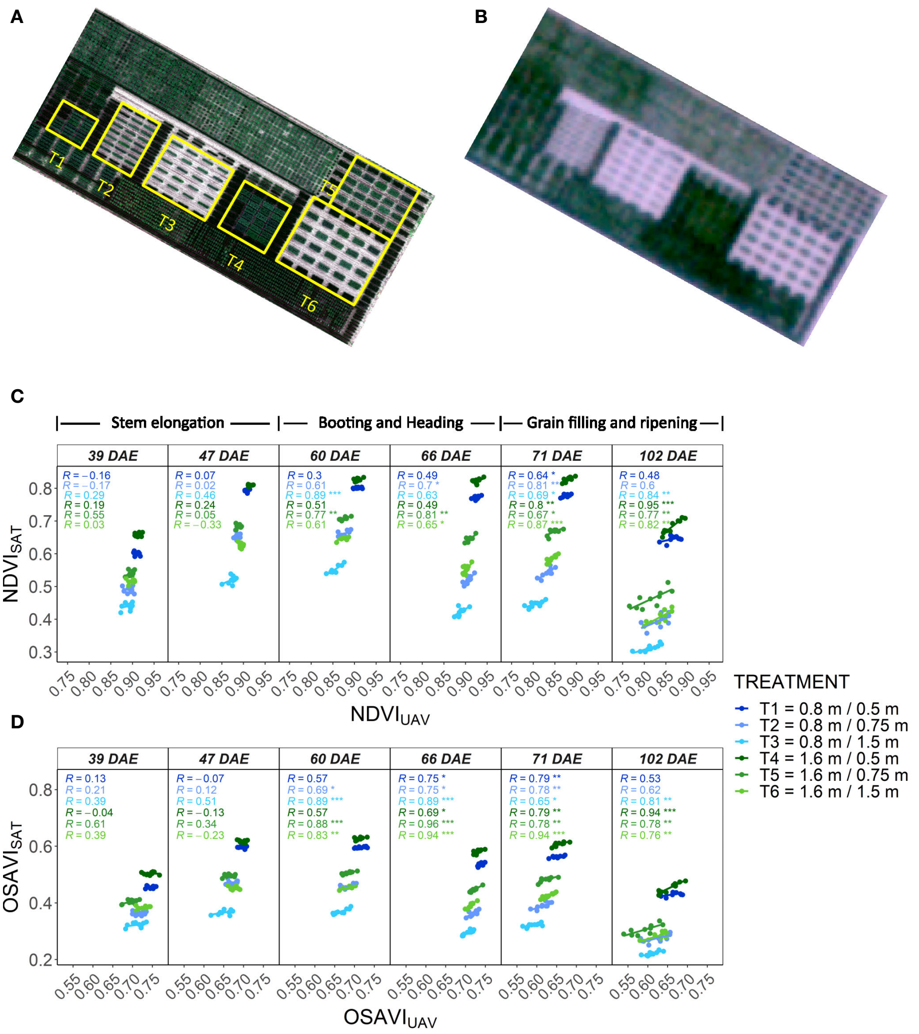

FIGURE 1

Assessment of SkySat images for the estimation of NDVI in wheat breeding plots with different size and spacing. **(A)** High-resolution RGB orthomosaic of the plot size and spacing experiment in wheat obtained from a UAV and boundaries of the different treatments. **(B)** RGB composite obtained from a SkySat image with a GSD of 0.5 m. **(C)** Correlations between $NDVI_{SAT}$ and $NDVI_{UAV}$ measured at different dates over the different treatments. **(D)** Correlations between $OSAVI_{SAT}$ and $OSAVI_{UAV}$ measured at different dates over the different treatments. NDVI and OSAVI values represent the best linear unbiased estimator (BLUE) computed individually at each measuring date for a given treatment based on a α-lattice design. Treatment description in the legend: "plot width/plot spacing". The corresponding growth stage for each measuring date is indicated on top of Figure 1C.

Mixed pixels may also limit the capability of NDVI and other spectral indices to detect phenotypic variability from satellite imagery. In the small plots, the reduction of plot spacing resulted in lower average heritability values for $NDVI_{SAT}$ and $OSAVI_{SAT}$ (Table 1). In larger plots, the heritability values were higher than in small plots but there was not an evident effect of the plot spacing. This suggests that genotypic variability detected in larger plots may be affected by other factors such as heterogeneity within the plots, and that differences in heritability between treatments may be more related to weather and field conditions during data collection. In the UAV data, the heritability values were much higher than those from satellite data. However, the plot size and distance did not show a clear effect across dates. Instead, differences in UAV-based heritability between treatments and dates may be better explained by changes in environmental and operating conditions. Slight variations in factors such as illumination conditions, wind or view angle, among others, can affect the accuracy of the spectral measurements causing great impact in the calculated heritability.

The time series of satellite images collected over the wheat experiment also depicted the influence of phenological stage on $NDVI_{SAT}$ and its variability within each treatment. The phenotypic variability of NDVI and OSAVI from both platforms, and the correlations between them, were lower or not significant during the first two measuring dates (Figure 1C), coinciding with a time of highest biomass development during stem elongation. The correlations and variability increased later, from booting and during the grain filling, when decreases in green biomass and the onset of senescence may have maximized the differences in the spectral signature between genotypes. These phenological changes

TABLE 1 Changes in broad sense heritability related to plot size, spacing, and measuring date in days after emergence (DAE) for NDVI and OSAVI calculated from satellite (SAT) and UAV imagery.

			DAE 39	DAE 47	DAE 60	DAE 66	DAE 71	DAE 102	Average
NDVI	NDVI_{SAT}	0.8 m / 0.5 m	0.00	0.04	0.00	0.00	0.00	0.00	0.01
		0.8 m / 0.75 m	0.23	0.00	0.00	0.52	0.44	0.56	0.29
		0.8 m / 1.5 m	0.33	0.33	0.48	0.86	0.63	0.50	0.52
		1.6 m / 0.5 m	0.00	0.00	0.25	0.75	0.75	0.90	0.44
		1.6 m / 0.75 m	0.25	0.31	0.38	0.00	0.15	0.82	0.32
		1.6 m / 1.5 m	0.52	0.00	0.00	0.63	0.41	0.81	0.40
	NDVI_{UAV}	0.8 m / 0.5 m	0.87	0.81	0.95	0.97	0.82	0.89	0.88
		0.8 m / 0.75 m	0.79	0.73	0.83	0.84	0.81	0.82	0.81
		0.8 m / 1.5 m	0.93	0.83	0.95	0.91	0.87	0.82	0.88
		1.6 m / 0.5 m	0.91	0.85	0.96	0.98	0.97	0.96	0.94
		1.6 m / 0.75 m	0.58	0.15	0.72	0.86	0.47	0.76	0.59
		1.6 m / 1.5 m	0.65	0.50	0.92	0.87	0.84	0.93	0.79
OSAVI	$\text{OSAVI}_{\text{SAT}}$	0.8 m / 0.5 m	0.12	0.41	0.00	0.43	0.00	0.00	0.16
		0.8 m / 0.75 m	0.28	0.00	0.00	0.59	0.51	0.62	0.33
		0.8 m / 1.5 m	0.31	0.24	0.52	0.00	0.64	0.47	0.36
		1.6 m / 0.5 m	0.00	0.00	0.29	0.77	0.84	0.86	0.46
		1.6 m / 0.75 m	0.37	0.36	0.53	0.00	0.14	0.86	0.37
		1.6 m / 1.5 m	0.57	0.00	0.00	0.72	0.60	0.89	0.46
	$\text{OSAVI}_{\text{UAV}}$	0.8 m / 0.5 m	0.62	0.82	0.94	0.85	0.77	0.72	0.79
		0.8 m / 0.75 m	0.73	0.84	0.81	0.77	0.92	0.87	0.83
		0.8 m / 1.5 m	0.91	0.87	0.96	0.89	0.75	0.61	0.83
		1.6 m / 0.5 m	0.84	0.89	0.97	0.90	0.92	0.93	0.91
		1.6 m / 0.75 m	0.63	0.42	0.71	0.62	0.58	0.67	0.60
		1.6 m / 1.5 m	0.69	0.84	0.88	0.82	0.85	0.87	0.82

were more contrasting when plot spacing was larger, with the bigger plots always showing the highest heritability and the best correlations between both platforms on all dates.

4 Discussion

The consolidation of satellite platforms as tools for high-throughput phenotyping in breeding trials relies on many factors, among which the spatial resolution plays an important role. As expected, for plots with widths close to the sensor GSD low accuracies were observed. However, the results indicate that high resolution satellites hold promise for phenotyping plots commonly used in wheat (1.2 m) and maize (1.5 m) breeding.

In addition to the spatial resolution, other sensor specifications can have great impact in the usability of this data for plot phenotyping, and should be considered carefully for interpretation. Saunier et al. (2022) performed a deep analysis on the performance of the SkySat constellation, revealing a high signal-to-noise ratio, high geometric accuracy, and confirming that the spectral and spatial resolutions were compliant with the specification of Planet.

Nevertheless, the same study detected some sources of uncertainties, such as variations in the quality of the data coming from different sensors and changes in the spectral signature due to resampling. This has implications for the interpretation and comparison of time series data or data collected from different locations, especially for small plots, as images may be collected from different satellites and from a different view angle (i.e. differences in native spatial resolution). In this sense, the implementation of plot-level models to characterize trait changes over time, such as the ones suggested by Roth et al. (2021) and Pérez-Valencia et al. (2022), can be used to smooth time series of data, helping to reduce noise coming for systematic or random errors while improving the genotypic variability at key phenological stages. The atmospheric correction of SkySat imagery also presents limitations that can affect the quality of the data (Planet, 2022b; Saunier et al., 2022).

Modifying the plot spacing helped us realize the extent to which neighboring surfaces affect the plot spectral signature. We demonstrated that increasing plot spacing helps with the identification of individual plots and improves apparent heritability. Similarly, working with larger plots improved the accuracies. However, these solutions are not suitable for breeding programs, which tend to comprise several hundred plots. Pleiades Neo (Airbus, 2022), as well as the upcoming Pelican fleet of satellites (Planet, 2022a) will offer multispectral data acquired at a resolution close to 0.3 m. Hence, limitations set by the resolution are likely to become less of an issue. A remaining challenge will be the accurate delineation of the plot boundaries. This can be achieved with high-resolution UAV imagery, although a UAV may not always be available, especially in under-resourced programs or in remote regions. An accurate geometric layout of the plots, possibly with the help of an RTK GPS, together with placing fixed ground control points that can be identified in the satellite images, will facilitate the image-to-image registration and lining up with the plot boundaries. Nursery trials are generally sown in flat areas; hence a perfect alignment can be achieved by a simple shifting of the images, a process that can be automated.

The SkySat images were able to capture spatial heterogeneity in the small areas covered by our trials. Similarly, the temporal changes in the spectra agreed with the phenology of the crops. This, together with the possibility of capturing images on demand, opens the possibility of using the satellite information to characterize the field level spatial variability in models for prediction of genetic value (Araus and Cairns, 2014; Smith et al., 2021), and to remotely monitor the development and management of the trials for quality control at a low cost.

The successful collection of six satellite images during the rainy season in Central Mexico, while monitoring in parallel a maize trial in Zimbabwe, amply demonstrate the flexibility of this tool. With the imminent improvement of the spatial resolution, a remaining challenge will be the development and fine-tuning of operational procedures that ensure high quality, standardized data that will enable us to harness the benefits of the modern breeding triangle.

Data availability statement

The data layers derived from the satellite images, such as NDVI and OSAVI, as well as all other data supporting the conclusions of this article, will be made available by the authors without undue reservation.

Author contributions

FP, MZ-A and US conceived the idea, analyzed the data and wrote the manuscript. FP and MZ-A designed the experiments and collected the data. US managed and coordinated the satellite data acquisition. MR provided critical feedback. All authors contributed to the article and approved the submitted version.

Funding

Foundation for Food and Agriculture Research: funded the field trials in wheat through the grant ID DFs-19-0000000013. CGIAR Research Program on Maize: funded purchase of satellite images. CGIAR Research Program on Wheat: funded purchase of satellite images. One CGIAR Digital Innovation Initiatives. One CGIAR F2R-CWANA Initiative. One CGIAR Accelerated Breeding Initiative.

Acknowledgments

The authors would like to thank the Foundation for Food and Agriculture Research for funding the field trials in wheat and the CGIAR Research Program on Maize (www.maize.org) and CGIAR Research Program on Wheat (www.wheat.org) for funding the purchase of the satellite images. We also would like to thank the One CGIAR Initiatives on Digital Innovation, F2R-CWANA, and Accelerated Breeding. Special thanks to Gilberto Thompson for the operation of the UAV and processing of the imagery from the wheat trials in Mexico, and to Jacinta Gimeno for managing the wheat field experiment.

Conflict of interest

The authors declare that the research was conducted in the absence of any commercial or financial relationships that could be construed as a potential conflict of interest.

Publisher's note

Supplementary material

The Supplementary Material for this article can be found online at: https://www.frontiersin.org/articles/10.3389/fpls.2023.1114670/full#supplementary-material

References

Airbus (2022). Available at: https://www.intelligence-airbusds.com.

Araus, J. L., and Cairns, J. E. (2014). Field high-throughput phenotyping: the new crop breeding frontier. *Trends Plant Sci.* 19, 52–61. doi: 10.1016/j.tplants.2013.09.008

Bernal-Vasquez, A. M., Utz, H. F., and Piepho, H. P. (2016). Outlier detection methods for generalized lattices: a case study on the transition from ANOVA to REML. *Theor. Appl. Genet.* 129, 787-804. doi: 10.1007/s00122-016-2666-6

Boogaard, H., Schubert, J., De Wit, A., Lazebnik, J., Hutjes, R., and van der Grijn, G. (2020). Agrometeorological indicators from 1979 to present derived from reanalysis. *Copernicus Climate Change Service (C3S) Climate Data Store (CDS)* doi: 10.24381/cds.6c68c9bb. [Accessed April 18, 2023]

Cooper, M., and Messina, C. D. (2021). Can we harness "Enviromics" to accelerate crop improvement by integrating breeding and agronomy? *Front. Plant Sci.* 12. doi: 10.3389/fpls.2021.735143

Crossa, J., Fritsche-Neto, R., Montesinos-Lopez, O. A., Costa-Neto, G., Dreisigacker, S., Montesinos-Lopez, A., et al. (2021). The modern plant breeding triangle: optimizing the use of genomics, phenomics, and enviromics data. *Front. Plant Sci.* 12. doi: 10.3389/fpls.2021.651480

Furbank, R. T., and Tester, M. (2011). Phenomics - technologies to relieve the phenotyping bottleneck. *Trends Plant Sci.* 16, 635–644. doi: 10.1016/j.tplants.2011.09.005

Hersbach, H., Bell, B., Berrisford, P., Biavati, G., Horányi, A., Muñoz Sabater, J., et al. (2018). ERA5 hourly data on single levels from 1959 to present. *Copernicus Climate Change Service (C3S) Climate Data Store (CDS)* doi: 10.24381/cds.adbb2d47 [Accessed April 18, 2023]

Jarquín, D., Crossa, J., Lacaze, X., Du Cheyron, P., Daucourt, J., Lorgeou, J., et al. (2014). A reaction norm model for genomic selection using high-dimensional genomic and environmental data. *Theor. Appl. Genet.* 127, 595–607. doi: 10.1007/s00122-013-2243-1

Jin, X., Zarco-Tejada, P. J., Schmidhalter, U., Reynolds, M. P., Hawkesford, M. J., Varshney, R. K., et al. (2021). High-throughput estimation of crop traits: a review of ground and aerial phenotyping platforms. *IEEE Geosci. Remote Sens Mag* 9, 200–231. doi: 10.1109/MGRS.2020.2998816

Jönsson, P., and Eklundh, L. (2004). TIMESAT–a program for analyzing time-series of satellite sensor data. *Comput. Geosci.* 30, 833–845. doi: 10.1016/j.cageo.2004.05.006

Korte, A., and Ashley, F. (2013). The advantages and limitations of trait analysis with GWAS : a review self-fertilisation makes arabidopsis particularly well suited to GWAS. *Plant Methods* 9, 29. doi: 10.1186/1746-4811-9-29

Leprince, S., Barbot, S., Ayoub, F., and Avouac, J. P. (2007). Automatic and precise orthorectification, coregistration, and subpixel correlation of satellite images, application to ground deformation measurements. *IEEE Trans. Geosci. Remote Sens* 45 (6), 1529-1558. doi: 10.1109/TGRS.2006.888937

Pérez-Valencia, D. M., Rodríguez-Álvarez, M. X., Boer, M. P., Kronenberg, L., Hund, A., Cabrera-Bosquet, L., et al. (2022). A two-stage approach for the spatio-temporal analysis of high-throughput phenotyping data. *Sci. Rep.* 12 (1), 3177. doi: 10.1038/s41598-022-06935-9

Planet (2022a). Available at: https://www.planet.com.

Planet (2022b) *Planet imagery product specifications*. Available at: https://assets.planet.com/docs/Planet_Combined_Imagery_Product_Specs_letter_screen.pdf.

Resende, R. T., Piepho, H. P., Rosa, G. J. M., Silva-Junior, O. B., e Silva, F. F., de Resende, M. D. V., et al. (2021). Enviromics in breeding: applications and perspectives on envirotypic-assisted selection. *Theor. Appl. Genet.* 134, 95–112. doi: 10.1007/s00122-020-03684-z

Rondeaux, G., Steven, M., and Baret, F. (1996). Optimization of soil-adjusted vegetation indices. *Remote Sens Environ.* 55 (2), 95-107. doi: 10.1016/0034-4257(95)00186-7

Roth, L., Rodríguez-Álvarez, M. X., van Eeuwijk, F., Piepho, H. P., and Hund, A. (2021). Phenomics data processing: a plot-level model for repeated measurements to extract the timing of key stages and quantities at defined time points. *F Crop Res.* 274, 108314. doi: 10.1016/j.fcr.2021.108314

Royer, A., Vincent, P., and Bonn, F. (1985). Evaluation and correction of viewing angle effects on satellite measurements of bidirectional reflectance. *Photogramm Eng Remote Sens* 51(12), 1899-1914.

Sankaran, S., Marzougui, A., Hurst, J. P., Zhang, C., Schnable, J. C., and Shi, Y. (2021). Can high-resolution satellite multispectral imagery be used to phenotype canopy traits and yield potential in field conditions? *Trans. ASABE* 64, 879–891. doi: 10.13031/trans.14197

Sankaran, S., Zhang, C., Hurst, P., Marzougui, A., Veeranampalayam–Sivakumar,A. N., et al. (2020). "Investigating the potential of satellite imagery for high-throughput field phenotyping applications," in *Autonomous air and ground sensing systems for agricultural optimization and phenotyping V* Eds. J. A. Thomasson and A. F. Torres-Rua (United States: SPIE) 11414, 1141402. doi: 10.1117/12.2558729

Saunier, S., Karakas, G., Yalcin, I., Done, F., Mannan, R., Albinet, C., et al. (2022). SkySat data quality assessment within the EDAP framework. *Remote Sens* 14 (7), 1646. doi: 10.3390/rs14071646

Smith, D. T., Potgieter, A. B., and Chapman, S. C. (2021). Scaling up high-throughput phenotyping for abiotic stress selection in the field. *Theor. Appl. Genet.* 134 (6), 1845-1866. doi: 10.1007/s00122-021-03864-5

Stamp, P., and Visser, R. (2012). The twenty-first century, the century of plant breeding. *Euphytica* 186, 585–591. doi: 10.1007/s10681-012-0743-8

Tattaris, M., Reynolds, M. P., and Chapman, S. C. (2016). A direct comparison of remote sensing approaches for high-throughput phenotyping in plant breeding. *Front. Plant Sci.* 7. doi: 10.3389/fpls.2016.01131

van Eeuwijk, F. A., Bustos-Korts, D., Millet, E. J., Boer, M. P., Kruijer, W., Thompson, A., et al. (2019). Modelling strategies for assessing and increasing the effectiveness of new phenotyping techniques in plant breeding. *Plant Sci.* 282 (2019), 23-39. doi: 10.1016/j.plantsci.2018.06.018

Xiong, W., Reynolds, M., and Xu, Y. (2022). Climate change challenges plant breeding. *Curr. Opin. Plant Biol.* 70, 102308. doi: 10.1016/j.pbi.2022.102308

Frontiers in Plant Science

TYPE Original Research
PUBLISHED 14 June 2023
DOI 10.3389/fpls.2023.1172359

EDITED BY
Shawn Carlisle Kefauver,
University of Barcelona, Spain

REVIEWED BY
Stephen Welch,
Kansas State University, United States
Nicolas Virlet,
Rothamsted Research, United Kingdom

*CORRESPONDENCE
George A. K. van Voorn
george.vanvoorn@wur.nl

†PRESENT ADDRESS
Ryan McCormick,
Gro Intelligence, New York, NY,
United States
Daniela Bustos Korts,
Institute of Plant Production and
Protection, Faculty of Agricultural Sciences,
Campus Isla Teja, Universidad Austral de
Chile, Valdivia, Chile

RECEIVED 23 February 2023
ACCEPTED 30 May 2023
PUBLISHED 14 June 2023

CITATION
van Voorn GAK, Boer MP, Truong SH, Friedenberg NA, Gugushvili S, McCormick R, Bustos Korts D, Messina CD and van Eeuwijk FA (2023) A conceptual framework for the dynamic modeling of time-resolved phenotypes for sets of genotype-environment-management combinations: a model library. *Front. Plant Sci.* 14:1172359.
doi: 10.3389/fpls.2023.1172359

A conceptual framework for the dynamic modeling of time-resolved phenotypes for sets of genotype-environment-management combinations: a model library

George A. K. van Voorn[1]*, Martin P. Boer[1], Sandra Huynh Truong[2], Nicholas A. Friedenberg[2], Shota Gugushvili[1], Ryan McCormick[2,3†], Daniela Bustos Korts[1,4†], Carlos D. Messina[2,5] and Fred A. van Eeuwijk[1]

[1]Biometris, Plant Sciences Group, Wageningen University & Research, Wageningen, Netherlands, [2]Research & Development, Corteva Agriscience, Johnston, IA, United States, [3]Gro Intelligence, New York, NY, United States, [4]Institute of Plant Production and Protection, Faculty of Agricultural Sciences, Universidad Austral de Chile, Valdivia, Chile, [5]Department of Horticultural Sciences, University of Florida, Gainesville, FL, United States

Introduction: Dynamic crop growth models are an important tool to predict complex traits, like crop yield, for modern and future genotypes in their current and evolving environments, as those occurring under climate change. Phenotypic traits are the result of interactions between genetic, environmental, and management factors, and dynamic models are designed to generate the interactions producing phenotypic changes over the growing season. Crop phenotype data are becoming increasingly available at various levels of granularity, both spatially (landscape) and temporally (longitudinal, time-series) from proximal and remote sensing technologies.

Methods: Here we propose four phenomenological process models of limited complexity based on differential equations for a coarse description of focal crop traits and environmental conditions during the growing season. Each of these models defines interactions between environmental drivers and crop growth (logistic growth, with implicit growth restriction, or explicit restriction by irradiance, temperature, or water availability) as a minimal set of constraints without resorting to strongly mechanistic interpretations of the parameters. Differences between individual genotypes are conceptualized as differences in crop growth parameter values.

Results: We demonstrate the utility of such low-complexity models with few parameters by fitting them to longitudinal datasets from the simulation platform APSIM-Wheat involving *in silico* biomass development of 199 genotypes and data of environmental variables over the course of the growing season at four Australian locations over 31 years. While each of the four models fits well to particular combinations of genotype and trial, none of them provides the best fit across the full set of genotypes by trials because different environmental drivers will limit crop growth in different trials and genotypes in any specific trial will not necessarily experience the same environmental limitation.

Discussion: A combination of low-complexity phenomenological models covering a small set of major limiting environmental factors may be a useful forecasting tool for crop growth under genotypic and environmental variation.

KEYWORDS

crop growth model, ordinary differential equation, dynamic model, genotype by environment by management interactions, model selection, phenomenological model, phenotyping, process-based model

1 Introduction

The prediction of crop yield remains a critical challenge (Peng et al., 2020). Yield is a complex trait, resulting from the interplay between many genes with relatively small contributions, environmental inputs, and management regimes (GxExM) integrated over the growing season (Van Eeuwijk et al., 2019). Crudely speaking, two major methodological approaches can be distinguished to decompose yield into genetic and environmental factors. The first approach is mainly statistical, where the underlying goal is yield improvement by the identification of superior genotypes through the use of relatively simple models in which genotypes differ from each other in mean performance across the range of included conditions and in sensitivities to either a small (Millet et al., 2019) or large number of environmental drivers (Jarquín et al., 2014; Van Eeuwijk et al., 2016). The second approach involves the use of process-based models, which typically relate yield to underlying processes that are affected by the environment and that are governed by genotype-dependent parameters that are expected to vary little across environments. The use of such models is more common in integrated assessments, such as implemented in AgMIP (Ruane et al., 2017), where the goal is to assess the effects of management and stress factors on yield, such as those resulting from climate change. Yield can also be disentangled following a prior dissection of yield into 'lower-level' yield components that are physiologically simpler than yield and that can be measured at multiple moments during the growing season, for example, with High Throughput Phenotyping platforms. Static yield dissection models may be applied that can better address equifinality issues, i.e., the same yield end point is achieved via different development paths, by allowing for the possible improvement of yield along multiple paths via different underlying components (Tsutsumi-Morita et al., 2021). Longitudinal data series of yield components allow dynamic modelling in the form of smoothed growth curves on P-spline bases in combination with extraction of growth characteristics that can be used to predict end point traits like yield (Roth et al., 2021; Pérez-Valencia et al., 2022). The disadvantage of such models is that they do not explicitly couple mechanistic descriptions of the underlying dynamic processes driving crop growth to genetic effects. Vice versa, crop simulation platforms integrate environmental factors over the growing season to forecast yield as an emergent end point. While mechanistic in nature, these models do not usually involve genetic differences, and the inclusion of such effects is far from trivial, as it is not obvious which crop growth parameters to choose to be genotype dependent and how to account for stochasticity in genetic effects. Moreover, despite the increasing availability of spatio-temporal information from non-destructive, cost-effective, and time-efficient methods (Shammi & Meng, 2021), such as longitudinal drone imagery (Panday et al., 2020) and earth observations freely available at relevant scales (Kasampalis et al., 2018; Huang et al., 2019), considerable limitations exist with respect to the availability of data, models, and algorithms to adequately handle GxExM in crop growth descriptions (Stöckle & Kemanian, 2020).

The generalization of crop growth models to contain genotype-dependent parameters is relevant for increasing the accuracy of predictions regarding the performance of genotypes in new environments (Technow et al., 2015). With thousands of genotype-by-environment combinations involved in modern breeding, there is a need for crop models that can cover the broad spectrum of GxExM interactions and make optimal use of the data that are becoming available. On the other hand, these models should also be sufficiently simple and parsimonious to aid human interpretation (Hammer et al., 2019). While many current crop simulation platforms are physically consistent (e.g., containing conservation of mass and energy) and are capable of simulating crop growth and development in great detail, crop model results are sensitive to calibration, i.e. estimation of crop growth parameters in the light of empirical data is cumbersome (Grassini et al., 2015). The number of parameters in a model can quickly outpace the ability to fully identify and/or estimate all parameters well from available data when considering a single calibration objective only (Wagener et al., 2003). Crop models currently may be too complex for proper calibration so that many uncertainties remain regarding their parameterization (Dokoohaki et al., 2021). Parameters are commonly correlated in such a way that their effects on the model output are indistinguishable, leading to what is termed unidentifiability (Cole et al., 2010). Modelling efforts also suffer from the existence of multiple candidate model parameterizations and model structures that can describe or explain the data equally well (Beven & Freer, 2001), yet suggest contradictory assessments when focused on practical problems such as yield gap estimates (Schils et al., 2022). High parameter correlations and equifinality are issues that can easily disrupt attempts at an accurate estimation of parameters and thus should be addressed to avoid a reduction in the utility of crop models (Lamsal et al., 2018). Given the right tools, the availability of high-resolution time series data can help in addressing these issues.

The burden of complexity in data-driven modeling calls for the periodic reassessment of simpler approaches to identify necessary and sufficient levels of detail, or granularity, to capture the essential GxExM interactions and utilize increasingly available data streams, while also being sufficiently realistic in the sense of trying to minimize issues around model structure identification and model calibration. In this paper and a follow-up paper the over-arching aim is the development of a modelling framework for describing the essential dynamical growth patterns of genotypes that lead to GxExM interactions, which should allow for the prediction of yield for existing and new genotypes across a wide range of management and environmental conditions, i.e. it is minimalistic yet sufficiently capable of allowing for genotype-dependent parameterizations. Model complexity should be balanced in terms of what is required by the application, the important characteristics of the system – those addressing essential GxExM interactions – and the support following from data (Wagener et al., 2001).

We present a small library consisting of four crop growth models based on differential equations for the dynamical description of biomass growth during the growing season and the interaction of biomass with important environmental drivers. For simplicity, we assume that biomass is proportional to the whole crop biomass, though only above-ground biomass is measured. Furthermore we assume that the end-of-season biomass is an approximation to yield. The proposed models each focus on one particular crop growth limitation. They omit phenological stages and thereby avoid the need for stage-specific parameterization. Differential equations typically have no closed-form solutions, which prohibits the use of regular statistical methods for data fitting or model analysis. In the current paper, we demonstrate the utility of the different models from the library by fitting them to longitudinal data of individual genotypes in individual environments, using established fitting procedures for ordinary differential equations. In a follow-up paper we will develop a hierarchical Bayesian framework to fit the models within our library to longitudinal data for populations or panels of genotypes with the hope of identifying genotype-dependent parameters that do show variation across genotypes while varying little across environments. Various options exist for combining the different models in our library to arrive at a prediction model for yield, an attractive one consisting in an ensemble model (Hoeting et al., 1999; McCormick et al., 2021) that encloses the fits of the member models of the library for the time series data of individual genotypes.

In this paper, we will fit our models to simulated, i.e., *in silico* generated and noise-free longitudinal data of daily biomass measurements for different wheat genotypes in different Australian environments. The advantage of using simulated data is that we have practically unlimited data available for model testing, and we can – for now – ignore uncertainty resulting from noise and poor temporal coverage. Genetic effects will occur as differences in the estimated values for the parameters. We acknowledge that parameters that show genetic variation in our model fits are not necessarily immediately useful for prediction of yield under all conditions. It is obvious that we will need to verify that parameters with genetic variation are not subject to genotype-by-environment interaction themselves (Lamsal et al., 2018). Hammer et al. (2006) state that fundamental physiological parameters should have fixed values. For our low-complexity models we do not necessarily expect that parameters are stable, because the modelled processes are high-level, and parameter values may be the net result of multiple underlying processes. Still, we believe that even when our dynamic parameters show some sensitivity to the environmental conditions, our models can be useful for yield prediction as long as this sensitivity can be modelled itself as a simple function of the environmental conditions.

2 Materials and methods

2.1 Proposed phenomenological models

Below we introduce four dynamic models, all containing some essential first principles of crop growth. The models we develop are extensions of general continuous model frameworks presented in the literature suitable for describing the growth of plants in an ecological context (Paine et al., 2012) or the within-season accumulation of crop biomass (Poudel et al., 2022). Though simple and largely phenomenological, the models are dynamic and therefore offer a biological interpretation of the parameters as well as the ability to produce varied output depending on environmental or management inputs. Variations in genotypic background can be conceptualized as differences in the values of these parameters, where we do not exclude that the values of these parameters may still be subject to some genotype by environment interaction, especially in situations where multiple limiting factors influence our phenotype biomass. The models we present are smooth in that they lack pre-determined non-linearities, such as imposed jumps, switches, and thresholds, that are often encountered in crop simulation platforms that contain connected sub-modules for different crop processes. As such, differential equation-based models can capture the dynamic nature of crop growth in explicit descriptions. An additional advantage of this smoothness is the access to higher-order derivatives with respect to time that can be used to calculate genotype-dependent sensitivities of growth to environmental inputs as function of time as well as the timing of critical developmental events. This also conceptually facilitates the extrapolation to other genotypes and environments, assuming that the base model is valid. In addition, smooth models are easier to fit.

2.1.1 Model #1: The logistic model

Model #1 – commonly referred to as the logistic model – is often used for the coupling of growth rate to biomass (Richards, 1959). For example, this model was already used more than a century ago to describe sunflower (*Helianthus*) growth (Reed and Holland, 1919). The model description is as follows:

$$\frac{dM(t)}{dt} = r\ M(t)\ \left(1 - \frac{M(t)}{M_{max}}\right) \qquad \text{Eq. (1)}$$

With explicit solution:

$$M(t) = \frac{M_{max}}{1 + \left(\frac{M_{max}}{M_0} - 1\right)\exp(-rt)}$$

The model symbols are given in Table 1. Here $M(t)$ indicates the total biomass at time t. The parameter r is an intrinsic growth rate (with a positive value), and M_{max} is an intrinsic (implicit) growth limitation (also with a positive value), i.e., the crop cannot grow larger than a maximum size. The initial condition M_0 (with a positive value) can be interpreted as seed weight or the biomass at the starting day of measurement (depending on the context); in the data we use, it is the biomass at the first day at which biomass can clearly be observed. Genotypic variation can be represented as variation in the parameters r, M_{max}, and possibly the initial condition M_0 – in which case it would represent genotypic differences in seed size and reserve content, and hence all three parameters/initial conditions are candidates for genotype-dependent parameters that require estimation for each included genotype. The logistic model has an explicit solution (given in Eq. 1) that can be used to verify the numerical implementation of the model. An important ramification of this property is that the biomass development for the growing season is fixed by the initial biomass M_0 together with the parameter values, in other words, the explicit solution means that no modifications of the growth rate during the growing season are accounted for in the forecasting by the model, and thus the end-of-season biomass is 'fixed'. This is likely unrealistic, as in reality the crop growth rate may be modified by externally imposed limitations occurring during the growing season. The logistic model cannot reproduce mid-season biomass loss that can occur, for instance, when resource acquisition falls short of maintenance respiration needs (Cannell and Thornley, 2000). Additionally, logistic growth has also been shown to violate mass balance assumptions (Kooi et al., 1998).

2.1.2 Model #2: The irradiance model

Model #2 – the irradiance model – assumes sunlight is the limiting factor during the growing season. The model description is as follows:

$$\frac{dM(t)}{dt} = \left(r + A\ \sin\left(\frac{2\pi}{365}(t+\varphi)\right)\right)\ M(t)\left(1 - \frac{M(t)}{M_{max}}\right) \qquad \text{Eq. (2)}$$

The newly introduced symbols in this model are given in Table 2. The base intrinsic growth rate r is now modified by the sinusoidal driver function with amplitude A and phase shift φ. This function links the level of irradiance to the yearly earth's orbit around the sun. This implies that the parameters A and φ may vary across environments but also may be genotype-dependent, as different genotypes may respond differently to the same environmental input. The advantage of this formulation is that no input is needed and hence no additional equations are needed for translating such input. This comes at the cost of ignoring day-to-day variations in the irradiance, e.g., resulting from clouds. Instead it assumes the generic seasonal pattern of increasing and decreasing day length and changing angle of sunlight reception. In principle one could opt for the inclusion of day-to-day irradiance measurements, in which case a data smoothing and translation function is needed similar to what we use for smoothing and translating temperature (see model #3). By selecting the correct phase shift, the growth rate can increase and decrease following seasonal effects. Parameters A and φ can both have positive and negative values, depending on location and timing; care should be taken that the total term does not become smaller than r to avoid negative growth, though a negative growth can occur for a small amount of time as long as biomass remains positive. In case A=0, the model collapses to the logistic model. The other parameters have the same meaning as in the logistic model (Eq. 1).

2.1.3 Model #3: The temperature model

Model #3 – the temperature model – includes an explicit effect of temperature on the growth rate. The model description is as follows:

$$\frac{dM(t)}{dt} = rf_T(t)M(t)\left(1 - \frac{M(t)}{M_{max}}\right) \qquad \text{Eq. (3a)}$$

$$f_T(t) = \left(1 + \exp\left(\frac{T_{AL}}{T(t)} - \frac{T_{AL}}{T_L}\right) + \exp\left(\frac{T_{AH}}{T_H} - \frac{T_{AH}}{T(t)}\right)\right)^{-1} \qquad \text{Eq. (3b)}$$

The base growth rate r in Eq. (3a) is modified by a function f_T that depends on the actual ambient temperature $T(t)$, which is a variable given by the data. The temperature response description

TABLE 1 Symbols introduced in the logistic model (Eq. 1), alphabetically ordered.

Symbol	Meaning	Units	Type of parameter
t	Time	day	Autonomous state variable
$M(t)$	Crop biomass	kg m^{-2}	Non-negative state variable
$M(0)$	Initial crop biomass	kg m^{-2}	Non-negative initial condition $M(t)$=M_0 at t=0
M_{max}	Natural crop biomass limitation	kg m^{-2}	Non-negative parameter
r	Crop intrinsic growth rate	day^{-1}	Non-negative parameter

Parameters and initial conditions are included in the fitting procedure, unless stated otherwise.

TABLE 2 Symbols introduced in the irradiance model (Eq. 2), alphabetically ordered.

Symbol	Meaning	Units	Type of parameter
A	Amplitude of time-dependent driver	day^{-1}	Parameter, genotype and environment-dependent
φ	Phase shift of driver	day	Parameter, genotype and environment-dependent

has been identified as a major source of uncertainty in simulation models used for crop growth predictions (Wang et al., 2017; Roth et al., 2022). The temperature response curve is often included in crop models as either a linear increase in the development rate from a given base temperature (usually zero degrees Celsius), and a linear decline in biomass growth beyond a certain maximum temperature, without assuming any optimal growth temperature, or a function that includes a minimum and an optimal temperature but without a maximum temperature, thus ignoring any effects of heat stress and senescence (Wang et al., 2017; see their Figure 1 for the different types of temperature response curves). Both response curves are unlikely, as crops have three cardinal temperatures. Wheat, for example, is sensitive to high temperatures during several developmental phases, while optimal temperatures for anthesis and grain filling are given around 12 to 22°C (Djanaguiraman et al., 2018) or up to 25°C for optimal growth in general, and with minimum and maximum growth temperatures of 3–4°C and 30–32°C, respectively (Porter and Gawith, 1999; Curtis, 2002).

The exact formulation of the temperature response is debatable. Different models with unimodal temperature dependence are reviewed by DeLong et al. (2017), who alternatively consider enzyme-assisted Arrhenius temperature responses. Arroyo et al. (2022) propose a general theory for temperature dependence based on Eyring-Evans-Polanyi's theory for chemical reaction rates. Here, we use the temperature response curve Eq. (3b) proposed by Sharpe and DeMichele (1977) and later Kooijman (2010). This formulation is based on the concept that enzymes become inactive at temperatures that are too high or too low. The reaction rate is multiplied by the active enzyme fraction, which is assumed to be in equilibrium. This formulation gives a smooth, nonlinear function that is based on three cardinal temperatures. Its parameters are given in Table 3. T_L and T_H represent the lower and upper boundary of the tolerance range, respectively, while T_{AL} and T_{AH} give the Arrhenius temperatures for the rate of decrease at these respective boundaries. The parameters for temperature response in Eq. (3b) were kept fixed at T_L=292K, T_H=303K, T_{AL}=20,000K, and T_{AH}=60,000K to generate a response curve that approximates the reported cardinal temperatures for wheat (Parent and Tardieu, 2012).

2.1.4 Model #4: The soil water model

Model #4 – the water model – involves water limitation, taking into account that many crop-growing environments are water-limited. The model description is as follows:

$$\frac{dW(t)}{dt} = p\left(\frac{M(t)+Kq}{M(t)+K}\right)P(t) - c\left(\frac{W(t)}{W(t)+n}\right)M(t)^{\nu} - RW(t) \qquad \text{Eq. (4a)}$$

$$\frac{dM(t)}{dt} = gc\left(\frac{W(t)}{W(t)+n}\right)M(t)^{\nu} - mM(t) \qquad \text{Eq. (4b)}$$

The symbols used in this model are given in Table 4. Contrary to temperature and irradiance, which are exogenous inputs for crop growth, there is a feedback between soil water and the crop, as one affects the other. The water model therefore includes a second differential equation that describes a soil water variable, $W(t)$, as well as a function that couples soil water to crop biomass growth. The water model is based on a formulation proposed for simulating plant growth in semi-arid areas (Van de Koppel and Rietkerk, 2004) with some modifications.

The first nonlinear term in Eq. (4a) represents the uptake of precipitation by the soil, which has limited uptake capability. The uptake increases with biomass, representing an increasing infiltration because of larger root structures. However, the uptake fraction remains small and under zero biomass, this term reduces to $pqP(t)$, representing the infiltration of precipitation in barren soil. Parameters p and q depend on environmental conditions and are expected to vary across environments but not across genotypes. Parameter K represents infiltration of water into the soil, which is affected by the root structure of the crop, and this parameter is therefore expected to depend on genotype and environment.

TABLE 3 Symbols introduced in the temperature model (Eq. 3), alphabetically ordered.

Symbol	Meaning	Units	Type of parameter
$T(t)$	Ambient temperature	K	Spline-smoothened input from daily measurements
T_{AH}	Arrhenius temperature for the rate of decrease at the upper boundary of the temperature tolerance range	K	Kept constant at $6{\cdot}10^4$
T_{AL}	Arrhenius temperature for the rate of decrease at the lower boundary of the temperature tolerance range	K	Kept constant at $2{\cdot}10^4$
T_H	Upper boundary of the temperature tolerance range	K	Kept constant at 303
T_L	Lower boundary of the temperature tolerance range	K	Kept constant at 292

TABLE 4 Symbols introduced in the water model (Eq. 4), alphabetically ordered.

Symbol	Meaning	Units	Type of parameter
c	Soil water uptake capacity of crop (c_{max} in KR2004)	kg^{-1} ml m^{-1} day^{-1}	Non-negative genotype-dependent parameter
g	Soil water to crop biomass conversion factor (comparable to g_{max} in KR2004, but note the difference to our gc)	kg ml^{-1} m	Non-negative genotype-dependent parameter
K	Infiltration constant related to crop (k in KR2004)	kg m^{-2}	Non-negative parameter that depends on genotype and environment
n	Half-rate parameter of Michaelis-Menten function (k_1 in KR2004)	ml m^{-3}	Non-negative genotype-dependent parameter
m	Density-dependent maintenance rate (comparable but not similar to ($d+\delta P$) in KR2004)	day^{-1}	Non-negative genotype-dependent parameter
$P(t)$	Precipitation (observed) (PPT in KR2004)	ml m^{-2} day^{-1}	Spline-smoothed input from daily measurements
p	Conversion constant from precipitation $P(t)$ to soil water $W(t)$ (missing in KR2004)	m^{-1}	Estimated environment-dependent parameter
q	Fraction of precipitation that infiltrates in soil (W_0 in KR2004)	–	Estimated environment-dependent parameter
R	Soil drying rate (r_w in KR2004)	day^{-1}	Estimated environment-dependent parameter
v	Parameter relating uptake volume to biomass (missing in KR2004)	–	Genotype-dependent parameter with range $0 < v \le 1$
$W(t)$	Soil water	ml m^{-3}	Non-negative state variable

For easy comparison, we also list the symbols used in the original model by Van de Koppel & Rietkerk (2004) – abbreviated as KR2004 – but note there is not a one-to-one match to the model in that paper.

The second nonlinear term in Eq. (4a) represents the uptake of water from the soil by the crop, which is limited by aquaporin (enzyme) activity and diffusion rates and thus described by a Michaelis-Menten function, with a half-rate parameter, n. This function mimics satiation, as the response is near-linear for small values of $W(t)$, but gradually approaches 1 as $W(t)$ continues to increase. Parameter v represents a scaling between the uptake surface of the crop and the volume over which maintenance is paid (Kooijman, 2010, Figure 4.14), where v is typically smaller than 1. Parameters c, n and v are involved in the uptake of soil water by the crop and are hence expected to be genotype-dependent.

Conceptually, in this model the crop 'competes' with the soil for water, and water is taken up from the soil either by the crop, or water disappears via the third term in Eq. (4a), $RW(t)$. This is a generic term that conceptually considers the soil to be a 'leaky bucket', where the drying out rate depends on soil water content. If unused, water will also disappear from the soil. Parameter R is therefore assumed to be environment-dependent. The *de facto* standard for evapotranspiration in crops for the EU and US is the Penman-Monteith method, covered by the FAO56 method (Pereira et al., 2015), which includes effects of temperature and wind speed on how fast water disappears from the soil. Evaporation from barren soil is the largest contributing factor for water loss from the soil early in the growth season. If biomass $M(t)$=0 and under constant precipitation – and implicitly assuming a constant temperature, wind speed, etc. – Eq. (4a) will eventually reach a steady state, i.e. the same amount of water will enter and leave the soil in a given time interval. If there is no precipitation, the leaky bucket formulation ensures the model will eventually approach the limit $W(t)$=0. In reality, the soil will never fully dry out because some water is retained through gravitational and capillary forces, but this water would also not be available to crops, so we ignore this feature. Moreover, the drying and re-wetting curves of soil moisture content as functions of water pressure differ (Shein & Mady, 2018) which is also ignored in the water model. Finally, we assume there is no measurable effect of temperature, wind speed, etc. on the rates at which water leaves the soil. Note, that in our fitting procedure we not only compare the predicted biomass $M(t)$ to the APSIM simulated biomass, but we also compare the variable $W(t)$ to the soil water output of the APSIM SoilWat module (Holzworth et al., 2018). This makes use of real-life environmental data like rainfall and temperature, but simulates soil water in time. Hence, this implies we have a considerable reduction in model complexity.

The first term in Eq. (4b) gives the conversion from taken up water from to soil to crop biomass, i.e. water is used in the creation of carbohydrates (photosynthesis). We consider this conversion to follow a fixed ratio, and hence the parameter g is also fixed. Part of the taken up water will also disappear again through evapotranspiration, but we assume this ratio now to be fixed as well. The negative density-term in the second term of Eq. (4b) represents maintenance respiration, which is considered to be proportional to biomass volume (Kooijman, 2010). This term allows for a temporary decrease in biomass (rate).

2.2 Data description and software implementation

To assess the suitability of our four minimalistic crop growth models in capturing biomass growth in real-life situations, we used simulated longitudinal biomass data for an Australian diversity panel with 199 genotypes in wheat (Bustos-Korts et al., 2019a; Bustos-Korts et al., 2019b). These data were generated with the crop growth simulation platform APSIM-Wheat (Keating et al., 2003; Holzworth et al., 2018). Environmental inputs were observed soil and meteorological data for 31 years (1993 through 2013) at four different locations in Australia – Emerald (−23.53 lat, 148.16 long), Merredin (−31.50 lat, 118.22 long), Narrabri (−30.32 lat, 149.78 long), and Yanco (−34.61 lat, 146.42 long) (Bustos-Korts et al., 2019b). The overall data set consisted of 23,880 output series of daily observations on simulated biomass and other traits. Genotypic specifications of crop growth parameters were chosen to mimic realistic genetic variation for Australian environmental conditions (Bustos-Korts et al., 2019a; Bustos-Korts et al., 2019b). We preferred to use simulated wheat data over data from field trials, because for our simulated data we could infer to a certain extent what the major stress had been to which the wheat genotypes were exposed in a particular simulated experiment. The latter information helped us to assess the appropriateness of our candidate minimalistic models when fitted to the simulated longitudinal biomass data for an individual genotype in a simulated experiment. We did not add noise to the APSIM simulated data because we wanted to establish the performance of our minimalistic models under the most discriminatory conditions. The simulated data covered multiple types of environments with different limitations (Bustos-Korts et al., 2019a; Bustos-Korts et al., 2019b).

Typically observations on biomass consist of measurements of the state variable biomass at specific time points, and not the rate parameters that determine biomass change. We therefore need to fit solutions of our candidate minimalistic crop growth models to the simulated wheat data to obtain estimates for the rate parameters and predictions for the state variables by numerical integration. The models were implemented in R version 4.1.0 (R Core Team, 2021). Parameter estimation methods for differential equations are discussed, for instance, by Ashyraliyev et al. (2009). For model fitting we used the R package ‘FME’ (Soetaert and Petzoldt, 2010), in combination with the R package ‘deSolve’ (Soetaert et al., 2010). This combination is tailored at fitting differential equations. The default solving option we used is ‘Marq’ (short for Levenberg-Marquardt), which is a gradient-based method that minimizes the sum of squared residuals. This method is fast, but it is known to be sensitive to the initial parameter vector, because by following the steepest descending gradient it can easily end up in a local minimum. We also used the alternative methods ‘Nelder-Mead’ and ‘Pseudo’ for crude-but-fast convergence to approximate solutions in cases where ‘Marq’ did not immediately provide satisfactory solutions. Other alternatives in the FME package include SANN (simulated annealing) and bobyqa; alternative fitting packages in R include Particle Swarm Optimization (Bendtsen, 2022) and Differential Evolution (Ardia et al., 2010; Mullen et al., 2011). As the focus in this paper is not on the parameter estimation *per se*, we selected the default option in FME, which is Marq (but note that we will focus on parameter estimation in the next paper). To enhance estimation procedures, biomass was rescaled by division by 1000.

The quality of the fits was evaluated by the inspection of the plots of the weighted residuals against time, which are defined as

$$r_i = f(x_i) - y_i \qquad \text{Eq. (5)}$$

Here y_i is the observation at index i, and $f(x_i)$ is the model predicted value. To compare the quality of the fits between models to the APSIM data, we heuristically looked at Akaike’s Information Criterion, AIC (Akaike, 1974)

$$\mathrm{AIC} = -2(\mathrm{LL}) + 2\ \#(\theta) \qquad \text{Eq. (6)}$$

Here LL is the log-likelihood, taken as the sum of squared errors which is given by the FME package, and $\#(\theta)$ is the total number of parameters. Note, that the models are not nested – with the exception of model #2 that can be collapsed into model #1 under the conditions stated earlier. The calculated AICs should therefore be interpreted as an assessment of the ability of the models to capture the crude patterns in the data rather than a quantitative model selection criterion. For real dynamic data, residuals will show various forms of autocorrelation. Such autocorrelations can be inspected by plots of partial autocorrelation functions, or PACFs (Hyndman and Khandakar, 2008; Hyndman et al., 2023) and tested by Durbin-Watson statistics (Fox & Weisberg, 2019). For our APSIM wheat data we did not add independent errors, and therefore the utility of inspections of residuals on autocorrelation is limited. In our follow-up paper, these issues will be revisited in the context of a hierarchical Bayesian framework for fitting the dynamics of a collection of genotypes across a series of trials and environmental conditions.

The parameters for temperature response in Eq. (3b) were kept constant across genotypes implying there is no genetic variation for these parameters. The fitting of the temperature model involved the use of penalized splines (R package ‘pspline’; Ramsay and Ripley, 2022) to smooth and interpolate daily temperatures for input to Eq. (3b). Daily rainfall was similarly smoothed before fitting Eq. (4a).

3 Results

We report some selected results of fits of the four models to the data for demonstrative purposes, that is, we select biomass time series of specific genotypes in specific trials to demonstrate the fitting of our minimalistic crop growth models. In all Figures, black indicates the noise-free APSIM biomass data, and green indicates the fit of our minimalistic crop growth model to the biomass data.

Figure 1 shows two examples of a fit of the logistic model (model #1). The top row shows the fit for one genotype (g006), and this particular fit is visually satisfactory. It will be no surprise that the weighted residuals (see top middle panel) are judged as not being i.d.d. according to the Durbin-Watson statistic, and they are clearly autocorrelated, as can be seen from the PACF (see top right panel). However, the autocorrelation is not an obvious reason to reject this model, and the fit suggests that a logistic model would be adequate for prediction purposes. At this point, one may argue the need for the inclusion of any additional explanatory factor. However, repeating an earlier point, the logistic model is fixed by the initial condition and does not allow for modifications in the growth rate by external inputs during the growing season. This would present a more pressing reason for any rejection of the

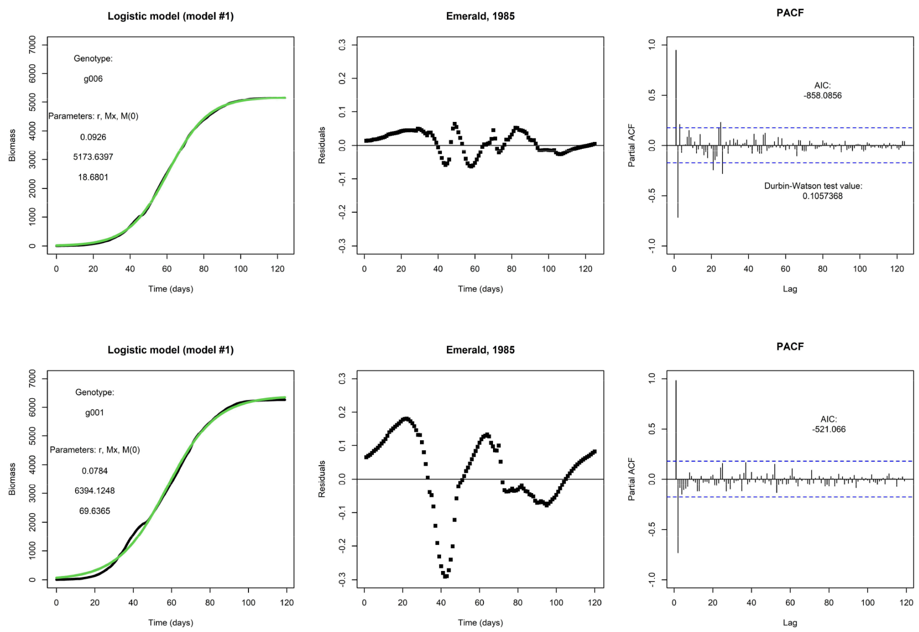

FIGURE 1

Top row: An example fit of the logistic model, with Emerald, 1985, g006. Fitted parameter values are displayed. Visually, the fit (in green) matches nicely with the daily biomass series (in black). Bottom row: An example of the same model and same environment, but genotype g001. The fit is visually less satisfactory than the fit for genotype g006.

model. In the bottom row, we fit the same model to the same environment but for a different genotype (g001); note that this genotype also takes fewer days to get to end-of-season. This fit is less satisfactory and the residuals plotted in time make larger excursions.

Figure 2 gives an example of how the fit to the data may be improved by the irradiance model (model #2). The fit for g001 with the irradiance model is considerably better than that with the logistic model: the AIC score is much lower, the residuals are smaller and even close to zero in the early and late parts of the growing season, and the initial condition $M(0)$ is much smaller. This suggests that the addition of two parameters for the seasonality is an improvement, and also suggests that the inclusion of day length as approximation of irradiance is worthwhile.

The temperature model exhibited more dynamic changes to within-season conditions for growth because it involves an exogenous variable (temperature). For comparison, Figure 3 shows a fit for genotype g001 in the same environment as the previous two models (upper left panel). It captures modifications to biomass growth rate that are relatively small and that took place on the scale of a couple of days (see Figure 3, upper right panel), producing realistic end-of-season biomass predictions. Figure 3, lower left panel shows the temperature response curve using Eq. (3b) and the parameter values given in Table 3. For many of our genotype by environment combinations, this model did not improve the fit in comparison to the fits by the logistic model or irradiance model, e.g., consider the plot of the residuals (Figure 3, lower right panel). Note, that the parameters in Eq. (3b) were kept

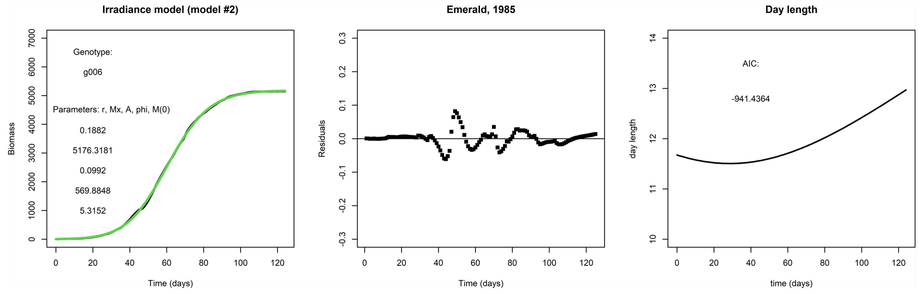

FIGURE 2

Left panel: A fit with the irradiance model to the same data set used to fit the logistic model in Figure 1, lower row. Middle panel: The residuals and AIC suggest that the irradiance model is a considerable improvement over the logistic model in this particular case. Right panel: Day length, taken from the APSIM model.

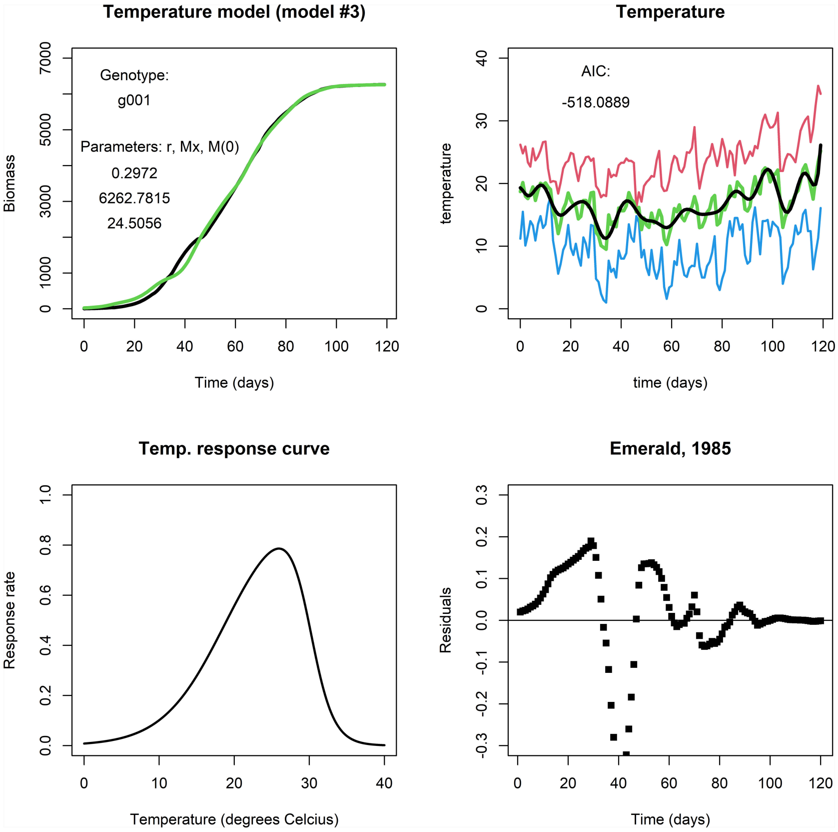

FIGURE 3
Upper left panel: A fit with the temperature model for Emerald, 1985, g001. Upper right panel: Red indicates maximum daily temperature, blue minimum, green the average temperature, and black the smoothened curve. Lower left panel: The temperature response curve, which was fixed in all simulations with the temperature model. Lower right panel: The fit mostly follows the biomass data during the growing season, but in particular in the period between day 25 through 50 the residuals are far off. This may be an indication that the temperature response curve should be adjusted, or that temperature is not the main factor that affects growth at this stage of the growing season.].

constant across genotypes and environments, and that different results may be obtained when the temperature response is adjusted. Also, in most of our simulated data, temperatures varied mildly within the (sub) optimal range for wheat growth, so it is perhaps not surprising that the temperature model did not translate to a considerable improvement in describing biomass development compared to the fits of the logistic model and the irradiance model.

None of the three models above, logistic, irradiance, or temperature, produced adequate fits for the biomass longitudinal data of genotype by environment combinations in which a ‘bump’ occurred near the end of the growing season (Figure 4, the top three rows, for an example involving g007, growing in Emerald, 2002). In this subset of genotype by environment combinations, there was a considerable biomass increase before the usual levelling-off at the end of the growing season, which seemed to coincide with changes in water availability. Figure 4, fourth row gives the biomass fit of the water model (Eq. 4b), including the (PACF of the) residuals of the biomass, while the bottom row gives the fit of the soil water (Eq. 4a), including residuals. In this set, the ‘bump’ started around day 92. The temperature remained approximately stationary for several days around day 92, while soil water levels were increased by precipitation around days 90-95 (Figure 4, lower left panel), suggesting that a depletion of soil water was the main driver responsible for the levelling off of the growth rate, at least towards the second half of the growing season. The water model qualitatively shows the same development in biomass and soil water as the data, though the residuals indicate that the fit is not perfect. This could be the result of an overestimated maintenance, the main term for biomass loss in the model, which was assumed to be scaling linearly with biomass. Also, growth in the first half of the growing season may have been limited not by soil water but by another factor.

4 Discussion

In this paper we considered parsimonious crop growth models consisting of differential equations with few parameters and variables that couple the rate of change in biomass to its own state. The aim was to present a modelling framework of limited complexity for genotype-dependent trait prediction involving essential GxExM interactions and that can respond to changes during the growing season as measured by proximal and remote sensing. The four presented models each had a different limiting environmental factor: a generic limitation described by logistic growth, irradiance via day length, temperature response, or soil

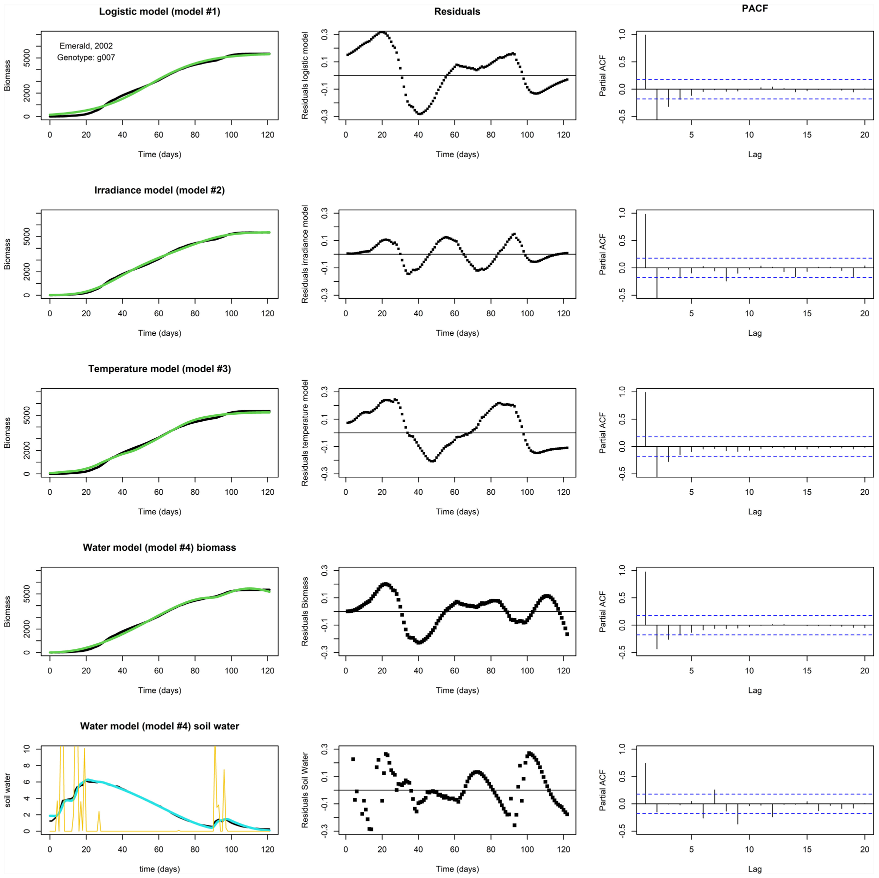

FIGURE 4
Fits to data set Emerald, 2002, g007. The biomass data (in black) shows a 'bump' around days 90-95. Left panels: Optimized fit of the model to the data. Middle panels: Residuals of the optimized fit. Right panels: PACF. Top row: A fit with the logistic model. Second row: The irradiance model. Third row: The temperature model. None of the models show a satisfactory fit. Fourth row: A fit of biomass with the water model, using Nelder-Mead, with resulting parameter values p=1.061, K=3.618·10^{2}, q=5.521·10^{-2}, c=7.824·10^{-2}, n=1.095, v=5.318·10^{-1}, R=1.320·10^{-3}, g=1.108, m=1.150·10^{-2}, W(0)=1.880, and M(0)=5.584·10^{-3}. Lower row: The fit of the soil water (in blue). Precipitation is plotted in yellow. Note the decrease in biomass near the end of the growing season in the water model fit, which is likely the result of an overestimated maintenance, the main term in the model that can lead to biomass reduction.

water availability, respectively. The models were fitted to *in silico* longitudinal data of 199 genotypes generated with APSIM-Wheat to demonstrate their performance. In many cases the logistic model gave already quite an adequate fit, but for many genotype by environment combinations there was at least one alternative model that matched the data convincingly better. This implies that for such genotype by environment combinations a specifically identified environmental limitation was dominant.

Depending on the specific combination of genotype and environment, where an environment refers to a trial simulated for a combination of year and location, one model may fit better than another. The calibration procedure may be limiting as well. In those situations in which we judged the logistic model to be adequate, we found that fitting this model by FME – deSolve was unproblematic, and often a single attempt at fitting this model sufficed. Fitting of the temperature model was more problematic and required the temperature response parameters in Eq. (3b) to be fixed, as leaving one or more of these parameters free in fitting in many cases led to temperature response curves that were unrealistic, as assessed by visual inspection. The water model proved most challenging in fitting and usually required several fitting attempts. The first term in Eq. (4a) involving the infiltration of precipitation in the soil turned out to be an essential part, as replacing the term with a linear response function of precipitation resulted in suspect and unrealistic fits (not shown). Note, that when we are fitting each combination of genotype and environment separately – like we did in this paper – then there are nine parameters and two initial conditions to fit. This makes it likely there are multiple local fitting optima, which may lead to spurious results. The use of alternative fitting approaches may produce better results. In a hierarchical approach to fitting we can divide the parameters into two groups that can be fitted separately: one group of parameters that vary across environments – and that hence should be approximately constant across genotypes grown in the same environment – and one group of parameters that mainly vary across genotypes.

While there is a decades-long history of developing crop simulation platforms (Jin et al., 2018), it remains challenging to balance a broad application range with model parsimony. The limited complexity of the proposed models in this paper hampers a more general application. In these models only one limitation is included. In reality, it is likely that two or more limitations occur during a growing season, and the particular limiting factor may change during the growing season: important limiting factors like irradiance, atmospheric carbon dioxide, soil water, and nutrients may operate at different moments and scales. Also, multiple limitations may occur at the same time. As an example of this phenomenon, Zhao et al. (2022) attributed considerable losses of winter wheat to the co-occurring extreme events of high temperatures, dryness and hard winds compared to events in which a single limiting factor occurred. Additionally, what parsimony offers in terms of elegance and statistical ease may come at the cost of fewer points of entry for discriminating among genotypes. In particular, the models proposed in this paper ignore phenology. Yet, the examples shown in this paper suggest one can already explain much of the crop growth in some situations with low-complexity models that ignore phenology.

Some dynamic crop models have been proposed that include essential processes and that try to balance limited model complexity with a broad application range. For example, the SIMPLE model consists of 13 parameters, involving cumulative temperature for phenological development and a multiplicative function including daily temperature, heat stress, drought stress, atmospheric carbon dioxide concentration, radiation use efficiency, and irradiance interception, and has been parameterized for 14 different crop species (Zhao et al., 2019).

A second step in modelling involves the introduction of functions that can smoothly and dynamically describe multiple resource limitations that occur during the growing season, i.e., that involve multiple co-limitations at different points in time and space. Arguably the best known multiple limitation description is Liebig's law of the minimum, where it is assumed there is only a single resource limitation at any given time, while any switch to another limitation is instantaneous (Cossani and Sadras, 2018). Functions that allow for a smoother transition to another limiting factor or that allow for multiple co-limiting factors have also been proposed in ecological models (Dutta et al., 2014). One example is the Synthesizing Unit (SU; Kooijman, 2010), which is a functional response comparable to the Michaelis-Menten (MM) functional response. Like the MM functional response, the SU is derived from law of mass action kinetics and includes multiple factors that are unique or mutually exchangeable in a smooth and continuous model formulation (Dutta et al., 2014). The SU has, for instance, been used to capture the co-limitation of light and nitrogen in the growth of heather shrubs and wavy hair-grass (Van Voorn et al., 2016). Another example is the description of the co-limitation of light, carbon dioxide, nitrogen, and phosphorus in the growth of cyanobacteria that were grown in a set of experiments across which these environmental factors were simultaneously varied in different combinations of higher and lower concentrations (Grossowicz et al., 2017).

With the inclusion of multiple limitations for the description of GxExM interactions comes the need for stronger data requirements for model fitting and reduction of uncertainties. In particular, the water model consisted of several parameters, initial conditions, and one explicit exogeneous input (precipitation). This model turned out to be more difficult to fit, even to the noise free data we had available. Furthermore, despite increasing data availability, proximal sensing data are still relatively rare and expensive. The fitting of the water model was further complicated by a conceptual mismatch between the soil water variable in our crop growth model (where it is an independent state variable interacting with the crop biomass) and the soil water supply variable in the APSIM simulated data (where it is calculated based on precipitation and available soil water following a submodule). Also, uncertainties remain that negatively affect forecasting. For instance, imprecision in soil, canopy state, and meteorological data propagate to uncertainty in model predictions (Hansen & Jones, 2000; Grassini et al., 2015), while various random events occur during the growing season, such as changes in irradiance due to clouds, irregular precipitation, or temperature changes.

In the current paper, we fitted dynamic models to longitudinal biomass data consisting of time series data corresponding to a single genotype in a single environment (year by location). We used an approach especially developed for fitting differential equations, focussing on the estimation of rates of change and initial conditions (Soetaert and Petzoldt, 2010; Soetaert et al., 2010). We concluded that the four minimalistic models may be useful to describe biomass dynamics in wheat. However, our ultimate aim goes far beyond the fitting of dynamical models for individual genotypes in individual environments. In the end, the goal is to develop a modelling framework for describing dynamical phenotypic behaviour of genotypes as functions of genetic (QTLs, SNPs in genomic prediction), management and environmental inputs. Such a modelling framework should allow us to predict yield and other traits for existing and new genotypes across a wide range of management and environmental conditions, and produce GxExM interactions in an emergent way. Leading contributions to the creation of such a modelling and prediction framework include papers by Technow et al. (2015), Cooper et al. (2016), and Messina et al. (2018). The starting point for these papers were existing crop growth models in which a small number of crop growth parameters were made genotype-dependent by regressing them on marker profiles inside a hierarchical Bayesian model. In the current paper, we intend to simplify the extensive dynamical crop growth model that was used in the papers mentioned above and reduce it to a small number of differential equations with a limited number of parameters. The challenge that we need to address is to identify a suitable dynamic model for each combination of genotype and environment and estimate genotype-dependent dynamic parameters, with little or no genotype by environment interaction, that can be made functions of marker profiles. Our hope is firstly that we will be able to model the dynamic behaviour of longitudinal traits as produced by especially proximal sensing devices by simple differential equations in a data driven way. Secondly, because the proposed differential equations have a limited number of parameters, we should be able to estimate genetic variation in the rate parameters. Of course, when explicit solutions exist to the differential equation system, a statistical approach to our problem could be found in the application of non-linear mixed models (Pinheiro and Bates, 2000). Without such explicit solutions, Bayesian hierarchical approaches may offer the best perspectives (Poudel et al., 2022), which is the route we will explore in a follow-up paper.

With dynamic models that incorporate data assimilation, the forecasting solution by the model may be adapted during the growing season. Remote and proximal sensing methodologies can provide actual state estimations at different scales, that can be used to update the state estimations by the crop model and thus steer forecasting by the model. Different assimilation approaches, including Particle Filter and Hierarchical Bayesian Method, have been proposed (Jin et al., 2018). For example, an Ensemble Kalman filter (EnKF) was used to assimilate sensor data of soil moisture to correct errors in the water balance of the WOFOST crop model (De Wit & Van Diepen, 2007). A similar approach was followed for constraining uncertainty in an upstream process in the model APSIM, with the goal of reducing uncertainty in the downstream processes (Kivi et al., 2022). Data assimilation for prediction updating also is a method for including exogenous input changes in 'static' models, such as the logistic growth.

Crop modelling has a critical role in forecasting crop growth of existing and new genotypes in existing and new environments. Future efforts for crop growth prediction should aim at a strategy of balancing crop model complexity: on the one hand, these models need to be process-based and describe multiple essential GxExM interactions to predict crop growth across a large genetic spectrum and multiple environments, while on the other hand they have to remain parsimonious to constrict issues around parameter fitting and uncertainty. This requires large-scale longitudinal data, that may become available with the increased remote and proximal sensing. More advanced fitting approaches should be tailored to support this strategy, while data assimilation can be used to reduce prediction uncertainty.

Data availability statement

The original contributions presented in the study are included in the article/Supplementary Material. Further inquiries can be directed to the corresponding author.

Author contributions

Modelling GxExM was conceived between Corteva Agriscience^{TM} and Wageningen University and Research – Biometris and led by CM and FV, respectively. Conceptualization and development was done by all authors. APSIM-Wheat simulation data were created by DB. Model fitting and first version manuscript writing and preparation was done by GV. Intermediate editing of manuscript was done by all authors. FV and GV did the final manuscript editing. All authors contributed to the article and approved the submitted version.

Acknowledgments

The authors would like to thank a reviewer whose valuable feedback has led to a considerable improvement of this paper.

Conflict of interest

Authors ST, RM, NF, and CM were employees of Corteva Agriscience™ when this manuscript was conceived.

The remaining authors declare that the research was conducted in the absence of any commercial or financial relationships that could be construed as a potential conflict of interest.

Publisher's note

References

Akaike, H. (1974). A new look at the statistical model identification. *IEEE* 19 (6), 716–723. doi: 10.1109/TAC.1974.1100705

Ardia, D., Boudt, K., Carl, P., Mullen, K. M., and Peterson, B. G. (2010). Differential evolution with 'DEoptim': an application to non-convex portfolio optimization. *R J.* 3 (1), 27–34. doi: 10.32614/RJ-2011-005

Arroyo, J. I., Díez, B., Kempes, C. P., West, G. B., and Marquet, P. A. (2022). A general theory for temperature dependence in biology. *PNAS* 119 (30), e2119872119. doi: 10.1073/pnas.2119872119

Ashyraliyev, M., Fomekong-Nanfack, Y., Kaandorp, J. A., and Blom, J. G. (2009). Systems biology: parameter estimation for biochemical models. *FEBS* 276 (4), 886–902. doi: 10.1111/j.1742-4658.2008.06844.x

Bendtsen, C. (2022). *Pso: particle swarm optimization* (R package version 1.0.4). Available at: https://CRAN.R-project.org/package=pso.

Beven, K., and Freer, J. (2001). Equifinality, data assimilation, and uncertainty estimation in mechanistic modelling of complex environmental systems using the GLUE methodology. *J. Hydrol.* 249 (1-4), 11–29. doi: 10.1016/S0022-1694(01)00421-8

Bustos-Korts, D., Boer, M. P., Malosetti, M., Chapman, S., Chenu, K., Zheng, B., et al. (2019a). Combining crop growth modeling and statistical genetic modeling to evaluate phenotyping strategies. *Front. Plant Sci.* 10. doi: 10.3389/fpls.2019.01491

Bustos-Korts, D., Malosetti, M., Chenu, K., Chapman, S., Boer, M. P., Zheng, B., et al. (2019b). From QTLs to adaptation landscapes: using genotype-to-phenotype models to characterize G×E over time. *Front. Plant Sci.* 10. doi: 10.3389/fpls.2019.01540

Cannell, M. G. R., and Thornley, J. H. M. (2000). Modelling the components of plant respiration: some guiding principles. *Ann. Bot.* 85 (1), 45–54. doi: 10.1006/anbo.1999.0996

Cole, D. J., Morgan, B. J., and Titterington, D. M. (2010). Determining the parametric structure of models. *Math. Biosci.* 228 (1), 16–30. doi: 10.1016/j.mbs.2010.08.004

Cooper, M., Technow, F., Messina, C., Gho, C., and Totir, L. R. (2016). Use of crop growth models with whole-genome prediction: application to a maize multienvironment trial. *Crop Sci.* 56 (5), 2141–2156. doi: 10.2135/cropsci2015.08.0512

Cossani, C. M., and Sadras, V. O. (2018). Water–nitrogen colimitation in grain crops. *Adv. Agron.* 150, 231–274. doi: 10.1016/bs.agron.2018.02.004

Curtis, B. C. (2002). "Wheat in the world," in *Bread wheat: improvement and production (No. CIS-3616. CIMMYT.).* Eds. B. C. Curtis, S. Rajaram and H. Gómez Macpherson (FAO Plant Production and Protection Series 30). Available at: https://www.fao.org/3/Y4011E/y4011e04.htm#bm04.

DeLong, J. P., Gibert, J. P., Luhring, T. M., Bachman, G., Reed, B., Neyer, A., et al. (2017). The combined effects of reactant kinetics and enzyme stability explain the temperature dependence of metabolic rates. *Ecol. Evol.* 7 (11), 3940–3950. doi: 10.1002/ece3.295

De Wit, A. D., and Van Diepen, C. A. (2007). Crop model data assimilation with the ensemble kalman filter for improving regional crop yield forecasts. *Agric. For. Meteorol.* 146 (1-2), 38–56. doi: 10.1016/j.agrformet.2007.05.004

Djanaguiraman, M., Boyle, D. L., Welti, R., Jagadish, S. V. K., and Prasad, P. V. V. (2018). Decreased photosynthetic rate under high temperature in wheat is due to lipid desaturation, oxidation, acylation, and damage of organelles. *BMC Plant Biol.* 18 (1), 1–17. doi: 10.1186/s12870-018-1263-z

Dokoohaki, H., Kivi, M. S., Martinez-Feria, R., Miguez, F. E., and Hoogenboom, G. (2021). A comprehensive uncertainty quantification of large-scale process-based crop modeling frameworks. *Environ. Res. Lett.* 16 (8), 084010. doi: 10.1088/1748-9326/ac0f26

Dutta, P. S., Kooi, B. W., and Feudel, U. (2014). Multiple resource limitation: nonequilibrium coexistence of species in a competition model using a synthesizing unit. *Theor. Ecol.* 7 (4), 407–421. doi: 10.1007/s12080-014-0228-6

Fox, J., and Weisberg, S. (2019). *An r companion to applied regression. 3rd ed.* (Thousand Oaks CA: Sage). Available at: https://socialsciences.mcmaster.ca/jfox/Books/Companion/.

Grassini, P., van Bussel, L. G., Van Wart, J., Wolf, J., Claessens, L., Yang, H., et al. (2015). How good is good enough? data requirements for reliable crop yield simulations and yield-gap analysis. *Field Crops Res.* 177, 49–63. doi: 10.1016/j.fcr.2015.03.004

Grossowicz, M., Marques, G. M., and van Voorn, G. A. K. (2017). A dynamic energy budget (DEB) model to describe population dynamics of the marine cyanobacterium prochlorococcus marinus. *Ecol. Modell.* 359, 320–332. doi: 10.1016/j.ecolmodel.2017.06.011

Hammer, G., Cooper, M., Tardieu, F., Welch, S., Walsh, B., van Eeuwijk, F., et al. (2006). Models for navigating biological complexity in breeding improved crop plants. *Trends Plant Sci.* 11 (12), 587–593. doi: 10.1016/j.tplants.2006.10.006

Hammer, G., Messina, C., Wu, A., and Cooper, M. (2019). Biological reality and parsimony in crop models–why we need both in crop improvement! *isP* 1 (1), diz010. doi: 10.1093/insilicoplants/diz010

Hansen, J. W., and Jones, J. W. (2000). Scaling-up crop models for climate variability applications. *Agric. Syst.* 65 (1), 43–72. doi: 10.1016/S0308-521X(00)00025-1

Hoeting, J. A., Madigan, D., Raftery, A. E., and Volinsky, C. T. (1999). Bayesian Model averaging: a tutorial (with comments by m. Clyde, David draper and EI George, and a rejoinder by the authors. *Stat. Sci.* 14 (4), 382–417. doi: 10.1214/ss/1009212519

Holzworth, D., Huth, N. I., Fainges, J., Brown, H., Zurcher, E., Cichota, R., et al. (2018). APSIM next generation: overcoming challenges in modernising a farming systems model. *Env. Model. Software* 103, 43–51. doi: 10.1016/j.envsoft.2018.02.002

Huang, J., Gómez-Dans, J. L., Huang, H., Ma, H., Wu, Q., Lewis, P. E., et al. (2019). Assimilation of remote sensing into crop growth models: current status and perspectives. *Agric. For. Meteorol.* 276, 107609. doi: 10.1016/j.agrformet.2019.06.008

Hyndman, R., Athanasopoulos, G., Bergmeir, C., Caceres, G., Chhay, L., O'Hara-Wild, M., et al. (2023). *Forecast: forecasting functions for time series and linear models* (R package version 8.21). Available at: https://pkg.robjhyndman.com/forecast/.

Hyndman, R. J., and Khandakar, Y. (2008). Automatic time series forecasting: the forecast package for r. *J. Stat. Software* 26 (3), 1–22. doi: 10.18637/jss.v027.i03

Jarquín, D., Crossa, J., Lacaze, X., Du Cheyron, P., Daucourt, J., Lorgeou, J., et al. (2014). A reaction norm model for genomic selection using high-dimensional genomic and environmental data. *Theor. Appl. Genet.* 127, 595–607. doi: 10.1007/s00122-013-2243-1

Jin, X., Kumar, L., Li, Z., Feng, H., Xu, X., Yang, G., et al. (2018). A review of data assimilation of remote sensing and crop models. *Eur. J. Agron.* 92, 141–152. doi: 10.1016/j.eja.2017.11.002

Kasampalis, D. A., Alexandridis, T. K., Deva, C., Challinor, A., Moshou, D., and Zalidis, G. (2018). Contribution of remote sensing on crop models: a review. *J. Imaging* 4 (4), 52. doi: 10.3390/jimaging4040052

Keating, B. A., Carberry, P. S., Hammer, G. L., Probert, M. E., Robertson, M. J., Holzworth, D., et al. (2003). An overview of APSIM, a model designed for farming systems simulation. *Eur. J. Agron.* 18 (3-4), 267–288. doi: 10.1016/S1161-0301(02)00108-9

Kivi, M. S., Blakely, B., Masters, M., Bernacchi, C. J., Miguez, F. E., and Dokoohaki, H. (2022). Development of a data-assimilation system to forecast agricultural systems: a case study of constraining soil water and soil nitrogen dynamics in the APSIM model. *Sci. Total Environ.* 820, 153192. doi: 10.1016/j.scitotenv.2022.153192

Kooi, B. W., Boer, M. P., and Kooijman, S. A. L. M. (1998). On the use of the logistic equation in models of food chains. *Bull. Math. Biol.* 60 (2), 231–246. doi: 10.1006/bulm.1997.0016

Kooijman, S. A. L. M. (2010). *Dynamic energy budget theory for metabolic organisation* (Cambridge university press).

Lamsal, A., Welch, S. M., White, J. W., Thorp, K. R., and Bello, N. M. (2018). Estimating parametric phenotypes that determine anthesis date in *Zea mays*: challenges in combining ecophysiological models with genetics. *PloS One* 13 (4), e0195841. doi: 10.1371/journal.pone.0195841

McCormick, R. F., Truong, S. K., Rotundo, J., Gaspar, A. P., Kyle, D., Van Eeuwijk, F., et al. (2021). Intercontinental prediction of soybean phenology via hybrid ensemble of knowledge-based and data-driven models *in silico. Plants* 3 (1), diab004. doi: 10.1093/insilicoplants/diab004

Messina, C. D., Technow, F., Tang, T., Totir, R., Gho, C., and Cooper, M. (2018). Leveraging biological insight and environmental variation to improve phenotypic prediction: integrating crop growth models (CGM) with whole genome prediction (WGP). *Eur. J. Agron.* 100, pp.151–pp.162. doi: 10.1016/j.eja.2018.01.007

Millet, E. J., Kruijer, K., Coupel-Ledru, A., Alvarez Prado, S., Cabrera-Bosquet, L., Lacube, S., et al. (2019). Genomic prediction of maize yield across European environmental conditions. *Nat. Genet.* 51, 952–956. doi: 10.1038/s41588-019-0414-y

Mullen, K., Ardia, D., Gil, D., Windover, D., and Cline, J. (2011). 'DEoptim': an r package for global optimization by differential evolution. *J. Stat. Software* 40 (6), 1–26. doi: 10.18637/jss.v040.i06

Paine, C. T., Marthews, T. R., Vogt, D. R., Purves, D., Rees, M., Hector, A., et al. (2012). How to fit nonlinear plant growth models and calculate growth rates: an update for ecologists. *Methods Ecol. Evol.* 3 (2), 245–256. doi: 10.1111/j.2041-210X.2011.00155.x

Panday, U. S., Pratihast, A. K., Aryal, J., and Kayastha, R. B. (2020). A review on drone-based data solutions for cereal crops. *Drones* 4 (3), 41. doi: 10.3390/drones4030041

Parent, B., and Tardieu, F. (2012). Temperature responses of developmental processes have not been affected by breeding in different ecological areas for 17 crop species. *New Phytol.* 194 (3), 760–774. doi: 10.1111/j.1469-8137.2012.04086.x

Peng, B., Guan, K., Tang, J., Ainsworth, E. A., Asseng, S., Bernacchi, C. J., et al. (2020). Towards a multiscale crop modelling framework for climate change adaptation assessment. *Nat. Plants* 6 (4), 338–348. doi: 10.1038/s41477-020-0625-3

Pereira, L. S., Allen, R. G., Smith, M., and Raes, D. (2015). Crop evapotranspiration estimation with FAO56: past and future. *Agric. Water Manage.* 147, 4–20. doi: 10.1016/j.agwat.2014.07.031

Pérez-Valencia, D. M., Rodríguez-Álvarez, M. X., Boer, M. P., Kronenberg, L., Hund, A., Cabrera-Bosquet, L., et al. (2022). A two-stage approach for the spatio-temporal analysis of high-throughput phenotyping data. *Sci. Rep.* 12 (1), 1–16. doi: 10.1038/s41598-022-06935-9

Pinheiro, J. C., and Bates, D. M. (2000). Linear mixed-effects models: basic concepts and examples. In: Mixed-effects models in S and S-Plus. 3–56.

Porter, J. R., and Gawith, M. (1999). Temperatures and the growth and development of wheat: a review. *Eur. J. Agron.* 10 (1), 23–36. doi: 10.1016/S1161-0301(98)00047-1

Poudel, P., Bello, N. M., Lollato, R. P., and Alderman, P. D. (2022). A hierarchical Bayesian approach to dynamic ordinary differential equations modeling for repeated measures data on wheat growth. *Field Crops Res.* 283, 108549. doi: 10.1016/j.fcr.2022.108549

Ramsay, J., and Ripley, B. (2022) *Penalized smoothing splines*. Available at: https://CRAN.R-project.org/package=pspline.

R Core Team (2021). *R: a language and environment for statistical computing* (Vienna, Austria: R Foundation for Statistical Computing). Available at: https://www.R-project.org/.

Reed, H. S., and Holland, R. H. (1919). The growth rate of an annual plant helianthus. *PNAS* 5 (4), 135–144. doi: 10.1073/pnas.5.4.135

Richards, F. J. (1959). A flexible growth function for empirical use. *J. Exp. Bot.* 10 (2), 290–301. doi: 10.1093/jxb/10.2.290

Roth, L., Piepho, H. P., and Hund, A. (2022). Phenomics data processing: extracting dose-response curve parameters from high-resolution temperature courses and repeated field-based wheat height measurements. *in silico Plants* 4 (1), 1–16. doi: 10.1093/insilicoplants/diac007

Roth, L., Rodríguez-Álvarez, M. X., van Eeuwijk, F., Piepho, H.-P., and Hund, A. (2021). "Phenomics data processing: a plot-level model for repeated measurements to extract the timing of key stages and quantities at defined time points.". *Field Crops Res.* 274, 108314. doi: 10.1016/j.fcr.2021.108314

Ruane, A. C., Rosenzweig, C., Asseng, S., Boote, K. J., Elliott, J., Ewert, F., et al. (2017). An AgMIP framework for improved agricultural representation in integrated assessment models. *Environ. Res. Lett.* 12 (12), 125003. doi: 10.1088/1748-9326/aa8da6

Schils, R. L., van Voorn, G. A. K., Grassini, P., and van Ittersum, M. K. (2022). Uncertainty is more than a number or colour: involving experts in uncertainty assessments of yield gaps. *Agric. Syst.* 195, 103311. doi: 10.1016/j.agsy.2021.103311

Shammi, S. A., and Meng, Q. (2021). Use time series NDVI and EVI to develop dynamic crop growth metrics for yield modeling. *Ecol. Indic.* 121, 107124. doi: 10.1016/j.ecolind.2020.107124

Sharpe, P. J., and DeMichele, D. W. (1977). Reaction kinetics of poikilotherm development. *J. Theor. Biol.* 64 (4), 649–670. doi: 10.1016/0022-5193(77)90265-X

Shein, E. V., and Mady, A. Y. (2018). Hysteresis of the water retention curve: wetting branch simulation based on the drying curve. *Mosc. Univ. Soil Sci. Bull.* 73 (3), 124–128. doi: 10.3103/S0147687418030080

Soetaert, K., and Petzoldt, T. (2010). Inverse modelling, sensitivity and Monte Carlo analysis in r using package FME. *J. Stat. Software* 33, 1–28. doi: 10.18637/jss.v033.i03

Soetaert, K., Petzoldt, T., and Setzer, R. W. (2010). Solving differential equations in r: package deSolve. *J. Stat. Software* 33, 1–25. doi: 10.18637/jss.v033.i09

Stöckle, C. O., and Kemanian, A. R. (2020). Can crop models identify critical gaps in genetics, environment, and management interactions? *Front. Plant Sci.* 11. doi: 10.3389/fpls.2020.00737

Technow, F., Messina, C. D., Totir, L. R., and Cooper, M. (2015). Integrating crop growth models with whole genome prediction through approximate Bayesian computation. *PloS One* 10 (6), e0130855. doi: 10.1371/journal.pone.0130855

Tsutsumi-Morita, Y., Heuvelink, E., Khaleghi, S., Bustos-Korts, D., Marcelis, L. F., Vermeer, K. M., et al. (2021). Yield dissection models to improve yield: a case study in tomato. *isP* 3 (1), diab012. doi: 10.1093/insilicoplants/diab012

Van de Koppel, J., and Rietkerk, M. (2004). Spatial interactions and resilience in arid ecosystems. *Am. Nat.* 163 (1), 113–121. doi: 10.1086/380571

Van Eeuwijk, F. A., Bustos-Korts, D. V., and Malosetti, M. (2016). What should students in plant breeding know about the statistical aspects of genotype× environment interactions? *Crop Sci.* 56 (5), 2119–2140. doi: 10.2135/cropsci2015.06.0375

Van Eeuwijk, F. A., Bustos-Korts, D., Millet, E. J., Boer, M. P., Kruijer, W., Thompson, A., et al. (2019). Modelling strategies for assessing and increasing the effectiveness of new phenotyping techniques in plant breeding. *Plant Sci.* 282, 23–39. doi: 10.1016/j.plantsci.2018.06.018

Van Voorn, G. A. K., Kooi, B. W., and Bregt, A. K. (2016). Over-shading is critical for inducing a regime shift from heathland to grassland under nitrogen enrichment. *Ecol. Complex.* 27, 74–83. doi: 10.1016/j.ecocom.2015.08.001

Wagener, T., Boyle, D. P., Lees, M. J., Wheater, H. S., Gupta, H. V., and Sorooshian, S. (2001). A framework for development and application of hydrological models. *Hydrol. Earth Syst. Sci.* 5 (1), 13–26. doi: 10.5194/hess-5-13-2001

Wagener, T., McIntyre, N., Lees, M. J., Wheater, H. S., and Gupta, H. V. (2003). Towards reduced uncertainty in conceptual rainfall-runoff modelling: dynamic identifiability analysis. *Hydrol. Process.* 17 (2), 455–476. doi: 10.1002/hyp.1135

Wang, E., Martre, P., Zhao, Z., Ewert, F., Maiorano, A., Rötter, R. P., et al. (2017). The uncertainty of crop yield projections is reduced by improved temperature response functions. *Nat. Plants* 3 (8), 1–13. doi: 10.1038/nplants.2017.102

Zhao, C., Liu, B., Xiao, L., Hoogenboom, G., Boote, K. J., Kassie, B. T., et al. (2019). A SIMPLE crop model. *Eur. J. Agron.* 104, 97–106. doi: 10.1016/j.eja.2019.01.009

Zhao, H., Zhang, L., Kirkham, M. B., Welch, S. M., Nielsen-Gammon, J. W., Bai, G., et al. (2022). US Winter wheat yield loss attributed to compound hot-dry-windy events. *Nat. Commun.* 13 (1), 7233. doi: 10.1038/s41467-022-34947-6

Frontiers in Plant Science

TYPE Original Research
PUBLISHED 03 January 2024
DOI 10.3389/fpls.2023.1214931

OPEN ACCESS

EDITED BY
Wei Guo,
The University of Tokyo, Japan

REVIEWED BY
Geng (Frank) Bai,
University of Nebraska-Lincoln,
United States
Sivakumar Sukumaran,
The University of Queensland, Australia

*CORRESPONDENCE
Moritz Paul Camenzind
✉ Moritz.camenzind@tum.de
Kang Yu
✉ Kang.Yu@tum.de

RECEIVED 30 April 2023
ACCEPTED 29 November 2023
PUBLISHED 03 January 2024

CITATION
Camenzind MP and Yu K (2024) Multi temporal multispectral UAV remote sensing allows for yield assessment across European wheat varieties already before flowering.
Front. Plant Sci. 14:1214931.
doi: 10.3389/fpls.2023.1214931

Multi temporal multispectral UAV remote sensing allows for yield assessment across European wheat varieties already before flowering

Moritz Paul Camenzind[1]* and Kang Yu[1,2]*

[1]Precision Agriculture Lab, School of Life Sciences, Technical University of Munich, Freising, Germany,
[2]World Agricultural Systems Center (Hans Eisenmann-Forum for Agricultural Sciences – HEF), Technical University of Munich, Freising, Germany

High throughput field phenotyping techniques employing multispectral cameras allow extracting a variety of variables and features to predict yield and yield related traits, but little is known about which types of multispectral features are optimal to forecast yield potential in the early growth phase. In this study, we aim to identify multispectral features that are able to accurately predict yield and aid in variety classification at different growth stages throughout the season. Furthermore, we hypothesize that texture features (TFs) are more suitable for variety classification than for yield prediction. Throughout 2021 and 2022, a trial involving 19 and 18 European wheat varieties, respectively, was conducted. Multispectral images, encompassing visible, Red-edge, and near-infrared (NIR) bands, were captured at 19 and 22 time points from tillering to harvest using an unmanned aerial vehicle (UAV) in the first and second year of trial. Subsequently, orthomosaic images were generated, and various features were extracted, including single-band reflectances, vegetation indices (VI), and TFs derived from a gray level correlation matrix (GLCM). The performance of these features in predicting yield and classifying varieties at different growth stages was assessed using random forest models. Measurements during the flowering stage demonstrated superior performance for most features. Specifically, Red reflectance achieved a root mean square error (RMSE) of 52.4 g m^{-2} in the first year and 64.4 g m^{-2} in the second year. The NDRE VI yielded the most accurate predictions with an RMSE of 49.1 g m^{-2} and 60.6 g m^{-2}, respectively. Moreover, TFs such as CONTRAST and DISSIMILARITY displayed the best performance in predicting yield, with RMSE values of 55.5 g m^{-2} and 66.3 g m^{-2} across the two years of trial. Combining data from different dates enhanced yield prediction and stabilized predictions across dates. TFs exhibited high accuracy in classifying low and high-yielding varieties. The CORRELATION feature achieved an accuracy of 88% in the first year, while the HOMOGENEITY feature reached 92% accuracy in the second year. This study confirms the hypothesis that TFs are more suitable for variety classification than for yield prediction. The results underscore the potential of TFs derived from multispectral images in early yield prediction and varietal classification, offering insights for HTP and precision agriculture alike.

KEYWORDS

wheat variety testing, yield prediction, UAV remote sensing, image texture features, machine learning, phenology

1 Introduction

Yield improvements are currently estimated to average less than 1% annually in Europe and are even decreasing in some European countries (Ray et al., 2013). One of the reasons for this stagnation are low breeding gains which are estimated to be only 0.45% (Cormier et al., 2013) per year. Grain yield is the product of the number of grains per area and the weight of a single grain, which are both controlled by a variety of genes. New molecular tools have emerged to advance breeding for such quantitative traits but their potential is still not exploited, partly due to our ability to phenotype (Araus and Cairns, 2014). Traditional methods for phenotyping of yield and yield related traits often require manual labor and are thus slow, expensive and subjective. Faster, cheaper and standardizable alternatives have emerged quickly in recent years and are referred to as high-throughput phenotyping (HTP) (Cabrera-Bosquet et al., 2012; Hund et al., 2019; Watt et al., 2020).

HTP employs a variety of advanced technologies such as digital imaging, remote sensing and artificial intelligence but to assess grain yield directly remains infeasible under field conditions. Major advances have been achieved in counting the number of spikes (David et al., 2020; David et al., 2021) and first attempts have been made to count the number of grains per spike (Xu et al., 2023). To our knowledge, grain weight has not been directly assessed under field conditions using remote sensing. Although these techniques are promising, they are based on computer vision and require images that show a high level of detail, resulting in a low throughput of the technology (Eskandari et al., 2020). To overcome this limitation, yield assessment often focuses on the estimation of secondary traits that are related to yield formation (Li et al., 2019a).

To identify suitable secondary traits, yield formation has to be well understood. With an average precipitation between 2010 and 2020 of 741 mm (Climate Data Center of the German Weather Service), the agricultural systems in the Freising District, Bavaria, Germany can be classified as radiation limited (Patrignani et al., 2014), although lack of precipitation and high temperatures can lead to yield losses in this region as well (Heil et al., 2023). Therefore, yield formation in this region can very broadly be described as a function of the incident radiation per day during the growing season, the intercepted radiation over the canopy life cycle, the green leaf duration, the radiation use efficiency as well as the harvest index (Araus et al., 2008). This indicates that a single time point may not be sufficient for an accurate yield assessment. Furthermore, yield formation is influenced by an interplay of sources and sinks. The sinks can be seen as the potential yield and sources as the actual supply of assimilates (Fischer, 2011). This interplay starts with the transition of the plants from the vegetative to the reproductive stage and continues during anthesis until the grain filling stage (Slafer and Rawson, 1994). Still, some stages are more critical for yield formation than others are. Fischer (1985) found that a relatively short period before flowering is critical for yield formation due to the source driven survival of floret primordia at the stem elongation stage (González et al., 2005) and is linked to the spike biomass (Slafer et al., 1996). Breeders however are interested in the yield potential as early as possible in the growing season in order to be able to focus their phenotyping efforts on well performing genotypes (Garriga et al., 2017). At the germination stage, the maximum number of plants and at the tillering stage, the maximum number of tillers is being formed which are all linked to the final number of grains harvested. However, the tillering potential is highly dependent on the environment and under high yielding environments no differences in yield were found between varieties with a low and such with a high tillering potential (Bastos et al., 2020). Furthermore, the sinks at these early stages are microscopically small and hidden in the developing stems, making their detection impossible by remote sensing technologies. Therefore, predicting yield at the tillering stage is difficult.

Secondary traits related to the sources such as leaf area index (LAI) (Bukowiecki et al., 2020), chlorophyll content (Pan et al., 2023) and finally biomass (Yue et al., 2019) have been phenotyped using a variety of techniques. Primary traits such as grain yield and quality have been assessed by estimating the mentioned secondary traits during the growth season (Duan et al., 2017; Hassan et al., 2019; Vatter et al., 2022). A variety of sensors have been employed such as RGB cameras (Fernandez-Gallego et al., 2019), multispectral cameras (Prey et al., 2022), hyperspectral sensors (Bowman et al., 2015), thermal cameras (Elsayed et al., 2017) and active sensors such as Lidar (Li et al., 2022) to mention a few. Among these technologies, multispectral cameras offer a high work efficiency for a relatively low cost. Along with the reflectance, multispectral cameras are imaging sensors and therefore have the advantage of capturing the structure or texture of an object. As a result, they allow for extracting a unique variety of features to assess yield in wheat. Generally, these features can be grouped into three categories. First, single-band reflectance in specific wavelengths can be directly extracted from multispectral data. Vatter et al. (2022) fed single band reflectances to a neural network and predicted durum wheat quality and yield before the harvest. Second, the reflectance of single bands can be combined to calculate vegetation indices (VIs), which are often more sensitive to specific traits and less affected by environmental conditions during measurement (Tucker, 1979). This approach has been used by several studies for yield prediction (Duan et al., 2017; Hassan et al., 2019; Prey et al., 2022). However, single-band reflectance and VIs may suffer from saturation, particularly when the canopies are closed (Rischbeck et al., 2016). Third, texture features (TFs) can be extracted to describe the distribution of pixels within a region of interest (ROI). TFs were originally designed for image classification (Haralick et al., 1973) and have since been used for classification of forest stands (Coburn and Roberts, 2004), wheat phenology (Zhou et al., 2023) and wheat seeds (Khojastehnazhand and Roostaei, 2022). Therefore, they might also be beneficial when identifying elite wheat varieties directly as suggested by Garriga et al. (2017). Several studies employed TFs for yield prediction in explorative studies and found that they often perform less effectively than single-band reflectance or VIs (Li et al., 2019b; Yue et al., 2019; Zhang et al., 2021) but can improve the prediction of leaf area and biomass when combined with VIs (Yue et al., 2019; Zhang et al., 2021).

Accurately predicting yield or identifying elite wheat varieties using multispectral reflectance further requires careful consideration of the phenological stage of the canopy. Late stages such as the anthesis stage and the grain filling stage are often identified as the most suitable stages for yield prediction in wheat when using VIs (Bowman et al., 2015; Duan et al., 2017; Hassan et al., 2019). Earlier stages such the tillering stage are generally and naturally performing worse (Prey et al., 2022). Still, Walsh et al. (2022) successfully predicted yield at the tillering stage and Marti et al. (2007) at the stem elongation stage, both using the normalized difference vegetation index (NDVI). To date, most studies focus on only one measurement date during a given phenological stage or test only one feature or feature class. A more detailed study is therefore needed to better understand the interaction of phenology stages and features for yield prediction. Particularly, phenology showed to have a big influence on the relationship between biomass and TFs (Li et al., 2019c). However, the performance of TFs at different phenological stages has been reported in a few studies only (Zhang et al., 2021). Multispectral cameras mounted on unmanned aerial vehicles (UAVs) further enable breeders and researchers to assess the aforementioned spectral and TFs at a high temporal frequency and precision. Within a proper time-window, using a time series for yield prediction allows for the extraction of dynamic canopy traits that could potentially be useful for yield prediction. For instance, Pinter et al. (1981) suggested summing measurement dates after heading to improve yield prediction in wheat and barley whereas Raun et al. (2001) suggested taking two spectral measurements after dormancy. Prey et al. (2022) showed that models containing data from multiple dates could improve yield predictions and compensate if data could not be collected on the optimal date due to practical reasons and phenological shifts between years.

Collectively, despite these successes, little is known about which traits determine yield nor which types of multispectral features may allow us to forecast yield potential in a variety testing trial in the early growth phase. Therefore, this study aims (1) to identify the best performing multispectral traits for yield prediction and classification in wheat (2) to investigate, if yield types can be classified in relatively early stages and finally (3) to investigate, how traits measured at different time points can be combined to predict yield more accurately.

2 Methods

2.1 Field trials

Field trials were conducted at the research station of the Technical University of Munich in Dürnast, Freising (48.40630° N, 11.69535° E) in the growing seasons of 2020/2021 and 2021/2022 further referred to as seasons 2021 and 2022. The soil at this location can be characterized by a homogeneous Cambisol with 20.8% clay, 61.5% silt and 16.6% sand. Precipitation during this period was 595 mm and 415 mm in the first and the second season, respectively. The average temperature was 7.2°C in the first and 8.0°C in the second season (Supplementary Figure 1). A lot of precipitation around flowering characterized season 2021 whereas the season 2022 suffered too little precipitation at the end of the tillering stage. Climate data was collected from a weather station (Station id 5404) operated by the Climate Data Center of the German Weather Service located a few hundred meters from the trials. The temperature was aggregated to phenologically meaningful growing degree-days (GDD) (Equation 1) (Bonhomme, 2000):

$$GDD = \sum_{d=1}^{n} Tmean_d \tag{1}$$

$$Tmean_d = \frac{\sum \frac{maxT_{d,h}+minT_{d,h}}{2} - baseT}{24} \tag{2}$$

where $Tmean_d$is the mean temperature for day d after sowing as determined by Equation 2, $maxT_{d,h}$ and $minT_{d,h}$ are hourly maximum and minimum temperatures for day d and $baseT$ is the base temperature, which was set to 0°C.

A panel consisting of 19 diverse European winter wheat elite varieties (*Triticum aestivum*) in 2021 and 18 varieties in 2022 was grown in plots with a size of 10 m x 1.85 m. All varieties grown in 2022 were grown in 2021 as well (Table 1). The plots were arranged in a randomized complete block design with four replicates, resulting in 76 plots in 2021. In 2022, the 72 plots were part of a bigger trial, which was arranged as a randomized strip-plot design with four replicates as well. Orthophotos of the trials can be found in Supplementary Figure 2 in the appendix. All plots used for this study were fertilized by applying 180 kg N ha^{-1} in three equal splits at BBCH 25, 32 and 65. Plant protection was carried out according to local practice. Sowing took place on the 10.11.2020 and the 20.10.2021 and all plots were harvested at full maturity on the 03.08.2021 and the 26.07.2022, respectively.

2.2 Grain yield, phenology assessment and Leaf area index measurements

The entire plots were harvested using a combine harvester. The water content of the grains was determined by weighing the grains after harvest, drying them at 65°C until constant weight was reached and weighing them again. The final yield was normalized to a moisture content of 14%. In each year, the three varieties with the lowest average yield were classified as low yielding and the three varieties with the highest average yield as high yielding. The

TABLE 1 Grain yield, yield group and phenology of the single varieties.

Variety	Grain Yield		Yield group		Stem Elongation		Booting		Heading		Flowering		Early Grain Filling		Late Grain Filling	
	2021	2022	2021	2022	2021	2022	2021	2022	2021	2022	2021	2022	2021	2022	2021	2022
Absalon	532.0 (32.8)	700.8 (47.6)			635.0 (27.7)	749.8 (7.2)	917.5 (37.3)	1061.8 (18.5)	1046.5 (23.6)	1172 (9.3)	1153.3 (38.7)	1273.3 (16.1)	1397.0 (59.2)	1404.5 (26.0)	1653.3 (79.2)	NA
Aurelius	541.9 (56.4)	759.7 (76.5)		H	609.3 (3.5)	762 (12)	963.5 (52.6)	1037.8 (75.0)	1069.3 (17.6)	1132.5 (51)	1109.0 (0.0)	1229.3 (34.2)	1368.8 (62.5)	1360.8 (26.9)	1673.3 (63.9)	NA
Axioma	473.0 (41.8)	631.0 (32.9)	L		607.5 (4.0)	765.3 (17)	950.3 (31.7)	1102.3 (59.7)	1042.8 (23.8)	1195.5 (66.9)	1121.5 (11.2)	1289.8 (80.2)	1350.0 (51.8)	1422.5 (71.8)	1636.5 (57.7)	NA
Bernstein	522.3 (33.7)	625.0 (102.2)			626.8 (16.6)	773.3 (17)	981.5 (6.9)	1145 (0.0)	1091.0 (30.2)	1225.8 (13.8)	1201.0 (70.6)	1311.5 (14.5)	1434.8 (27.3)	1460 (14.0)	1684.8 (93.6)	NA
Bologna	490.7 (33.3)	660.7 (29.0)			625.5 (16.7)	751.8 (32.4)	926.8 (61.1)	1081 (84.5)	1038.5 (30.0)	1178 (88.1)	1109.0 (0.0)	1271.8 (85.3)	1363.0 (69.7)	1408.3 (68.4)	1651.5 (64.4)	NA
CH-Nara	559.4 (30.2)	683.2 (108.0)			635.0 (27.7)	757.5 (9.9)	921.3 (16.7)	1126.5 (37.0)	1042.0 (16.2)	1208 (37.4)	1137.0 (30.9)	1283 (38.1)	1356.3 (47.8)	1405.8 (41.1)	1601.5 (23.7)	NA
Chevignon	598.5 (63.5)	672.5 (43.9)	H		615.5 (30.6)	776.5 (39.8)	911.8 (17.7)	1082 (44.3)	1050.8 (25.4)	1200 (46.2)	1144.8 (21.1)	1283.3 (45.3)	1358.3 (45.9)	1446 (26.8)	1579.3 (13.0)	NA
Costello	478.6 (38.8)	589.0 (52.8)		L	635.5 (22.3)	786.0 (32.0)	959.0 (31.2)	1145 (0.0)	1103.0 (38.0)	1256.5 (8.2)	1207.8 (67.8)	1338 (9.9)	1411.8 (39.7)	1477.7 (21.4)	1739.8 (2.5)	NA
Dagmar	617.1 (45.4)	725.2 (65.1)	H	H	611.0 (0.0)	803.3 (32.1)	969.0 (41.6)	1108.8 (82.1)	1052.0 (22.3)	1210.5 (77.2)	1114.0 (16.0)	1311 (67.5)	1345.3 (53.3)	1447.6 (81.6)	1653.5 (74.5)	NA
Elixer	540.4 (76.2)	721.3 (93.3)			643.0 (27.7)	768.5 (8.2)	953.0 (43.2)	1086.8 (75.7)	1118.3 (34.7)	1180.3 (60.5)	1219.5 (87.4)	1290.3 (57.4)	1444.0 (20.8)	1436.5 (61.0)	1742.0 (5.8)	NA
Hyvento	576.2 (51.1)	685.3 (128.0)			641.3 (21.0)	775.3 (29.3)	956.0 (34.8)	1126.5 (37.0)	1121.8 (6.0)	1220.3 (30.8)	1181.8 (41.7)	1299.3 (19.1)	1418.5 (23.7)	1438.8 (40.1)	1756.0 (119.6)	NA
Julie	544.2 (95.9)	661.8 (94.6)			635.0 (27.7)	754.0 (19.6)	915.3 (21.8)	1059 (67.1)	1057.3 (15.8)	1155 (58.7)	1142.8 (16.8)	1253.5 (59.1)	1347.3 (44.6)	1383.5 (39.0)	1648.5 (65.7)	NA
Julius	443.3 (14.6)	544.0 (25.5)	L	L	639.0 (17.3)	827.8 (45.9)	962.0 (26.9)	1157.8 (25.5)	1092.0 (40.1)	1277.3 (41.4)	1201.3 (65.4)	1366.8 (32.9)	1442.8 (28.5)	1475.6 (17.1)	1782.0 (62.2)	NA
Montalbano	584.1 (68.8)	681.1 (33.3)			612.8 (3.5)	768.8 (14.2)	954.0 (29.5)	1086.8 (75.7)	1104.0 (14.6)	1183.3 (55.7)	1192.0 (24.0)	1284 (43.9)	1428.0 (18.9)	1392.8 (21.5)	1720.5 (78.5)	NA
Mv Nador	552.4 (45.0)	591.9 (53.0)			643.0 (27.7)	751.0 (11.8)	962.3 (62.6)	1077.5 (80.4)	1084.3 (40.4)	1156.8 (59.8)	1157.3 (76.5)	1238.8 (43.8)	1343.8 (47.7)	1399.8 (53.7)	1624.5 (74.4)	NA
Nogal	504.2 (81.6)	557.8 (59.2)		L	633.3 (29.9)	751.0 (11.8)	972.8 (51.7)	1010 (27.7)	1058.8 (27.3)	1104.3 (19.1)	1084.0 (7.7)	1197.8 (12.7)	1281.5 (26.4)	1331.3 (13.4)	1602.0 (16.9)	NA

(Continued)

TABLE 1 Continued

Variety	Grain Yield		Yield group		Stem Elongation		Booting		Heading		Flowering		Early Grain Filling		Late Grain Filling	
	2021	2022	2021	2022	2021	2022	2021	2022	2021	2022	2021	2022	2021	2022	2021	2022
RGT-Reform	411.4 (60.2)	671.6 (36.0)	L		629.0 (20.8)	792.3 (28.6)	941.0 (14.3)	1130 (39.9)	1105.0 (9.9)	1246.5 (28.1)	1179.0 (48.3)	1328.8 (24.1)	1426.8 (18.9)	1460 (14.0)	1641.3 (69.7)	NA
Rumor	543.9 (15.5)	NA			623.0 (24.0)	NA	926.8 (22.5)	NA	1045.3 (14.5)	NA	1124.8 (23.2)	NA	1403.8 (10.5)	NA	1635.5 (67.6)	NA
Skyfall	642.7 (49.6)	773.2 (47.1)	H	H	658.7 (82.6)	808.3 (66.8)	909.0 (41.2)	1133.5 (111.8)	1067.8 (34.2)	1222.8 (109.1)	1157.5 (32.8)	1323.5 (104.1)	1424.8 (21.0)	1438.7 (72.5)	1642.8 (84.7)	NA
All	535.5 (73.8)	663.1 (87.7)			628.5 (26.4)	773.4 (33)	945.1 (39.3)	1097.7 (65.9)	1073.2 (35.8)	1195.8 (64.1)	1154.6 (54.3)	1287.4 (55.3)	1386.6 (56.6)	1421.7 (55.3)	1666.8 (80.1)	NA

Values represent the mean of the four replicates; the values in parenthesis represent the standard deviation of the four replicates. Group "L" stands for low yielding, group "H" for high yielding; varieties without character have not been classified for the respective year.

phenology of each plot was visually rated using the BBCH scale (Meier et al., 2009) on a plot level. Leaf area index (LAI) was measured using a Licor 2000 leaf area meter (LI-COR Biosciences, Lincoln, USA.) with a 45° view cap to minimize operator influence. One measurements was taken at the top of the canopy and four measurements were taken under the canopy at three different locations per plot, which were then averaged.

2.3 Multispectral image acquisition and processing

Spectral measurements were acquired using a Phantom 4 Multispectral RTK (DJI, Shenzhen, China) unmanned aerial vehicle (UAV) in the first year. The UAV captures reflectance in wavelengths of 450, 560, 650, 730 and 840 nm and measures the incoming sunlight by a sensor on top of the UAV. Flight height was set to 10 m above ground level (AGL) resulting in a ground sampling distance (GSD) of 0.7 cm. In the second year, images were acquired using a MicaSense Dual Camera Kit (AgEagle Aerial Systems Inc., Wichita, USA) capturing reflectance in wavelengths of 444, 560, 650, 717, 842 nm. The camera was mounted to a DJI Matrice M300 RTK UAV (DJI, Shenzhen, China). Flight height was set to 30 m AGL resulting in a GSD of 2.5 cm. In both years, overlap in both directions was set to 90%. Before and after each flight, images of a panel with a known reflectance were taken. Flights were carried out twice per week during heading and flowering stages and once per week at other stages. First flight was carried out on the 25.03.2021 and the 24.02.2022 and the last flight on the 20.07.2021 and the 27.07.2022 when the canopies were fully senescent. This resulted totally in 19 flights in 2021 and 22 flights in 2022. Images were taken around the solar noon and under sunny conditions, if possible. The images from each flight were mosaicked using the Agisoft Metashape Professional 1.8.4 (Agisoft, St. Petersburg, Russia) structure-from-motion software and were radiometrically calibrated using the reflectance panels on the ground and the incident light sensor on the UAV. The processing parameters used for all flight dates were similar (Figure 1). The point cloud was georeferenced using the real-time kinetic global positioning system (RTK-GPS) integrated into the UAS, with the RTK correction signal provided by SAPOS (Deutsche Landesvermessung, 2023) in 2021 and ground control points were used in 2022. Orthomosaics acquired in 2021 were resampled to the same GSD as in 2022 by the average method implemented in gdal (Gdal/Ogr Contributors, 2023). Reflectance of individual bands was extracted by calculating the median of a specific region of interest (ROI) representing a plot using a custom Python 3.7 script (Python Software Foundation, https://www.python.org/).

2.3.1 Selection and calculation of spectral indices

To compare our approach across a range of vegetation indices (VIs), we classified them into five main groups based on their calculation method and selected a representative VI for each group. The five groups were differential-type, simple-ratio type, normalized differential type, three-band type, and combination of two spectral indices type (Table 2). We calculated the indices using

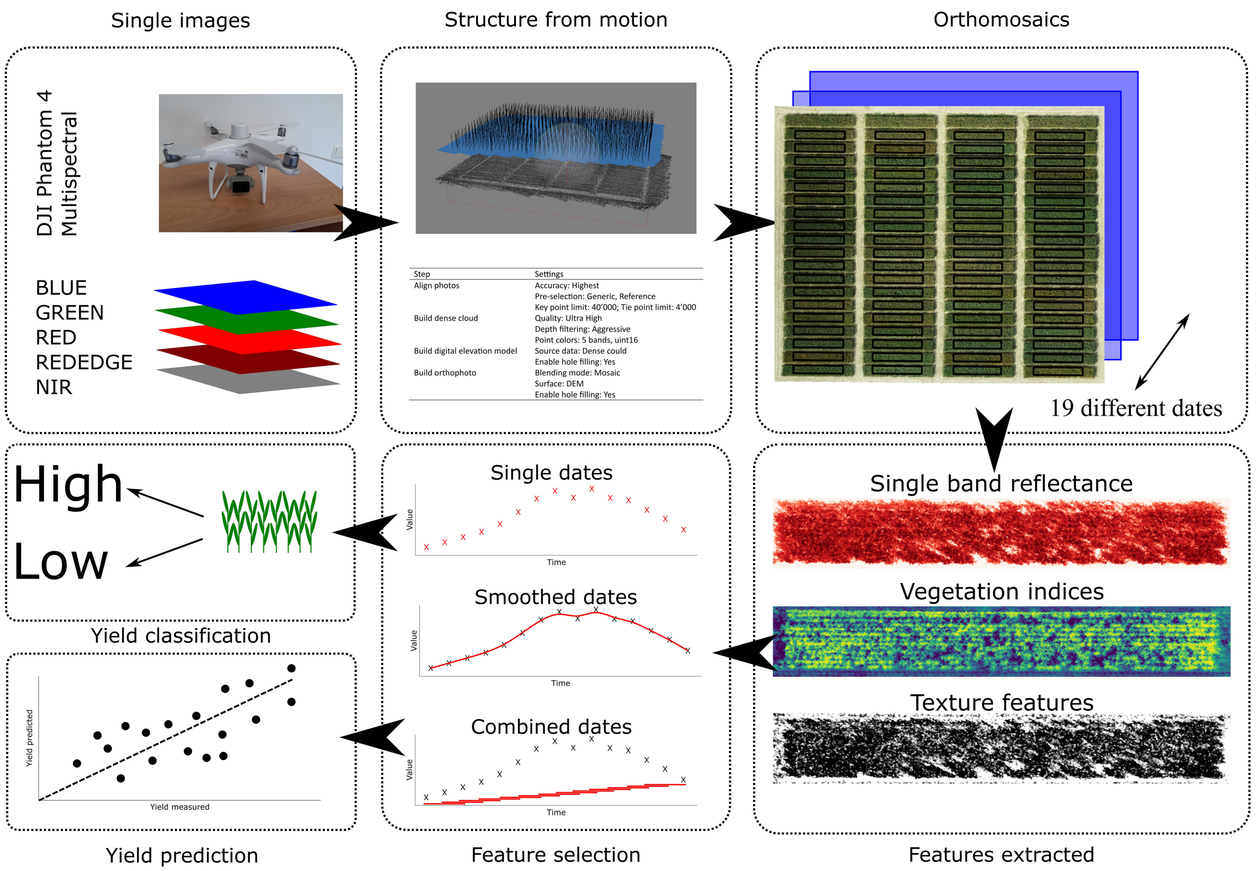

Step	Settings
Align photos	Accuracy: Highest Pre-selection: Generic, Reference Key point limit: 40’000; Tie point limit: 4’000
Build dense cloud	Quality: Ultra High Depth filtering: Aggressive Point colors: 5 bands, uint16
Build digital elevation model	Source data: Dense could Enable hole filling: Yes
Build orthophoto	Blending mode: Mosaic Surface: DEM Enable hole filling: Yes

FIGURE 1
Workflow applied.

a custom Python 3.7 script (Python Software Foundation, https://www.python.org/) and computed the median value for each index over the regions of interest (ROIs) corresponding to the plots.

2.3.2 Selection and calculation of texture features

Texture features (TFs) can be calculated on any data in a raster format, on single band reflectances and VIs likewise. In order to reduce the number of features to be tested, we focused on single band reflectances only. Hall-Beyer (2017) suggests to calculate TFs on the band showing the highest contrast and therefore we calculated the coefficient of variation (CV) for each plot and band. Over all dates, the RED band showed on average the highest CV in 2021 (0.324) and the second highest in 2022 (0.180) after BLUE (0.187). The CV of all bands and dates can be found in Supplementary Figure 3 in the appendix. Furthermore, Zhang et al. (2021) found that TFs calculated on RED bands were correlated with LAI as well as leaf dry matter. Therefore, we chose the RED band as a base for the calculation of all TFs included in this study. A 5 x 5 kernel size was used to calculate the GLCM features over the entire raster. This small kernel size was chosen because wheat leaf sizes are relatively small compared to our GSD. A quantization level of 32 was used, with the lowest level corresponding to the first percentile of the respective raster and the highest level corresponding to the 99th percentile. This ensured that we could still capture the variation in the image. GLCMs were constructed with a moving distance of 1 pixel and moving directions of 0°, 45° and 90° to eliminate possible effects of direction. The CONTRAST, CORRELATION, DISSIMILARITY, ENERGY, and HOMOGENEITY features were extracted from each GLCM (Haralick et al., 1973) and saved as the center pixel in a raster. From these rasters, the final value per plot was extracted by averaging all values within the ROI. All calculations were performed using a custom Python 3.7 script (Python Software Foundation, https://www.python.org/). The extracted features are listed in Table 3.

2.3.3 Temporal processing of the extracted features

Temporal feature selection was carried out in R (R Core Team, 2021). Three temporal feature selection strategies were evaluated (Figure 1). The first strategy involved selecting data from individual dates, resulting in one feature per observation. The second strategy involved smoothing the values per plot using splines, implemented in the package *statgenHTP* (Millet et al., 2022), with the default settings applied. Summed GDD from harvest were used as the time axis. Finally, features were selected using a moving time window with a width of 3. For each recorded date, the model included features from the current date and the previous as well as the following date, resulting in a total of three features per observation. This strategy is referred to as the moving window model.

TABLE 2 Vegetation indices (VIs) calculated.

Index type	Index	Formula	Reference
Difference	**DVI**	$\mathrm{Nir} - \mathrm{Red}$	(Shibayama et al., 1999)
Ratio	**RVI**	$\frac{\mathrm{Nir}}{\mathrm{Red}}$	(Shibayama et al., 1999)
Normalized	**NDRE**	$\frac{\mathrm{Nir} - \mathrm{Rededge}}{\mathrm{Nir} + \mathrm{Rededge}}$	(Barnes et al., 2000)
Three Band	**MCARI**	$((\mathrm{Rededge} - \mathrm{Red}) - 0.2{*}\ (\mathrm{Rededge} - \mathrm{Green})){*}\left(\frac{\mathrm{Rededge}}{\mathrm{Red}}\right)$	(Daughtry et al., 2000)
Combination of indices	**CCII**	$\frac{TCARI}{OSAVI}$	(Haboudane et al., 2002)
	TCARI	$3{*}\left[(\mathrm{Rededge} - \mathrm{Red}) - 0.2{*}(\mathrm{Rededge} - \mathrm{Green}){*}\left(\frac{\mathrm{Rededge}}{\mathrm{Red}}\right)\right]$	
	OSAVI	$(1 + 1.16){*}\left(\frac{(\mathrm{Nir} - \mathrm{Red})}{\mathrm{Nir} + \mathrm{Rededge} + 0.16}\right)$	

Green corresponds to 560 nm, the Red to 650 nm, Rededge to 730 and 717 and Nir to 840 and 842 nm wavelength in the first and the second year, respectively.

2.4 Yield prediction model and yield potential classification model

To predict yield on a plot level and classify yield performance groups, we employed Random Forest (RF) machine learning models in R 4.2 (R Core Team, 2021). We optimized the number of trees per forest to 500 and used the R package *caret* (Kuhn, 2008). The number of trees per forest was set to 500 and the number of features per node was optimized by minimizing the root mean square error (RMSE) for the regression models and the accuracy for the classification models if more than one feature was available as in the moving window model.

2.5 Statistical analysis

Pearson correlation coefficient between yield and spectral features was calculated using measurements taken during tillering and flowering. At this date, most varieties were in the mid to end flowering and the correlation of VIs and yield was maximal for most VIs. The performances of the regression RF models were assessed by the coefficient of determination (R^2) (Equation 3) as well as the RMSE (Equation 4) using a 10-fold cross validation that was repeated 3 times and averaged:

$$R^2 = \frac{\sum_{i=1}^{n}(x_i - \bar{x}_i)^2 * (y_i - \bar{y}_i)^2}{\sum_{i=1}^{n}(x_i - \bar{x}_i)^2 * \sum_{i=1}^{n}(y_i - \bar{y}_i)^2} \tag{3}$$

$$RMSE = \sqrt{\frac{\sum_{i=1}^{n}(x_i - y_i)^2}{n}} \tag{4}$$

Where x_i and y_i represent the observed and the predicted yield, $\bar{x}_i$ and $\bar{y}_i$ represent the mean of the observed and the predicted yield, respectively. n represents the number of samples. The performances of the classification RF models were assessed by the accuracy (Equation 5) of the prediction using a 10-fold cross validation that was repeated 3 times and averaged:

$$Accuracy = \frac{True\ \ positive + True\ \ negative}{Total\ \ number\ \ of\ \ classified\ \ objects} \tag{5}$$

TABLE 3 Calculation of grey correlation matrix features according to Haralick et al. (1973).

Texture feature calculated on RED raster	Formula	Explanation
Contrast	$\sum_{i,j=0}^{N-1} P_{ij}(i-j)^2$	Amount of local variation in pixel values
Correlation	$\sum_{i,j=0}^{N-1} P_{ij}\frac{(i-\ \mu)(j-\mu)}{\sigma^2}$	Linear dependency of grey level values in the GLCM
Dissimilarity	$\sum_{i,j=0}^{N-1} P_{i,j}\lvert i-j\rvert$	Local roughness of the pixel values
Energy	$\sum_{i,j=0}^{N-1} (P_{ij})^2$	Local steadiness of the gray levels
Homogeneity	$\sum_{i,j=0}^{N-1} \frac{P_{ij}}{1+(i-j)^2}$	Homogeneity of the pixel values

3 Results

3.1 Yield, LAI and phenology

Substantial grain yield variation was observed between experimental plots, with the season 2021 yielding about 128 g m^{-2} less than the second season (Table 1). Variety Julius was classified into the low yielding group in both years, while Skyfall and Dagmar were classified as high yielding in both years. The temperature sum to achieve a specific growth stage did not show significant differences between the yield groups. However, in both years a tendency towards an advanced phenology in the low yielding varieties could be observed (Figure 2). The Leaf Area Index (LAI) was notably higher in the first year of the trial compared to the second. In 2021, the high-yielding varieties showed a significantly higher LAI during the stem elongation, the booting and the late grain filling stage than the low-yielding varieties. This difference could not be observed in the second year (Figure 2).

3.2 Correlations between grain yield, the UAV-based reflectance, vegetation indices and texture features at tillering and flowering

Figures 3A–D show the Pearson correlation coefficient examining the relationship between reflectance, vegetation indices and TFs for the two years of trial at the end of the tillering and end of the flowering stages for the two years of trial. The analysis reveals that most features exhibit high correlations with one another during the tillering stage in both years, with few exceptions. Exceptions are the REDEDGE band in 2021, the REDEDGE and NIR bands in 2022 and the CORRELATION TF in both years. Correlation to

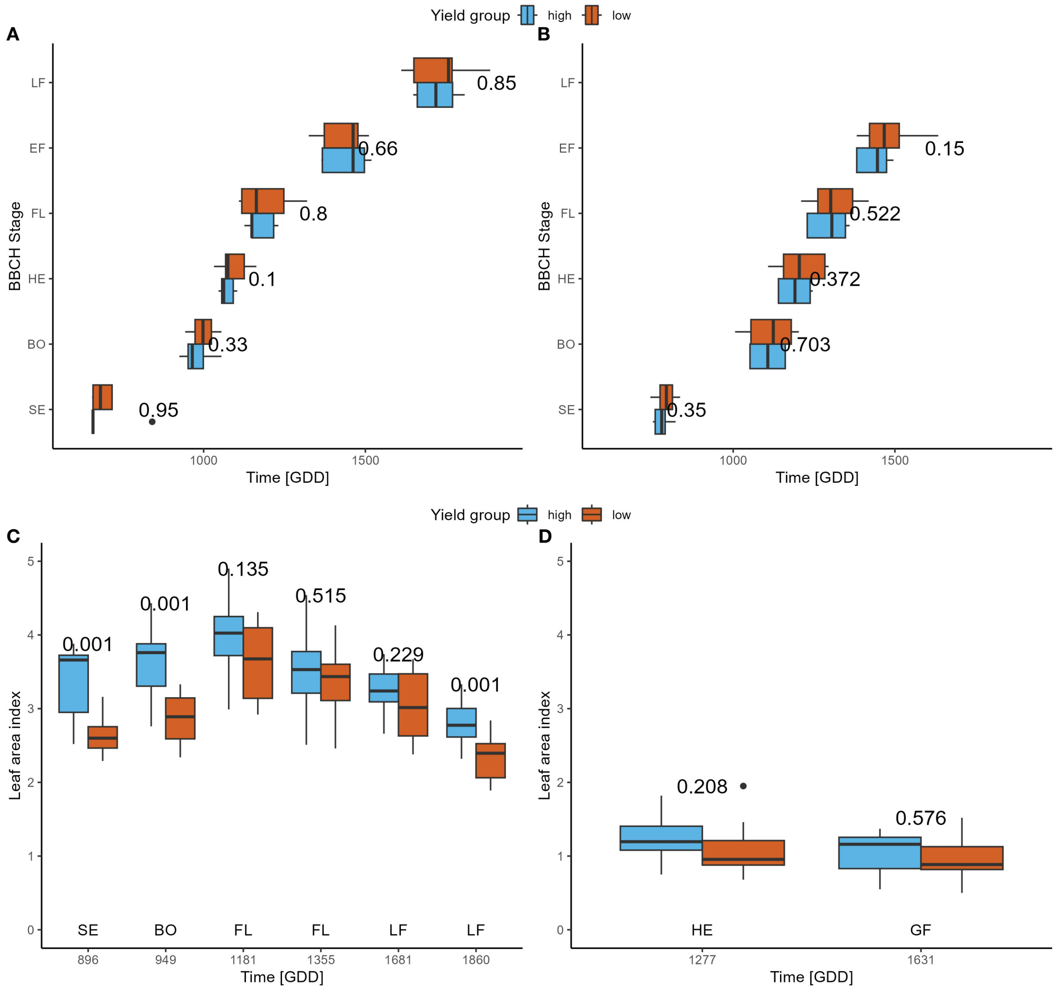

FIGURE 2

Subfigures **(A, B)** display the phenologies of the low and high yielding varieties during the two seasons of trial. Subfigures **(C, D)** display the LAI at different time points during the growth season. Numbers next or above the boxplot pairs show the p-value of a t-test.

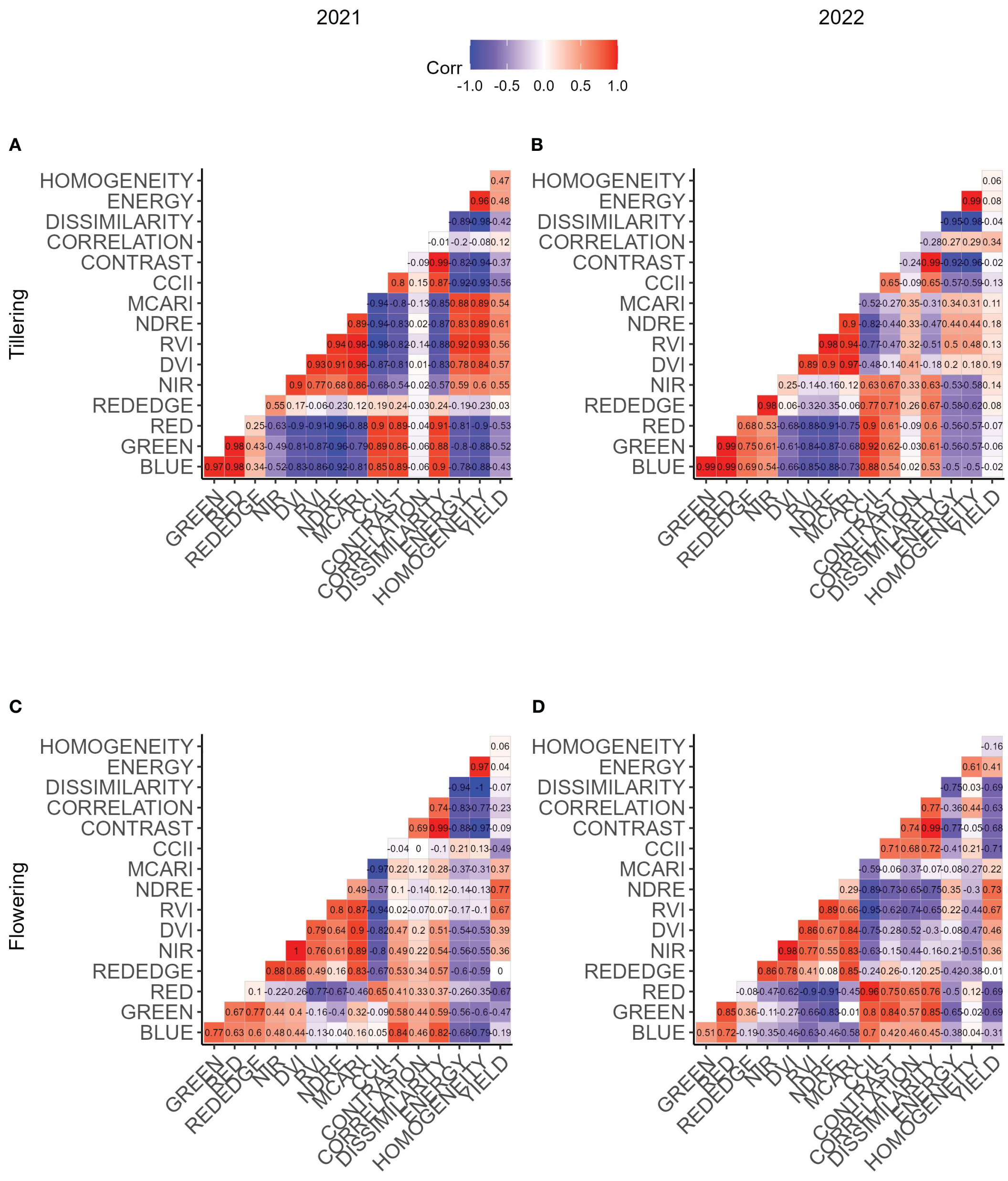

FIGURE 3
Correlation matrices of all features extracted for a single date and yield. Subfigures **(A, B)** display measurements that were taken at tillering, **(C, D)** measurements taken at flowering. Subfigures **(A, C)** belong to the first, **(B, D)** to the second year of trial.

yield at the tillering stage is high for all features in 2021 with a maximal R of 0.61 for the NIR band (Figure 3A). In 2022, correlations to yield are generally low, the highest correlation was found for the CORRELATION TF (R = 0.38) (Figure 3B).

At the flowering stage, correlation coefficients among features tend to decrease, especially between features of distinct feature groups. For instance, VIs are strongly correlated among themselves, while TFs similarly demonstrate robust correlations within their group. However, features belonging to the VI group are weakly with features belonging to the TF group. The absolute correlation of the features to yield generally decreases for TFs, increases for VIs and single band reflectances show few differences. In 2022, the absolute correlations increase towards the flowering stage, except for the REDEGE reflectance. For both years, the NDRE was the feature showing the highest correlation to yield, whereas the REDEDGE reflectance was not correlated to yield.

3.3 Time series of UAV-based reflectance, vegetative indices, texture features

Reflectance of the GREEN and the RED band decreased with plant growth during the tillering and stem elongation stages followed by an increased with the onset of the grain filling stage. This trend resulted in a minimal reflectance around booting and flowering stages (Figure 4). In 2021, the high yielding group consistently displayed significantly lower GREEN and RED reflectances across various stages ranging from tillering to late grain filling. However, in the subsequent season, these marked differences between yield groups only emerged from the latter half of the stem elongation stage onward.

Both the RVI and NDRE indices showed significant disparities between the low and high yielding groups in 2021 at all recorded dates, except for the first one. In 2022, these distinctions were noticeable from the flowering stage to the initial segment of the stem elongation stage. Particularly, NDRE exhibited differences from the conclusion of the stem elongation stage onward (Figure 4). The TF CORRELATION decreased until booting and increased towards the end of grain filling in 2021.The feature does not show a clear development with time in 2022. The DISSIMILARITY TF decreases from the tillering until the booting stage and slight increases until harvest in both years. Significant differences between the two yield groups were found in 2021 for stages ranging from tillering to the end of flowering. In 2022, differences were found on few dates after flowering only (Figure 4).

3.4 RF regression model for yield prediction using individual flights and time series of UAV traits

The performance of the yield prediction models depends highly on the features and the time point selected. Overall, the 2021 season demonstrated superior results, exhibiting lower average RMSE in contrast to the 2022 season. Generally, predictions improve from the tillering to the booting stage and deteriorate after flowering (Figure 5).

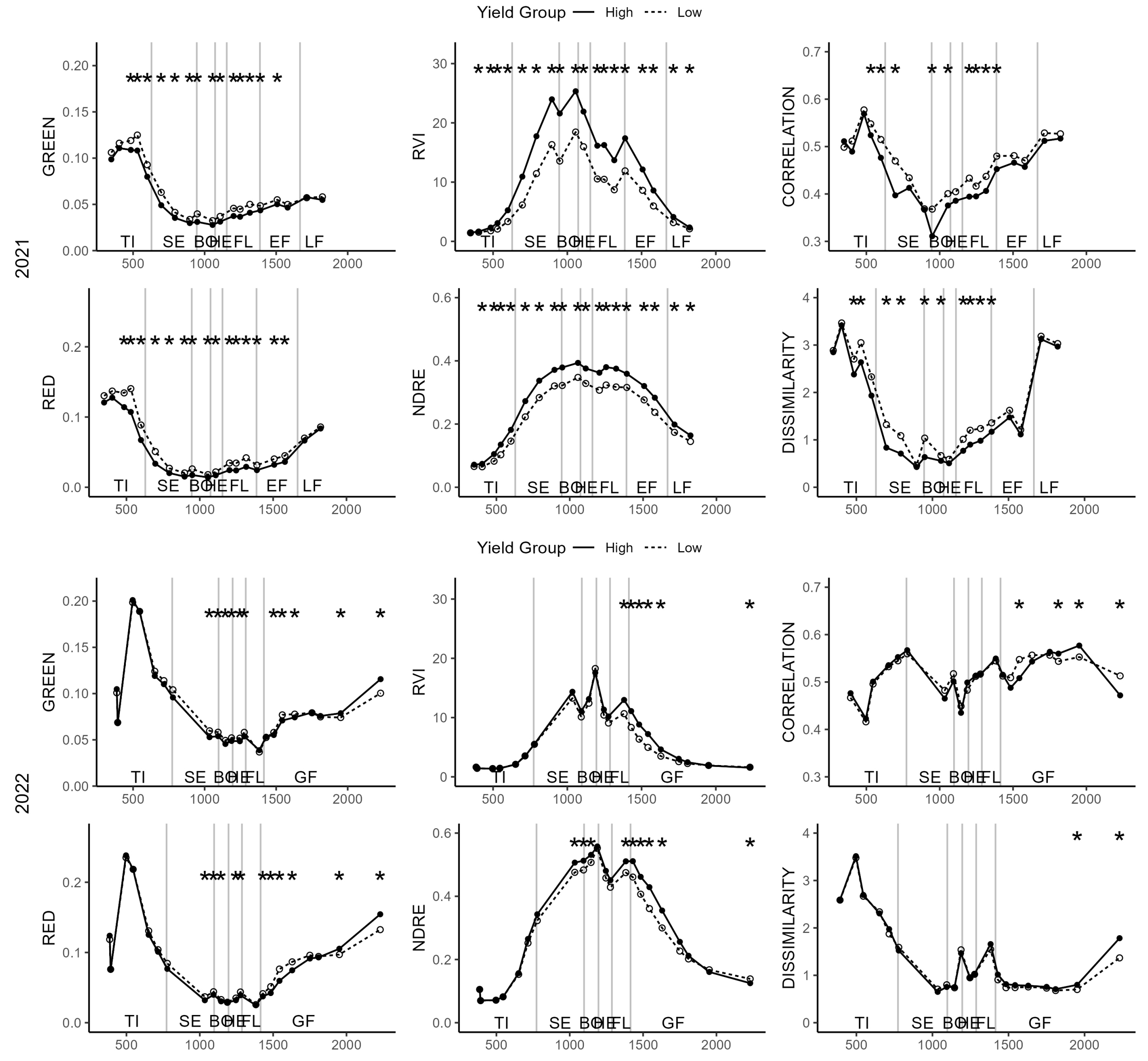

FIGURE 4
Dynamics of single band reflectances (left), vegetation indices (middle) and texture features (right) for different dates. The solid line shows the high yield group, the dashed line the mean value for the low yield group. The asterisks display significant differences after a t-test ($p < 0.05$) in the respective values and dates between the two yield groups. The plots are grouped into the first year of trial (top) and the second year of trial (bottom). Asterisks may overlap but only one significance level is given.

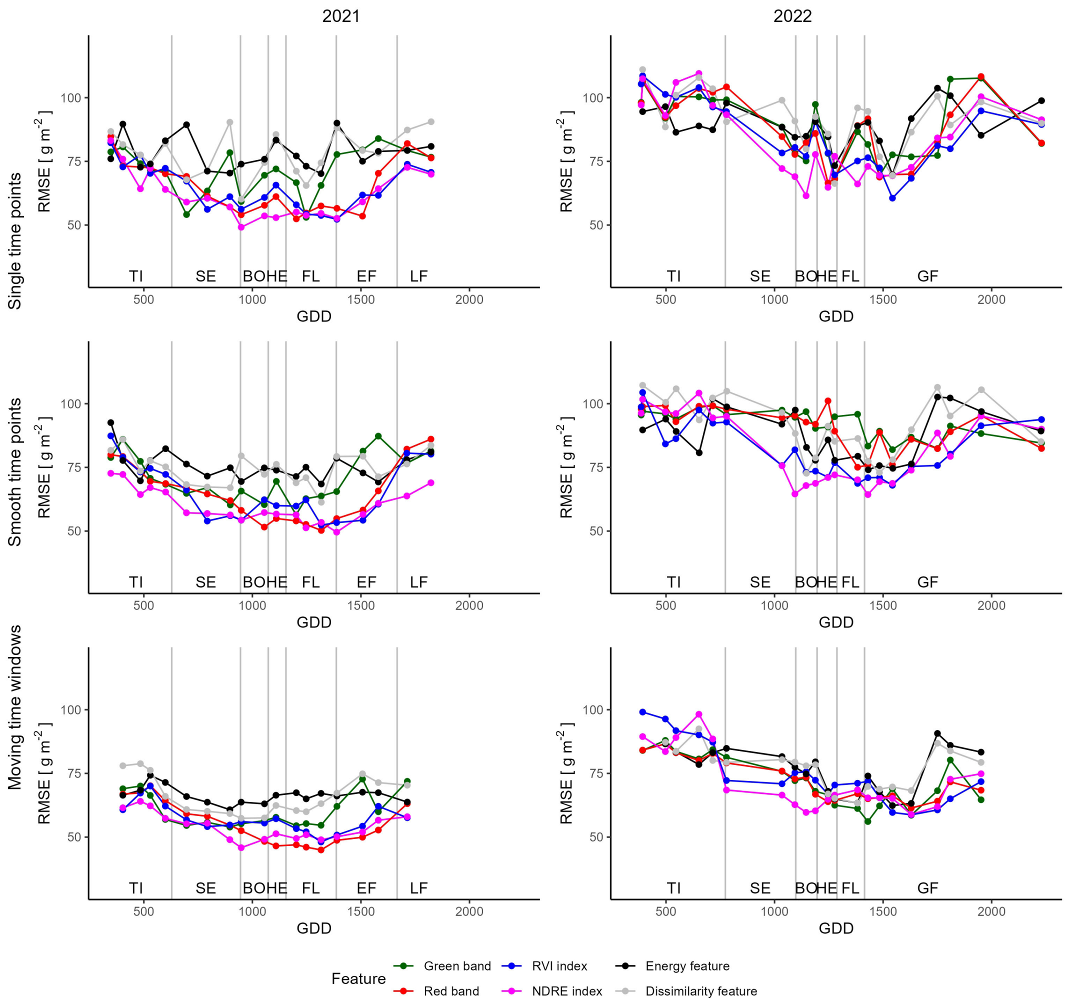

FIGURE 5

Root mean square errors of yield prediction models built using single dates (top), smoothed dates (middle) and combining adjacent dates (bottom). The figures on the right display models built for the first, the ones on the left for the second year of trial.

In 2021, the most successful feature was the Normalized Difference Red Edge (NDRE) index at the booting stage, displaying an RMSE of 49.1 g m^{-2}. In 2022, the Difference Vegetation Index (DVI) at the grain filling stage showed the best performance (RMSE = 60.6 g m^{-2}). Individual bands, such as the RED band, produced good results, particularly in the 2021 season. However, on average they were outperformed by the VIs in both seasons (Table 4). The TFs were the feature group that led to regression models with the highest RMSE. On average, the RMSE was 10.3 g m^{-2} higher for the TFs than the VIs in 2021.

Although data smoothing had a marginal influence the seasonal average RMSE, but worsened a few minimal RMSE. Additionally, smoothing altered the phenological stage at which the minimal RMSE was attained, illustrating shifts in the optimal time points for yield prediction. For instance, after smoothing, the NDRE feature in 2021 displayed an optimal time point for yield prediction during the early grain filling stage as opposed to the unsmoothed time points, which indicated the booting stage as optimal (Table 4).

Combining features from three adjacent time points notably enhanced the average RMSE models by approximately 10 g m^{-2} and reduced the minimal RMSE by 5 g m^{-2} for both years across all feature groups. Employing the moving window method revealed that the lowest RMSE of 45.0 g m^{-2} was achieved using the RED reflectance band at the flowering stage, while in 2022, the Vegetation Index (VI) CCII reached an RMSE of 50.8 g m^{-2}. The combination of TFs from various dates yielded models that were comparable to models constructed with a single reflectance band or VI. Specifically, the DISSIMILARITY feature reached a minimal RMSE of 57.4 g m^{-2} at the booting stage in 2021, and the HOMOGENEITY feature achieved an RMSE of 56.9 g m^{-2} at the flowering stage in 2022 (Table 4).

3.5 RF classification model for classifying the high and low yielding varieties using individual flights and time series of UAV traits

The efficacy of classification models depends on the chosen features and time points, paralleling the observation in regression models. On average, the models in the first season exhibited higher

TABLE 4 Display of the time points yielding the lowest RMSE for yield prediction for all reflectance bands, vegetation indices and texture features.

Raster	Mean RMSE		Min RMSE		PS		VI	Mean RMSE		Min RMSE		PS		TF	Mean RMSE		Min RMSE		PS	
Single time points																				
	2021	2022	2021	2022	2021	2022		2021	2022	2021	2022	2021	2022		2021	2022	2021	2022	2021	2022
BLUE	76.8	95.2	58.7	80.4	BO	SE	DVI	70.6	86.7	61.6	64.4	SE	GF	CON	79.5	94.1	59.7	68.7	SE	HE
GREEN	71.3	88.5	53.0	68.0	FL	HE	RVI	64.7	85.6	52.3	**60.6**	EF	**GF**	COR	77.6	**92.1**	62.2	67.7	FL	TI
RED	**65.1**	**87.5**	**52.4**	66.5	**FL**	HE	NDRE	**61.8**	**83.5**	**49.1**	61.5	**BO**	BO	DIS	78.4	94.5	57.7	**66.3**	FL	**HE**
REDEDGE	77.6	87.6	56.0	**64.4**	LF	**SE**	MCARI	72.4	93.5	61.7	67.2	BO	GF	ENE	**76.4**	94.6	**55.5**	71.2	**SE**	GF
NIR	71.9	87.1	64.8	68.7	SE	GF	CCII	67.9	86.7	57.0	66.3	SE	GF	HOM	77.0	93.7	59.4	68.7	FL	FL
Mean	72.5	89.2	57.0	69.6				67.5	87.2	56.3	64.0				77.8	93.8	58.9	68.5		
Smoothed time points																				
	2021	2022	2021	2022	2021	2022		2021	2022	2021	2022	2021	2022		2021	2022	2021	2022	2021	2022
BLUE	76.6	96.3	67.1	86.4	SE	GF	DVI	69.3	84.7	63.7	65.9	EF	GF	CON	77.4	95.8	68.2	79.0	**SE**	BO
GREEN	70.7	92.0	56.4	82.0	FL	GF	RVI	65.4	**82.0**	52.3	68.0	**FL**	GF	COR	75.6	**87.6**	68.5	74.1	FL	GF
RED	**64.9**	90.9	**50.2**	75.1	**FL**	FL	NDRE	**60.1**	**82.0**	49.6	64.3	**EF**	GF	DIS	**74.5**	91.6	**61.3**	**72.7**	**SE**	**BO**
REDEDGE	78.1	93.9	65.8	83.8	SE	GF	MCARI	70.8	91.9	60.2	70.7	FL	GF	ENE	76.4	91.6	63.5	74.9	FL	GF
NIR	69.9	**90.8**	62.9	**72.7**	EF	**GF**	CCII	68.0	84.0	56.0	**61.4**	EF	**GF**	HOM	76.1	90.7	62.6	74.4	TI	BO
Mean	72.0	92.8	60.5	80.0				66.7	84.9	56.4	66.1				76.0	91.5	64.8	75.0		
Moving time window																				
	2021	2022	2021	2022	2021	2022		2021	2022	2021	2022	2021	2022		2021	2022	2021	2022	2021	2022
BLUE	65.1	83.0	52.7	76.5	BO	GF	DVI	62.8	76.6	58.1	62.7	EF	GF	CON	66.4	82.4	58.8	62.8	SE	FL
GREEN	60.4	**72.0**	53.9	**56.1**	SE	**GF**	RVI	57.2	74.6	48.1	58.7	FL	GF	COR	66.4	**80.6**	60.8	62.4	SE	GF
RED	**55.3**	72.1	**45.0**	61.4	**FL**	GF	NDRE	**54.0**	**71.5**	**45.8**	58.9	**BO**	GF	DIS	**66.1**	82.6	**57.4**	63.3	**BO**	FL
REDEDGE	66.1	74.5	57.5	61.1	SE	GF	MCARI	62.8	84.1	54.9	65.4	FL	GF	ENE	65.9	82.9	58.6	63.1	SE	GF
NIR	62.3	76.8	56.7	66.2	SE	GF	CCII	59.4	72.7	53.8	**50.8**	BO	**GF**	HOM	65.4	81.3	57.6	**56.9**	BO	**FL**
Mean	61.8	75.7	53.2	64.3				59.2	75.9	52.1	59.3				66.0	82.0	58.6	61.7		

Mean RMSE are all RMSE values averaged over the whole season. Min RMSE values show the lowest RMSE of a season. The phenology stages (PS) are reported at which the min RMSE was recorded.
Bold values indicate minimal Mean and Min RMSE values for a respective feature, featue selection and year combination. Phenology stages in bold indicate the stage when the minimal RMSE value was recorded.

accuracy compared to those in the subsequent season. However, the maximum accuracies achieved in both years were similar. Notably, in 2021, an accuracy of 0.938 was attained using the BLUE band during the late grain filling stage, while the HOMOGENEITY TF in 2022 achieved the maximum accuracy of 0.915 during the grain filling stage. In 2021, VIs generally outperformed single-band reflectances and TFs for yield predictions, whereas in 2022, TFs slightly surpassed the other two groups. The model performances in both years exhibited substantial variability across different dates. Although data smoothing mitigated some fluctuations, significant differences between adjacent dates persisted. Similar to the regression models, the average and maximum performance of the models remained largely consistent after the smoothing of data points.

Incorporating more than one date into the models generally yielded a slightly higher average accuracy for all features in both years. On average, the best-performing feature was the RED band with an accuracy of 0.758 in 2021 and the Modified Chlorophyll Absorption Ratio Index (MCARI) in 2022, displaying an average accuracy of 0.615. However, the maximal accuracies remained largely unaltered compared to those achieved using single dates (Table 5). Despite this, fluctuations between individual dates were reduced (Figure 6). A trend towards increased accuracy with time was evident in 2021, particularly notable with the RED band, consistently yielding high accuracies after heading. In the second year, accuracies improved and were higher than 0.5 for all features at the end of the heading stage. Moreover, fluctuations between dates were notably reduced in this subsequent year (Figure 6).

4 Discussion

4.1 Dynamic responses of individual bands

Rededge bands have been widely studied for assessing crop performance and yield in various crops, including wheat (Horler et al., 1983; Pavuluri et al., 2015). Canopy reflectance in the red, rededge and near-infrared (NIR) wavelength range is influenced by two primary optical properties of canopies: chlorophyll absorption in the red region and multiple scattering effects on the NIR due to canopy structural properties. The red-edge region is more sensitive to chlorophyll content than to leaf area (Xie et al., 2018). Hence, the variability in LAI might have been bigger or more important for yield formation compared to the chlorophyll content in our specific panel. Moreover, the correlation of reflectance in the red-edge region with yield is known to change quickly with the exact wavelength measured (Pavuluri et al., 2015), making the selection of the exact wavelength difficult and leading to inconsistent results.

In contrast, visible bands (Blue, Green and Red) can be more sensitive to yield-related variations in chlorophyll, and biomass accumulation during the tillering and the stem elongation stage until the beginning of the booting stage. They are known to be correlated to a certain extent to both, chlorophyll concentration and LAI (Daughtry et al., 2000). Accordingly, our results showed that the RED, GREEN, and BLUE bands were among the most effective spectral features for yield prediction, exhibiting significant differences between high- and low-yielding varieties at almost all measurement dates in the first year of trial and during several in the second year. Their reflectances decrease during the transition from the stem elongation to the beginning of the booting stage when LAI and chlorophyll density is known to be maximal (Hinzman et al., 1984; Hinzman et al., 1986) due to the optical properties of chlorophyll. From heading until harvest the reflectances in these bands increase due to senescence when chlorophyll degradation takes place (Spano et al., 2003).

The NIR region is known to be sensitive to leaf area and especially ground cover (Korobov and Railyan, 1993), making it a useful band for predicting biomass and therefore yield. Our results indicate that the NIR band performed best during the stem elongation stage for yield prediction and at the booting stage when there were significant differences in (LAI) between the two yield groups. In the second season, the differences in the reflectances were significantly different only once before booting in the second season possibly due to a lack of differences in LAI between the two yield groups. This aligns with the findings by Korobov and Railyan (1993), who reported a higher correlation of NIR reflectance with dry matter and ground cover the during booting stage compared to later stages. Thus, normalizing the difference of the NIR and the REDEDGE reflectance in the form of the NDRE index, showed a good performance for chlorophyll estimation (Barnes et al., 2000).

Usually, VIs containing information from the rededge region of the spectrum are considered being more sensitive to chlorophyll absorption in dense canopies (Nguy-Robertson et al., 2012). It is expected that combining the highly LAI-sensitive NIR band with the rededge band that contains more information about leaf pigments in the canopy and therefore improves the performance of our yield prediction model at the flowering to early grain filling stages.

4.2 The influence of growth stages on yield prediction and classification

The performance of yield prediction and classification depends highly on the phenological stage of the crop. Our study found that the flowering stage and early grain filling stage allowed for the best predictions of yield and classification of varieties in winter wheat, which is consistent with the findings of several other studies (Hassan et al., 2019; Prey et al., 2020; Prey et al., 2022). From a physiological stand point of view, at the time around flowering the crop has to provide enough assimilates in order to maximize the number of fertile florets per spike, leading to a higher number of kernels per spike and finally a higher yield (Fischer, 1985). Therefore, estimating biomass and chlorophyll content at these stages is optimal for yield estimation. Unfortunately, the spectral signal often saturates at these stages making the estimation challenging, especially in high yielding years (Prey et al., 2020).

Early differences in biomass and LAI dynamics between wheat genotypes are well-documented (Pang et al., 2014; Grieder et al., 2015) and Raun et al. (2001) proposed to follow the biomass formation after dormancy for yield prediction. Marti et al. (2007) hypothesized that a high biomass at the end of the tillering stage

TABLE 5 Display of the time points yielding the lowest RMSE for yield prediction for all reflectance bands, vegetation indices and texture features.

Raster	Mean Accuracy		Max Accuracy		PS		VI	Mean Accuracy		Max Accuracy		PS		TF	Mean Accuracy		Max Accuracy		PS	
Single time points																				
	2021	2022	2021	2022	2021	2022		2021	2022	2021	2022	2021	2022		2021	2022	2021	2022	2021	2022
BLUE	0.609	0.501	**0.938**	0.693	**LF**	GF	DVI	0.640	0.502	0.825	**0.838**	EF	**GF**	CON	**0.594**	0.526	0.800	0.832	SE	GF
GREEN	0.643	0.488	0.833	0.772	FL	GF	RVI	0.595	0.504	0.880	0.745	EF	GF	COR	0.588	0.516	**0.877**	0.835	**TI**	HE
RED	**0.673**	0.506	0.817	**0.783**	EF	**GF**	NDRE	0.632	0.533	0.877	0.718	LF	GF	DIS	0.564	**0.538**	0.852	0.778	SE	GF
REDEDGE	0.584	**0.545**	0.798	0.707	LF	TI	MCARI	0.637	**0.567**	0.823	0.795	EF	GF	ENE	0.533	0.527	0.790	0.787	FL	SE
NIR	0.620	0.493	0.912	0.768	TI	BO	CCII	**0.673**	0.491	**0.885**	0.735	**FL**	GF	HOM	0.575	0.532	0.867	**0.915**	FL	**GF**
Mean	0.625	0.507	0.860	0.745				0.635	0.519	0.858	0.766				0.571	0.528	0.837	0.829		
Smoothed time points																				
	2021	2022	2021	2022	2021	2022		2021	2022	2021	2022	2021	2022		2021	2022	2021	2022	2021	2022
BLUE	0.674	0.551	0.853	0.813	LF	GF	DVI	0.600	0.521	0.815	0.860	TI	GF	CON	0.546	0.463	**0.875**	0.750	**EF**	GF
GREEN	0.640	0.538	0.880	**0.873**	HE	**GF**	RVI	0.609	0.535	0.810	0.747	FL	GF	COR	**0.612**	0.524	0.793	0.750	TI	GF
RED	**0.676**	**0.580**	**0.963**	0.790	**EF**	GF	NDRE	0.625	0.556	0.828	0.735	LF	GF	DIS	0.605	0.534	0.830	0.720	HE	GF
REDEDGE	0.594	0.553	0.830	0.813	HE	GF	MCARI	**0.647**	**0.586**	0.755	**0.868**	FL	**GF**	ENE	0.547	0.506	0.830	**0.840**	TI	**GF**
NIR	0.573	0.512	0.802	0.832	TI	GF	CCII	0.630	0.512	**0.858**	0.835	**FL**	GF	HOM	0.601	**0.537**	0.782	**0.840**	FL	**BO**
Mean	0.6314	0.547	0.866	0.824				0.622	0.542	0.813	0.809				0.582	0.513	0.822	0.780		
Moving time window																				
	2021	2022	2021	2022	2021	2022		2021	2022	2021	2022	2021	2022		2021	2022	2021	2022	2021	2022
BLUE	0.697	0.535	**0.884**	0.712	**LF**	GF	DVI	0.684	0.499	**0.833**	0.815	**TI**	GF	CON	0.617	0.572	0.903	0.813	SE	GF
GREEN	0.712	**0.604**	0.814	0.757	FL	GF	RVI	0.674	**0.581**	0.758	0.863	EF	GF	COR	**0.652**	0.567	0.867	0.833	TI	GF
RED	**0.758**	0.598	0.853	0.764	FL	GF	NDRE	0.630	0.573	0.722	0.828	LF	GF	DIS	0.602	**0.584**	0.840	0.793	EF	GF
REDEDGE	0.659	0.577	0.800	0.777	HE	GF	MCARI	**0.719**	0.615	0.795	0.783	TI	GF	ENE	0.634	0.558	**0.918**	**0.852**	**SE**	**GF**
NIR	0.668	0.578	0.788	**0.868**	TI	**GF**	CCII	0.708	0.559	0.827	**0.900**	HE	**GF**	HOM	0.638	0.553	0.882	0.815	SE	GF
Mean	0.698	0.578	0.828	0.776				0.683	0.565	0.787	0.838				0.629	0.567	0.882	0.821		

Mean RMSE are all RMSE values averaged over the whole season. Min RMSE values show the lowest RMSE of a season. The phenology stages (PS) are reported at which the min RMSE was recorded.
Bold values indicate maximal Mean and Max Accuracy values for a respective feature, featue selection and year combination. Phenology stages in bold indicate the stage when the Maximal RMSE value was recorded.

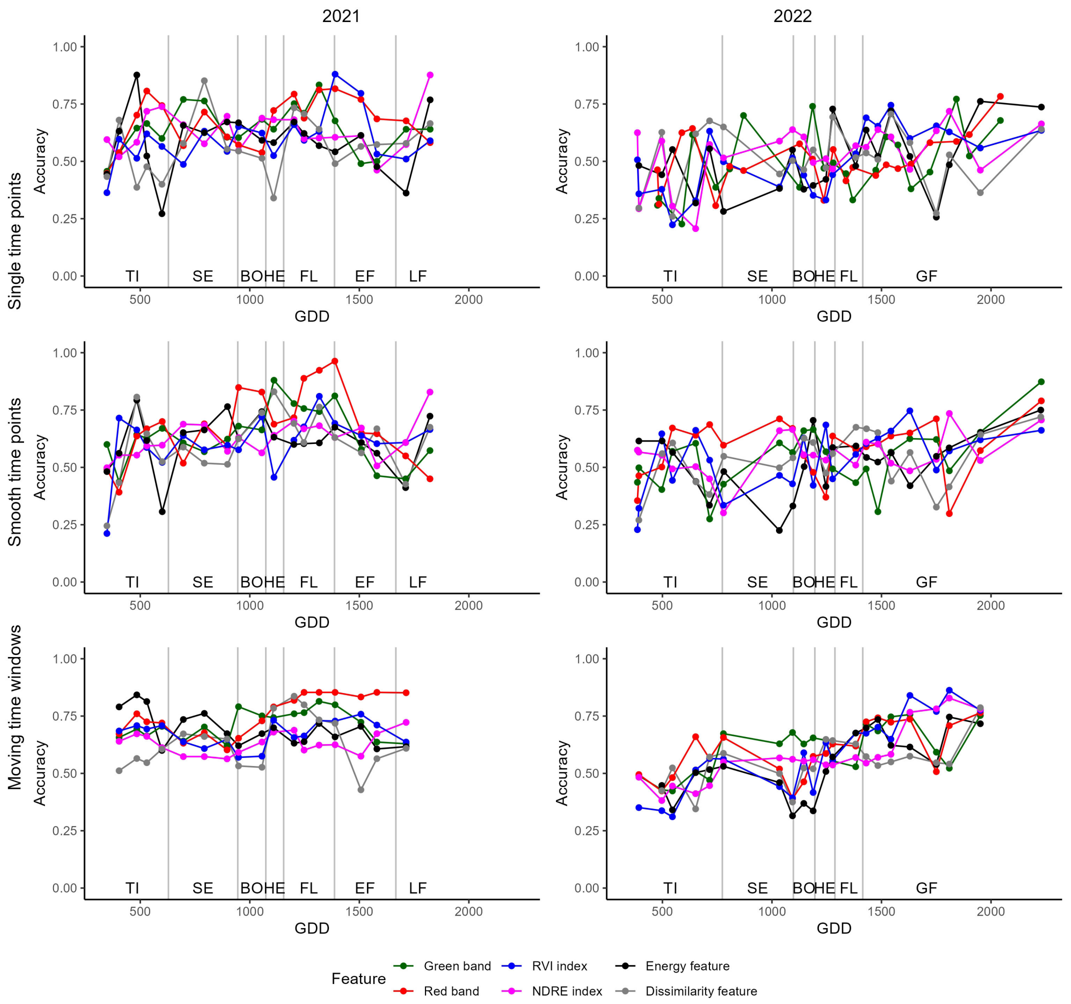

FIGURE 6
Accuracy of variety classification models built using single dates (top), smoothed dates (middle) and combining adjacent dates (bottom). The figures on the right display models built for the first, the ones on the left for the second year of trial.

detected by NDVI estimates the growth during the stem elongation stage which in turn is crucial for the number of kernels per area produced (González et al., 2005). Yield prediction at tillering therefore already yielded some success especially in the first year of the trial. From tillering to harvest, wheat is known to compensate for, as an example, a low stand count by altering the number of yield components (Holen et al., 2001), therefore predictions at these early stages are prone to changes later in the season, subsequently leading to prediction errors.

After flowering, the RMSE of the models for prediction increases again in the first year whereas they start to increase later during grain filling in the second year. The flowering stage is longer in the first compared to the second year of trial (232 GDD and 134.4 GDD). The reason for this difference is unclear, the end of flowering is generally difficult to rate, since the dry anthers tend to fall to the ground or are washed of by rain. Therefore, the end of flowering might have been later in the second year as well. Differences in stay-green characteristics can influence yield, especially by influencing the weight of single grains (Wu et al., 2012) which were higher in the high yielding varieties compare to the lower yielding ones. A further indication of this difference is the slightly advanced phenology of the lower yielding varieties in both years and the higher LAI measured in the first year of the trial.

The classification models showed a less clear trend during the season and fluctuations between dates are more severe than for the regression models. Garriga et al. (2017) did not find a difference in classification model performance between the anthesis and the grain filling stages. Successful classification in our case can be achieved directly by identifying high yielding plots or indirectly by identifying varieties. The algorithm learns either to recognize high yield or to classify a certain variety, regardless of their yield potential. Wheat variety classification for yield classification for breeding purposes other than by Garriga et al. (2017) is scarce. Works often focus on the classification of kernels (Porker et al., 2017; Khojastehnazhand and Roostaei, 2022), which is done under laboratory environments and therefore less prone to errors induced by the measurement conditions. Still, if the optimal feature at the optimal time point is selected, classification of low and high yielding varieties can be a promising tool for plant breeding applications (Garriga et al., 2017).

4.3 Comparison of variable- and feature types for yield prediction and classification

Our study found that single-band reflectance, such as the RED band, was as effective as or even more effective than vegetation indices (VIs) for predicting yield, especially in the first year of trial. The RED band is known to be related to leaf area index (LAI), although this relationship is often non-linear (Hinzman et al., 1984) and therefore requires non-linear methods such as RF to perform well for yield prediction. Pavuluri et al. (2015) found a saturation of RED reflectance when predicting yield, which can also be found in our prediction models. In contrast, VIs typically show good linear correlations with grain yield, with NDVI being widely used for yield prediction (Duan et al., 2017; Hassan et al., 2019). Furthermore, the VIs show a more consistent performance between dates compared to the single band reflectances. The NDRE was the best performing feature for yield assessment, which is in accordance with other studies (Prey et al., 2022) possibly due to its strong correlation to biomass (Argento et al., 2021). Many VIs have been screened by Prey et al. (2020) and few have been showing a consistent performance over the years, which makes a general selection difficult, similar to our study. Further, VIs narrow down the information that is accessible and Vatter et al. (2022) found good performances for yield prediction when using 11 wavebands from a multispectral camera that were fed to a deep learning model. This might be good strategy to obtain the optimal prediction model from multispectral cameras without any prior knowledge and the need for feature selection.

TFs are complex in their calculation and they offer a variety of possible ways of calculation, possible combinations with underlying rasters and ways to be calculated. Detailed information on how TFs are calculated is often lacking (Zheng et al., 2019; Wang et al., 2021; Zhang et al., 2021). Therefore, TFs still have to be examined in detail and their parameters optimized under different experimental conditions and scenarios of sensing data collection. We calculated TFs in a standardized way, but still found a high variability between dates. They are further known to be highly dependent on the GSD and therefore, the flight height (Zheng et al., 2019). In our study smoothing aided in enhancing the stability of the yield prediction models, although it did not improve their performances. A novel approach was presented by Herrero-Huerta et al. (2020) who calculated so-called canopy roughness directly on the point cloud from the structure from motion processing and showed its correlation to biomass. Often, the TFs are difficult to interpret and their link to yield relevant canopy traits is often unclear. Originally, the TFs were developed for classification (Haralick et al., 1973) and therefore classifying varieties corresponds more to their intended purpose than yield prediction. TFs are further often used in combination because there might be additional information (Wang et al., 2021; Liu et al., 2022), especially in the later stage, when they are not strongly correlated to single band reflectances and VIs anymore, as indicated by our results.

4.4 Effects of temporal feature selection for yield prediction and classification

Models using individual dates showed generally a worse performance than models containing three adjacent dates. Furthermore, the performance between different dates is fluctuating strongly, even if the phenological stage is similar. Prey et al. (2022) found combining data from multiple dates to yield more improved predictions especially if the features used were performing poorly. In our case, the improvement for the yield prediction was in a similar range, regardless of the initial performance of the feature. In rice, Zhou et al. (2017) found that combining data from different growth stages by a multilinear regression model, can improve the estimation accuracy. For practical applications, finding the optimal date might be difficult and requires very close monitoring of the phenology, which can be very diverse among varieties as in our variety-testing panel. Therefore combining multiple dates might be especially performant, if features are used that show a high fluctuation between dates such as the TFs. The RF algorithm however is capable of dealing with different suitability of dates and therefore neglect the ones that do not perform well by attributing different importance to the features. The downside of the method is that, obtaining the additional measurements requires substantial work. Therefore, the number and time points measured should be considered carefully and be optimized in future studies.

4.5 Limitations and outlook

The red-edge position and its shape is often used to estimate the stress status of field crops (Guyot et al., 1988; Boochs et al., 1990). However, it is obvious that the dynamics (time series) of the Red-edge band is difficult to interpret compared to the visible bands. During the early stages of tillering, the red-edge reflectance increased, possibly due to an increase of ground cover, whereas later it decreased again, when the canopy height increased during the SE stage. At the beginning of the heading stage, another increase in the red-edge reflectance could be observed, accompanied with the increase of reflectance in the visible bands. However, in contrast to other bands, the Red-edge reflectance decreases with the onset of senescence at the early grain-filling stage, possibly due to a reduction in chlorophyll and a shrinking canopy structure (Wang et al., 2022). However, fluctuation also occurs during the mentioned stable period running from the beginning of booting to the end of flowering. These fluctuations can be of various origins. For instance, the appearance of the canopy might change significantly due to the emergence of the spikes. Although this study was unable to exploit the entire shape of the red-edge reflectance, due to limitations in our multispectral camera having one band in the red-edge region, future work should further advance the understanding of the dynamics of red-edge reflectance and responsible canopy characteristics. Also, features should, in addition to their performance for yield prediction be assessed regarding their heritability (H^2) since breeders are interested in knowing the genetic variation underlying a trait or in our case a spectral feature. Generally, this study shows that a trait time series followed by smoothing and a moving window allows for more stable predictions when also not better predictions.

5 Conclusions

Most spectral and TFs derived from the canopy multispectral images were related to variations in yield and delivered the best predictions of yield between booting and the beginning of senescence. Still, predictions before and after this stages yielded respectable results as well. Vegetation indices (VIs) generally outperformed single indices in assessing yield and in classifying varieties. Particularly the Normalized Difference Red Edge (NDRE) index performed well in both years and at several phenology stages. Single bands, especially the RED band showed a comparable performance but with more fluctuations between dates. In contrast, the REDEDGE reflectance showed poorer performance in yield and variety classification. TFs generally performed poorly for yield prediction, and their performances were inconsistent across dates in this study. TFs showed a good performance when classifying varieties. Further research is still needed to better understand the applicability of different TFs for yield- and traits predictions. Smoothing or combining data across a time series can enhance the performance of yield prediction and classification models, particularly in the early growth stages. Future studies should combine different feature types to leverage complementary information captured by different types of multispectral features and variables.

Data availability statement

The raw data supporting the conclusions of this article will be made available by the authors, without undue reservation.

Author contributions

KY designed the experiment. MC managed the UAV flights for aerial imagery, analyzed the data, and conducted the ground-based field measurements with supervision from KY. MC and KY wrote and revised the manuscript. All authors contributed to the article and approved the submitted version.

Funding

The author(s) declare financial support was received for the research, authorship, and/or publication of this article. The work has been partly supported by the HEF seed fund 2021 and the TUM Plant Technology Center (PTC).

Acknowledgments

We thank Juan Herrera (Agroscope, Switzerland) for composing the variety-testing panel and providing the seeds. Further, we thank Wolfgang Heer for trial management, Jürgen Plass for technical support with the spectral measurements and Michael Thaler as well as Muhammad Rehan for the help with data collection.

Conflict of interest

The authors declare that the research was conducted in the absence of any commercial or financial relationships that could be construed as a potential conflict of interest.

Publisher's note

Supplementary material

The Supplementary Material for this article can be found online at: https://www.frontiersin.org/articles/10.3389/fpls.2023.1214931/full#supplementary-material

References

Araus, J. L., and Cairns, J. E. (2014). Field high-throughput phenotyping: the new crop breeding frontier. *Trends Plant Sci.* 19, 52–61. doi: 10.1016/j.tplants.2013.09.008

Araus, J. L., Slafer, G. A., Royo, C., and Serret, M. D. (2008). Breeding for yield potential and stress adaptation in cereals. *Crit. Rev. Plant Sci.* 27, 377–412. doi: 10.1080/07352680802467736

Argento, F., Anken, T., Abt, F., Vogelsanger, E., Walter, A., and Liebisch, F. (2021). Site-specific nitrogen management in winter wheat supported by low-altitude remote sensing and soil data. *Precis. Agric.* 22, 364–386. doi: 10.1007/s11119-020-09733-3

Barnes, E., Clarke, T., Richards, S., Colaizzi, P., Haberland, J., Kostrzewski, M., et al. (2000). Coincident detection of crop water stress, nitrogen status and canopy density using ground based multispectral data. *Proc. Fifth Int. Conf. Precis. Agriculture Bloomington MN U.S.A.* 1619, 6.

Bastos, L. M., Carciochi, W., Lollato, R. P., Jaenisch, B. R., Rezende, C. R., Schwalbert, R., et al. (2020). Winter wheat yield response to plant density as a function of yield environment and tillering potential: A review and field studies. *Front. Plant Sci.* 11. doi: 10.3389/fpls.2020.00054

Bonhomme, R. (2000). Bases and limits to using 'degree.day' units. *Eur. J. Agron.* 13, 1–10. doi: 10.1016/S1161-0301(00)00058-7

Boochs, F., Kupfer, G., Dockter, K., and Kühbauch, W. (1990). Shape of the red edge as vitality indicator for plants. *Int. J. Remote Sens.* 11, 1741–1753. doi: 10.1080/01431169008955127

Bowman, B. C., Chen, J., Zhang, J., Wheeler, J., Wang, Y., Zhao, W., et al. (2015). Evaluating grain yield in spring wheat with canopy spectral reflectance. *Crop Sci.* 55, 1881–1890. doi: 10.2135/cropsci2014.08.0533

Bukowiecki, J., Rose, T., Ehlers, R., and Kage, H. (2020). High-throughput prediction of whole season green area index in winter wheat with an airborne multispectral sensor. *Front. Plant Sci.* 10. doi: 10.3389/fpls.2019.01798

Cabrera-Bosquet, L., Crossa, J., Von Zitzewitz, J., Serret, M. D., and Luis Araus, J. (2012). High-throughput phenotyping and genomic selection: the frontiers of crop breeding convergeF. *J. Integr. Plant Biol.* 54, 312–320. doi: 10.1111/j.1744-7909.2012.01116.x

Coburn, C. A., and Roberts, A. C. B. (2004). A multiscale texture analysis procedure for improved forest stand classification. *Int. J. Remote Sens.* 25, 4287–4308. doi: 10.1080/0143116042000192367

Cormier, F., Faure, S., Dubreuil, P., Heumez, E., Beauchêne, K., Lafarge, S., et al. (2013). A multi-environmental study of recent breeding progress on nitrogen use efficiency in wheat (Triticum aestivum L.). *Theor. Appl. Genet.* 126, 3035–3048. doi: 10.1007/s00122-013-2191-9

Daughtry, C. S. T., Walthall, C. L., Kim, M. S., De Colstoun, E. B., and Mcmurtrey, J. E. (2000). Estimating corn leaf chlorophyll concentration from leaf and canopy reflectance. *Remote Sens. Environ.* 74, 229–239. doi: 10.1016/S0034-4257(00)00113-9

David, E., Daubige, G., Joudelat, F., Burger, P., Comar, A., De Solan, B., et al. (2021). Plant detection and counting from high-resolution RGB images acquired from UAVs: comparison between deep-learning and handcrafted methods with application to maize, sugar beet, and sunflower. *bioRxiv*2021.2004.2027.441631. doi: 10.1101/2021.04.27.441631

David, E., Madec, S., Sadeghi-Tehran, P., Aasen, H., Zheng, B., Liu, S., et al. (2020). Global wheat head detection (GWHD) dataset: A large and diverse dataset of high-resolution RGB-labelled images to develop and benchmark wheat head detection methods. *Plant Phenomics* 2020. doi: 10.34133/2020/3521852

Deutsche Landesvermessung. (2023). *Satellitenpositionierungsdienst der Deutschen Landesvermessung*. Available at: https://www.ldbv.bayern.de/produkte/gis_gps/dgps/dgps.html (Accessed 22.02.2023).

Duan, T., Chapman, S. C., Guo, Y., and Zheng, B. (2017). Dynamic monitoring of NDVI in wheat agronomy and breeding trials using an unmanned aerial vehicle. *Field Crops Res.* 210, 71–80. doi: 10.1016/j.fcr.2017.05.025

Elsayed, S., Elhoweity, M., Ibrahim, H. H., Dewir, Y. H., Migdadi, H. M., and Schmidhalter, U. (2017). Thermal imaging and passive reflectance sensing to estimate the water status and grain yield of wheat under different irrigation regimes. *Agric. Water Manage.* 189, 98–110. doi: 10.1016/j.agwat.2017.05.001

Eskandari, R., Mahdianpari, M., Mohammadimanesh, F., Salehi, B., Brisco, B., and Homayouni, S. (2020). Meta-analysis of unmanned aerial vehicle (UAV) imagery for agro-environmental monitoring using machine learning and statistical models. *Remote Sens.* 12, 3511. doi: 10.3390/rs12213511

Fernandez-Gallego, J. A., Kefauver, S. C., Vatter, T., Aparicio Gutiérrez, N., Nieto-Taladriz, M. T., and Araus, J. L. (2019). Low-cost assessment of grain yield in durum wheat using RGB images. *Eur. J. Agron.* 105, 146–156. doi: 10.1016/j.eja.2019.02.007

Fischer, R. A. (1985). Number of kernels in wheat crops and the influence of solar radiation and temperature. *J. Agric. Sci.* 105, 447–461. doi: 10.1017/S0021859600056495

Fischer, R. A. (2011). Wheat physiology: a review of recent developments. *Crop Pasture Sci.* 62, 95–114. doi: 10.1071/CP10344

Garriga, M., Romero-Bravo, S., Estrada, F., Escobar, A., Matus, I. A., Del Pozo, A., et al. (2017). Assessing wheat traits by spectral reflectance: do we really need to focus on predicted trait-values or directly identify the elite genotypes group? *Front. Plant Sci.* 8. doi: 10.3389/fpls.2017.00280

Gdal/Ogr Contributors (2023). *GDAL/OGR Geospatial Data Abstraction software Library* (Delaware, USA: Open Source Geospatial Foundation).

González, F. G., Slafer, G. A., and Miralles, D. J. (2005). Floret development and survival in wheat plants exposed to contrasting photoperiod and radiation environments during stem elongation. *Funct. Plant Biol.* 32, 189–197. doi: 10.1071/FP04104

Grieder, C., Hund, A., and Walter, A. (2015). Image based phenotyping during winter: a powerful tool to assess wheat genetic variation in growth response to temperature. *Funct. Plant Biol.* 42, 387–396. doi: 10.1071/FP14226

Guyot, G., Baret, F., and Major, D. (1988). High spectral resolution: determination of spectral shifts between the red and near infrared. *ISPRS Congress*. 11, 750–760.

Haboudane, D., Miller, J. R., Tremblay, N., Zarco-Tejada, P. J., and Dextraze, L. (2002). Integrated narrow-band vegetation indices for prediction of crop chlorophyll content for application to precision agriculture. *Remote Sens. Environ.* 81, 416–426. doi: 10.1016/S0034-4257(02)00018-4

Hall-Beyer, M. (2017). Practical guidelines for choosing GLCM textures to use in landscape classification tasks over a range of moderate spatial scales. *Int. J. Remote Sens.* 38, 1312–1338. doi: 10.1080/01431161.2016.1278314

Haralick, R. M., Shanmugam, K., and Dinstein, I. (1973). Textural features for image classification. *IEEE Trans. Systems Man Cybernetics* SMC-3, 610–621. doi: 10.1109/TSMC.1973.4309314

Hassan, M. A., Yang, M., Rasheed, A., Yang, G., Reynolds, M., Xia, X., et al. (2019). A rapid monitoring of NDVI across the wheat growth cycle for grain yield prediction using a multi-spectral UAV platform. *Plant Sci.* 282, 95–103. doi: 10.1016/j.plantsci.2018.10.022

Heil, K., Klöpfer, C., Hülsbergen, K.-J., and Schmidhalter, U. (2023). Description of meteorological indices presented based on long-term yields of winter wheat in southern Germany. *Agriculture* 13, 1904. doi: 10.3390/agriculture13101904

Herrero-Huerta, M., Bucksch, A., Puttonen, E., and Rainey, K. M. (2020). Canopy roughness: A new phenotypic trait to estimate aboveground biomass from unmanned aerial system. *Plant Phenomics* 2020, 6735967. doi: 10.34133/2020/6735967

Hinzman, L., Bauer, M. E., and Daughtry, C. (1984). *Growth and reflectance characteristics of winter wheat canopies* (West Lafayette, IN, USA: Purdue University).

Hinzman, L. D., Bauer, M. E., and Daughtry, C. S. T. (1986). Effects of nitrogen fertilization on growth and reflectance characteristics of winter wheat. *Remote Sens. Environ.* 19, 47–61. doi: 10.1016/0034-4257(86)90040-4

Holen, D. L., Bruckner, P. L., Martin, J. M., Carlson, G. R., Wichman, D. M., and Berg, J. E. (2001). Response of winter wheat to simulated stand reduction. *Agron. J.* 93, 364–370. doi: 10.2134/agronj2001.932364x

Horler, D. N. H., Dockray, M., and Barber, J. (1983). The red edge of plant leaf reflectance. *Int. J. Remote Sens.* 4, 273–288. doi: 10.1080/01431168308948546

Hund, A., Kronenberg, L., Anderegg, J., Yu, K., and Walter, A. (2019). “Non-invasive field phenotyping of cereal development,” in *Advances in breeding techniques for cereal crops.* (Cambridge, Uited Kingdom: Burleigh Dodds Science Publishing), 249–292.

Khojastehnazhand, M., and Roostaei, M. (2022). Classification of seven Iranian wheat varieties using texture features. *Expert Syst. Appl.* 199, 117014. doi: 10.1016/j.eswa.2022.117014

Korobov, R. M., and Railyan, V. Y. (1993). Canonical correlation relationships among spectral and phytometric variables for twenty winter wheat fields. *Remote Sens. Environ.* 43, 1–10. doi: 10.1016/0034-4257(93)90059-7

Kuhn, M. (2008). Building predictive models in R using the caret package. *J. Stat. Software* 28, 1–26. doi: 10.18637/jss.v028.i05

Li, J., Bhatta, M., Garst, N. D., Stoll, H., Veeranampalayam-Sivakumar, A.-N., Baenziger, P. S., et al. (2019a). “Principal variable selection to explain grain yield variation in winter wheat from UAV-derived phenotypic traits,” in *2019 ASABE Annual International Meeting.* (St. Joseph, MI: ASABE).

Li, J., Veeranampalayam-Sivakumar, A.-N., Bhatta, M., Garst, N. D., Stoll, H., Baenziger, S. P., et al. (2019b). Principal variable selection to explain grain yield variation in winter wheat from features extracted from UAV imagery. *Plant Methods* 15, 123. doi: 10.1186/s13007-019-0508-7

Li, Q., Jin, S., Zang, J., Wang, X., Sun, Z., Li, Z., et al. (2022). Deciphering the contributions of spectral and structural data to wheat yield estimation from proximal sensing. *Crop J.* 10, 1334–1345. doi: 10.1016/j.cj.2022.06.005

Li, S., Yuan, F., Ata-Ui-Karim, S. T., Zheng, H., Cheng, T., Liu, X., et al. (2019c). Combining color indices and textures of UAV-based digital imagery for rice LAI estimation. *Remote Sens.* 11, 1763. doi: 10.3390/rs11151763

Liu, Y., Feng, H., Yue, J., Li, Z., Yang, G., Song, X., et al. (2022). Remote-sensing estimation of potato above-ground biomass based on spectral and spatial features extracted from high-definition digital camera images. *Comput. Electron. Agric.* 198, 107089. doi: 10.1016/j.compag.2022.107089

Marti, J., Bort, J., Slafer, G. A., and Araus, J. L. (2007). Can wheat yield be assessed by early measurements of Normalized Difference Vegetation Index? *Ann. Appl. Biol.* 150, 253–257. doi: 10.1111/j.1744-7348.2007.00126.x

Meier, U., Bleiholder, H., Buhr, L., Feller, C., Hack, H., Heß, M., et al. (2009). The BBCH system to coding the phenological growth stages of plants–history and publications. *J. für Kulturpflanzen* 61, 41–52. doi: 10.5073/20180906-074619

Millet, E. J., Rodriguez Alvarez, M. X., Perez Valencia, D. M., Sanchez, I., Hilgert, N., Van Rossum, B.-J., et al. (2022). statgenHTP: high throughput phenotyping (HTP) data analysis.

Nguy-Robertson, A., Gitelson, A., Peng, Y., Viña, A., Arkebauer, T., and Rundquist, D. (2012). Green leaf area index estimation in maize and soybean: combining vegetation indices to achieve maximal sensitivity. *Agron. J.* 104, 1336–1347. doi: 10.2134/agronj2012.0065

Pan, Y., Zhou, R., Zhang, J., Guo, W., Yu, M., Guo, C., et al. (2023). A new spectral index for estimation of wheat canopy chlorophyll density: considering background interference and view zenith angle effect. *Precis. Agriculture*. 24, 2098–2125. doi: 10.1007/s11119-023-10032-w

Pang, J., Palta, J. A., Rebetzke, G. J., and Milroy, S. P. (2014). Wheat genotypes with high early vigour accumulate more nitrogen and have higher photosynthetic nitrogen use efficiency during early growth. *Funct. Plant Biol.* 41, 215–222. doi: 10.1071/FP13143

Patrignani, A., Lollato, R. P., Ochsner, T. E., Godsey, C. B., and Edwards, J. T. (2014). Yield gap and production gap of rainfed winter wheat in the southern great plains. *Agron. J.* 106, 1329–1339. doi: 10.2134/agronj14.0011

Pavuluri, K., Chim, B. K., Griffey, C. A., Reiter, M. S., Balota, M., and Thomason, W. E. (2015). Canopy spectral reflectance can predict grain nitrogen use efficiency in soft red winter wheat. *Precis. Agric.* 16, 405–424. doi: 10.1007/s11119-014-9385-2

Pinter, P. J., Jackson, R. D., Idso, S. B., and Reginato, R. J. (1981). Multidate spectral reflectance as predictors of yield in water stressed wheat and barley. *Int. J. Remote Sens.* 2, 43–48. doi: 10.1080/01431168108948339

Porker, K., Zerner, M., and Cozzolino, D. (2017). Classification and authentication of barley (Hordeum vulgare) malt varieties: combining attenuated total reflectance mid-infrared spectroscopy with chemometrics. *Food Analytical Methods* 10, 675–682. doi: 10.1007/s12161-016-0627-y

Prey, L., Hanemann, A., Ramgraber, L., Seidl-Schulz, J., and Noack, P. O. (2022). UAV-based estimation of grain yield for plant breeding: applied strategies for optimizing the use of sensors, vegetation indices, growth stages, and machine learning algorithms. *Remote Sens.* 14, 6345. doi: 10.3390/rs14246345

Prey, L., Hu, Y., and Schmidhalter, U. (2020). High-throughput field phenotyping traits of grain yield formation and nitrogen use efficiency: optimizing the selection of vegetation indices and growth stages. *Front. Plant Sci.* 10. doi: 10.3389/fpls.2019.01672

Raun, W. R., Solie, J. B., Johnson, G. V., Stone, M. L., Lukina, E. V., Thomason, W. E., et al. (2001). In-season prediction of potential grain yield in winter wheat using canopy reflectance. *Agron. J.* 93, 131–138. doi: 10.2134/agronj2001.931131x

Ray, D. K., Mueller, N. D., West, P. C., and Foley, J. A. (2013). Yield trends are insufficient to double global crop production by 2050. *PloS One* 8, e66428. doi: 10.1371/journal.pone.0066428

R Core Team (2021). *R: A language and environment for statistical computing* (Vienna, Austria: R foundation for statistical computing).

Rischbeck, P., Elsayed, S., Mistele, B., Barmeier, G., Heil, K., and Schmidhalter, U. (2016). Data fusion of spectral, thermal and canopy height parameters for improved yield prediction of drought stressed spring barley. *Eur. J. Agron.* 78, 44–59. doi: 10.1016/j.eja.2016.04.013

Shibayama, M., Salli, A., Häme, T., Iso-Iivari, L., Heino, S., Alanen, M., et al. (1999). Detecting phenophases of subarctic shrub canopies by using automated reflectance measurements. *Remote Sens. Environ.* 67, 160–180. doi: 10.1016/S0034-4257(98)00082-0

Slafer, G., Calderini, D., and Miralles, D. (1996). Yield components and compensation in wheat: opportunities for further increasing yield potential. *Increasing yield potential wheat: Breaking Barriers*, 101–133.

Slafer, G., and Rawson, H. (1994). Sensitivity of wheat phasic development to major environmental factors: a re-examination of some assumptions made by physiologists and modellers. *Funct. Plant Biol.* 21, 393–426. doi: 10.1071/PP9940393

Spano, G., Di Fonzo, N., Perrotta, C., Platani, C., Ronga, G., Lawlor, D. W., et al. (2003). Physiological characterization of 'stay green' mutants in durum wheat. *J. Exp. Bot.* 54, 1415–1420. doi: 10.1093/jxb/erg150

Tucker, C. J. (1979). Red and photographic infrared linear combinations for monitoring vegetation. *Remote Sens. Environ.* 8, 127–150. doi: 10.1016/0034-4257(79)90013-0

Vatter, T., Gracia-Romero, A., Kefauver, S. C., Nieto-Taladriz, M. T., Aparicio, N., and Araus, J. L. (2022). Preharvest phenotypic prediction of grain quality and yield of durum wheat using multispectral imaging. *Plant J.* 109, 1507–1518. doi: 10.1111/tpj.15648

Walsh, O. S., Marshall, J., Jackson, C., Nambi, E., Shafian, S., Jayawardena, D. M., et al. (2022). Wheat yield and protein estimation with handheld- and UAV-based reflectance measurements. *Agrosystems Geosciences Environ.* 5, e20309. doi: 10.1002/agg2.20309

Wang, F., Li, W., Liu, Y., Qin, W., Ma, L., Zhang, Y., et al. (2022). Characterization of N distribution in different organs of winter wheat using UAV-based remote sensing. *bioRxiv*2022.2011.2002.514839. doi: 10.1101/2022.11.02.514839

Wang, F., Yi, Q., Hu, J., Xie, L., Yao, X., Xu, T., et al. (2021). Combining spectral and textural information in UAV hyperspectral images to estimate rice grain yield. *Int. J. Appl. Earth Observation Geoinformation* 102, 102397. doi: 10.1016/j.jag.2021.102397

Watt, M., Fiorani, F., Usadel, B., Rascher, U., Muller, O., and Schurr, U. (2020). Phenotyping: new windows into the plant for breeders. *Annu. Rev. Plant Biol.* 71, 689–712. doi: 10.1146/annurev-arplant-042916-041124

Wu, X.-Y., Kuai, B.-K., Jia, J.-Z., and Jing, H.-C. (2012). Regulation of leaf senescence and crop genetic improvementF. *J. Integr. Plant Biol.* 54, 936–952. doi: 10.1111/jipb.12005

Xie, Q., Dash, J., Huang, W., Peng, D., Qin, Q., Mortimer, H., et al. (2018). Vegetation indices combining the red and red-edge spectral information for leaf area index retrieval. *IEEE J. Selected Topics Appl. Earth Observations Remote Sens.* 11, 1482–1493. doi: 10.1109/JSTARS.2018.2813281

Xu, X., Geng, Q., Gao, F., Xiong, D., Qiao, H., and Ma, X. (2023). Segmentation and counting of wheat spike grains based on deep learning and textural feature. *Plant Methods* 19, 77. doi: 10.1186/s13007-023-01062-6

Yue, J., Yang, G., Tian, Q., Feng, H., Xu, K., and Zhou, C. (2019). Estimate of winter-wheat above-ground biomass based on UAV ultrahigh-ground-resolution image textures and vegetation indices. *ISPRS J. Photogrammetry Remote Sens.* 150, 226–244. doi: 10.1016/j.isprsjprs.2019.02.022

Zhang, J., Qiu, X., Wu, Y., Zhu, Y., Cao, Q., Liu, X., et al. (2021). Combining texture, color, and vegetation indices from fixed-wing UAS imagery to estimate wheat growth parameters using multivariate regression methods. *Comput. Electron. Agric.* 185, 106138. doi: 10.1016/j.compag.2021.106138

Zheng, H., Cheng, T., Zhou, M., Li, D., Yao, X., Tian, Y., et al. (2019). Improved estimation of rice aboveground biomass combining textural and spectral analysis of UAV imagery. *Precis. Agric.* 20, 611–629. doi: 10.1007/s11119-018-9600-7

Zhou, M., Zheng, H., He, C., Liu, P., Awan, G. M., Wang, X., et al. (2023). Wheat phenology detection with the methodology of classification based on the time-series UAV images. *Field Crops Res.* 292, 108798. doi: 10.1016/j.fcr.2022.108798

Zhou, X., Zheng, H. B., Xu, X. Q., He, J. Y., Ge, X. K., Yao, X., et al. (2017). Predicting grain yield in rice using multi-temporal vegetation indices from UAV-based multispectral and digital imagery. *ISPRS J. Photogrammetry Remote Sens.* 130, 246–255. doi: 10.1016/j.isprsjprs.2017.05.003

Frontiers in
Plant Science

Cultivates the science of plant biology and its applications

The most cited plant science journal, which advances our understanding of plant biology for sustainable food security, functional ecosystems and human health.

Discover the latest Research Topics

See more →

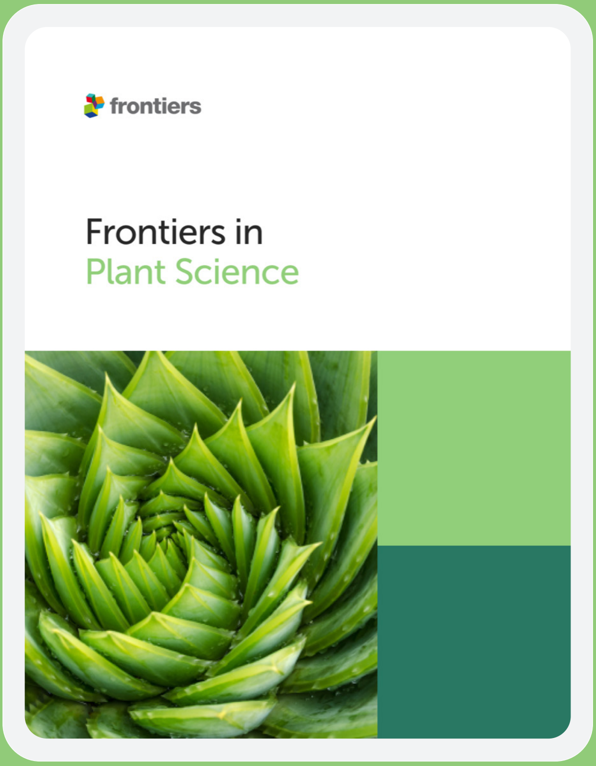

frontiers

Frontiers in
Plant Science

Frontiers

Avenue du Tribunal-Fédéral 34
1005 Lausanne, Switzerland
frontiersin.org

Contact us

+41 (0)21 510 17 00
frontiersin.org/about/contact